Transactions of the ASME®

Transactions of the ASME, The Journal of Fluids Engineering (ISSN 0098-2202) is published quarterly (Mar., June, Sept., Dec.) for $95 per year by The American Society of Mechanical Engineers, 345 East 47th Street, New York, NY 10017. Second class postage paid at New York, NY and additional mailing offices. POSTMASTER: Send address changes to The Journal of Fluids Engineering, c/o THE AMERICAN SOCIETY OF MECHANICAL ENGINEERS, 22 Law Drive, Box 2300, Fairfield, NJ 07007-2300.
CHANGES OF ADDRESS must be received at Society headquarters seven weeks before they are to be effective. Please send old label and new address.
PRICES: To members, $27.00, annually; to nonmembers, $95. Add $12.00 for postage to countries outside the United States and Canada.
STATEMENT from By-Laws. The Society shall not be responsible for statements or opinions advanced in papers or . . . printed in its publications (B7.1, Par. 3).

INDEXED by Applied Mechanics Reviews and Engineering Information, Inc.

Journal of Fluids Engineering

Published Quarterly by The American Society of Mechanical Engineers

VOLUME 109 • NUMBER 4 • DECEMBER 1987

A Calculation Scheme for Three-Dimensional Viscous Incompressible Flows

M. Reggio

R. Camarero

Ecole Polytechnique,
Montreal, Canada

A numerical procedure to solve three-dimensional incompressible flows in arbitrary shapes is presented. The conservative form of the primitive-variable formulation of the time-dependent Navier-Stokes equations written for a general curvilinear coordiante system is adopted. The numerical scheme is based on an overlapping grid combined with opposed differencing for mass and pressure gradients. The pressure and the velocity components are stored at the same location: the center of the computational cell which is used for both mass and the momentum balance. The resulting scheme is stable and no oscillations in the velocity or pressure fields are detected. The method is applied to test cases of ducting and the results are compared with experimental and numerical data.

1 Introduction

When a fluid moves through a curved duct, the centrifugal forces arising from the channel curvature set up a secondary motion which is superimposed to the primary flow. These phenomena give rise to an helical movement that has the effect of shifting high velocity regions toward the walls, with the consequent increase of the frictional losses.

Progress in internal fluid mechanics demands the study of this type of three-dimensional flow, because it constitutes an analysis tool allowing a better understanding of problems of practical interest. In view of the impossibility of finding analytical solutions for such phenomena, the research capability is intimately related to the availability of appropriate numerical tools.

The objective of this paper is to present a numerical scheme to predict some of the characteristics of the incompressible flow through ductings which are important in a design process. This is achieved by solving the three-dimensional time-dependent incompressible Navier-Stokes equations using a control volume approach.

The main difficulties associated with the solution of this type of problem are the treatment of the boundary conditions on the geometries that bound the domain, the choice of a proper storage location for the dependent variables and the lack of an explicit equation for the pressure.

The problem of the complex boundaries is treated by formulating and solving the conservation equations on a curvilinear coordinate system that matches the domain boundary. This is useful because the boundary conditions can be implemented accurately in the numerical solution of the governing equations. Different techniques can be used to numerically generate a curvilinear mesh, and a detailed review of the subject has been given in [1], and a specific 3-D generation procedure can be found in [2].

The computational discretization currently used for solving incompressible fluid flow problems is based on a staggered grid [3]. This technique requires a different location, together with a distinct computational cell for each velocity component and the pressure. In the present study it is proposed to compute the pressure and the velocity components at the same grid location. These parameters are located at the center of the same computational cell which is used for both the momentum and continuity balances. To avoid unrealistics fields, that normally would appear with such discretization, an opposed difference scheme for pressure and fluxes is used in the main flow direction.

Finally the pressure and velocity fields are coupled by means of a pressure equation derived on the basis of the SIMPLE method [4] modified for a curvilinear grid.

The present method has been applied to obtain the numerical solution of flows within ducts of different geometries. The results reveal the complex nature of the three-dimensional phenomena showing some aspects of the secondary flow.

2 Conservation Equations

The equations of motion written in the conservative form for a curvilinear system can be written as [5, 6]:

$$\frac{\partial q}{\partial t}+\frac{\partial E}{\partial \xi}+\frac{\partial F}{\partial \eta}+\frac{\partial G}{\partial \zeta}=\frac{\partial R}{\partial \xi}+\frac{\partial S}{\partial \eta}+\frac{\partial T}{\partial \zeta} \tag{1}$$

where ξ represents the "streamwise" direction, η, the "normal" direction and ζ the "binormal" direction as illustrated in Fig. 1

Contributed by the Fluids Engineering Division for publication in the JOURNAL OF FLUIDS ENGINEERING. Manuscript received by the Fluids Engineering Division July 8, 1986.

The flux and diffusion terms in equation (1) are:

$$q = J\begin{pmatrix} 0 \\ u \\ v \\ w \end{pmatrix} \qquad E = J\begin{pmatrix} U \\ uU + p\xi_x \\ uV + p\xi_y \\ wU + p\xi_z \end{pmatrix}$$

$$F = J\begin{pmatrix} V \\ uV + p\eta_x \\ vV + p\eta_y \\ wV + p\eta_z \end{pmatrix} \qquad G = J\begin{pmatrix} W \\ uW + p\zeta_x \\ vW + p\zeta_y \\ wW + p\zeta_z \end{pmatrix}$$

$$R = \mu J\begin{pmatrix} 0 \\ g^{11}u_\xi + g^{12}u_\eta + g^{13}u_\zeta \\ g^{11}v_\xi + g^{12}v_\eta + g^{13}v_\zeta \\ g^{11}w_\xi + g^{12}w_\eta + g^{13}w_\zeta \end{pmatrix}$$

$$S = \mu J\begin{pmatrix} 0 \\ g^{21}u_\xi + g^{22}u_\eta + g^{23}u_\zeta \\ g^{21}v_\xi + g^{22}v_\eta + g^{23}v_\zeta \\ g^{21}w_\xi + g^{22}w_\eta + g^{23}w_\zeta \end{pmatrix}$$

$$T = \mu J\begin{pmatrix} 0 \\ g^{31}u_\xi + g^{32}u_\eta + g^{33}u_\zeta \\ g^{31}v_\xi + g^{32}v_\eta + g^{33}v_\zeta \\ g^{31}w_\xi + g^{32}w_\eta + g^{33}w_\zeta \end{pmatrix}$$

where μ represents the viscosity.

The cartesian velocity components u, v, w and the contravariant velocity components U, V, W are related by:

$$\begin{aligned} U &= u\xi_x + v\xi_y + w\xi_z \\ V &= u\eta_x + v\eta_y + w\eta_z \\ W &= u\zeta_x + v\zeta_y + w\zeta_z \end{aligned} \tag{2}$$

The metric terms ξ_x, ξ_y, ξ_z, etc., the jacobian J and the contravariant metric tensor components g_{ij}, are obtained from:

$$\begin{aligned} \xi_x &= (y_\eta z_\zeta - y_\zeta z_\eta)/J \\ \xi_y &= (z_\eta x_\zeta - x_\eta z_\zeta)/J \\ \xi_z &= (x_\eta y_\zeta - y_\eta x_\zeta)/J \end{aligned}$$

$$\begin{aligned} \eta_x &= (z_\xi z_\zeta - y_\xi z_\zeta)/J \\ \eta_y &= (x_\xi z_\zeta - x_\zeta z_\xi)/J \\ \eta_z &= (y_\xi x_\zeta - x_\xi y_\zeta)/J \end{aligned}$$

$$\begin{aligned} \zeta_x &= (y_\xi z_\eta - z_\xi y_\eta)/J \\ \zeta_y &= (x_\eta z_\xi - x_\xi z_\eta)/J \\ \zeta_z &= (x_\xi y_\eta - y_\xi x_\eta)/J \end{aligned}$$

$$\begin{aligned} J = {} & x_\xi y_\eta z_\zeta + x_\zeta y_\xi z_\eta + x_\eta y_\zeta z_\xi \\ & - x_\xi y_\zeta z_\eta - x_\eta y_\xi z_\zeta - x_\zeta y_\eta z_\xi \end{aligned}$$

$$g_{ij} = \frac{\partial x_k \partial x_k}{\partial \xi^i \partial \xi^j}$$

with $\xi^1 = \xi$, $\xi^2 = \eta$, $\xi^3 = \zeta$

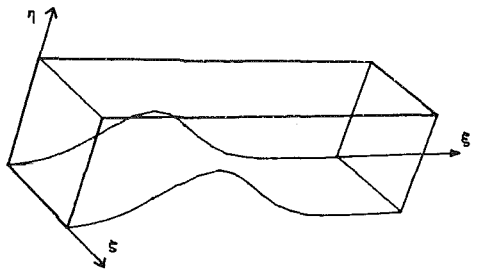

Fig. 1 Curvilinear axes

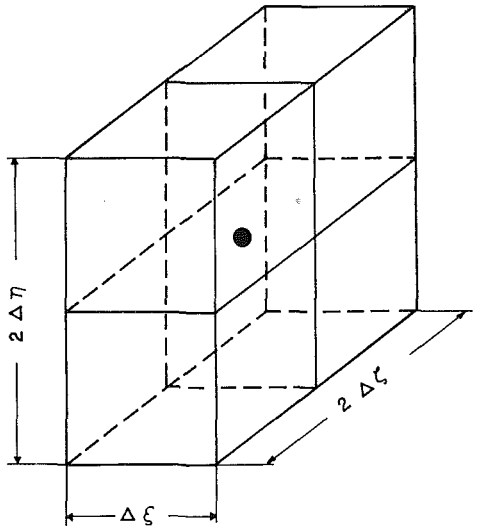

Fig. 2 Computational three-dimensional cell

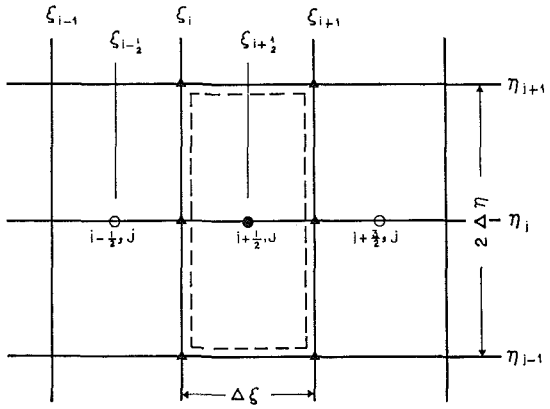

Fig. 3 Computational cell in 2 plane ζ = const

3 Discretization

In the proposed grid structure the pressure and cartesian velocity components are stored at the center of the computational cell. Figure 2 depicts this general cell which is made up of one unit in the "streamwise" direction and two units in the two other directions. Figure 3 shows a two-dimensional cell configuration on the computational $\xi - \eta$ (k = const) plane for ease of visualization. This basic cell is used for both mass and momentum balance.

Based on the above grid structure the discretization is carried out on the computational domain. Central differences are used to evaluate mass and pressure gradients in the η and ζ

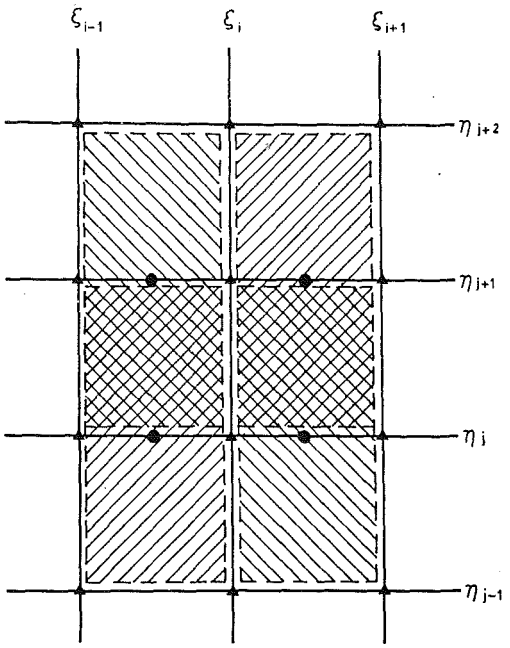

Fig. 4 Overlapping grid

directions. This yields a system of equations which requires the values of velocity at the $j+1,k$ and $j-1,k$ and $j,k-1$ and $j,k+1$ faces. These are not interpolated but are calculated by overlapping elements in those directions. The pressure is obtained by the averaging of neighboring points.

To gain insight into this overlapping procedure, we turn to an example in 2-D for a $k=$ const plane. To simplify the notation the third subscript will be omitted in the following discussion.

When solving the system (1) both cartesian and curvilinear components are required. The first set of components is calculated and stored at the center $i+1/2,j$ of the element (Fig. 3). As a result of the overlapping procedure in the j direction as illustrated on Fig. 4, these properties are also known at the $i+1/2$, $j+1$ location that corresponds to the center of the one cell half unit above. The same reasoning applies for the $j-1$, $k+1$, and $k-1$ levels.

With the cartesian velocity components known at all j and k levels, the V and W components are computed from equation (2) using:

$$V_{i+1/2,j\pm1} = u_{i+1/2,j\pm1}(\eta_x)_{i+1/2,j\pm1} + v_{i+1/2,j\pm1}(\eta_y)_{i+1/2,j\pm1} + w_{i+1/2,j\pm1}(\eta_z)_{i+1/2,j\pm1}$$

for $k=$ const, and

$$W_{i+1/2,k\pm1} = u_{i+1/2,k\pm1}(\zeta_x)_{i+1/2,k\pm1} + v_{i+1/2,k\pm1}(\zeta_y)_{i+1/2,k\pm1} + w_{i+1/2,k\pm1}(\zeta_z)_{i+1/2,k\pm1}$$

for $j=$ const.

In the "streamwise" direction ξ, no averaging or overlapping is used. Mass gradients are obtained by upwind differencing, so the flux through the downstream $i+1,j,k$ face is controlled by the velocity located at the center of the cell $i+1/2,j,k$. With this in mind the U velocity component is obtained from equation (2) for the $k=$ const levels as:

$$U_{i,j} = u_{i-1/2,j}(\xi_x)_{i,j} + v_{i-1/2,j}(\xi_y)_{i,j} + w_{i-1/2,j}(\xi_z)_{i,j}$$

On the other hand, pressure gradients are calculated by downwind differencing. This can be interpreted as if the pressure at the center of the element acts on its upstream face i, j, k.

The following u momentum equation summarizes the proposed discretization.

$$J_{i+1/2,j,k}\frac{(u^{n+1}-u^n)_{i+1/2,j,k}}{\Delta t} + \frac{(JuU)_{i+1,j,k}-(JuU)_{i,j,k}}{\Delta\xi} + \frac{(JuV)_{i+1/2,j+1,k}-(JuV)_{i+1/2,j-1,k}}{2\Delta\eta} \frac{(JuW)_{i+1/2,j,k+1}-(JuW)_{i+1/2,j,k-1}}{2\Delta\eta} + \frac{p_{i+3/2,j,k}(J\xi x)_{i+1,j,k}-p_{i+1/2,j,k}(J\xi x)_{i,j,k}}{\Delta\xi} + \frac{p_{i+1/2,j+1,k}(J\eta x)_{i+1/2,j+1,k}-p_{i+1/2,j-1,k}(J\eta_x)_{i+1/2,j-1,k}}{2\Delta\eta} + \frac{p_{i+1/2,j,k+1}(J\zeta_x)_{i+1/2,j,k+1}-p_{i+1/2,j,k-1}(J\zeta_x)_{i+1/2,j,k-1}}{2\Delta\zeta} + \mathrm{VIS}=0$$

where VIS represents the resulting viscous terms over the element.

A similar combination of backward and forward differences has been used by reference [7] for the solution of the compressible Euler equations. References [8, 9] have also used the opposed-differencing idea to solve the steady Navier-Stokes equations.

To evaluate the convected momentum fluxes and diffusion terms at the cell faces, the weighted upstream difference scheme of Raithby and Torrance [10] has been adopted. These authors propose the use of weights depending on the Peclet number to calculate the degree of upwinding.

4 Solution Procedure

The scheme is explicit and in a general form can be written as:

$$\Delta q + \Delta t(E_\xi + F_\eta + G_\zeta)^n = \Delta t(R_\xi + S_\eta + T_\zeta)^n \qquad (3)$$

where Δ denotes the forward time difference operator and the superscript n the time level.

The sequence of calculations is as follows. The velocity and pressure fields are first guessed. Then the three cartesian momentum components characterized by equation (3), are solved to get the three velocity components over the whole domain. These intermediate values do not satisfy mass conservation.

The next step is to adjust the velocity field in order that the continuity equation be satisfied. This is achieved through a suitable variation of the pressure field. The velocity-pressure coupling is based on the SIMPLE method [4]. By using the momentum equations, corrections to the curvilinear velocity components can be related to corrections to the pressure as:

$$\delta U = f^U(\delta p)$$
$$\delta V = f^v(\delta p) \qquad (4)$$
$$\delta W = f^W(\delta p)$$

These expressions together with the use of the continuity constraint lead to a Poisson-like equation for the pressure cor-

rection, which leads to the following relation:

$$A_p \delta p_p + \Sigma A_{nb} \delta p_{nb} = -D_p/\Delta t \tag{5}$$

Where the A's represent coefficients which are functions of the metric terms, δp is the pressure correction, and D the velocity divergence. The subscripts p and nb denote the center and the neighboring nodes, respectively.

This can be significantly simplified by neglecting the contribution of the surrounding points, which then reduces equation (5) to:

$$\delta p_p = -D_p/A_p \Delta t \tag{6}$$

and the pressure correction can be computed directly in terms of the divergence of the pressure field.

Once δp is evaluated, the corresponding curvilinear velocity corrections δU, δV, δW are calculated. These are then combined with the inexact velocity and pressure fields in order to verify the mass constraint requirement; that is:

$$\begin{aligned} U &= U^* + \delta U \\ V &= V^* + \delta V \\ W &= W^* + \delta W \\ p &= p^* + \delta p \end{aligned} \tag{7}$$

where U, V, W, p and U^*, V^*, W^*, p^* represent those values that do and do not respectively satisfy both mass and momentum equations. More details on the way that equations (5) to (7) are derived can be found in [6].

The sequence represented by equations (6) and (7) which involve the computing of the pressure change and the mass correction, respectively, is applied in such a way that no overlapping cells take part at this step. In particular, the correction procedure is applied to all the cells in the main flow direction, but only to every other cell in the secondary directions. In doing so, the continuity control volumes do not overlap (as the momentum cells do), and there is no particular difficulty associated with this discretization.

As a result of this methodology, only one corrected curvilinear velocity component is known on each face (U, V, W on the ξ, η, and ζ faces, respectively), and also the corrected pressure is not available at all the stations needed for the computing of the momentum equations. This inconvenience is solved by obtaining the two corresponding contravariant components, as well as the unknown pressure, as the average of surrounding known values. The cartesian velocity components are decoded by using the inverse relations of equations (2).

To update the working variables over the entire domain, a similar practice to the MAC method [11] is used. The grid is swept point-by-point in successive planes in the inlet-to-outlet direction. Improved values are immediately used as the procedure advances; consequently the right-hand-side term of equation (6) is intrinsically modified as the iterations progress. This is repeated until a desired level of accuracy is reached.

Finally the time step is advanced and the cycle is repeated until steady state is reached. This is estimated by comparing the root mean square of a velocity component between two consecutive time steps.

5 Boundary Conditions

5(*a*) Velocity. In the present approach both cartesian and curvilinear velocities take part in the calculation procedure, so boundary conditions should be given for both of them.

At the inlet a velocity profile in terms of the cartesian and contravariant components is specified. At a no-slip surface only one curvilinear component has to be supplied, because the other two do not contribute to the flow balance over the adjacent elements through these surfaces. This means for example that for the triad U, V, W along the ξ, η, ζ coordinates, only the W component is needed at a wall coincident with a ξ-η surface; and this value is zero.

In spite of the fact that the null mass flow is assured at the solid walls by the boundary condition on the curvilinear components, the cartesian velocity components are also required; they simply are $u = v = w = 0$.

At the outflow boundary, a zero gradient of the curvilinear components is specified from which the cartesian components are derived.

5(*b*) Pressure. The inspection of equation (6) reveals that the discrete form of the pressure correction equation will depend on the velocity components, including those next to the boundaries where the velocity is known (with the exception of the outlet). Consequently, the boundary conditions for the pressure correction equation are automatically incorporated through the right-hand-side term of equation (6) where the divergence of the velocity appears.

From this it follows that the pressure correction equation has no other boundary conditions than those applied on the velocity. However for the computation of the momentum equations, the pressure gradient has to be evaluated, and for the elements adjacent to the boundary a numerical boundary condition is needed.

At a solid wall a second order profile is fitted to the discrete points in order to obtain a pressure with a second order accuracy. This guarantees an approximation consistent over the entire computational domain. At the inflow boundary no condition is needed for the pressure because of the downwind scheme. At the outflow boundary with the assumption of a developed flow, a simple linear extrapolation is used, because the numerical error introduced by this calculation is not expected to propagate upstream. Once again, this estimation is carried out only for the momentum computation and not for the pressure correction equation.

6 Applications

6.1 Exponential Constriction. First, the behavior of the method was analyzed on a simple curvilinear geometry; the "hump test case" investigated by references [12, 13], who used a vector potential difference method. This geometry consists of a channel with an exponential constriction where the function $y = 1. - .5e^{-2x}$ represents the lower surface for all depths; while $y = 1.$ represents the flat upper surface. The mesh used was of $31 \times 11 \times 11$ points as shown in Fig. 5. A developed profile specified as $u = 36yz(1-y)(1-z)$, $v = 0.$, $w = 0.$ set at the inlet completes the problem description.

Figure 6(*a*) shows the velocity field in the obstruction planes $z = 0.1$ and $z = 0.5$ for a flow Reynolds number of 80. This form of the recirculation zone, evidently due to the three-dimensional character of the flow agrees with the results obtained by reference [12]. This phenomenon can also be observed from the velocity vectors in $\xi =$ constant sections, even though these sections are not strictly normal to the primary flow motion. This is presented in Fig. 6(*b*). When the flow reaches the obstruction, the bottom surface layer is forced towards the center line. As it falls down the rear of the constriction, this layer is forced towards the centerline. Finally two symmetric vortices are developed.

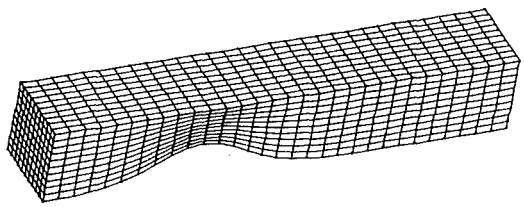

Fig. 5 3-D view of the duct mesh

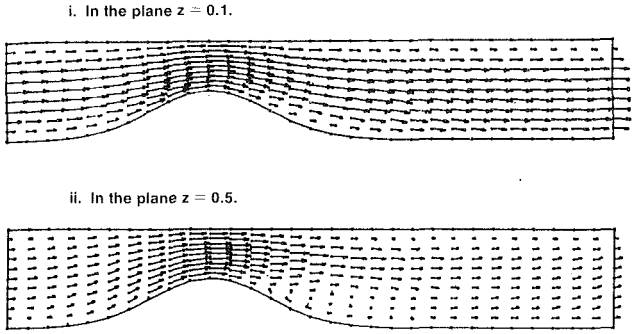

Fig. 6(*a*) Velocity field in planes = const., $R_e = 80$

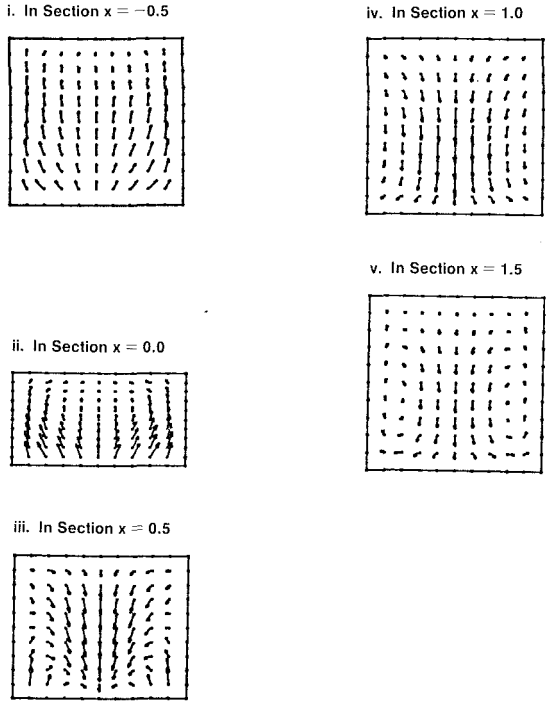

Fig. 6(*b*) Velocity development in ξ = const. surfaces

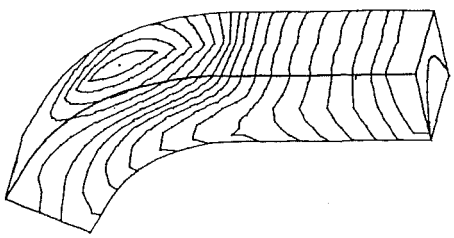

Fig. 7(*a*) Static pressure distribution for $R_e = 80$

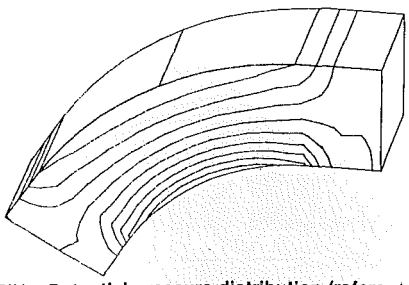

Fig. 7(*b*) Potential pressure distribution (reference [13])

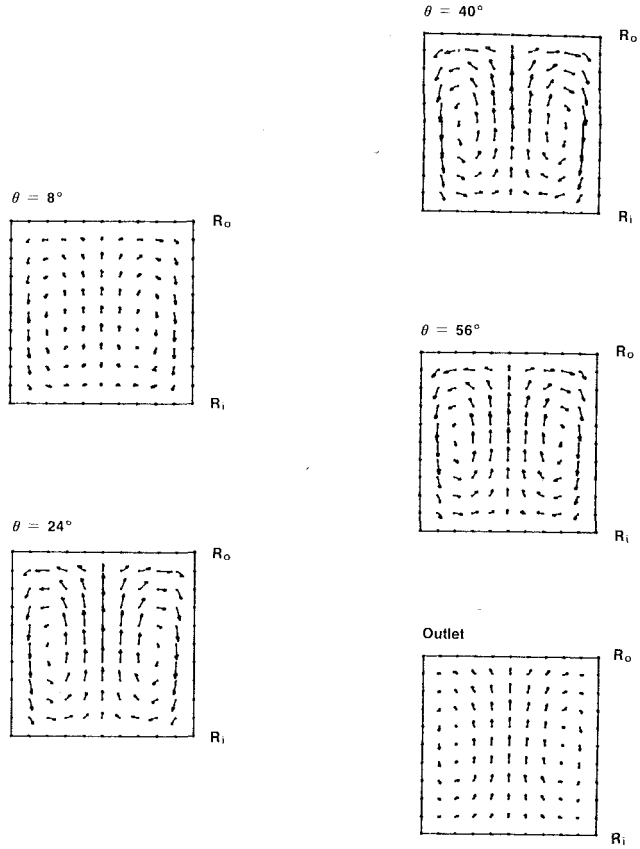

Fig. 7(*c*) Development of the secondary flow, $R_e = 80$

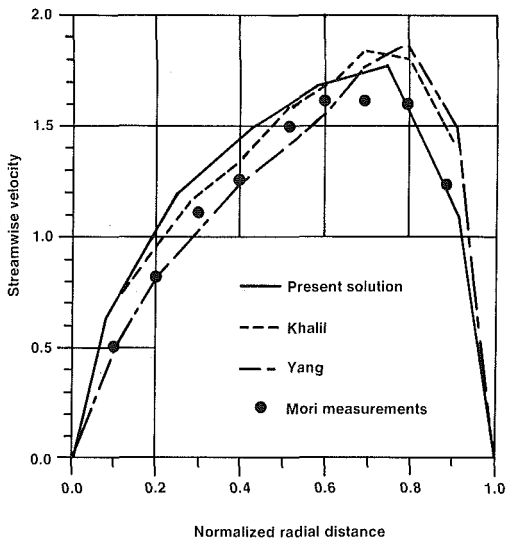

Fig. 7(*d*) Fully developed velocity profile

6.2 Circular Channel. A second calculation was carried out in a circular arc channel of square cross section with a Reynolds number of 80. For this case the Dean number defined as:

$$De = Re(H/R_m)^{0.5} \tag{7}$$

is 50.95964, where $H = 1$ is the radial distance in the channel, and $R_m = 2.5$ is the channel mean radius of curvature. Upstream and downstream lengths of a straight channel of 1.254H and 3.H, respectively, are attached to the curved duct. The turning angle of the elbow is 90 degrees. In the streamwise

direction 33 stations were used, while 17×13 points were used for the cross section. As in the previous case a parabolic velocity profile with no transverse component was set at the inlet.

The distribution of the pressure on the bounding surfaces is shown in Fig. 7(*a*) by contours of constant values of the pressure. The importance of the viscous influence can be appreciated if one compares this result with the potential pressure solution obtained by Yang [13], Fig. 7(*b*).

The development of secondary flow is illustrated in Fig. 7(*c*). Low momentum fluid is drawn from the side wall and convected downstream towards the suction surface and high streamwise velocities near the centerline are displaced ac-

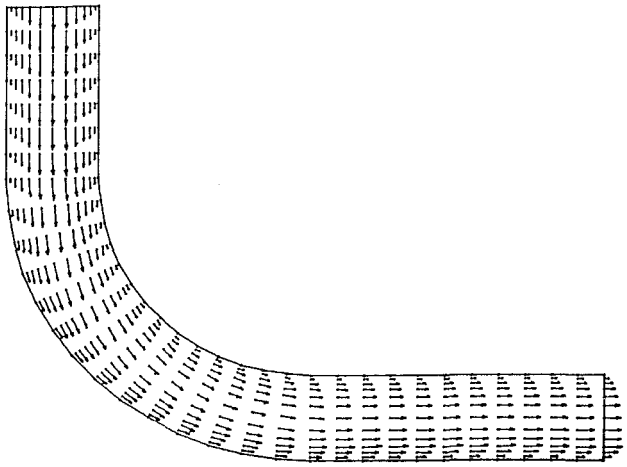

Fig. 8(*a*) Velocity distribution in the plane of symmetry, $R_e = 1093$

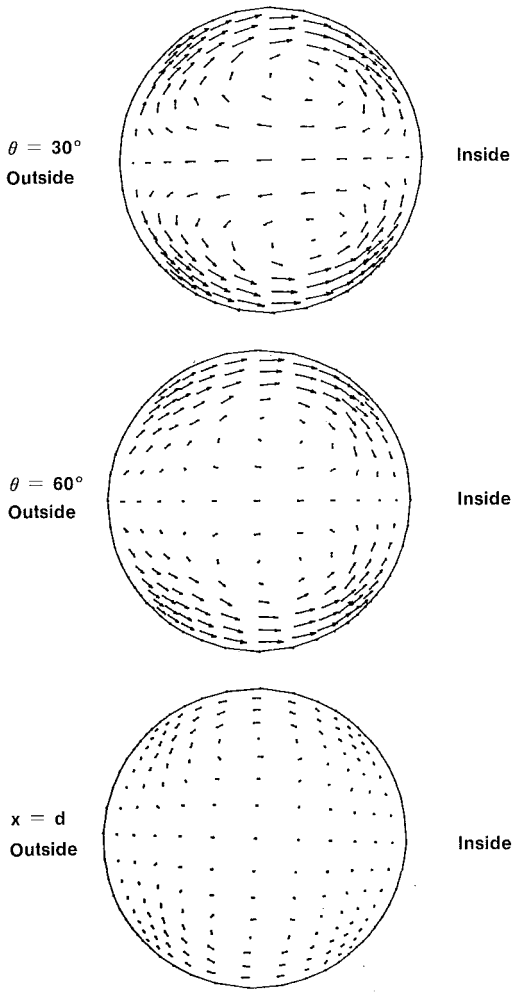

Fig. 8(*b*) Secondary flow development in a pipe bend, $R_e = 1093$

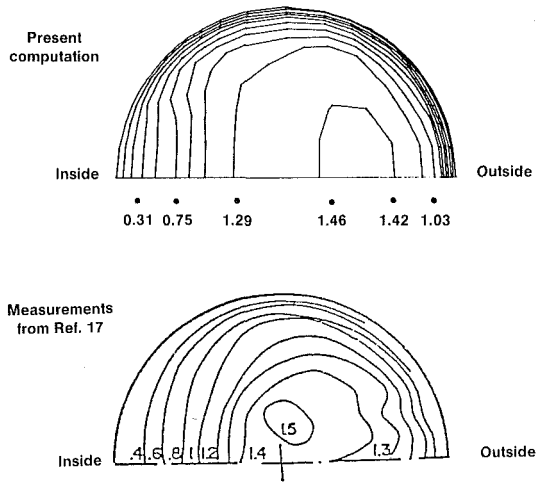

Fig. 8(*c*) Comparison of axial velocity contours at $\theta = 30$ deg, $R_e = 1093$

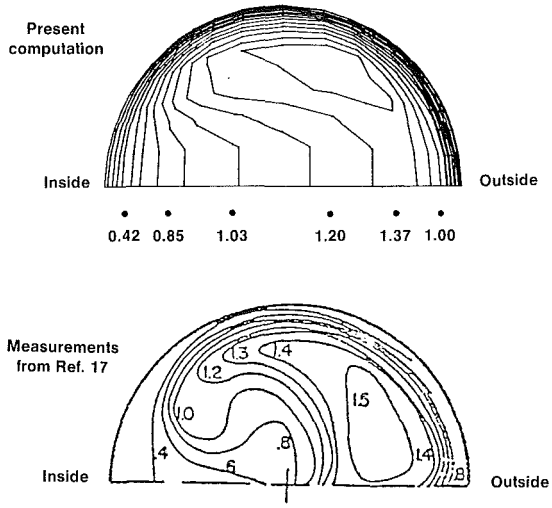

Fig. 8(*d*) Comparison of axial velocity contours at $\theta = 60$ deg, $R_e = 1093$

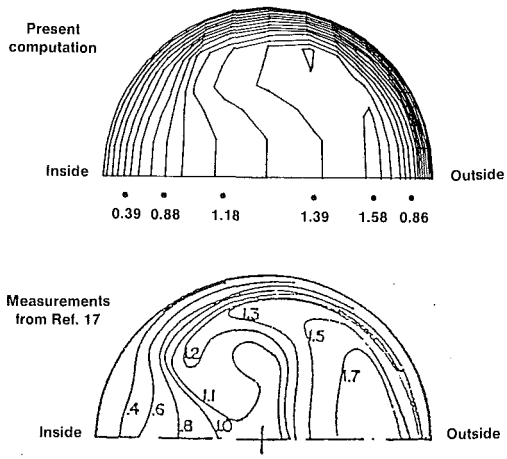

Fig. 8(*e*) Comparison of axial velocity contours at $x = d$, $R_e = 1093$.

cordingly toward the pressure surface. This helical motion is observed from the beginning of the turning of the channel and increases as the flow progresses in the duct. At the exit the secondary flow is not as strong but still does not disappear entirely because the downstream extension is not sufficiently long to allow a redevelopment of the flow.

To assess the present solution, a comparison of the computed fully developed streamwise velocity profile with the available experimental and numerical data has been carried out. This is illustrated on Fig. 7(*d*) which shows a good qualitative and quantitative agreement between the present calculation and the numerical predictions obtained by references [14, 15]. The present numerical solution does not agree well with the experimental measurements obtained by Mori et al [16], but this is also the case of other computer results using totally different formulations [14, 15].

6.3 Pipe Bend. In this test the flow in a pipe described in reference [17] was computed and studied. It consist of a 90 degrees bend with a mean radius of curvature of 3.2 times the diameter of the pipe, and where inlet and outlet extensions of 2. and 3.2 times the diameter respectively complete the geometry. The grid chosen for this case is 33 points in the ξ direction, 17 in the η direction and 13 in the ζ direction. The inlet flow was fully developed, and the flow Reynolds number is 1093.

In Fig. 8(*a*) the development of the flow in the streamwise direction is shown. Figure 8(*b*) depicts the secondary flow at the locations 30 deg, and 60 deg, and at one diameter length downstream from the end of the pipe turning. From these representations it can be seen that the center of the symmetric pair of vortices moves from the inside to the outside of the pipe as the turning angle progresses. Finally the vortex motion weakens as it leaves the bend. This behaviour is as expected and confirm the results obtained by reference [18].

All Figs. 8(*c*), 8(*d*), and 8(*e*), the calculated axial velocity contours at the 30 deg and 60 deg planes and at a distance equal the pipe diameter from the exit bend, are displayed and are compared to the measurements of reference [17]. From these figures we can conclude that the agreement of the computed results with the experimental data is generally satisfactory.

6.4 Twisted Elbow. In order to illustrate the general prediction capability of the present model, a final numerical application was carried out on a fully three-dimensional geometry.

The channel chosen is shown in Fig. 9(*a*) and its geometric characteristics were devised by Yang [14]. The cross section is a square, upstream and downstream tangents of 0.524H and 2.1H (H being the radial distance), respectively, are added to the elbow section. This section has a 60 degrees turning angle

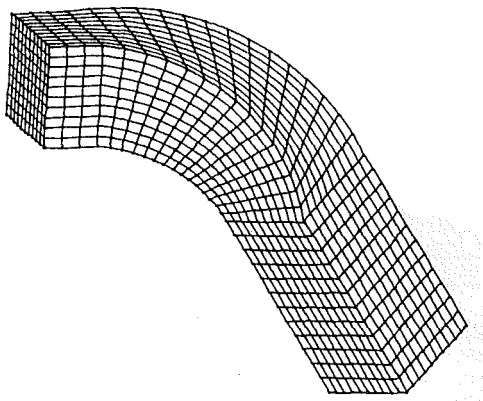

Fig. 9(*a*) Twisted elbow representation

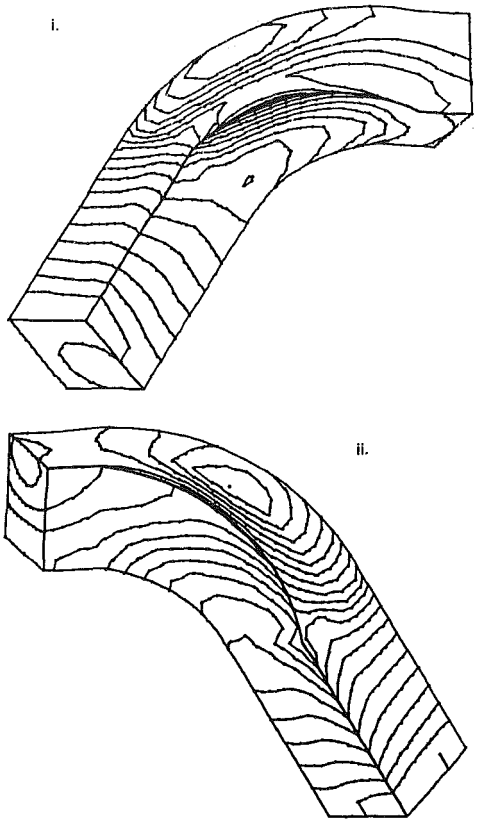

Fig. 9(*b*) Isopressure distribution on outmost surfaces
i. View from back
ii. View from front

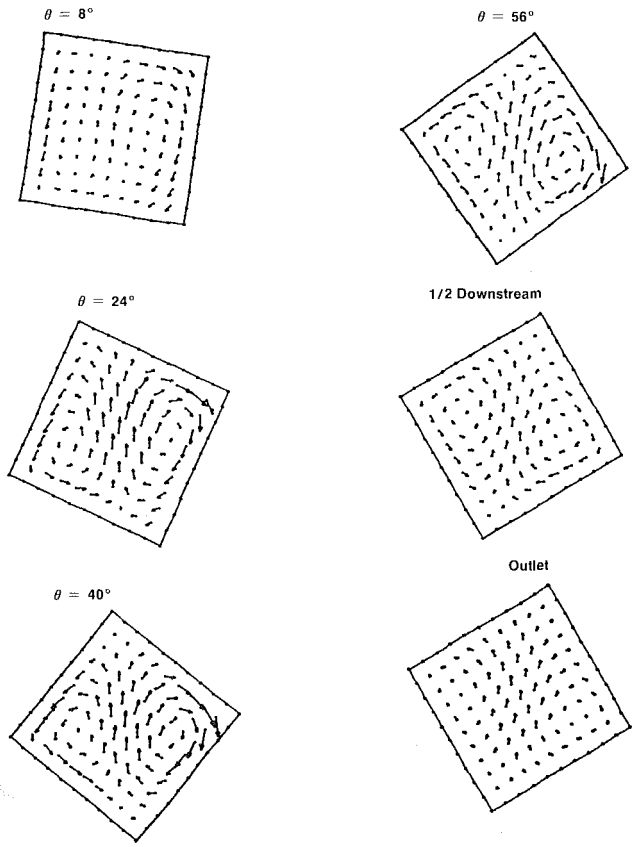

Fig. 9(c) Development of the secondary flow, $R_e = 80$

together with a 60 degrees twist around its central line, so the three-dimensionality is fully present.

The discretization was carried out using $31 \times 11 \times 11$ mesh points, a flow Reynolds number of 80, and as in the previous numerical experiments a parabolic profile with no transverse components was set at the inlet.

Figure 9(*b*) shows the pressure plotted in contours of constant values viewed from opposite directions.

Probably the most interesting phenomena in such a complex geometry is the development of the secondary flow, which is presented in Fig. 9(*c*). It consists of the generation of a vortex pair that remains normal to the plane of the duct turning. The twisting seems to have no effect on the location of the vortices; however it does increase the strength of one side of the vortex pair, while decreasing the other. This influence becomes more evident after $\theta = 40$ deg (Fig. 9(*c*)). After the channel stops twisting and turning at $\theta = 60$ deg, the flow begins to recover, but as the length of the downstream tangent is relatively short for the present Reynolds number, it still cannot reach the straight channel flow type.

7 Concluding Remarks

The preliminary goal of the present work was the development of a numerical procedure to solve 3-D incompressible laminar flows in general curved passages. The reported results are in general good agreement with the available data. The proposed method predicts the complex nature of the three-dimensional viscous flow phenomena inside ductings and in particular the helical shape and changing strength of the secondary flow. A typical computation for the tested geometries requires about 0.4 seconds of CPU time per grid point on an IBM 4341-II.

References

1 Thompson, J. F., "Grid Generation Techniques in Computational Fluids Dynamics," *AIAA Journal*, Vol. 22, No. 11, 1984, pp. 1505–1523.

2 Camarero, R., and Reggio, M., "A Multigrid Scheme for Three-Dimensional Body-Fitted Coordinates in Turbomachine Applications," ASME JOURNAL OF FLUIDS ENGINEERING, Vol. 105, 1983, pp. 76–82.

3 Hallow, F. H., and Welch, J. E., "Numerical Calculation of Time Dependent Viscous Incompressible Flow of Fluid with Free Surface," *Physics of Fluids*, Vol. 8, 1965, pp. 2182–2189.

4 Patankar, S. V., *Numerical Heat Transfer and Fluid Flow*, Hemisphere Publishing Corporation, Washington, D.C., 1980.

5 Reggio, M., and Camarero, R., "A Three-Dimensional Solution Method for Turbomachinery Analysis," ASME, WAM, Miami, Nov. 1985.

6 Reggio, M., and Camarero, R., "A Numerical Solution Procedure for Viscous Incompressible Flows," *Numerical Heat Transfer*, Vol. 10, 1986, pp. 131–146.

7 Denton, J. D., "A Time Marching Method for Two and Three Dimensional Blade-to-Blade Flows," A.R.C., REM 3775, 1975.

8 Roscoe, D. F., "The Numerical Solution of the Navier-Stokes Equations for Three-Dimensional Laminar Flow in Curved Pipes using Finite Differences Methods," *J. of Engineering Mathematics*, Vol. 12, 1978, pp. 303–323.

9 Fuchs, L., and Zhao, H-S., "Solution of Three-Dimensional Viscous Incompressible Flow By A Multigrid Method," *Int. Journal for Numerical Methods in Fluids*, Vol. 4, 1984, pp. 539–555.

10 Raithby, G. D., and Torrance, K. E., "Upstream Weighted Differencing Schemes and their Application to Elliptic Problems Involving Fluid Flows," *Computer Fluids*, Vol. 2, 1974, pp. 191–206.

11 Hirt, C. W., Nichols, B. D., and Romero, N. C., "SOLA – A Numerical Solution Algorithm for Transient Fluid Flows," Report LA-5852, 1975, Los Alamos Scientific Laboratory, Los Alamos, NM.

12 Lacroix, M., Camarero, R., and Tapucu, A., "Etude d'écoulements Internes Tridimensionnels," EP84-R-9, 1984, Ecole Polytechnique de Montréal.

13 Yang, H., and Camarero, R. "The Vorticity-Potential Method for Numerical Solution of Viscous Duct Flow in Three-Dimensions," EPM/RT-85-3, Ecole Polytecnique de Montréal.

14 Yang, H., and Camarero, R., "An Improved Vorticity-Potential Method for Three-Dimensional Duct Flow Simulations," *International Journal for Numerical Methods in Fluids*, Vol. 6, 1986, pp. 35–45.

15 Khalil, I. M., Weber, H. G., "Modeling of Three-Dimensional Flow in Turning Channels," ASME *Journal of Engineering for Power*, Vol. 106, 1984, pp. 682–691.

16 Mori, Y., Uchida, Y., and Ukon, T., "Forced Convective Heat Transfer in a Curved Channel with a Square Cross Section," *Int. J. Heat and Mass Transfer*, Vol. 14, 1971, p. 1781.

17 Enayet, M., Gibson, M., Taylor, A., and Yianneskis, M., "Laser-Doppler Measurements of Laminar and Turbulent Flow in a Pipe Bend," *Int. J. Heat Fluid Flow*, Vol. 3, No. 4, 1982.

18 El Dib, Iman Esmat Osman, "Numerical Calculation of Internal Flows with Curvature," Ph.D. thesis, Northwestern University, 1985.

G. Cau

N. Mandas

Associate Professor,
Dipartimento di Ingegneria Meccania,
Universita' di Cagliari, Italy

G. Manfrida

Associate Professor,
Dipartimento di Energetica,
Universita' di Firenze, Italy

F. Nurzia

Professor,
Dipartimento di Ingegneria Meccanica,
Universita' di Cagliari, Italy

Measurements of Primary and Secondary Flows in an Industrial Forward-Curved Centrifugal Fan

An industrial-type centrifugal-flow fan was instrumented and tested in order to obtain a fully detailed relative flow pattern at impeller discharge. Testing entailed investigation of both primary flows (jet-wake pattern and presence of return flows) and secondary flows (due to streamwise vorticity either from meridional curvature or rotation effects). In addition to conventional probing, a crossed hot-wire probe was employed in the tests. Ensemble-averaging the hot-wire signals made it possible to obtain the three-dimensional phase-averaged relative flow pattern at discharge by means of double positioning of the probe. Results show secondary-flow effects of appreciable magnitude interacting with primary flows (e.g., return flow in the hub region and variations in vortex structure and wake position with variations in flowrate).

Introduction

Prediction of flow patterns in centrifugal compressors has long been recognized by turbomachine researchers and designers as representing a particular challenge. Moreover, the inherent difficulties connected with three-dimensionality, turbulence, secondary effects, and relative flow rotationality are made even more complicated by the notable gap existing between experimental and theoretical results. This gap has been further widened by evidence that a certain degree of separation in the impeller—unpredictable by current theoretical methods—can be instrumental in achieving top performance levels (Dean, 1974). As a result, extensive research has been undertaken to examine the structure of secondary flows in centrifugal impellers (Johnson and Moore, 1980, 1983a and 1983b) and the effects of rotation on shear layers, including both profile boundary layers and free jet-wake interfaces (Johnston, 1974; Bradshaw, 1977). Despite the fact that the foregoing flow models are not wholly successful in describing the loss mechanism or in theoretically predicting machine efficiency, they have, on the whole, allowed to learn a great deal about the physics of centrifugal impeller flow thereby opening the way to the application of advanced measurement methods to this field (Eckardt, 1975 and 1976) and to viscous flow modeling (Rahmatalla and Bosman, 1984; Moore and Moore, 1980).

Up to now, however, both experiments and calculations have always involved advanced machines (Eckardt, 1975 and 1976), sometimes with rotating speeds reduced for the purpose of simplifying experimental techniques (Johnson and Moore, 1980, 1983a, and 1983b). Spinoffs from this research to the industrial fan and compressor market have been few (Wright, 1984; Raj and Swim, 1981), mainly because the design features of industrial centrifugal fans differ notably from those of high-performance centrifugal compressors. A typical list of industrial centrifugal fan features would include:

1. Forward-curved blades (whereas backward-curved impellers are commonly employed in high-performance machines).
2. Simple blade shapes built from sheet metal.
3. Poor matching of diffuser and impeller. This often happens because it is common practice to couple the same discharge scroll and casing to different impellers (or vice versa) so that the broadest range of throughputs and delivery pressures can be covered with the smallest number of design modifications.

Rig testing of industrial fans and compressors is the sole way to dispel such misgivings. Moreover, experimental testing can lead to a deeper understanding of flow structures and hence to improved performance in these widely-marketed machines, employed especially in industrial applications such as process and air-conditioning plants. The investigation of an industrial-type centrifugal fan undertaken in the DIMECA (Dipartimento di Ingegneria Meccanica - Universitá di Cagliari) Research Facility and reported herein is part of this effort.

Secondary-Flow Theory for Mixed-Flow Impellers

For incompressible inviscid flow the simplified equation for transport and generation of the streamwise component of vorticity (Smith, 1957; Hawthorne, 1974) stands:

$$\frac{\partial}{\partial s}\left(\frac{\Omega_s}{w}\right) = \frac{2}{\rho w^2}\left(\frac{1}{R_n}\frac{\partial p^*}{\partial b} + \frac{\omega}{w}\frac{\partial p^*}{\partial z}\right) \qquad (1)$$

Contributed by the Fluids Engineering Division of THE AMERICAN SOCIETY OF MECHANICAL ENGINEERS and presented at the Joint Applied Mechanics, Bioengineering, and Fluids Engineering Conference, Cincinnati, Ohio, June 14-17, 1987. Manuscript received by the Fluids Engineering Division May 28, 1986. Paper No. 87-FE-4.

where p^* is the rotary stagnation pressure and s, n, b are the streamwise, normal, and binormal directions. Two contributions can be noticed on the right-hand side:

1. Curvature on the $s-n$ surface of a p^* profile uneven in b direction. In mixed-flow impellers, this curvature is mainly meridional (axial-to-radial bend) and p^* gradients are associated with blade boundary layers (*SS* and *PS*).
2. Rotation and axially-directed p^* gradients. The latter can be identified for mixed-flow designs with hub and shroud boundary layers.

The relative importance of the two terms is often expressed by the Rossby number, Ro (Johnson and Moore, 1980, 1983a and 1983b):

$$\mathrm{Ro} = [w/(\omega R_n)] \tag{2}$$

Test Rig and Experimental Approach

The tested centrifugal-flow fan (with 18 forward-curved sheet-metal blades as sketched in Fig. 1) was directly powered by a 7.5 kW ac motor rotating at ca. 3000 rpm. The machine's reference frame and characteristic curve (on which the three tested flow coefficients have been marked) also appear in Fig. 1.

After determining the average flow pattern at impeller inlet and exit by means of special-design pneumatic directional probes, the instantaneous flow vector was measured by a crossed hot-wire probe (Fig. 2). The hot-wire probe was placed in seven different axial positions from hub to shroud at impeller discharge (actually, at 2 mm from the edge of the impeller). Noise from random turbulent fluctuations (Evans, 1974; Kiock, 1973) was eliminated through use of ensemble-averaging, synchronized by rotor revolution, of the hot-wire data from 50 samples. After this first traverse, the probe was extracted from the machine and rotated 90 deg around its axis, thus obtaining a measurement plane orthogonal to the previous one (Nurzia, 1979). The probe was recalibrated and the traverse repeated with the same probe positioning. The ensemble-averaging technique allowed composing the four hot-wire signals (actually simultaneously taken in pairs). Processing with reference to the three-dimensional probe calibration curves, with an original iterative procedure to determine velocity, pitch and yaw angles (Fig. 2) allowed extracting the three-dimensional flow vector (Nurzia, 1979; Cau et al., 1984; Cau et al., 1987).

Data were sampled at a rate of 200,000 per second on a two-channel digital oscilloscope. The oscilloscope was controlled by a microcomputer which also served to correct for temperature drift (Bearman, 1971), signal linearization, and data storage, as well as to perform offline data processing.

Measuring accuracy of the hot-wire probe can be estimated as ±5 percent of the velocity value and ±1 deg for pitch or yaw angles over ranges of ±30 deg and ±45 deg, respectively.

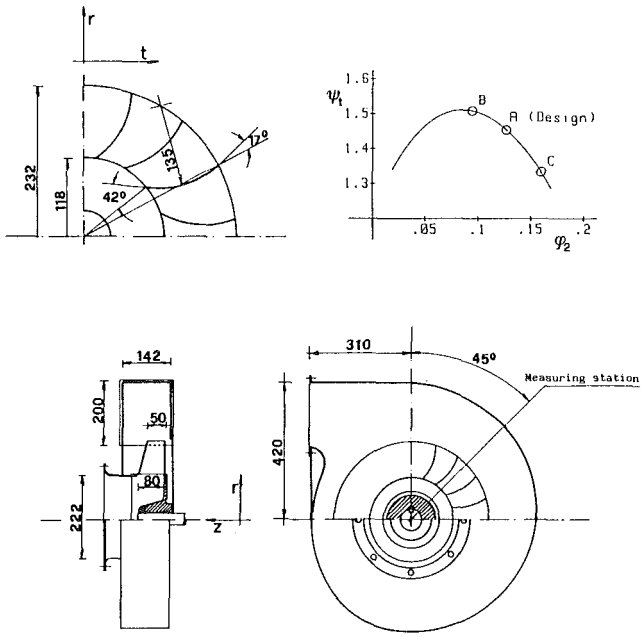

Fig. 1 Geometry and nondimensional characteristic curve of the tested machine (all dimensions in mm)

Frequent calibration of the hot-wire probe (actually after each traverse) was essential in achieving these results.

Flow Analysis

Pitch-Averaged Flow Pattern. The first flow analysis was performed by pitch-averaging the velocity components with respect to the reference frame r, z, t defined in Fig. 1. The hub-to-shroud distribution of radial and axial velocity components c_r, c_z at compressor discharge is illustrated in Fig. 3. The large values of c_r close to the shroud and the low ones close to the hub—together with positive c_z components in the hub region (meaning flow directed toward the shroud)—indicate flow separation at hub discharge for all three mass flow rates.

The flowrates, computed by averaging four blade-to-blade passages and integrating from hub to shroud at impeller discharge, are 0.843, 0.946, and 1.101 m^3/s, which should be compared with values measured at the reference nozzle of 0.655, 0.877, and 1.1 m^3/s. The corresponding values of tested flow coefficients are, respectively, 0.089, 0.119, and 0.149 and will be referred to as B, A, C throughout this paper. The discrepancy at low flow rates can be ascribed to the presence of a recirculating flow leaking through the large (3.5 mm) gap between the casing inlet cone and the impeller

Nomenclature

c = absolute velocity
p = static pressure
p^* = rotary stagnation pressure, $p^* = p + \rho(W^2 - U^2)/2$
R_n = radius of curvature of the streamline in normal direction
Ro = Rossby number
s, n, b = streamwise, normal, binormal directions
t = tangential direction
u = peripheral velocity
w = relative velocity
z = axial direction
α = flow angle from axial direction, $r-z$ plane
β = relative flow angle, $r-t$ plane
φ = flow coefficient
ψ_t = total pressure coefficient
ρ = density
ω = angular velocity
Ω_s = streamwise component of relative vorticity

Subscripts

r = vector component in radial direction
t = vector component in tangential direction
z = vector component in axial direction
2 = conditions at impeller discharge

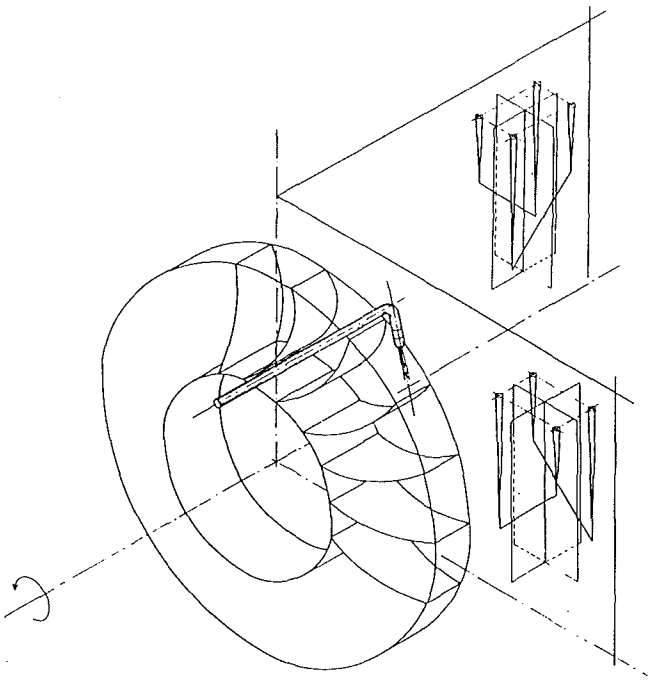

Fig. 2 Crossed hot-wire probe schematic and reference frame

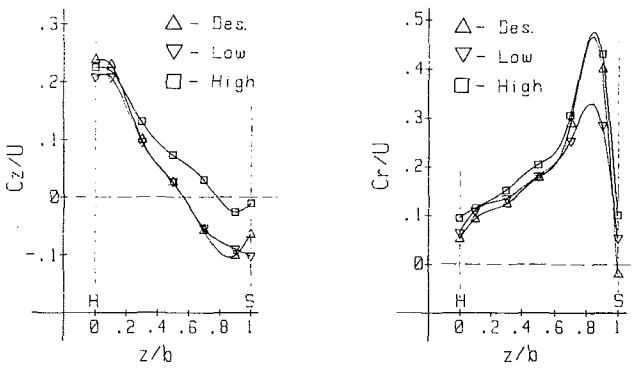

Fig. 3 Hub-to-shroud profile of axial and radial velocity components at impeller discharge

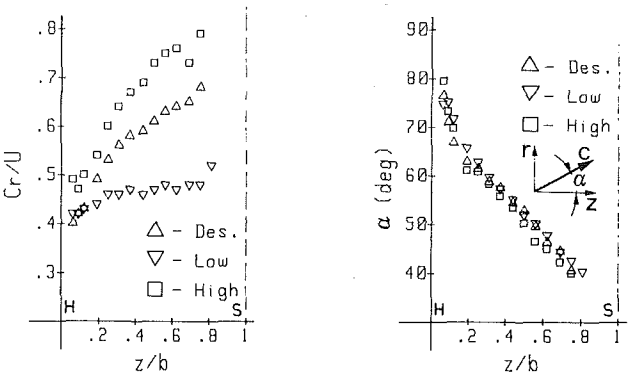

Fig. 4 Hub-to-shroud profile of radial velocity component and meridional flow angle at impeller inlet

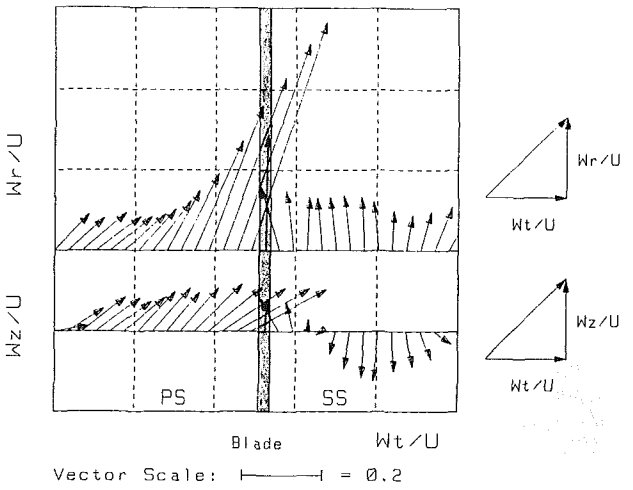

Fig. 5 Typical output of hot-wire data processing

sideplate. This kind of leakage, typical of industrial machines (Wright, 1984), becomes considerable when discharge is throttled.

Measurements were made about 3 mm upstream of the blade leading edge by traversing a miniature pneumatic disc probe through the inlet cone-impeller sideplate gap. Decreasing values of c_r were found passing from shroud to hub, particularly at large flow coefficients (Fig. 4). The low values close to the hub, meaning a large incidence on the rotor blades (20–25 deg), and the formation of a low-pressure area close to the shroud could be the triggering mechanism for hub flow separation.

The inlet flow angle in the $r-z$ (meridional) plane is also illustrated in Fig. 4. The flow deviation from radial, particularly apparent close to the shroud, suggests that a considerable amount of the meridional curvature takes place inside the impeller, thereby inducing secondary flows which should be absent in purely radial machines and which instead are well documented for mixed-flow designs (Johnson and Moore, 1980, 1983a and 1983b; Inoue and Cumpsty, 1984). Flow near the shroud so closely approached axial direction that the pitch response range of the probe was exceeded, thus leaving ca. 25 percent of the blade span without significant measurements (Fig. 4).

The slip factor at impeller discharge was also calculated by averaging in axial and tangential directions. As the measuring nozzle flowrate was always used as reference condition, the effect of recirculation was neglected and the slip factor itself was thus underestimated. The values for the three flowrates resulted as 0.92, 0.93, and 0.89, which are comparable to the average value of 0.895 obtained by the Stanitz correlation (Wiesner, 1967).

Ensemble-Averaged Local Flow at Design Flowrate. A typical output of the first processing of the hot-wire data, representing a vector plot of the three relative velocity components over a single blade pitch at midspan appears in Fig. 5. The appreciable extension of the wake over the suction side is clearly visible. Also apparent is a significant local inversion of w_t and w_z.

A complete picture of the main and secondary flow patterns is obtained when data collected from all the axial test positions are combined in a representation of the w_t and w_z vectors and constant w_r lines. This is shown in Fig. 6 with all velocity components nondimensionalized by the measured peripheral speed.

A reference schematic illustrating flow regions is shown in Fig. 7(*a*). It can be readily seen that the primary flow is dominated by the main core flow labeled C, extending over the whole pressure and most of the shroud side and having large through-flow but small tangential and axial velocity components. Sizable return flow, running nearly 50 percent

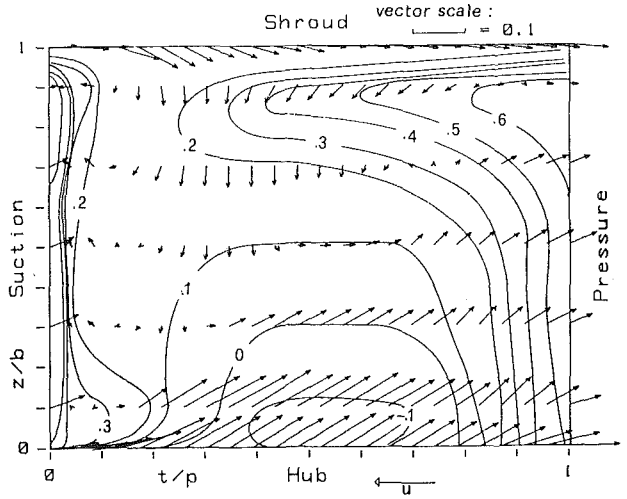

Fig. 6 Relative flow pattern at impeller discharge (design flow rate)

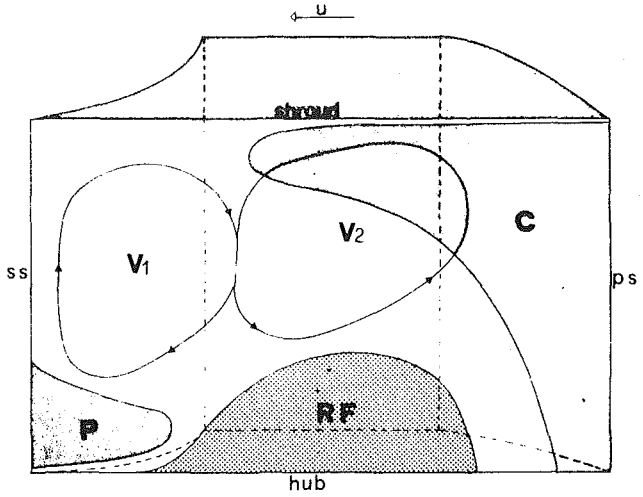

Fig. 7(*a*) Design and low flow rate

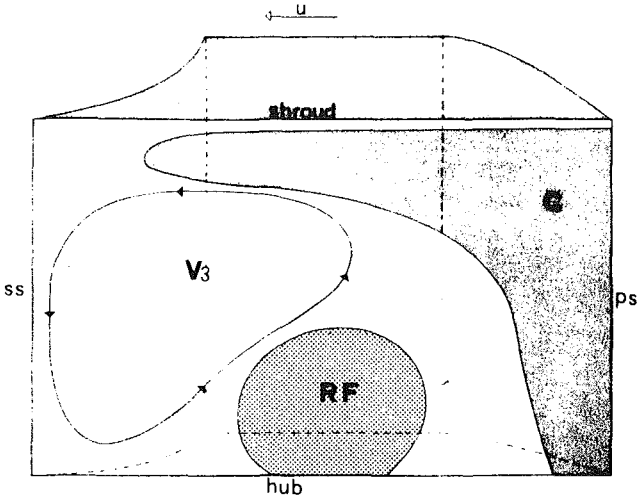

Fig. 7(*b*) Large flow rate

Fig. 7 Sketch of relative flow pattern at impeller discharge

pitchwise and 30 percent axially, appears at the midpitch region of the hub (labeled RF). Large positive tangential and axial components (respectively opposed to rotation and directed toward the shroud) are present in this region.

The presence of the wake can be detected along the suction side as the region of low positive radial velocity in Fig. 6. A large secondary flow region with clockwise vorticity (labeled V1 in Fig. 7(*a*)) extends wholly over the wake. This vortex, responsible for the local change of sign in w_t and w_z (Figs. 5 and 6), can be recognized as the suction-side vortex induced by the presence of meridional curvature on the suction-side boundary layer. As predicted in the model (Johnson and Moore, 1980), a second, counter-rotating vortex (V2 in Fig. 7(*a*)) is present in the shroud-pressure side region where the main core flow is located. Loss of guidance from the blades in proximity to discharge superimposes a notable "slip" component in tangential direction, as was also found in Johnson and Moore (1983a and 1983b).

Another core flow region (*P* in Fig. 7(*a*)), featuring notable w_r components and limited extension, was found within 10 and 20 percent blade span from the hub on suction side, confined at impeller discharge between the wake and return-flow regions. The presence of core flow *P* is not noticeable in all machines where flow separation at discharge occurs at the shroud (Johnson and Moore, 1980, 1983a and 1983b; Eckardt, 1975 and 1976). In such case, there is no retaining action from return-flow RF, so that *P* is allowed to spread out in the pressure-side direction; the same happens whenever the wake is displaced toward the shroud. In terms of the blade-to-blade w_r profile, the presence of this second core produces the typical two-lobed pattern discernible in Fig. 8, where the w_r profiles over the blade pitch are compared for different blade sections from hub to shroud.

Local slip factors were also calculated (Fig. 9). Slip factors tend to be large close to the shroud on account of the secondary vortex V2 (Fig. 7(*a*)). Instead, the large slip factor region along the SS can be identified with the wake (low radial velocity component in Fig. 6).

Ensemble-Averaged Local Flow at Off-Design Flowrates. Flowrate variations markedly affect both primary and secondary flow structures. Throttling to operating point B represented in Fig. 1 causes considerable reduction in w_r over core flow region *C* (Fig. 10) and a lesser extension of return flow in the hub area. This happens because, as shown in Figs. 3 and 4, a reduction in flowrate implies redistribution of the flowrate itself from hub to shroud, with c_r values comparatively higher at the hub and much lower at the shroud. At the same time, the location of the return-flow region shifts toward the pressure side, while core flow *P* on the suction side by the hub grows in width and force. In terms of secondary flow, the two passage vortexes (V1 and V2 of Fig. 7(*a*)) are still visible (although the suction-side one has spread tangentially toward midpitch).

According to secondary flow theory in radial impellers (Johnson and Moore, 1980, 1983a, and 1983b), one would expect to find a shift in the wake along the suction side toward the hub due to the dominant effect of rotation over meridional curvature following flowrate reduction. With respect to design flow, a displacement of the large slip factor region towards the hub is particularly evident from our data (Fig. 11). Actually, examining Figs. 10 and 11 together, low w_r and high slip factor values can be noticed along the suction side.

The increase in flowrate up to operating point C in Fig. 1 does not substantially affect the pitch-averaged c_r profile with respect to design flow (Fig. 3). However, the penetration of main core flow at the shroud in the suction-side direction is considerably greater (Fig. 12). Here, too, the size and force of the return-flow region RF are reduced with respect to the design flowrate, mainly by the action of the natural trend toward positive through-flow values in the whole blade-to-blade passage. Comparison of Figs. 10, 6, and 12 indicates a

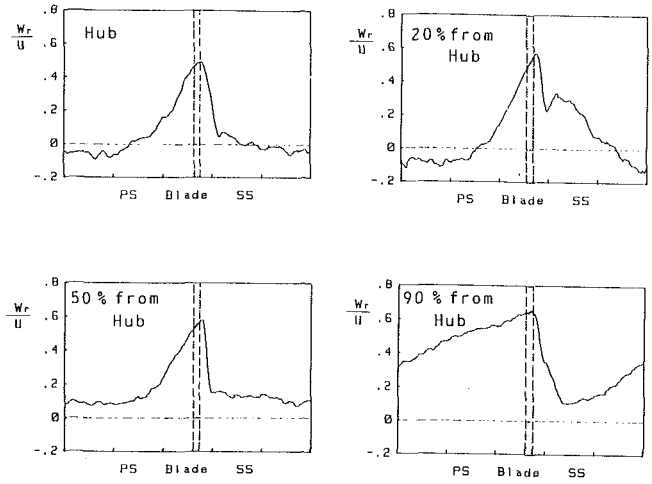

Fig. 8 Radial velocity distribution at discharge over blade pitch at different hub-to-shroud locations

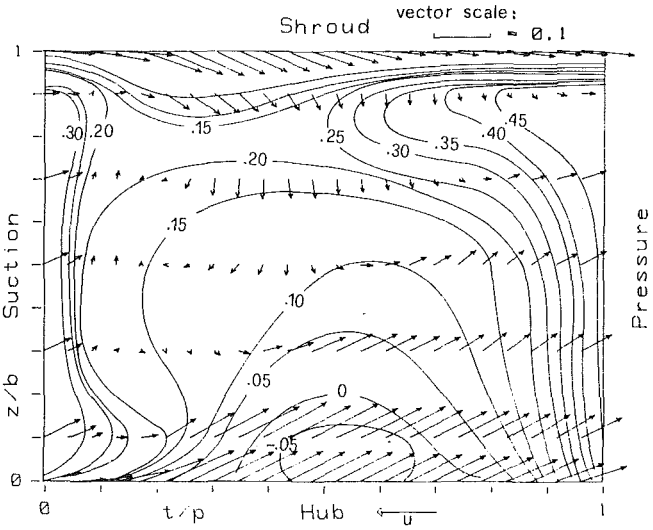

Fig. 10 Relative flow pattern at impeller discharge (lower flow rate)

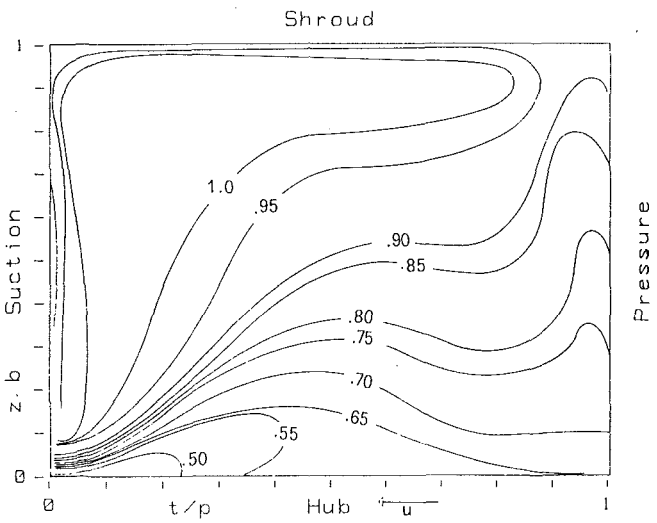

Fig. 9 Slip factor distribution at design flow rate

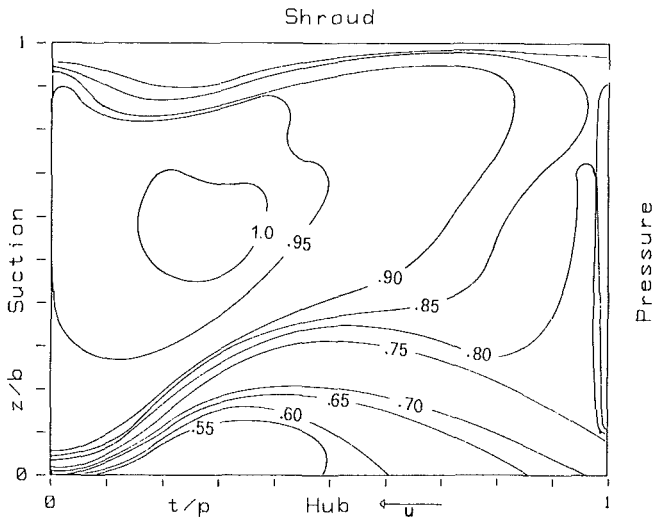

Fig. 11 Slip factor distribution at lower flow rate

tendency of the return-flow region to detach from the hub with increasing flowrate—possibly because of attraction generated by the low static-pressure region at shroud exit. This trend was also confirmed by measurements at other tangential locations. In terms of secondary flow, the V1 vortex along suction side has vanished and has been replaced by a large, counter-rotating vortex (V3) in the shroud-suction side region (Fig. 7(*b*)).

An attempt has been made to interpret the different secondary flow structure: At large flowrates, incidence over the blades at inlet decreases and flow separation on the suction side is either considerably delayed or even wholly avoided. Should there be separation, the flow has already assumed a radial direction so that the suction-side boundary layer can offer only a slight contribution to generating streamwise vorticity deriving from meridional curvature (equation (1)). Instead, the opposite rotational contribution (equation (1)) is thus dominant, and an opposing streamwise vorticity is produced in the suction side-shroud region. The result is the large-size vortex labeled V3 in Fig. 7(*b*). The main modifications in the primary flow pattern are also sketched in Fig. 7(*b*).

As the extension of the suction-side boundary layer is limited at large flow rates, the wake is smaller and weaker (Fig. 12). Nonetheless, Fig. 13 shows that the large slip factor region is now more or less aligned along the shroud—an opposite trend with respect to flow reduction (Fig. 11). Only a very slight trace of core flow *P* remains on the suction side by the hub as an effect of wake reduction and displacement.

Conclusions

The following conclusions can be drawn:

1 The unsatisfactory design of the meridional flow channel causes a severely distorted primary flow, with large through-flow velocity components at the shroud and smaller ones triggering flow separation at the hub. This phenomenon is enhanced at high flowrates.

2 Appreciable secondary-flow effects induced by meridional curvature (axial-to-radial bend) can also be present in purely radial machines on account of significant axial velocity components at shroud inlet. No significant contribution of meridional curvature to secondary flows can be expected in the hub region of the tested machine, where flow enters the impeller in radial direction (Fig. 4). This behavior is signficantly different from that of high-performance centrifugal compressors, where a bladed axial inducer is present, so that meridional curvature of the SS and PS boundary layers takes place both at hub and shroud.

3 The large aerodynamic load produces early flow separation on the suction side at both low and design flowrates. As

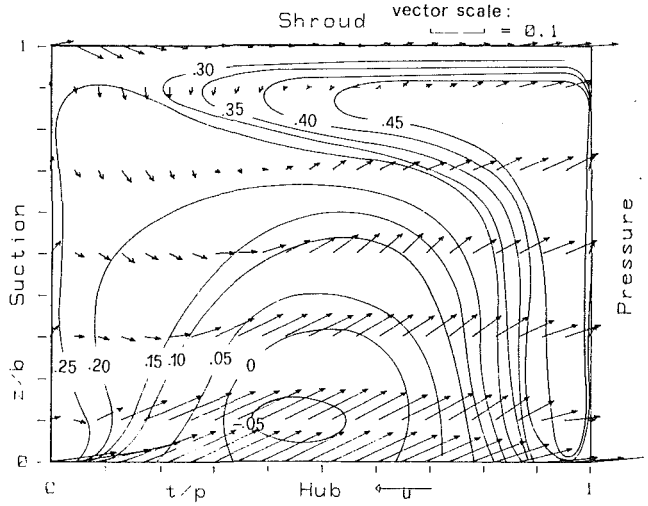

Fig. 12 Relative flow pattern at impeller discharge (higher flow rate)

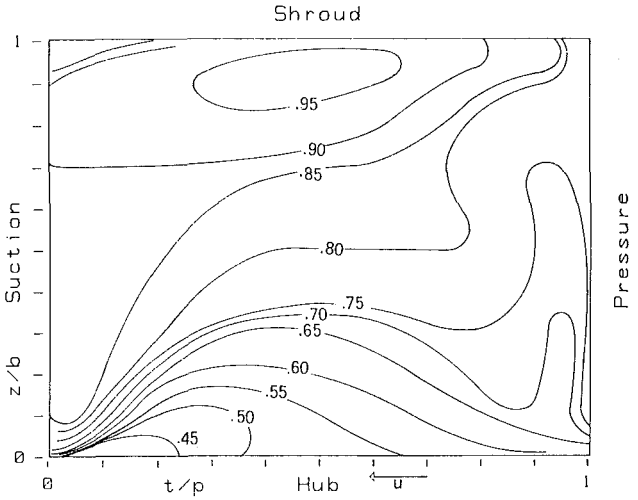

Fig. 13 Slip factor distribution at higher flow rate

this occurs prior to completion of the flow-bending from axial to radial along the shroud, it results in a major contribution to streamwise vorticity and secondary flow development.

4 The simplified secondary flow theory is of great help in explaining the observed secondary flow patterns. Distinctive features with respect to high-performance centrifugal compressors (e.g., the existence of a second core-flow plume in the suction side-hub region) are due to interaction between return flow at the hub and secondary flows.

5 Flowrate variation produces different secondary flow patterns, with rotation prevailing over meridional curvature at high flowrates. This behavior, opposed to that found in high-performance centrifugal compressors (Johnson and Moore, 1980, 1983a, and 1983b), can be interpreted in terms of flowrate variation. Flowrate increase certainly leads to a thinner SS boundary layer and possibly induces flow separation at the shroud-inlet corner. Both these factors (equation (1)) contribute to suppression of the clockwise vortex V1 along the suction side (Figs. 7(*a*), 6, and 10). On the pressure side, the effects of curvature and rotation get superimposed, so that only one strong counterclockwise vortex V3, extending over the shroud-suction side region, can be noticed (Fig. 7(*b*) and 12). Displacement of the large slip factor region with flowrate follows the trend indicated for wake location by Johnson and Moore (1980, 1983a, and 1983b). The size and existence of typical flow regions (e.g., return-flow RF and the suction-side core-flow plume mentioned in Conclusion 4) are also influenced by flow rate.

Inefficiencies on this machine can be ascribed to an excessively sharp axial-to-radial bend, to the large inlet gap between inlet cone and impeller sideplate, and to poor matching of the impeller and casing at outlet.

Acknowledgments

Research funded by CNR (Consiglio Nazionale delle Ricerche) and ENEA (Ente Nazionale Energie Alternative) as part of the Energy Project (CNR Contract 84.2868.59).

References

Bearman, P. W., 1971, "Corrections for the Effect of Ambient Temperature Drift on Hot-Wire Measurements in Incompressible Flow," DISA Information 11, May.

Bradshaw, P., 1977, "Effects of Streamline Curvature on Turbulent Flow," AGARDograph No. 196, August.

Cau, G., Mandas, N., and Nurzia, F., 1984, "Studio sperimentale sul flusso relativo all'uscita di una girante di ventilatore industriale," 39th ATI Congress, L'Aquila, Sept.

Cau, G., Mandas, N., and Nurzia, F., "Un sistema di misura per lo studio del flusso nei ventilatori centrifughi industriali con sonde ad alta risposta in frequenza," to be published.

Dean, R. C., 1974, "The Fluid Dynamic Design of Advanced Radial Compressors," VKI LS66, Advanced Radial Compressors.

Eckardt, D., 1975, "Instantaneous Measurements in the Jet-Wake Discharge Flow of a Centrifugal Compressor Impeller," ASME *Journal of Engineering for Power*, Vol. 99, July, pp. 337–345.

Eckardt, D., 1976, "Detailed Flow Investigations within a High-Speed Centrifugal Compressor Impeller," ASME *Journal of Fluids Engineering*, Sept., pp. 390–402.

Evans, R. L., "Turbulence and Unsteadiness Measurements Downstream of a Moving Blade Row," ASME Paper No. 74-GT-73.

Hawthorne, W. R., 1974, "Secondary Vorticity in Stratified Compressible Fluids in Rotating Systems," Cambridge University, Dept. of Engineering, Report N. CUED/A Turbo/TR 63.

Inoue, M. and Cumpsty, N. A., 1984, "Experimental Study of Centrifugal Impeller Discharge Flow in Vaneless and Vaned Diffusers," ASME *Journal of Engineering for Gas Turbines and Power*, Vol. 106, Apr., pp. 455–467.

Johnson, M. W., and Moore, J., 1980, "The Development of Wake Flow in a Centrifugal Impeller," ASME *Journal of Engineering for Power*, Vol. 102, Apr., pp. 382–390.

Johnson, M. W., and Moore, J., 1983, "Secondary Flow Mixing Losses in a Centrifugal Impeller," ASME *Journal of Engineering for Power*, Vol. 105, Jan., pp. 24–32.

Johnson, M. W., and Moore, J., 1983, "The Influence of Flow Rate on the Wake in a Centrifugal Impeller," ASME *Journal of Engineering for Power*, Vol. 105, Jan., p. 33.

Johnston, J. P., 1974, "The Effects of Rotation on Boundary Layers in Turbomachinery Rotors," NASA SP-304, Part I, pp. 207–249.

Kiock, R., "Turbulence Downstream of Stationary and Rotating Cascades," ASME Paper No. 73-GT-80.

Moore, J., and Moore, J. G., 1980, "Calculation of Three-Dimensional, Viscous Flow and Wake Development in a Centrifugal Impeller," in *Performance Prediction of Centrifugal Pumps and Compressors*, ASME, pp. 61–67.

Nurzia, F., 1979, "Un'indagine con anemometro a filo caldo sul flusso a valle di un rotore di compressore assiale," ISMAGE R. 240, Aug.

Rahmatalla, M. A. F., and Bosman, C., 1984, "The Calculation of Turbulent Flow Effects in a Centrifugal Impeller," IMECH C68/84, pp. 57–66.

Raj, D., and Swim, W. B., 1981, "Measurements of the Mean Flow Velocity Fluctuations of an FC Centrifugal Fan Rotor," ASME *Journal of Engineering for Power*, Vol. 103, Apr., pp. 393–399.

Smith, A. G., 1957, "On the Generation of a Streamwise Component of Vorticity in a Rotating Passage," *Aero. Quart.*, Vol. 8, pp. 369–383.

Wiesner, F. J., 1967, "A Review of Slip Factors for Centrifugal Impellers," ASME *Journal of Engineering for Power*, Oct.

Wright, T., 1984, "Centrifugal Fan Performance With Inlet Clearance," ASME *Journal of Engineering for Gas Turbines and Power*, Vol. 106, Oct., pp. 906–912.

A Study of Performance Improvement for High Specific Speed Centrifugal Compressors by Using Diffusers With Half Guide Vanes

Y. Yoshinaga
Senior Researcher,
Mechanical Engineering
Research Laboratory.

T. Kaneki
Senior Engineer, Tsuchiura Works.

H. Kobayashi
Researcher, Mechanical
Engineering Research Laboratory.

M. Hoshino
Researcher, Mechanical
Engineering Research Laboratory,

Hitachi Ltd., Tokyo, Japan

The experimental results from eighteen different centrifugal compressor stages showed that the pressure recovery of vaneless diffusers for high specific speed compressors was extremely low compared with the value expected by an ideal two-dimensional analysis. Consequently a new type of diffuser with half guide vanes on the shroud side wall was proposed. The pressure recovery of this diffuser at distorted inlet flow was considerably improved by the half guide vanes. The optimum height of the vanes was a little less than one half of the diffuser width. Measurements of the velocity distribution in the diffusers using Pitot tubes and a laser-two-focus velocimeter, clearly showed that the small height guide vanes gave a uniform flow in the axial direction and improved the pressure recovery of the diffuser.

Introduction

High specific speed stages with high flow coefficients and high tip speed Mach numbers are sometimes used as a first stage with multistage process compressors to increase the volumetric capacity of the given casing and reduce the number of stages. Raising the specific speed necessitates increasing the aspect ratio at the impeller inlet and the outlet width of the impeller. However, an impeller design meeting these requirements, has the effect that the kinetic flow energy at the impeller outlet enters the diffusers rather irregularly in both circumferential and axial directions [1]. The highly distorted flow discharged from impellers could be expected to have a determining effect on the performance of the diffusers [2].

Many experimental and theoretical studies have been made for radial vaneless diffusers [3], [4], however, it seems that a clear account is not given of the effect of highly distorted inlet flow on the diffuser performance. Senoo et al. [5], [6] have investigated the distorted flow in vaneless diffusers. They showed that flow distortion in the axial direction did not decay easily compared with the rotating circumferential flow distortion. Further, their theoretical analysis of the development of axial distortion with respect to the radius in the diffuser demonstrated good agreement with experimental results.

The present work is planned to show the influence of distorted inlet velocity distribution in the axial direction on the aerodynamic performance of vaneless diffusers. Eighteen different specific speed centrifugal compressors were tested, and the experimental results were compared with the results calculated by the theoretical method [6]. The results show: (1) the impeller exit flow distortion increases with increasing specific speed of the stages, and (2) the pressure recovery of a vaneless diffuser for a high specific speed stage is extremely low compared with the value expected by an ideal two-dimensional analysis.

Then, a new type of diffuser with half guide vanes set on the shroud side wall was proposed in order to improve the pressure recovery of the diffuser for high specific speed centrifugal compressors. Measurements of pressure and velocity distributions at the inlet and exit of the diffusers, by using three-hole Pitot tubes, were carried out in a test rig. Other measurements, using a laser velocimeter, were made to provide more detailed velocity distributions in the diffuser with half guide vanes. These experiments were carried out in another low speed test rig. The present paper discusses the effect of the guide vanes on equilization of the inlet flow distortion, and also the influence of vane height on the pressure recovery of the diffuser.

Test Rig and Instrumentation

Experiments were made with a centrifugal compressor test rig, consisting of a single stage compressor, a torque meter, a dc motor with buit in gears, an air cooler, and flow piping. The closed loop of air piping made use of varying suction pressure and temperature to control the inlet conditions of the compressor. Figure 1 shows a cross-sectional view of the single stage test rig which simulates the flow passage of a multi stage

Contributed by the Fluids Engineering Division for publication in the JOURNAL OF FLUIDS ENGINEERING. Manuscript received by the Fluids Engineering Division July 9, 1986.

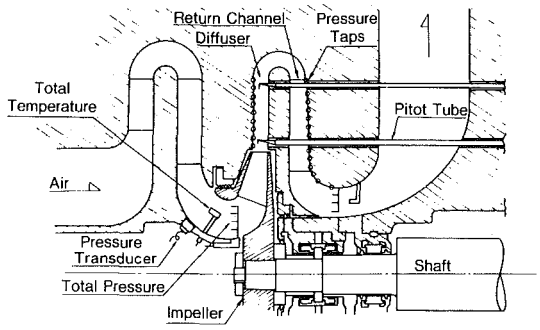

Fig. 1 Sectional view of the model compressor rig

centrifugal compressor. A vaneless diffuser, a return channel, and a collector casing were set downstream from an impeller.

Eighteen different stages were tested in these experiments; the impellers each had the same outside diameter (300mm), the vaneless diffusers with parallel walls had the same radius ratio ($r/r_2 = 1.6$), and their specific speed was varied from 250 to 500 (rpm, m^3/min, m), that is, from 0.61 to 1.22 in nondimensional number. Tip circumferential speed of the impellers was varied from 270 to 300 m/s, the machine Reynold's numbers ($\mathrm{Rem} = ub_2/\nu_0$, ν_0 is kinetic viscosity of air at impeller inlet) were between 2×10^5 and 5.6×10^5, and the Mach number of the diffuser inlet flow was about 0.55.

The total and static pressures at the diffuser inlet ($r_i/r_2 = 1.067$) and exit ($r_e/r_2 = 1.533$) were measured at three circumferential positions with cobra type yaw probes consisting of 1mm dia stainless steel tubes. The pressure recovery factors and the pressure loss coefficients of the vaneless diffusers were rated on the mass averaged values of the time mean measured pressure. Mean flow angles were calculated by the equation $\bar{\alpha} = \tan^{-1}(\overline{C_{mm}}/\overline{C_{um}})$, where $\overline{C_{mm}}$ and $\overline{C_{um}}$ were mass averaged mean radial and circumferential velocities, respectively. The performance of each compressor stage was evaluated on the basis of the total-to-total rating at the inlet and exit of the stage was shown in Fig. 1. The flow rate was controlled with a valve, and was measured with an orifice type flow meter. The main dimensions of the eighteen test diffusers, such as diffuser width ratios b/r_i and inlet flow angles at design flow rate, are listed in Table 1 together with their performance values.

Table 1 Diffuser geometries, inlet flow distortions and performances

Diffuser	b/r_i	α_i (deg.)	C_p	ζ	B_f
1	0.066	26.6	0.43	0.18	1.03
2	0.074	24.0	0.42	0.17	1.02
3	0.089	30.7	0.43	0.14	1.04
4	0.094	28.2	0.40	0.18	1.02
5	0.094	30.4	0.34	0.21	1.05
6	0.103	31.4	0.44	0.15	1.07
7	0.112	30.7	0.28	0.25	1.10
8	0.126	27.6	0.30	0.21	1.04
9	0.126	27.3	0.32	0.22	1.02
10	0.126	33.6	0.29	0.23	1.04
11	0.126	31.1	0.31	0.23	1.09
12	0.150	35.5	0.24	0.29	1.14
13	0.150	25.9	0.32	0.27	1.10
14	0.156	31.4	0.25	0.29	1.09
15	0.156	34.7	0.25	0.27	1.14
16	0.156	35.4	0.23	0.14	1.09
17	0.187	34.3	0.04	0.21	1.23
18	0.187	30.8	0.02	0.22	1.22

$r_i/r_2 = 1.067$, $r_e/r_i = 1.44$ for all cases

Pressure Recovery of Vaneless Diffusers with Various Specific Speeds

Influence of Diffuser Width. The pressure recovery coefficients C_p and the loss coefficients of the eighteen test diffusers measured at the design flow rate are listed in Table 1. When the inlet velocity distribution is uniform, it is generally known that the pressure recovery of vaneless diffusers, which have the same radius ratio r_e/r_i and the same inlet flow angle α_i, increases with increasing diffuser width ratio b/r_i [4]. In Fig. 2, the solid lines indicate the pressure recovery and loss coefficients, which are calculated on the basis of the theory shown in reference [6] and the assumption of a uniform inlet condition. The parameter K_f is a constant for the wall friction coefficient expressed as

$$C_f = \lambda K_f (U_\delta/\nu)^{-1/4} \tag{1}$$

where λ is a constant for compressibility, U is free stream velocity, θ is boundary layer thickness, and ν is kinematic

Nomenclature

A = cross-sectional area of a diffuser passage
b = diffuser width
B_f = velocity distortion coefficient, $\overline{C_{mm}}/\overline{C_m}$
C = absolute velocity
C_f = wall friction coefficient
$\overline{C_m}$ = area averaged mean radial velocity, $\int\rho C_m dA/\int\rho dA$
$\overline{C_{mm}}$ = mass averaged mean radial velocity, $\int\rho C_m^2 dA/\int\rho C_m dA$
C_p = pressure recovery coefficient, (Pse-Psi)/(Pti-Psi)
g = gravitational acceleration parameter
h = height of guide vanes
H_{ad} = adiabatic head
K_f = constant for wall friction coefficient, equation (1)
ℓ = distance between circumferential pitch of adjacent vanes in Fig. 13
M = Mach number
N = rpm
n = distance from a vane in Fig. 13
n_s = specific speed, $NQ^{1/2}/H_{ad}^{3/4}$ (rpm, m^3/min, m) or nondimension
P = pressure
P_s = static pressure
P_0 = total pressure at inlet of impeller
Q = flow rate
r = radius
u = tip speed of impeller
w = relative velocity
y = distance from shroud side wall
α = flow angle, from circumferential direction
β = vane angle, from circumferential direction
ζ = pressure loss coefficient, $(P_{ti}-P_{te})/(P_{ti}-P_{si})$
ρ = density
η = efficiency
η_{ad} = adiabatic efficiency
θ = radian of rotation
φ = flow coefficient, $Q/(\pi r_2^2 u_2)$
ψ = pressure coefficient, $H_{ad}/(u_2^2/g)$
ψ_s = static pressure coefficient, $(P_s-P_0)/(\rho u_2^2)$

Subscripts

2 = impeller exit
e = diffuser exit
i = diffuser inlet
des = design condition
m = meridional component
u = circumferential component
ref = reference condition
$-$ = mean value

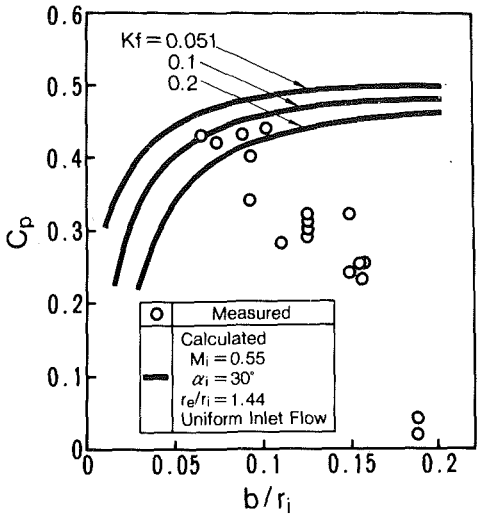

(a) Pressure recovery coefficient

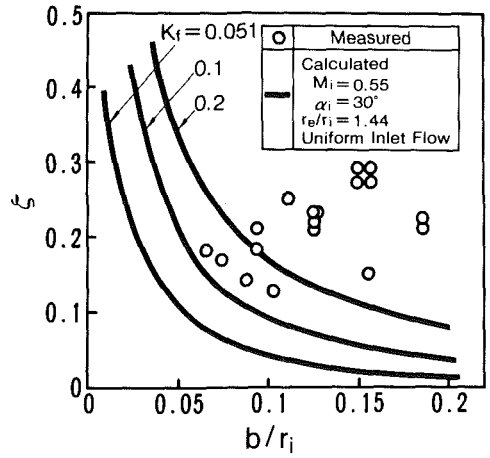

(b) Pressure loss coefficient

Fig. 2 Effects of diffuser width on pressure recovery and pressure loss coefficients (Uncertainty in $C_p = \pm 0.015$ and in $\zeta = \pm 0.013$ at the 95% confidence level)

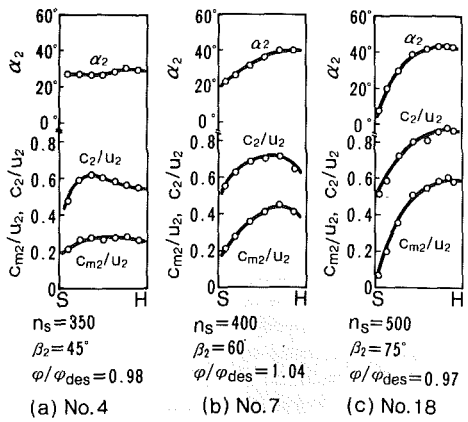

(a) No.4 (b) No.7 (c) No.18

Fig. 3 Velocity distributions at selected impeller exit (Uncertainty in $\alpha_2 = \pm 1.2$ deg, in $C_{m2}/u_2 = +0.02$, and in $C_2/u_2 = \pm 0.03$ at the 95% confidence level)

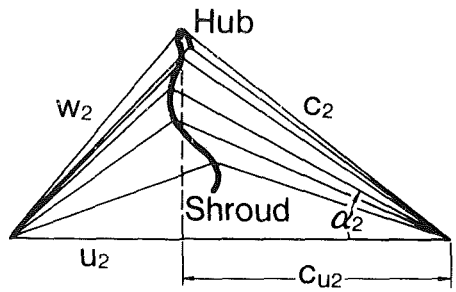

Fig. 4 Velocity triangles at the impeller exit

viscosity. According to reference [6], $K_f = 0.051$ was recommended for vaneless diffusers which were tested with a blower impeller.

The experimental data of Table 1 are included in Fig. 2. There are many pressure recovery coefficients which are smaller than the calculated values especially for the wide diffusers. The measured loss coefficients are also large compared with the calculated values assuming a uniform inlet condition. Many data of pressure recovery coefficients and loss coefficients in Table 1 were tested at the inlet flow angle not equal to 30 deg, which was used for the prediction. Since not only the diffuser width ratio, but also the inlet flow angle was varied in the eighteen different stages, the experimental data in Fig. 2 are not considered to show the influence of the diffuser width only. But according to the example calculations, the pressure recovery coefficient is not sensitive to the inlet flow angle from 24 to 36 deg for the high specific speed compressor. Only a ±5 percent difference is estimated as compared with the pressure recovery coefficient of the 30 deg inlet flow angle. The difference between the experimental and calculated results in Fig. 2 are due to other effects such as the inlet flow distortion which increases with the diffuser width ratio.

Velocity Distributions at an Impeller Exit. The flow discharged from a centrifugal compressor impeller is extremely distorted. A few examples of measured velocity distributions at the impeller exit ($r/r_2 = 1.067$) are presented in Fig. 3. Figures 3(*a*), (*b*), and (*c*) show the impeller exit velocity distributions of the No. 4, No. 7, and No. 18 diffusers in Table 1 respectively, where the specific speed of each stage was 350, 400, and 500 (rpm, m^3/min, m), that is, 0.85, 0.98, and 1.22 in nondimensional number. The measured velocity distributions indicate that the flow at the impeller exit, or at the diffuser inlet, is highly distorted in the axial direction with increasing specific speed of the impellers.

Figure 4 shows the velocity triangles at the impeller exit (No. 18 diffuser inlet). These triangles show that the circumferential velocity component is fairly uniform across the width and inlet distortion is mainly induced by the distorted distribution of the radial velocity component. The distortion of the inlet velocity distribution is expressed by the following velocity distortion coefficient,

$$B_f = \frac{\int \rho C_m^2 dA / \int \rho C_m dA}{\int \rho C_m dA / \int \rho dA}$$

where ρ is the density, C_m is the radial component of velocity, and A is the area at the diffuser inlet. The coefficient B_f denotes the ratio of the mass averaged mean radial velocity ($\overline{C_{mm}}$) and the area averaged mean radial velocity ($\overline{C_m}$).

The B_f values are included in Table 1. They are related to the diffuser width ratios b/r_i plotted in Fig. 5. The velocity distortion coefficient increases with increasing b/r_i values. Though the velocity distribution coefficient is more a function of the impeller design than of the ratio b/ri, the experimental results clearly show that the axial distribution of the velocity is quite distorted for a high specific speed compressor, which has a large b/r_i.

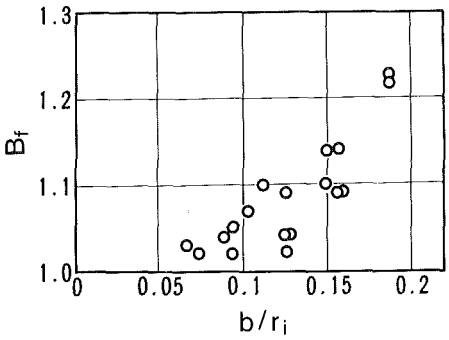

Fig. 5 Variation of velocity distortion coefficient with respect to diffuser width ratio (Uncertainty in $B_f = \pm 0.015$ at the 95% confidence level)

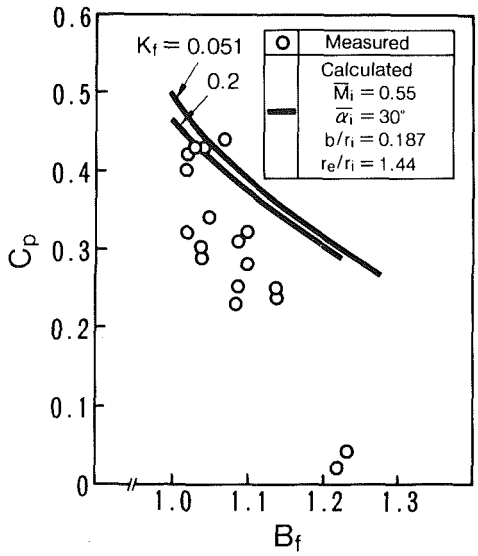

(a) Pressure recovery coefficient

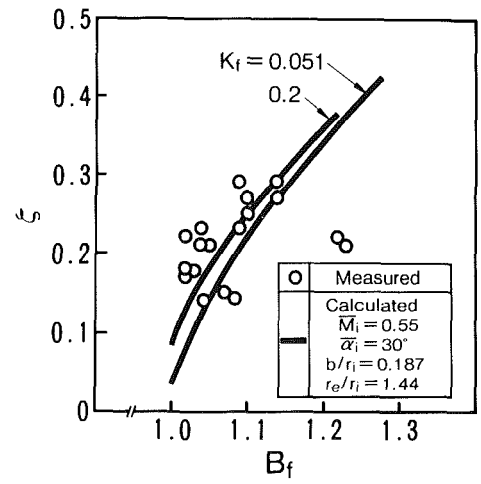

(b) Pressure loss coefficient

Fig. 6 Effects of velocity distortion coefficient on pressure recovery and pressure loss coefficients

Influence of Distorted Inlet Velocity Distribution. Using the flow analysis [6], [7] on the axially distorted flow, the influence of the distorted inlet velocity distribution on the diffuser performance is discussed next.

In the flow analysis [6] it was assumed that the circumferential component of velocity was uniform across the diffuser width and that the radial component of the velocity varied

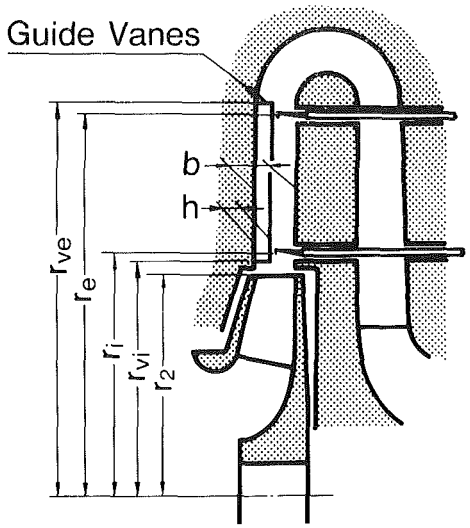

Fig. 7 Half guide vanes set on the shroud side wall of a diffuser

linearly from one wall to the other. The present calculations were performed at various values of velocity gradient across the width keeping the mean inlet flow angle equal to 30 deg, as modeled after the velocity triangles in Fig. 4, and inlet Mach number nearly equal to 0.55. The diffuser width was 0.187 times the inlet radius.

The experimental and calculated pressure recovery coefficients C_p and the total pressure loss coefficients ζ are plotted against B_f in Fig. 6. It should be noted that many of the experiments were not performed at the inlet flow angle of 30 deg nor was the diffuser width ratio equal to 0.187 as indicated in Table 1. Additionally, the actual velocity distributions were not always similar to the ones used in the flow analysis, even though the velocity distortion coefficient was identical. Therefore, these experimental data can be compared with the prediction only approximately. But both the predictions and the experimental data clearly demonstrate that pressure recovery deteriorates due to distortion of the inlet velocity distribution.

Improvement of Pressure Recovery by Means of Half Guide Vanes

In cases of high specific speed compressors, the pressure recovery coefficient of the vaneless diffuser is quite small (Fig. 2), because the flow accumulates along the hub side due to the large curvature of the shroud.

A new type of diffuser with half guide vanes set on the shroud side wall, was tested in order to improve the pressure recovery of the diffuser for high specific speed compressors. The effect of similar guide vanes for a conical diffuser for mixed flow blowers has been reported [8]. The flow in the conical diffuser is quite unstable because of the curvature of the inner wall, but guide vanes effectively prevented a skewed boundary layer distortion on the convex inner wall. The present work intended to investigate the effects of the half guide vanes on the equalization of the highly distorted inlet flow discharged from high specific speed centrifugal impellers, and on the improvement of the pressure recovery of the radial diffuser and the stage efficiency.

The guide vanes of a new concept were applied to the No. 15 diffuser. The specific speed was 500 (rpm, m^3/min, m), that is, 1.22 in nondimensional number, and the impeller had 20 blades, which were inclined 60 deg from the circumference at the exit. There were 20 guide vanes which had a vane angle of 35 deg all the way through and a constant thickness of 2.3 mm. They were installed from 1.02 r_2 to 1.6 r_2 as shown in Fig. 7. The vane height was changed in several steps.

Influence of the Height of Guide Vanes. The characteristic curves of the compressor stage are presented in Fig. 8. A sizable improvement is achieved when the vane height is about one half of the diffuser width. On the other hand, the stage performance of the diffuser with full vanes ($h/b = 1.0$) is unfavorable especially at high flow rate. The relationship between the compressor efficiency and the vane height is shown in Fig. 9, where the efficiencies are shown as relative values for a defined efficiency of one for the vaneless diffuser stage. The stage efficiency near the design flow rate reaches its maximum value when the guide vanes have a height between $0.4b$ and $0.5b$.

Figure 10 shows that the best pressure recovery coefficient is achieved near a height of $0.4b$. These coefficients of the diffusers were measured at the center of a pitch of adjacent guide vanes by using three-hole yaw probes. The pressure recovery coefficients of the diffusers with guide vanes increase with the height of the vanes until the height reaches about one half of the diffuser width. When the height of the guide vanes is larger than this value, the pressure recovery coefficient decrease with increasing height of vanes.

Velocity Distributions at the Inlet and Exit of the Diffusers. The half guide vanes at the diffuser inlet were effective for improving the pressure recovery for extremely distorted flow, as shown in Fig. 10. In the following, the relationship between the velocity distribution across the diffuser width and the diffuser pressure recovery is discussed. The velocity distributions were measured across the diffuser width at the middle of the vane pitch.

Figure 11 shows the velocity and the flow angle distributions in the axial direction at the inlet and exit of a diffuser with the vane height of 0.4b together with those values of a vaneless diffuser, at 0.92 times the design flow rate. The velocity distributions at the diffuser exit in the same two diffusers are plotted in Fig. 12 at various flow rates. Both Figs. 11 and 12 show that the maximum pressure recovery of the diffuser in Fig. 10 is closely related to the uniformity of the axial velocity distributions attained by the half guide vanes. More detailed measurements of velocity distributions in the diffusers are discussed in the following section.

Measurements of Flow in Diffusers Using a Laser Velocimeter

Test Rig and Instrumentation. Measurements using a laser-two-focus (L2F) velocimeter were made with an intention to show more detailed velocity distributions in the diffusers with and without half guide vanes. The experiments were made using the low speed test rig shown in Figs. 13 and 14. The specific speed was about 400 (rpm, m^3/min, m), that is, 0.98 in nondimensional number, and the impeller with a tip

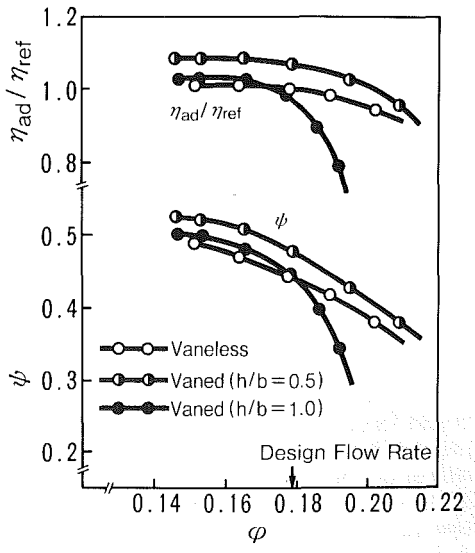

Fig. 8 Stage performance values of a compressor with different diffusers (Uncertainty in $\eta_{ad}/\eta_{ref} = \pm 0.005$, in $\psi = \pm 0.0013$, and in $\varphi = \pm 0.002$ at the 95% confidence level)

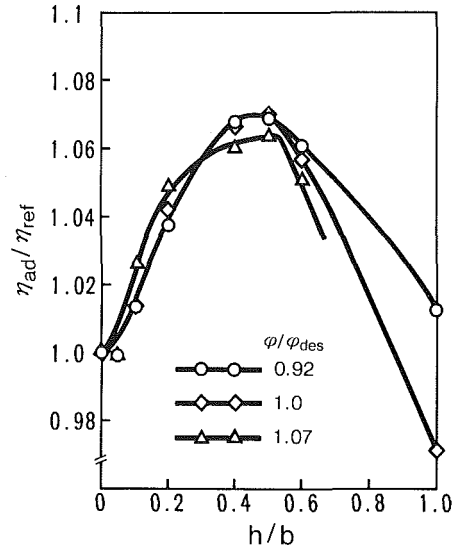

Fig. 9 Effect of guide vane height on compressor efficiency

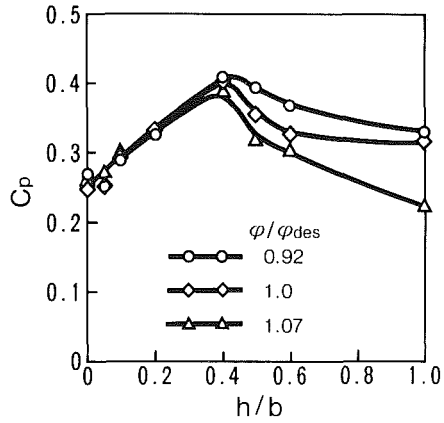

Fig. 10 Effect of guide vane height on pressure recovery coefficient

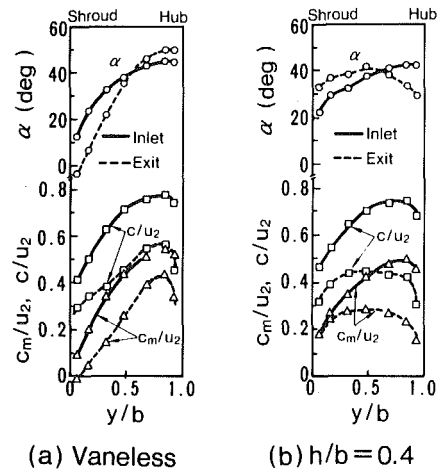

Fig. 11 Velocity distributions at the inlet and exit of diffusers with and without half guide vanes

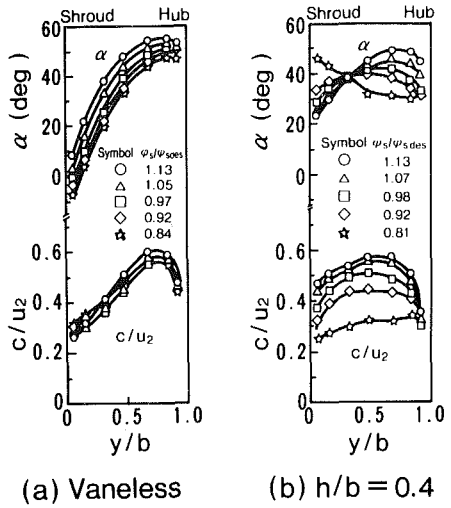

Fig. 12 Velocity distributions at the diffuser exit for different flow rates

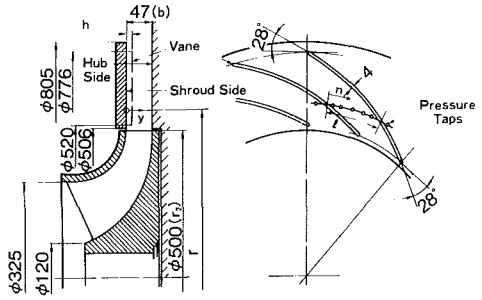

Fig. 13 Low speed test rig and arrangement of guide vanes

diameter of 500mm, had 18 blades which were inclined 50 deg from the circumference at the exit. The rotational speed of the impeller was 1500rpm. At this speed the air is essentially incompressible, therefore the shroud contour of the impeller was modified [2] to have the same diffusion ratio as the original impeller, i.e., about 1.6 between inlet and outlet. The exit radius from the diffuser was 805mm, and the axial width of the diffuser was constant and equal to the impeller passage width at the outlet, 47 mm. Eighteen guide vanes which had a vane angle of 28 deg all the way through were set on the shroud side wall from 1.04 r_2 to 1.55 r_2 as shown in Fig. 13, and the vane height was changed in several steps.

Figure 14 shows a photograph of the measurement section of the L2F velocimeter [9], [10]. An optical head faces an optical glass window mounted on the hub side diffuser wall, and laser beams are introduced into the diffuser passage at the various radii. Measurements of velocity distributions in circumferential direction were made at sixteen distinct positions over one blade pitch of an impeller. Static pressure distributions were measured by pressure taps located in the shroud side wall along the half guide vanes, five holes at every ten different radii. Figure 15 shows the characteristics curve of the low speed test compressor and the three different flow rates where the velocity distributions were measured.

Radial Distribution of Static Pressure in Diffusers. The radial distributions of the static pressure in diffusers with and without half guide vanes at the design flow rate are shown in Fig. 16. The static pressure is averaged in the circumferential direction at each radius for the diffusers with vanes. The maximum static pressure rise is attained with a vane height of 0.4b, the same value which was attained in the case of the high speed test of Fig. 10.

Detailed Measurements of Velocity Distributions Using a L2f Velocimeter. Figure 17 shows the rotating circumferential velocity distortions measured across the diffuser width at the inlet of a vaneless diffuser ($r/r_2 = 1.04$). The abbreviations, PS and SS denote the pressure side and the suction side of the impeller blades. A narrow wake behind the blade is clearly seen at or above the design flow rate, however, a wide wake region is observed near the suction side of the blade at lower flow rate. The flow distortion in the circumferential direction, especially in the flow angle α and in C_m, increases at the shroud side ($y/b = 0.23$) as compared with the hub side ($y/b = 0.85$).

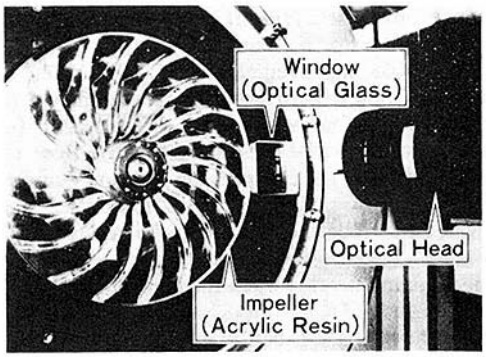

Fig. 14 Photograph of laser velocimeter operating on the low speed test rig

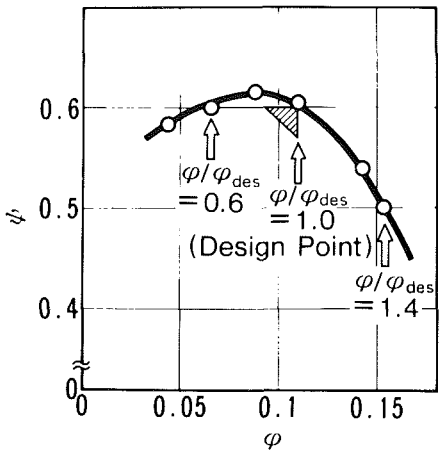

Fig. 15 Characteristics curve of the test compressor

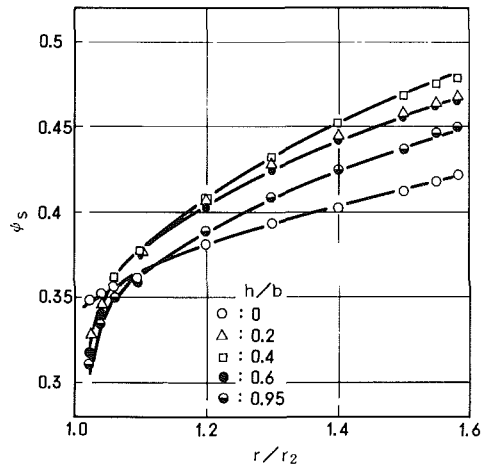

Fig. 16 Radial distribution of static pressure in diffusers with and without guide vanes (Uncertainty in $\psi_s = \pm 0.0012$ at the 95% confidence level)

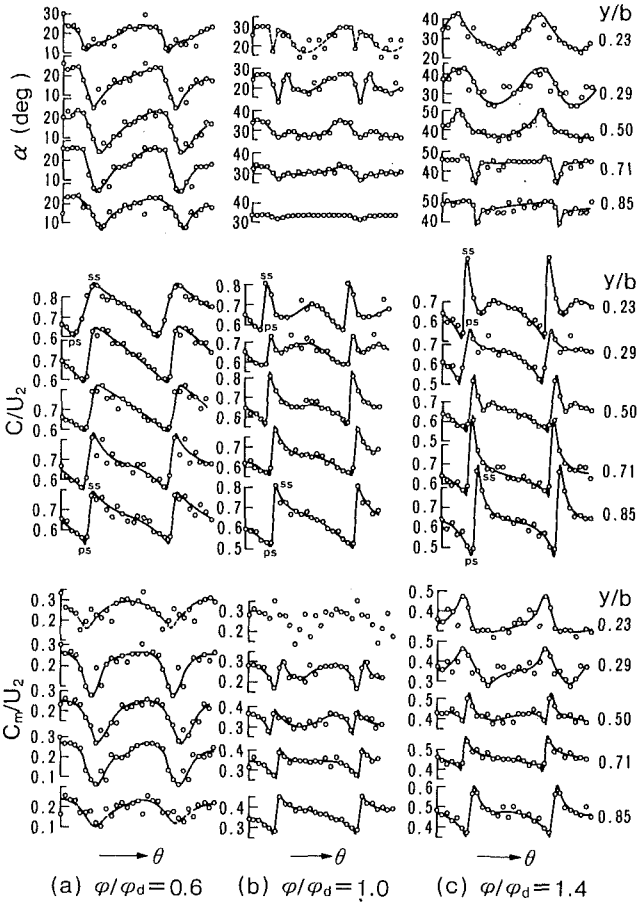

Fig. 17 Velocity fluctuations at the inlet of a vaneless diffuser measured across the diffuser width ($r/r_2 = 1.04$)

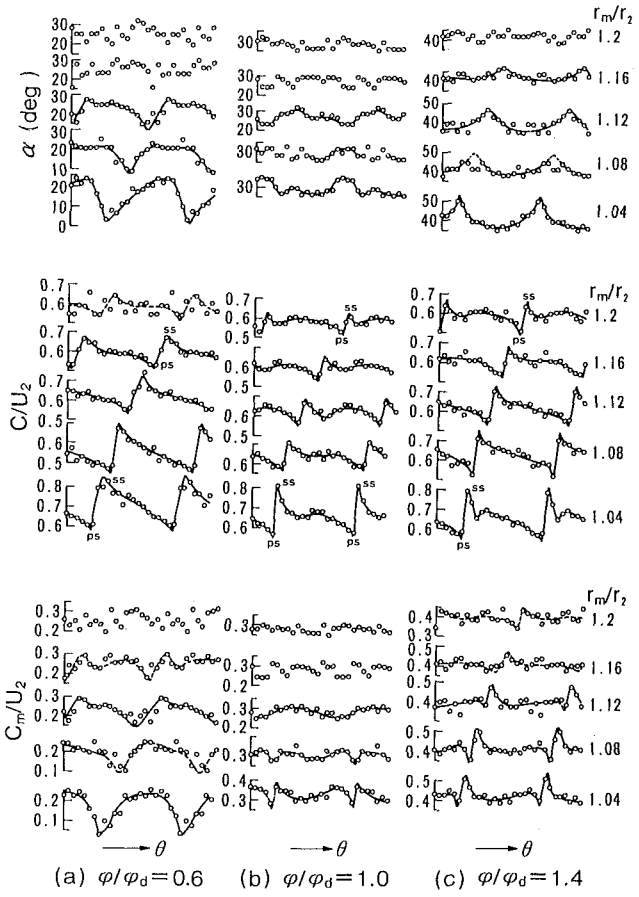

Fig. 18 Velocity fluctuations at various radii in a vaneless diffuser ($y/b = 0.5$)

The velocity distributions in the circumferential direction at various radii from $1.04r_2$ to $1.2r_2$ are presented in Fig. 18. The rotating circumferential velocity distortion decays quickly for radius ratios of 1.0 to 1.2 as reported earlier [5].

A few measurements of the circumferential distortion at the inlet of the diffuser with half guide vanes are shown in Fig. 19. The circumferential distortions measured at different diffuser widths differ from each other. In the result measured at different diffuser widths differ from each other. In the result measured at the width of $0.23b$, under the tip of the guide vanes, an interaction between impeller blades and half guide vanes is observed. On the other hand, this is not observed in the velocity distributions in the circumferential direction measured at the width of $0.66b$, beyond the tip of the guide vanes.

Figure 20 plots the velocity fluctuations at various radii in diffusers with and without guide vanes in terms of $\Delta C/\bar{C}$, where $\Delta\bar{C}$ is the peak-to-peak value of the absolute velocity fluctuation and $\bar{C}$ is the time mean absolute velocity. It seems that the circumferential velocity distortions decay quickly near the diffuser inlet whether the diffuser has half guide vanes or not.

Velocity Distribution in Axial Direction at Various Radii in the Diffusers. Time mean velocity distributions in the axial direction with and without guide vanes are presented in Fig. 21. Unlike the circumferential distortions, the axial distortions in a vaneless diffuser increase with the radius, and the flow separation seems to occur just downstream from the diffuser inlet. On the other hand, the axial distortion in the diffuser with half guide vanes is much more uniform, with the most

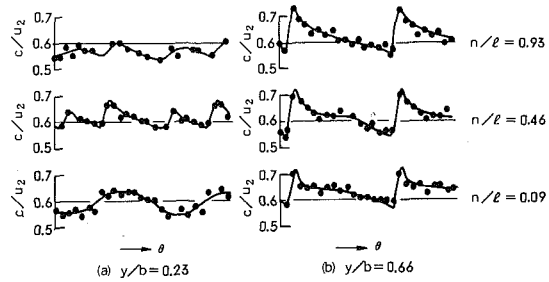

Fig. 19 Velocity fluctuations at the inlet of a diffuser with half guide vanes, measured across diffuser width ($y/b = 0.23$ and 0.66, $h/b = 0.4$, $r/r_2 = 1.1$, and φ $|\varphi$des $= 1.0$)

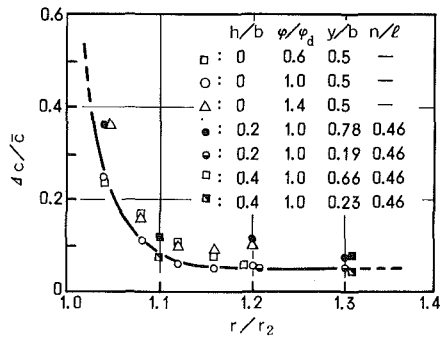

Fig. 20 Radial variation of velocity fluctuations in diffusers with and without guide vanes
(Uncertainty in $\Delta C/\bar{C} = \pm 0.014$ at the 95 percent confidence level)

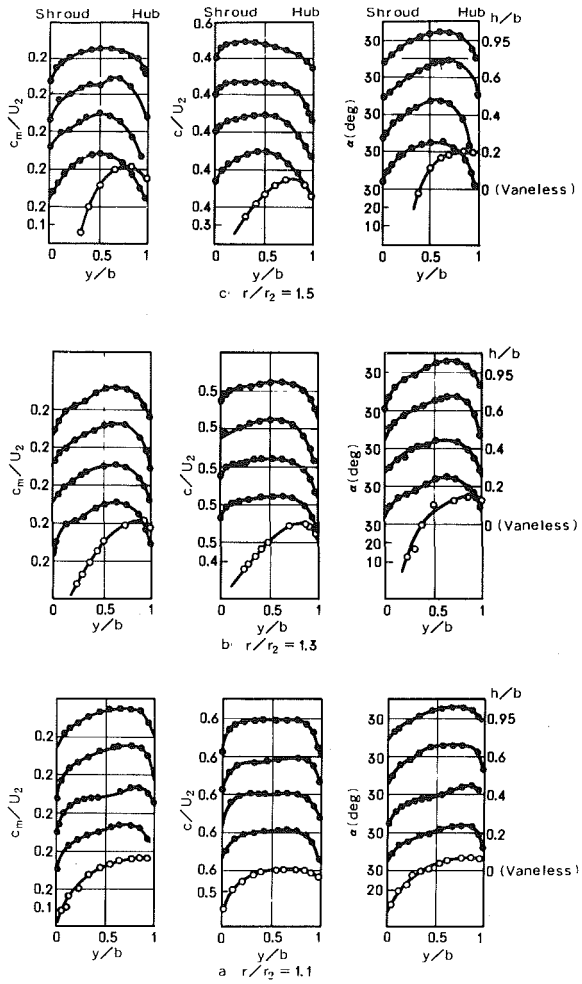

Fig. 21 Time mean velocity distributions in axial direction at various radii in diffuser with and without guide vanes
(○ symbols show a vaneless diffuser, ● symbols show vaned diffusers)

uniform velocity distribution being attained at a vane height of about 0.4*b*.

The experimental results verify that the maximum pressure recovery coefficient as shown in Fig. 10 is related to the uniformity of the axial velocity distribution attained with the half guide vanes.

Conclusions

The performance of vaneless diffusers and the velocity distributions discharged from the impellers of various specific speed centrifugal compressors were studied. A new type of diffuser with half guide vanes on the shroud side wall was tested in order to determine its ability to improve the pressure recovery coefficient. Detailed measurements of velocity distributions in the various diffusers were carried out with use of Pitot tubes and a laser-two-focus velocimeter.

The following results were obtained:

(1) The performance of the vaneless diffuser for high specific speed centrifugal compressors is reduced considerably compared with the value expected by a uniform two-dimensional analysis.

(2) The highly distorted flow in the axial direction, discharged from high specific speed centrifugal impellers, has a strong effect on the diffuser performance.

(3) The pressure recovery of a diffuser at distorted inlet flow is considerably improved by using half guide vanes. The optimum half guide vane height is a little less than one half of the diffuser width.

(4) Measurements of the velocity distribution in the diffuser using Pitot tubes and a laser-two-focus velocimeter, clearly show that the half guide vanes provide a uniform flow in the axial direction and improve the pressure recovery of the diffuser.

Acknowledgments

The authors would like to express their appreciation to Professor Y. Senoo of Kyushu University and Professor I. Ariga of Keio University for their suggestions and helpful discussions during this investigation.

References

1 Bammert, K., et al., "Vaneless Diffuser Flow with Extremely Distorted Inlet Profile," ASME paper No. 78-GT-47.

2 Inoue, M., and Cumpsty, N. A., "Experimental Study of Centrifugal Impeller Discharge Flow in Vaneless and Vaned Diffusers," ASME *Journal of Engineering for Gas Turbines and Power*, Vol. 106, 1984, p. 455.

3 Dean, R. C., Jr., and Senoo, Y., "Rotating Wakes in Vaneless Diffusers," ASME *Journal of Basic Engineering*, Vol. 82, No. 3, 1960, p. 563.

4 Johnston, J. P. and Dean, R. C., Jr., "Losses in Vaneless Diffusers of Centrifugal Compressors and Pumps," ASME *Journal of Basic Engineering*, Vol. 88, No. 1, 1966, p. 49.

5 Senoo, Y., and Ishida, M., "Behavior of Severely Asymmetric Flow in a Vaneless Diffuser," ASME *Journal of Engineering for Power*, Vol. 97, 1975, p. 375.

6 Senoo, Y., et al., "Asymmetric Flow in Vaneless Diffusers of Centrifugal Blowers," ASME JOURNAL OF FLUIDS ENGINEERING, Vol. 99, 1977, p. 104.

7 Senoo, Y., and Kinoshita, Y., "Influence of Inlet Flow Conditions and Geometries of Centrifugal Vaneless Diffuser on Critical Flow Angle for Reverse Flow," ASME JOURNAL OF FLUIDS ENGINEERING, Vol. 99, 1977, p. 98.

8 Sakai, T., et al., "Experimental Study on Diffusers for Mixed-Flow Machines," ASME Paper, 78-GT-120.

9 Schodl, R., "A Laser-Two-Focus (L2F) Velocimeter for Automatic Flow Vector Measurements in the Rotating Components of Turbomachines," ASME JOURNAL OF FLUIDS ENGINEERING, Vol. 102, 1980, p. 412.

10 Krain, H., "A Study on Centrifugal Impeller and Diffuser Flow," ASME *Journal of Engineering for Power*, Vol. 103, 1981, p. 688.

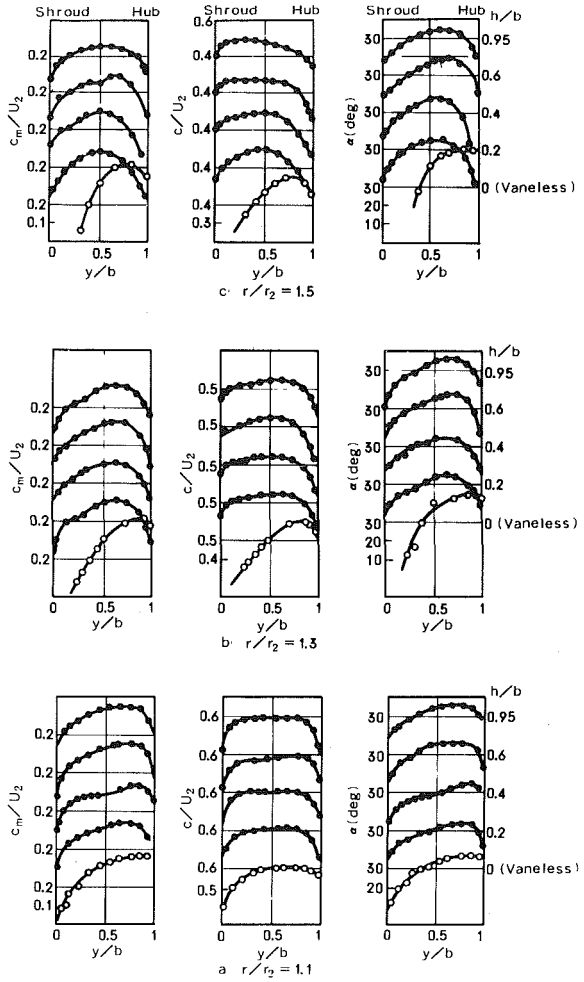

Fig. 21 Time mean velocity distributions in axial direction at various radii in diffuser with and without guide vanes
(○ symbols show a vaneless diffuser, ● symbols show vaned diffusers)

uniform velocity distribution being attained at a vane height of about 0.4*b*.

The experimental results verify that the maximum pressure recovery coefficient as shown in Fig. 10 is related to the uniformity of the axial velocity distribution attained with the half guide vanes.

Conclusions

The performance of vaneless diffusers and the velocity distributions discharged from the impellers of various specific speed centrifugal compressors were studied. A new type of diffuser with half guide vanes on the shroud side wall was tested in order to determine its ability to improve the pressure recovery coefficient. Detailed measurements of velocity distributions in the various diffusers were carried out with use of Pitot tubes and a laser-two-focus velocimeter.

The following results were obtained:

(1) The performance of the vaneless diffuser for high specific speed centrifugal compressors is reduced considerably compared with the value expected by a uniform two-dimensional analysis.

(2) The highly distorted flow in the axial direction, discharged from high specific speed centrifugal impellers, has a strong effect on the diffuser performance.

(3) The pressure recovery of a diffuser at distorted inlet flow is considerably improved by using half guide vanes. The optimum half guide vane height is a little less than one half of the diffuser width.

(4) Measurements of the velocity distribution in the diffuser using Pitot tubes and a laser-two-focus velocimeter, clearly show that the half guide vanes provide a uniform flow in the axial direction and improve the pressure recovery of the diffuser.

Acknowledgments

The authors would like to express their appreciation to Professor Y. Senoo of Kyushu University and Professor I. Ariga of Keio University for their suggestions and helpful discussions during this investigation.

References

1 Bammert, K., et al., "Vaneless Diffuser Flow with Extremely Distorted Inlet Profile," ASME paper No. 78-GT-47.

2 Inoue, M., and Cumpsty, N. A., "Experimental Study of Centrifugal Impeller Discharge Flow in Vaneless and Vaned Diffusers," ASME *Journal of Engineering for Gas Turbines and Power*, Vol. 106, 1984, p. 455.

3 Dean, R. C., Jr., and Senoo, Y., "Rotating Wakes in Vaneless Diffusers," ASME *Journal of Basic Engineering*, Vol. 82, No. 3, 1960, p. 563.

4 Johnston, J. P. and Dean, R. C., Jr., "Losses in Vaneless Diffusers of Centrifugal Compressors and Pumps," ASME *Journal of Basic Engineering*, Vol. 88, No. 1, 1966, p. 49.

5 Senoo, Y., and Ishida, M., "Behavior of Severely Asymmetric Flow in a Vaneless Diffuser," ASME *Journal of Engineering for Power*, Vol. 97, 1975, p. 375.

6 Senoo, Y., et al., "Asymmetric Flow in Vaneless Diffusers of Centrifugal Blowers," ASME JOURNAL OF FLUIDS ENGINEERING, Vol. 99, 1977, p. 104.

7 Senoo, Y., and Kinoshita, Y., "Influence of Inlet Flow Conditions and Geometries of Centrifugal Vaneless Diffuser on Critical Flow Angle for Reverse Flow," ASME JOURNAL OF FLUIDS ENGINEERING, Vol. 99, 1977, p. 98.

8 Sakai, T., et al., "Experimental Study on Diffusers for Mixed-Flow Machines," ASME Paper, 78-GT-120.

9 Schodl, R., "A Laser-Two-Focus (L2F) Velocimeter for Automatic Flow Vector Measurements in the Rotating Components of Turbomachines," ASME JOURNAL OF FLUIDS ENGINEERING, Vol. 102, 1980, p. 412.

10 Krain, H., "A Study on Centrifugal Impeller and Diffuser Flow," ASME *Journal of Engineering for Power*, Vol. 103, 1981, p. 688.

DISCUSSION

C. Rogers[1]

The major conclusion of this paper relates low vaneless diffuser static pressure recovery with nonuniform high specific speed impeller discharge conditions.

The results in particular, Fig. 2, contrast those of Rodgers reference [1]: "Static Pressure Recovery Characteristics of Some Radial Vaneless Diffusers," *Canadian Aeronautics and Space Journal*, Vol. 30, No. 1, March 1984. Reference [1] corroborates that high specific speed centrifugal impellers generally exhibit less uniform exit, flow, precipitating higher "equivalent" friction coefficients for downstream vaneless diffusers. These higher equivalent friction losses did not, however, cause the static pressure recovery to *decrease* with increasing width to radius ratio b/r_i. Reference [1] data are summarized in Fig. 10 in more specific terms of vaneless diffuser static pressure recovery versus inlet flow angle, with b/r_i as a parameter.

Differences in the compressor rig, compared to reference [1] are two dimensional versus three dimensional impellers, and vaneless diffuser exit conditions, return bend versus scroll. Perhaps these differences contribute to the conflicting static pressure recovery trends?

[1]Sundstrand Turbomach, San Diego, Calif. 92138-5757.

Authors' Closure

The authors wish to thank Dr. Rodgers for his valuable comments on the paper. The pressure recovery of vaneless diffusers for centrifugal compressors generally increases with increasing diffuser width ratio when the inlet velocity distribution is not distorted highly.

In Fig. 2, the authors intend to indicate the contrast to the ordinary relation between C_p and b/r_i which is predicted when the inlet velocity distribution is not highly distorted. Figure 5 shows the variation of the intensity of inlet flow distortion of each stage in Table 1. Since the inlet distortion coefficient B_f increases with increasing width to radius ratio b/r_i, the experimental data in Fig. 2 may be considered to show the effects not only of the width radius ratio but also of the inlet flow distortion.

Considering that actual velocity distributions and the intensity of the distortion are not always similar to those of this experiment, the effect of the inlet flow distortion may vary between experiments.

The authors do wish to emphasize that decreasing the pressure recovery of vaneless diffusers or not, largely depends on the intensity of the distortion of inlet velocity distributions; and even if the low pressure recovery is caused by the nonuniform inlet flow conditions, the inlet distorted flow can be made uniform by using half guidevanes for instance, and the pressure recovery is possible to be improved considerably as shown in Figs. 10 and 11, and Figs. 16 and 21, respectively.

Valve and In-Cylinder Flow Generated by a Helical Port in a Production Diesel Engine

C. Arcoumanis
C. Vafidis
J. H. Whitelaw

Imperial College of Science and Technology, Department of Mechanical Engineering, Fluids Section, London SW7 2BX, United Kingdom

The flow generated by the helical port of a production Diesel engine has been investigated by laser Doppler anemometry under steady flow and operating conditions at ~900 rpm and compression ratio of 8. The flow around the valve periphery was found to be non-uniform with the axial velocity distribution being more sensitive to valve lift. The in-cylinder swirl distribution at inlet valve closure exhibited an axial stratification in the disc-chamber while turbulence intensity remained constant in the clearance volume during the rest of the compression stroke with levels of 0.5 $\bar{v}_p$ and a minimum of about 0.4 $\bar{v}_p$ at top-dead-center following a rapid decay at $\theta = 340°$.

Introduction

It has long been recognized that the performance of direct injection Diesel engines depends on induction swirl and spray characteristics for efficient mixing of fuel and air prior and during combustion. However, as the engine speed requirements increase and legislation concerning gaseous emissions and noise gets worldwide more stringent, better control and more accurate characterization of induction-generated air motion over an extended speed range has become a prerequisite to the development of high speed direct injection (HSDI) Diesel engines for passenger cars. The parallel development of multidimensional computer models for predicting the in-cylinder flowfield has placed an additional emphasis on experimental techniques to provide accurate boundary conditions to the computer codes and validation data for their assessment.

There are two main types of swirl producing inlet ports depending on whether swirl is produced upstream or downstream of the valve; prevalve swirl is produced by helical ports and postvalve mainly by directed ports. In helical ports, which have found extensive application in truck engines, swirl is generated by the spiral shape of the port and an angular momentum flux is imparted to air as it flows out of the valve and enters the engine cylinder. Helical ports in general tend to produce higher swirl at lower valve lifts [1-3], more ordered motion during compression and higher swirl levels inside the piston-bowl [3]. They also give higher discharge coefficients than directed ports at equivalent swirl levels and better performance over a wide speed range [4] and at the same time are less sensitive to variations caused by manufacturing tolerances.

The assessment of the performance of a helical port requires investigation of the flow at the exit plane of the intake valve and at inlet valve closure (IVC), before its transformation by compression and piston-bowl geometry. The flow characteristics in the valve gap are determined by the geometry of the inlet port and valve but can be influenced by the piston proximity at TDC of induction. It is the piston clearance during early induction which controls the degree of development of the port-generated helical motion later in the stroke and the crucial flowfield at IVC; from then on compression takes over by organizing swirl into a more ordered type of motion but without altering its main characteristics. The angular momentum of the swirling air decays from IVC to TDC by 30-45 percent [5] due to wall friction, which follows the increase of surface to volume ratio, and turbulent dissipation. The geometry of the piston-bowl, in addition to affecting the valve flow during early induction, determine near TDC of compression the degree of swirl amplification and squish-generated turbulence inside the bowl [6].

Due to experimental difficulties in measuring the valve flow under operating conditions, steady flow experiments have been employed to simulate the inlet flow as a function of valve lift and pressure drop. Both probes [7, 8] and laser Doppler anemometers [9, 10] have been used but it is only recently that the quasi-steady assumption has been experimentally verified under idealized conditions [11, 12] and the range of its applicability determined as a function of engine speed [13]. In the present investigation the flow generated by the helical port of a Ford Diesel engine has been quantified by laser Doppler anemometry at the valve exit plane under steady flow conditions and the validity of this assumption has been examined by a limited number of measurements in a motored research engine where the development of the valve flow during induction and compression has been subsequently investigated. The in-cylinder velocity measurements were obtained at relatively low engine speed and compression ratio and with a flat piston to allow focusing on the port generated mean flow and turbulence without any influences from piston-bowl geometry near TDC of compression. The experimental system employed with the flow configurations are described in the next section followed by results and conclusions.

Contributed by the Fluids Engineering Division of THE AMERICAN SOCIETY OF MECHANICAL ENGINEERS and presented at the Symposium on Fluid Mechanics of Internal Combustion Engineering, Winter Annual Meeting, Miami Beach, Fla., November 17-22, 1985. Manuscript received by the Fluids Engineering Division January 21, 1986.

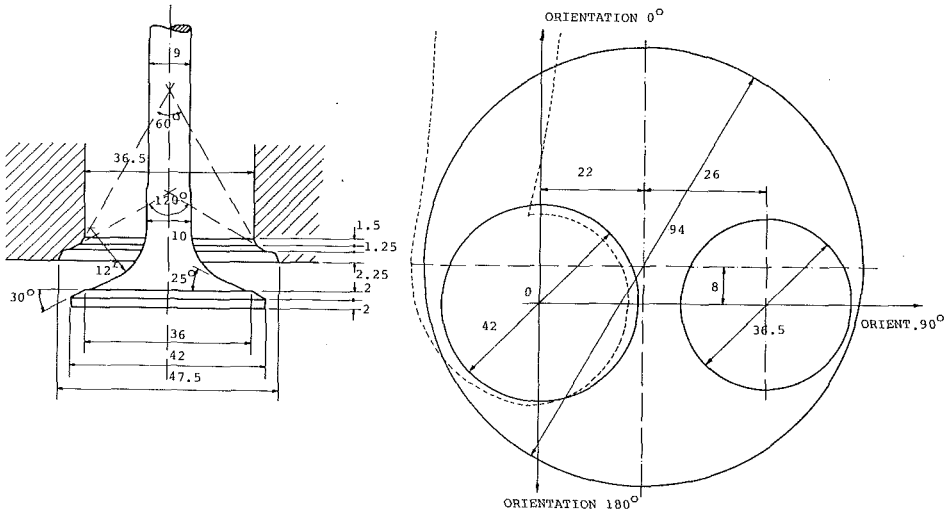

Fig. 1 Intake valve and cylinder head geometry. Definition of measurement planes.

Experiment

Flow Configurations

Steady Flow. The cylinder head of a Ford 2.5L HSDI Diesel engine which has been described in [14] was mounted on a blow-down type steady flow rig and fitted with a plexiglass open-ended thin wall cylinder of 94mm bore. The inlet port was of the helical type (Fig. 1) and was connected to a stagnation chamber through a smooth transition. Air from a compressed air supply was fed at a constant flow rate of 101 kg/h to the chamber and discharged through the intake valve into the open-ended cylinder. A small part of the flow (0.5 percent) was bypassed upstream of the stagnation chamber to atomize the silicone-oil used as seeding material for the laser Doppler anemometry measurements. The cylinder head was able to rotate around the cylinder axis to allow measurements to be obtained at three orientations (0, 90, 180 deg) around the valve periphery (Fig. 1); all three velocity components have been measured at valve lifts of 4, 7, and 10mm but only a representative sample will be presented here to allow comparison with the limited number of results obtained under operating conditions.

In-Cylinder Flow. The cylinder head together with the attached stagnation chamber were mounted on a single cylinder Petter engine which was modified (Fig. 2) to provide an identical cylinder bore (93.7mm) to the Ford engine. The liner of the Petter engine was extended with a plexiglass cylinder of 13mm wall thickness which was long enough to allow full optical access for forward-scatter LDA measurements around IVC. Similarly, the piston of the Petter engine was extended to provide a flat piston-crown. The engine was motored at a nominal speed of 916 rpm which corresponded to the air mass flowrate used for the steady flow measurements calculated in terms of the mean piston speed. The geometric and operating characteristics of the research engine are summarized in Table 1.

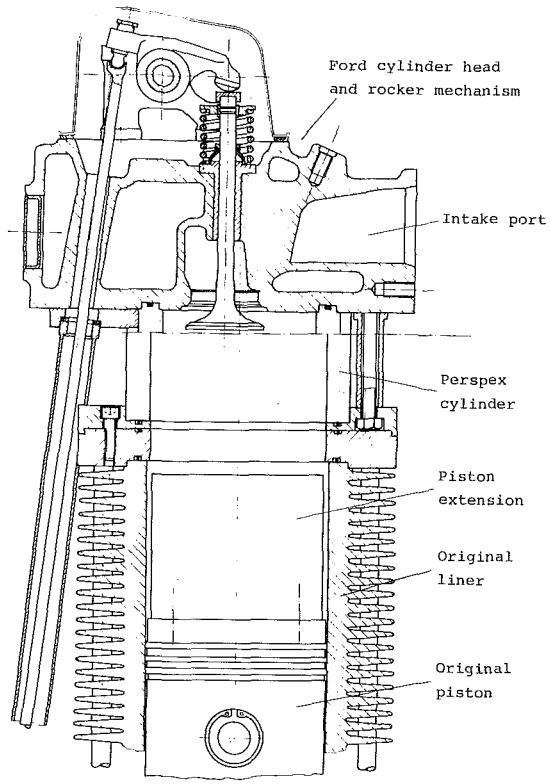

Fig. 2 Schematic of the research engine incorporating the Ford 2.5L cylinder head

Measurement System. The velocity measurements in the steady flow rig and in the motored engine were obtained by laser Doppler anemometry (LDA). Depending on the flow configuration, the measured velocity component and the

Nomenclature

D = valve diameter
L = valve lift
$\bar{U}, \bar{V}, \bar{W}$ = ensemble-averaged mean axial, radial and swirl velocity
$\tilde{u}, \tilde{v}, \tilde{w}$ = ensemble-averaged rms axial, radial and swirl velocity
v_p = instantaneous piston speed
$\bar{v}_p$ = mean piston speed
r = radial coordinate
z = axial coordinate
BDC = bottom-dead-center
IVC = inlet-valve-closure
TDC = top-dead-center
θ = crank angle

Table 1 Engine characteristics

Bore, mm	93.7
Stroke, mm	110
Compression ratio	8
Connecting rod length, mm	231.9
Clearance height at TDC, mm	15.85
Intake valve : Diameter, mm	42
: Maximum lift, mm	11
: Opens at	4.5° BTDC
: Closes at	215.5° ATDC
Exhaust valve : Diameter, mm	36.5
: Opens at	215.5° BTDC
: Closes at	4.5° ATDC
Engine speed, rpm	916

range of Doppler frequencies encountered, different LDA systems have been employed which will be described briefly in the following paragraphs; more details can be found in [15].

The axial and radial velocity components at the valve exit under steady flow conditions were measured with a dual beam LDA system operating in the forward-scatter mode and using a 5mW He-Ne laser while the tangential (swirl) component was measured with backward-scattered light and a 1.4W Argon-ion laser at 488nm. In both cases a frequency shift of 40 MHz provided by a Bragg cell was used to allow unambiguous measurements in regions where Doppler frequency spectra with bandwidths of up to 20 MHz were observed. This range of frequencies precluded the use of either a standard rotating grating with frequency shifts up to 7 MHz or downmixing with commercially available systems which are limited to an effective shift of not more than 10 MHz. For the in-cylinder meassurements, which required lower than 40 MHz but higher than 7 MHz frequency shifts, a different optical system was used which made use of the second order beams from a rotating diffraction grating and a 0.4W Argon-ion laser; this system allowed measurements to be made with shifts up to 14 MHz. The ouptut signal from the photomultiplier was in all cases high-pass filtered and amplified before it was input to a high resolution (lns) frequency counter interfaced to a microcomputer for data collection and ensemble-averaged analysis. In the steady flow measurements, the unprocessed signal was also input to a spectrum analyser to provide information about the bandwidth of the Doppler frequency spectrum which was subsequently compared with the probability density distribution of the counter-processed frequency data.

Experimental Uncertainty. The measurement position and the magnitude of the velocity components were corrected, when required, for refraction effects of the laser beams through the cylindrical wall according to the procedure described in [15]. Crank-angle broadening, which is one of the most significant error sources in ensemble-averaged engine measurements, was rendered insignificant by following the recommendations of [16] in terms of maximum permissible window size during the engine cycle. No corrections were applied for velocity bias and fringe bias was estimated to be negligible due to the high frequency shift employed. Overall, the maximum uncertainty in the measurement of the mean and rms velocity is expected to be 5 and 10 percent respectively.

Results and Discussion

Valve Exit Flows. The flow at the exit plane of the intake valve has been investigated under steady conditions and compared with a few measurements obtained in the research engine to examine the validity of the quasi-steady assumption. All steady flow results were obtained with a constant air mass flowrate of 101 kg/h which corresponds to the mean rate of air displacement at an engine speed of 916 rpm and atmospheric conditions. The use of constant air flowrate rather

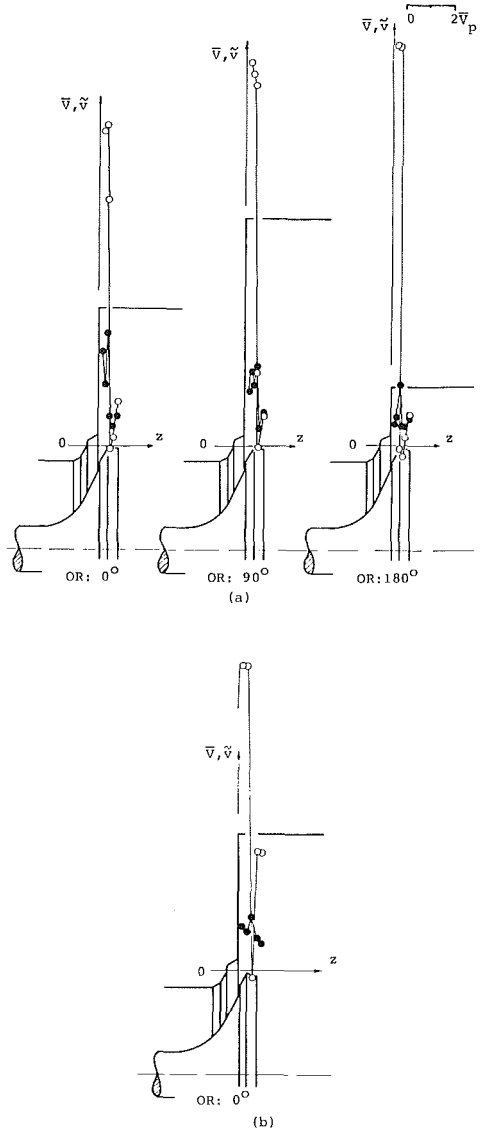

Fig. 3 Radial mean (o) and rms (•) velocity distribution at the valve exit plane for lift $L = 4$mm. (*a*) Steady flow (*b*) Engine operating conditions at $\theta = 29$ deg.

than constant pressure drop was based on the results of [15] which showed that for dimensionless valve lifts (L/D) greater than 0.07 the discharge coefficients obtained with the previously defined mean mass flowrate and the instantaneous flowrate at corresponding lifts were in good agreement. A representative sample of the velocity measurements in the valve gap obtained at three different lifts and in three orientations is shown in Figs. 3-5. Figure 3(*a*) shows the distribution of the radial mean and rms velocity at the valve exit plane for a lift of 4mm under steady flow conditions. Although the radial velocity component is uniformly distributed across the valve gap its distribution around the valve periphery is not uniform as indicated by the significant velocity variation between the 0° and 180°measurement planes. This was expected due to the helical port geometry and the asymmetric confinement imposed by the cylinder wall on the valve exit flow. The radial normal stresses, represented by the measured rms velocities, follow the trends of the mean flow and are not uniformly distributed around the valve periphery. However, they exhibit high levels especially in the 0° plane which may be due to a local flow instability near the cylinder head. Figure 3(*b*) shows the distribution of the radial mean and rms velocities at the

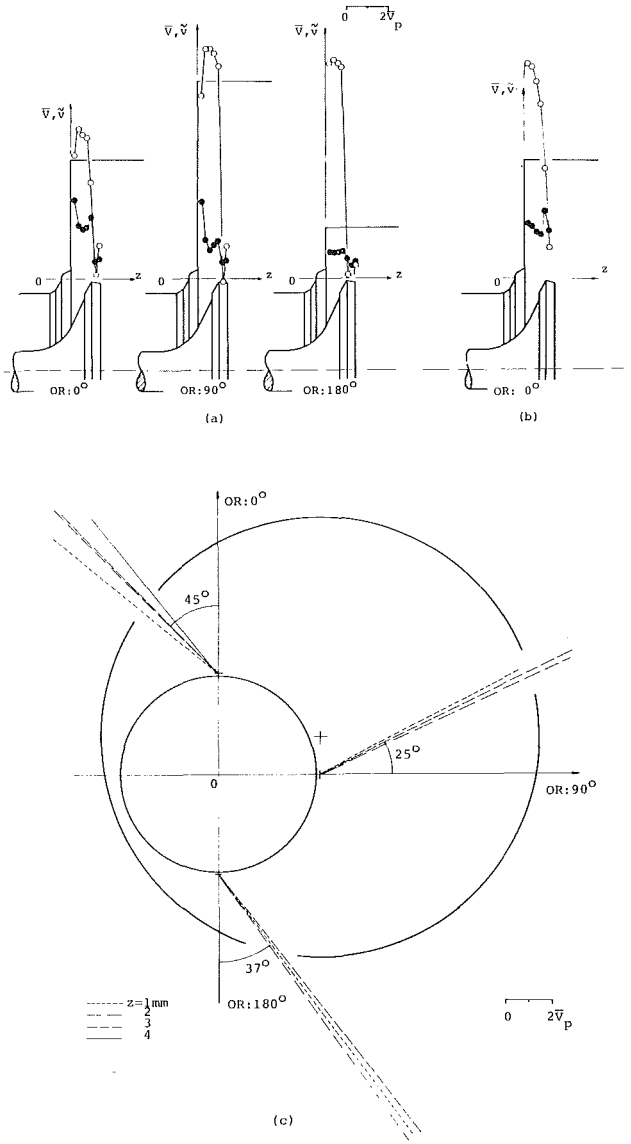

Fig. 4 Valve exit flow for lift $L = 7$mm. (*a*) Steady flow, radial mean (o) and rms (•) velocity distribution. (*b*) Engine operating conditions at $\theta = 47$ deg. (*c*) Vector addition of radial and swirl velocity components under steady flow conditions.

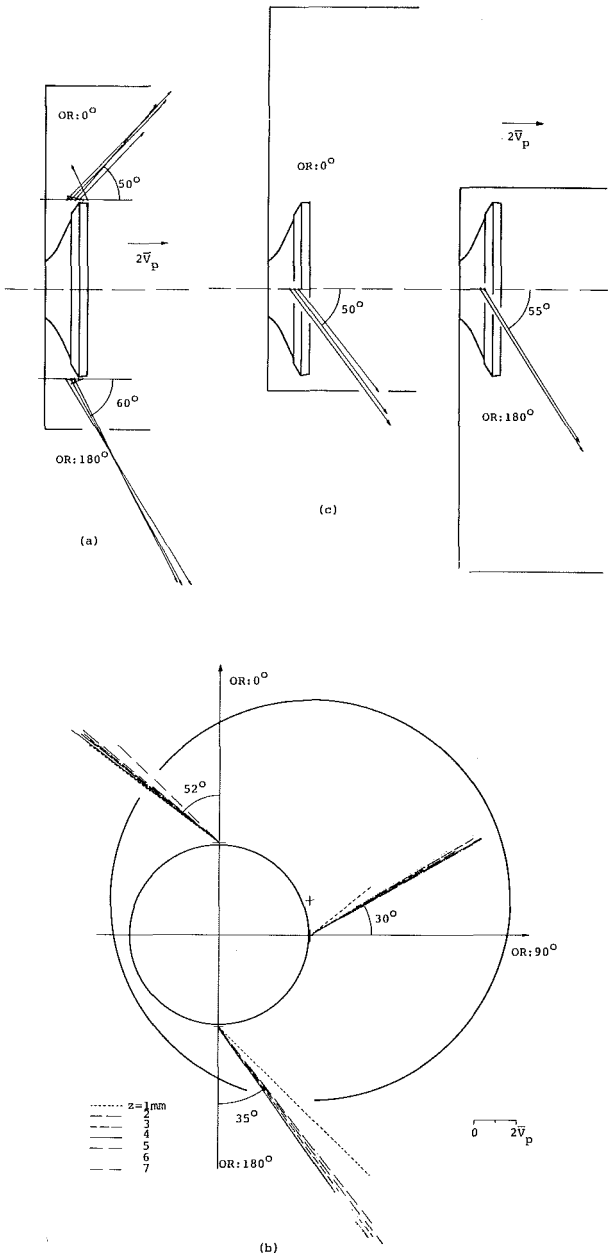

Fig. 5 Valve exit flow for lift $L = 10$mm under steady flow conditions. (*a*) Vector addition of axial and radial velocities. (*b*) Vector addition of radial and swirl velocities. (c) Vector addition of axial and swirl velocities.

same valve lift and in the 0° orientation but obtained under engine operating conditions at $\theta = 29$ deg which corresponds to a valve lift of 4mm. The mean velocity distribution is very similar to that measured under steady flow conditions and, when scaled with the instantaneous piston speed at $\theta = 29°$, the magnitudes of the maximum velocities agree within 2 percent. The measured normal stresses, when also scaled, were found to be lower than those under steady flow conditions which provides evidence of the developing nature of the flow during early induction [11]. It is interesting to note that the peak of the normal stresses at $z = 2$ mm and in the 0° orientation shown in Fig. 3(*a*) is no longer present which implies that even if there was a local flow instability in the steady case, a similar phenomenon was not observed under operating conditions. The radial velocity distribution at the medium valve lift of 7mm is shown in Fig. 4(*a*) and exhibits similar trends to the low lift case in that the flow is not uniform around the valve periphery with variations of up to 40 percent. Both mean and rms velocities are maximum in the 90 deg plane, which corresponds to the end of the helical ramp of the port, in agreement with the results of [10]. Comparison of the steady flow results with those obtained at the same valve lift under operating conditions at $\theta = 47$ deg, (Fig. 4(*b*)), shows similar velocity distributions and maximum velocities which, when normalized with the instantaneous piston speed, agree within 5 percent. The vector addition of the measured radial and swirl velocity components under steady flow conditions (Fig. 4(*c*)) provides a better picture of the flow around the valve; the flow angle with respect to the valve radius in the tangential plane is shown to exhibit small variations within the valve gap but significant variations along the valve periphery ranging from 25 deg to 45 deg. Similar trends have been reported in [9] for the valve flow generated by a similar helical port.

The flow at the higher valve lift of 10mm has also been examined and is presented in more detail in Fig. 5 in the form of vector plots under steady flow conditions. The vector addition of the axial and radial velocity components shown in Fig. 5(*a*) indicates that the flow angle with respect to the valve axis varies between orientations of 0 and 180 deg from 50 to 60 deg

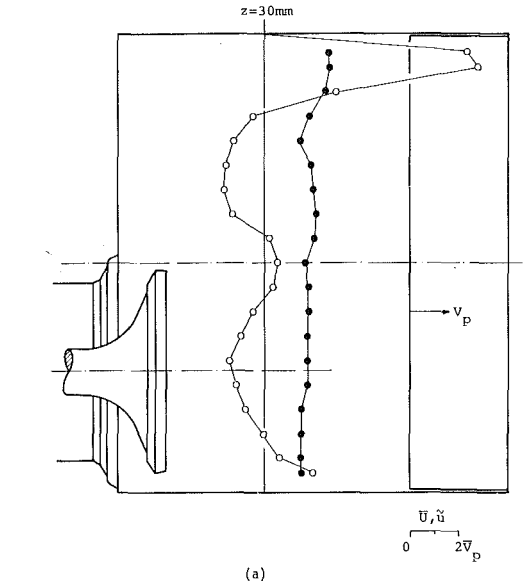

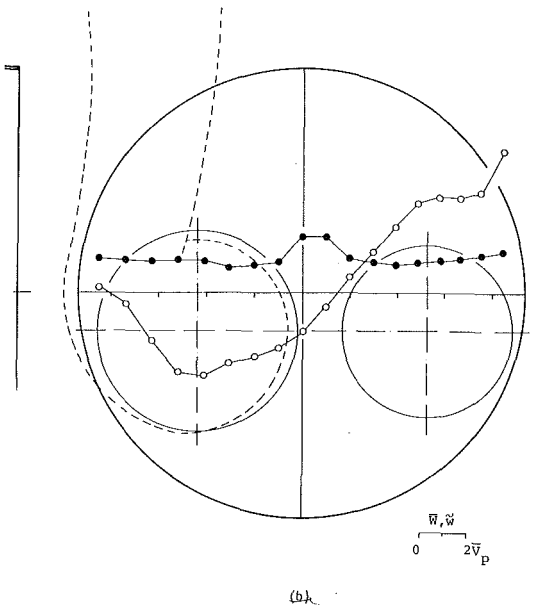

Fig. 6 In-cylinder axial (*a*) and swirl (*b*) mean (O) and rms (•) velocity distribution at $z = 30$mm and $\theta = 72$ deg with $L = 10$mm.

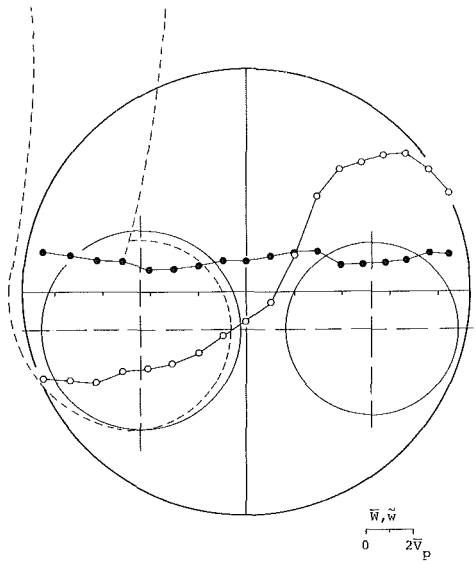

Fig. 7 In-cylinder mean (o) and rms (•) swirl velocity distribution at $z = 47$mm, $\theta = 166$ deg and $L = 7$mm

which corresponds to the valve seat angle. The vector addition of the radial and swirl components (Fig. 5(*b*)) shows similar trends to those observed at the lower lifts while the addition of the axial and swirl components (Fig. 5(*c*)) allowed the determination of the angle of the helical motion with respect to the valve axis which was found to be about 50 deg. In general, valve lift was found to exert greater influence on the flow angle in the axial plane but smaller influence on the flow in the tangential plane due to swirl generation upstream of the valve.

In-Cylinder Flow. The axial and swirl velocity distributions during the first half of induction have been measured at crank angle $\theta = 72$ deg which corresponds to a valve lift of 10mm and are shown in Fig. 6. As it is deduced from Fig. 6(*a*), the flow pattern in the axial plane parallel to the 90 deg orientation consists of a system of ring and toroidal vortices. At an axial location $z = 30$mm, the meam velocities peak at the far-valve side of the cylinder contrary to other engine configurations with smaller valve eccentricity and without port-generated swirl where opposite trends have been observed [12, 17]. The small positive velocities measured around the cylinder axis and attributed in [12] to the low pressure field generated by piston acceleration during early induction ($\theta = 30$ deg), are enhanced here by the swirl-induced radial pressure gradient which sustains the central vortex longer during induction. The swirl velocities at $\theta = 72$ deg, shown in Fig. 6(*b*), exhibit a double vortex pattern with the off-axis main vortex deviating significantly from solid body rotation and an rms velocity distribution which is nearly uniform in the outer part of the cylinder but with much higher levels around the cylinder axis. This could be attributed as will be discussed later to a broadening of the ensemble-averaged rms velocity distribution due to cyclic precession of the swirl center.

Later in the induction stroke and at $\theta = 166$ deg which corresponds to a 7 mm lift at the closing period of the valve, the swirl velocities at $z = 47$mm exhibit a single vortex pattern offset from the cylinder axis (Fig. 7). Comparison with Fig. 6(*b*) indicates that the peak in the rms velocities near the swirl center observed earlier during induction has disappeared. This is attributed to the different measurement location and crank angle since cycle-resolved and ensemble-averaged swirl measurements reported in [5] showed that the movement of the swirl center in space and time is more evident near the cylinder head with associated broadening of the ensemble-averaged rms velocities.

Figure 8 shows the swirl velocity distributions along two perpendicular planes at the same axial location and valve lift but obtained under steady flow conditions. Comparison with Fig. 7 shows that there are significant differences between the swirl profiles under steady and operating conditions which are due to the integrated effect of the developing swirl throughout induction and the absence of a flow boundary (piston) in the steady flow case. It is interesting to note that the steady flow swirl profile of Fig. 8 is in good agreement with the unsteady flow pattern at $\theta = 72$ deg even though their respective valve lifts and measurement locations are different. Comparison between these two profiles also reveals that although the mean swirl distributions are very similar, with almost identical velocity gradients around the center of rotation, the corresponding rms velocities differ in that, under steady flow conditions, they do not exhibit maxima near the swirl center as in the engine case but are rather uniform over the cylinder diameter. This indicates that the ensemble-averaged rms velocities in the engine case overestimate significantly the ac-

tual normal stresses due to cyclic variations in the position of the swirl center in regions of steep velocity gradients [5].

The double and single swirl patterns measured at $\theta = 72$ deg and $\theta = 166$ deg, respectively, have been also observed under steady flow conditions at a distance of one cylinder diameter downstream of the valve [18] and were associated with correspondingly low and high valve lifts. In the engine, the transition from a double vortex pattern to a single vortex is attributed to valve lift variation during induction and evolution of the in-cylinder swirl distribution towards a dynamically more stable and persisting flow pattern. As the profiles at IVC show (Fig. 9), the distribution of the swirl velocity component near the cylinder head ($z = 15$ mmn) shown in Fig. 9(a) exhibits similar trends to the swirl profile at $\theta = 166$ deg with evidence of forced vortex characteristics near the center of rotation and nearly uniform velocities at the outer part of the cylinder. The swirl center has moved from the exhaust valve side at $\theta = 166$ deg toward the inlet valve at IVC, providing evidence of its helical motion in phase with piston displacement [5, 17]. Comparison of Fig. 9(a) with Fig. 9(b), which shows the swirl distribution at the same crank angle about an axial location closer to the piston, reveals that an axial stratification of the swirl distribution is present at IVC. Near the cylinder head the profile shows memory effects of the swirl distribution in the second half of induction contrary to that near the piston where signs of the evolution towards a solid body type of rotation are clearly evident. The normal stresses follow the trends of the mean motion exhibiting higher values ($0.9\bar{V}_p$) near the cylinder head and lower ($0.7\bar{V}_p$) closer to the piston. Overall, the magnitude of the normal stresses is considerably reduced relative to those measured during induction. The axial velocity distributions at IVC were also measured at the same axial locations with the swirl distributions and are shown in Fig. 9(c); the intake-generated axial flow pattern has decayed considerably and only a weak vortex is present near the cylinder head. Very similar results have been obtained in an axisymmetric low speed engine with vane-induced swirl [19] which confirms that the swirl-induced pressure field generates after IVC an axial motion rotating in the opposite direction to the main vortex during induction with no signs of inlet flow structures persisting through to the compression stroke. The axial rms velocities are of similar magnitude with the corresponding swirl velocities showing a tendency toward isotropy.

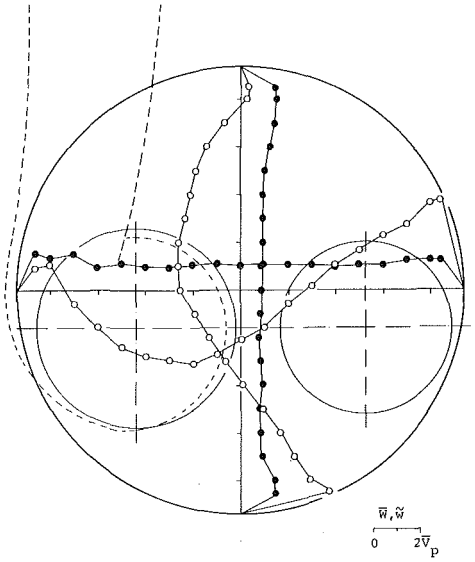

Fig. 8 In-cylinder mean (o) and rms (•) swirl velocity distribution at $z = 47$mm. Steady flow, $L = 7$mm.

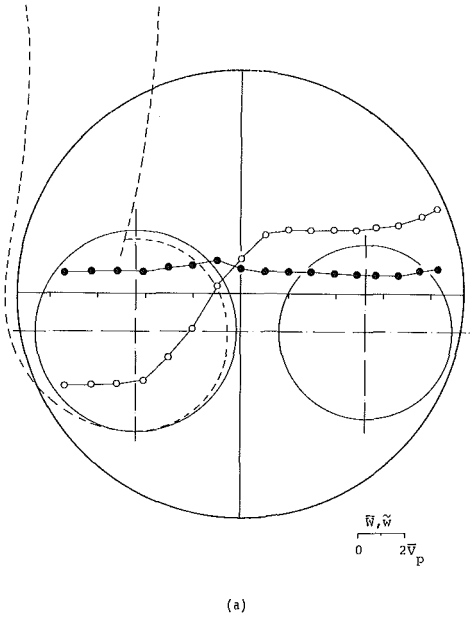

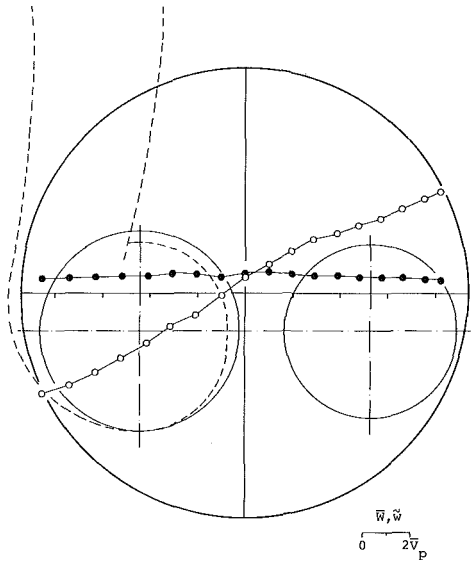

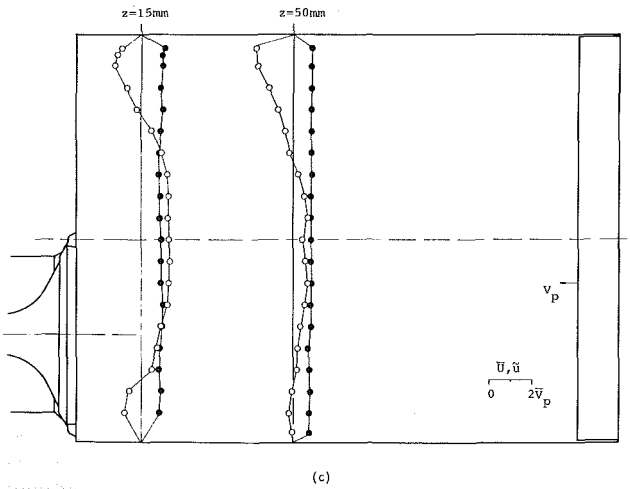

Fig. 9 In-cylinder mean (o) and rms (•) velocity distribution at $\theta = 220$ deg (IVC). (a) Swirl component at $z = 15$mm (b) Swirl component at $z = 50$mm (c) Axial component at $z = 15$ and 50mm.

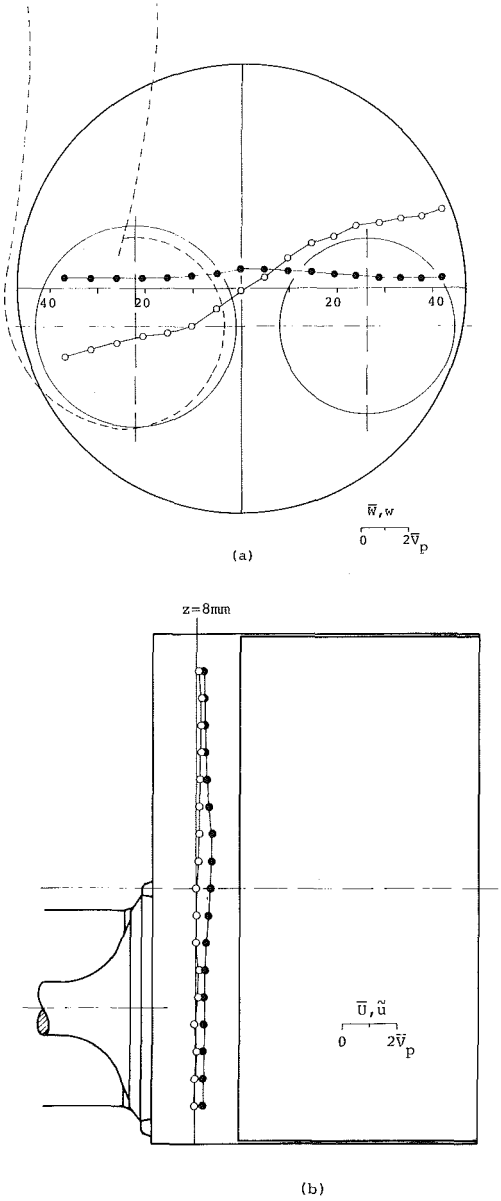

Fig. 10 In-cylinder swirl (*a*) and axial (*b*) mean (o) and rms (•) velocity distribution at $z = 8$mm and $\theta = 360$ deg (TDC).

Finally, the flow at TDC of compression has been measured in order to examine the evolution of the induction-generated flow structure through compression. The swirl velocity distribution shown in Fig. 10(*a*) is very similar to that measured at IVC near the piston, exhibiting solid body rotation characteristics but with reduced maximum velocities indicative of the wall frictional losses during the compression stroke. The magnitude of the otherwise homogeneous stresses has been also reduced to levels of 0.4–0.5 $\bar{V}_p$. The swirl center, after its helical trajectory during induction and compression, returns at TDC to a dynamically more stable position at the cylinder axis. The swirl ratio was calculated by integrating the swirl profile of Fig. 10(*a*) and found to be 4.5. The axial velocity distribution at TDC shown in Fig. 10(*b*) in the mid-clearance plane does not provide evidence of any type of motion with very small or zero velocities; however, it is expected that the vortex pattern observed at IVC may be identifiable at another plane. The axial normal stresses have decayed to levels of 0.3–0.4 $\bar{V}_p$ and are nearly uniform along the mid-plane; similar levels have been measured in idealized model engines at lower speeds with totally different induction systems (19). The

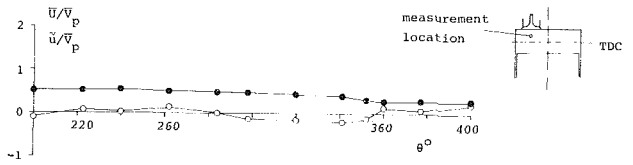

Fig. 11 Temporal variation of the axial mean (o) and rms (•) velocity at a point in the clearance volume ($r = 20$m and $z = 8$mm) from $\theta = 200$ to $\theta = 400$ deg.

temporal variation of the mean and rms axial velocity at a point in the clearance volume during the compression stroke is shown in Fig. 11 and is in close agreement in both trend and magnitude with the temporal profiles of [19]. In both cases, the rms velocities remain constant with magnitudes of 0.5 $\bar{V}_p$ until $\theta = 340$ deg and then suddenly decay to 0.3–0.4 $\bar{V}_p$ at TDC of compression. These results provide further evidence that, for different induction systems, the normal stresses at TDC of compression for a flat piston in the absence of squish scale with the mean piston speed with a proportionality constant of 0.3–0.5 [17, 19–21]. However, certain induction geometries give rise to significantly higher turbulence levels at TDC of compression through generation of a long-lived axial tumbling motion [22, 23].

Conclusions

Investigation by laser Doppler anemometry of the valve and in-cylinder flow generated by the helical port of a Ford Diesel engine revealed the following:

1. The flow through the inlet valve at ~900 rpm can be simulated with acceptable accuracy by steady flow measurements at fixed valve lifts with a constant air mass flow rate corresponding to the mean piston speed under operating conditions.
2. The flow pattern at the valve exit is not uniform around the valve periphery with the axial velocity distribution being more sensitive to valve lift.
3. The in-cylinder flow during induction cannot be simulated with steady flow measurements at corresponding valve lifts.
4. The in-cylinder swirl distribution exhibits an axial stratification at inlet valve closure with a tendency toward solid body type of rotation near the flat piston. In the axial plane, a weak vortex motion is generated by the swirl-induced pressure field with no signs of induction flow structures persisting through compression.
5. The turbulence levels near the cylinder head of the disc-chamber remain constant during most of the compression stroke with levels of 0.5 $\bar{V}_p$ but decay suddenly at $\theta = 340$ deg to 0.3–0.4 $\bar{V}_p$.

The present results provide support to conclusions drawn on the basis of previous measurements in model engines with idealized geometries and low speeds as well as boundary conditions and validation data for the assessment of relevant multidimensional computer codes.

Acknowledgments

The authors would like to thank Ford Motor Company Ltd., for the financial support provided for this work and permission to publish this paper. They would also like to thank Messrs. N. Frost and O. Vis for technical assistance.

References

1 Monaghan, M. L., and Pettifer, H. F., "Air Motion and its Effect on Diesel Performance and Emissions," S.A.E. Paper 810255, 1981.

2 Uzkan, T., Borgnakke, C., and Morel, T., "Characterization of Flow Produced by a High-Swirl Inlet Port," S.A.E. Papeer 830266, 1983.

3 Tindal, M. J., Williams, T. J., and Aldoory, M., "The Effect of Inlet Port Design on Cylinder Gas Motion in Direct Injection Diesel Engines," *Proc.*

Symposium on Flows in Internal Combustion Engines, ASME Winter Annual Meeting, Phoenix, 1982.

4 Brandl, F., Reverencic, I., Cartellieri, W., and Dent, J. C., "Turbulent Air Flow in the Combustion Bowl of a DI Diesel Engine and its Effect on Engine Performance," S.A.E. Paper 790040, 1979.

5 Vafidis, C., "Influence of Induction Swirl and Piston Configuration on Air Flow in a Four-Stroke Model Engine," *Proc. I. Mech. E.*, Vol. 198C, 1984, p. 71.

6 Arcoumanis, C., Bicen, A. F., and Whitelaw, J. H., "Squish and Swirl-Squish Interaction in Motored Model Engines," ASME JOURNAL OF FLUIDS ENGINEERING, Vol. 105, 1983, p. 105.

7 Kastner, L. S., Williams, T. J., and White, J. B., "Poppet Inlet Valve Characteristics and their Influence on the Induction Process," *Proc. I. Mech. E.*, Vol. 178, 1963-1964, p. 955.

8 Haghgooie, M., Kent, J. C., and Tabaczynski, R. J., "Intake Valve Cylinder Boundary Flow Characteristics in an Internal Combustion Engine," *Comb. Sci. Tech.*, Vol. 38, 1984, p. 49.

9 Wigley, G., and Glanz, R., "Application of Laser Anemometry to Diesel Engine Port Flow Development," S.I.A. Conference on Diesel Engines for Automotive Applications, Lyon, 1984.

10 Brandstatter, W., Johns, R. J. R., and Wigley, G., "The Effect of Inlet Port Geometry on In-Cylinder Flow Structure," S.A.E. Paper 850499, 1985.

11 Bicen, A. F., Vafidis, C., and Whitelaw, J. H., "Steady and Unsteady Air Flow Through an Intake Valve of a Reciprocating Engine," *Proc. Symposium on Flows in Internal Combustion Engines*, ASME Winter Annual Meeting, New Orleans, 1984.

12 Vafidis, C., and Whitelaw, J. H., "Intake Valve and In-Cylinder Flow Development in Reciprocating Model Engines," Proc. I. Mech. E., Vol. 200, No. C2, 1986.

13 Fukutani, I., and Watanabe, E., "Air Flow Through Poppet Inlet Valves—Analysis of Static and Dynamic Flow Coefficients," S.A.E. Paper 820154, 1982.

14 Bird, G. L., "The Ford 2.5 Litre High Speed Direct Injection Diesel Engine—Its Performance and Future Possibilities," S.A.E. Paper 850262, 1985.

15 Vafidis, C., "Aerodynamics of Reciprocating Engines," Ph.D. thesis, Imperial College, University of London, 1985.

16 Arcoumanis, C., Bicen, A. F., and Whitelaw, J. H., "Application of LDA to Four-Stroke Motored Model Engines," In "*Laser Anemometry in Fluid Mechanics*" ed. R. Adrian et al., Ladoan, Lisbon, 1984.

17 Arcoumanis, C., Bicen, A. F., Vafidis, C., and Whitelaw, J. H. "Three-Dimensional Flow Field in Four-Stroke Model Engines," S.A.E. Paper 841360, 1984.

18 Coghe, A., et al., "In-Cylinder Air Motion Measurements by Laser Velocimetry under Steady-State Flow Conditions," S.A.E. Paper 850123, 1985.

19 Arcoumanis, C., Bicen, A. F., and Whitelaw, J. H., "Effect of Inlet Parameters on the Flow Characteristics in a Four-Stroke Model Engine, S.A.E. Paper 820750, 1982.

20 Liou, T. M., Hall, M., Santavicca, D. A., and Bracco, F. V., "Laser Doppler Velocimetry Measurements in Valved and Ported Engines," S.A.E. Paper 840375, 1984.

21 Hayder, M. E., Varma, A. K., Bracco, F. V., "A Limit to TDC Turbulence Intensity in Internal Combustion Engines," 1984, Submitted to *AIAA J.*

22 Gosman, A. D., Tsui, Y. Y., and Vafidis, C., "Flow in a Model Engine with a Shrouded Valve—A Combined Experimental and Computational Study," S.A.E. Paper 850498, 1985.

23 Witze, P. O., Martin, J. K., and Borgnakke, C., "Measurements and Predictions of the Precombustion Fluid Motion and Combustion Rates in a Spark Ignition Engine," S.A.E. Paper 831697, 1983.

Experimental and Numerical Investigations of Plane Duct Flows With Sudden Contraction

F. Durst

W. F. Schierholz

A. M. Wunderlich

Lehrstuhl für Strömungsmechanik,
Universität Erlangen-Nürnberg,
Egerlandstr. 13, 8520 Erlangen,
Federal Republic of Germany

The present paper reports on experimental and numerical studies of laminar, two-dimensional flow through plane ducts with sudden contractions in cross-sectional area. A laser-Doppler anemometer and a flow computational program were complementarily employed to study details of the flow close to the step. The results reveal details of the velocity profile variations in the vicinity of the contraction. Information is also provided on the separated flow region in the front concave corner of the duct and on the separated flow region just downstream of the lip of the step. The dimensions of the front separation region are shown to agree well with existing data. The recirculating flow region just downstream of the lip is much smaller than occasionally assumed. At higher contraction ratios off-axis velocity maxima occur just downstream of the contraction. It is shown that strong elongational flow fields occur. These are concentrated to a very small region close to the step.

1 Introduction

Fluid flows in ducts with symmetric sudden contractions in cross-sectional area resemble flow features that are of interest in many fields of engineering where basic knowledge on separated flows is needed to improve the performance of flow equipment. A number of studies have been carried out using test sections of different contraction ratios and out of this work interesting results emerged that are summarized by Boger [1] and recently by Durst and Loy [2]. These papers show that some information on velocity distributions for laminar flows is available together with information on the extensions of the separated flow regions which appear in the concave corners in front of the contraction and just downstream of the two lips of the symmetric "double step." Hence, the general features of the flow can be taken as being known inspite of the fact that the existing information is only available for a limited set of parameters, see Boger [1].

In more recent years, the flow region close to a sudden contraction in a duct has captured the attention of rheologists and fluid mechanicians interested in the cause of the high pressure increase observed in the vicinity of contractions for flows of dilute polymer and/or dilute surfactant solutions. A closer study of this shows that, at low flow rates, such solutions resemble fluid flow properties very similar to those of Newtonian fluids, but drastic changes of the effective fluid properties occur, if the flow rate is raised beyond an onset value; for high flow rates the fluid shows strong non-Newtonian flow properties in the vicinity of the contraction only and these are reflected in the high pressure increases mentioned above. It appears, at least for elastic macromolecules, that this increase in pressure is caused by the elongational strain the fluid elements experience in the flow region adjacent to the contraction. If the elongational strain rate exceeds a certain onset value, typical for the solvent-molecule-system, the dissolved molecules get stretched and this requires the measured additional driving pressure to pass the fluid through the contraction. In order to provide a closer understanding of these phenomena, the present literature does not provide sufficient information on the flow field close to sudden contractions in ducts. Information on Newtonian fluids is missing and little information also exists on the variation of those flow fields that activate the molecules in dilute polymer solutions. This paper attempts to remedy the present situation by providing detailed information on the flow field under consideration. Results of combined experimental and numerical studies are provided and demonstrate that laser-Doppler anemometry and computer programs for flow predictions can be complementarily employed to yield the required flow information. This information is presented for Newtonian fluids only. Results are given for different contraction ratios so that a good physical understanding of the flow emerges from the studies.

Section 2 of the present paper provides information on the flow duct employed in the present study and on the pumping facility to drive the flow. Information is also provided on the laser-Doppler measuring instrumentation used for local velocity measurements. The traversing equipment employed to get entire velocity profiles recorded is also described.

Section 3 provides information on the flow equations employed in the numerical study and the major features of a computer program are introduced which was employed for carrying out flow predictions. Results obtained with this computer program are presented in Section 4 together with results from the experimental study. It is shown that good agreement is obtained in most parts of the flow. This justifies the employment of the numerical code to get information on the distribution of elongation and shear strain rates. Through these, a

Contributed by the Fluids Engineering Division for publication in the JOURNAL OF FLUIDS ENGINEERING. Manuscript received by the Fluids Engineering Division July 3, 1985.

detailed understanding of the flow in the vicinity of the step results, yielding conclusions and final remarks that are presented in Section 5.

2 Test Rig and Measuring Equipment

2.1 The Flow Facility. The experimental investigations described in this report were carried out in a flow facility consisting of a two-dimensional, plane duct with inlet- and outlet parts to carefully control the flow. The flow channel was mounted on top of the storage tank for the test fluid which was water in all the experiments described here. As Fig. 1(*a*) shows the entire flow equipment was mounted on a three-dimensional traverse table to allow the test section to be traversed relatively to the spatially fixed laser-Doppler anemometer, i.e., to a fixed measuring point.

The entire test fluid was stored in the storage tank which facilitated the application of a heat exchanger to control the fluid temperature to be 20.4°C and to maintain it constant to within ±0.1°C. This control of the temperature assured the fluid properties to be constant during an entire test run.

To drive the test fluid from the storage tank through the two-dimensional duct, a rotary pump was employed and equipped with a speed control to keep the pump speed to within ±0.5 percent of the preadjusted speed for each test run. By controlling the fluid temperature and by also controlling the back pressure of the pump, the constant running speed of the pump corresponded to a constant volume rate in the test section. In this way, for each test run, the Reynolds number of the flow was maintained constant.

To provide the test fluid from the pump to the flow duct, the outlet pipe of the pump was split into four pipe connectors which entered into the back part of the plenum chamber. This chamber contained flow straighteners and wire meshes to homogenize the flow and to assure a flow of low turbulence level to enter the contraction section of the plenum chamber. From there, the flow entered the flow duct through a matched inlet section which assured a starting flow in the duct showing very little disturbances.

The actual test section consisted of a two-dimensional channel of 10 mm in height and 180 mm in width, corresponding to an aspect ratio of 1:18. This channel was made up of metal top and bottom plates and contained glass side walls in order to allow the optical access to the inside of the channel needed for the laser beams of the Doppler anemometer. Spacers were used along the outside of the entire test section in order to assure the constant height of 10 mm within ±0.02 mm. This measure was also the manufacturing tolerance of the entire channel.

The inlet length of the test section was 600 mm. This required length was computed previous to the test section construction to ensure for all Reynolds numbers fully developed laminar velocity profiles upstream of the sudden contraction. This contraction was made up of two anodized-aluminium plates which were mounted inside the channel. Particular attention was given to manufacturing the edges of the inserted plates in order to provide sharp-edged-lips to be available at the contraction inlet. Plates were available to allow contraction ratios of 2:1 and 4:1 yielding $d = 5$ mm and 2.5 mm for the duct height downstream of the contraction.

2.2 The LDA-Measuring Equipment. To obtain local velocity measurements, laser-Doppler anemometry was employed in the present study, a technique well-described in reference [3]. Since the flow was two-dimensional over a large part of the channel center (see Section 4.1), it was sufficient to carry out measurements of the U-velocity component only. The corresponding V-velocities can be computed by an integration of the continuity equation.

The major parts of the one-dimensional laser-Doppler anemometer are shown in Fig. 1(*a*) and details of the optical set-up in Fig. 1(*b*). The transmission side consisted of a 15mW-Helium-Neon laser (Model: NEC GLG 5600) and a modified integrated optics manufactured by OEI-Opto Elektronische Instrumente GmbH. The modification consisted of a rhomboid prism addition in order to allow one of the beams to be passed through the center of the transmission lens of 248 mm focal length. In this way, measurements close to the contraction were obtainable without inclining the axis of the optics relatively to the direction of the flow. The closest measurements obtainable were given by the finite diameter of the measuring volume of about 200 μm and by light scatter-reflections on the step and the walls, respectively.

The receiving optics of the employed LDA-system consisted of a light collecting lens of 120 mm focal length with two stops for the incident light beams at the front plane of the lens. The scattered light passing the light collecting lens was focused on to the pinhole of a photomultiplier (Model: EMI-9558). The pinhole diameter was 200 μm and the imaging properties of the receiving optics were adjusted so that the pinhole only covered 80 percent of the center of the crossing region of the two incident laser light beams.

The entire optical system was mounted on a special bench with arms on both sides of the test section to allow the transmission and receiving optics to be positioned on opposite sides of the traversing table on which the test section was mounted. In this way, LDA-measurements using forward scattered laser radiation became possible yielding good signal-to-noise ratios at the output of the photomultiplier.

The output signals of this device were prefiltered using a Krohn and Hite band-pass filter (Model: 3103), in order to remove the low frequency component of the signal and to restrict the high frequency noise components. The band-pass filtered, high frequency component of the LDA-signal was passed on to a transient recorder (Type: Datalab 1080), which allowed the individual Doppler-bursts to be digitized and stored for further processing on a computer. On-line processing was carried out on a HP 1000-computer (Model: HP A 700) to yield the Doppler-frequencies of the individual bursts. Measurements for approximately 1000 bursts were carried out

Nomenclature

D, d = duct height upstream (downstream) of the sudden contraction
D^* = half duct height upsteam of the sudden contraction
N = number of grid nodes
P = static pressure
P^* = intermediate pressure in computations
P' = pressure correction
Pe = Peclet number
Re = Reynolds number, $\bar{U} \cdot D/\nu$
Re* = Reynolds number referred to D^*
U = horizontal velocity
$\bar{U}$ = cross-sectional average velocity
U_{cl} = center line velocity
U^* = intermediate horizontal velocity in computations
V = vertical velocity
V^* = intermediate vertical velocity in computations
x = streamwise coordinate
X/D = dimensionless length
y = normal coordinate
Y/D = dimensionless height
ϵ_{ij} = deformation stress tensor
ρ = density
μ = dynamic viscosity
ν = kinematic viscosity

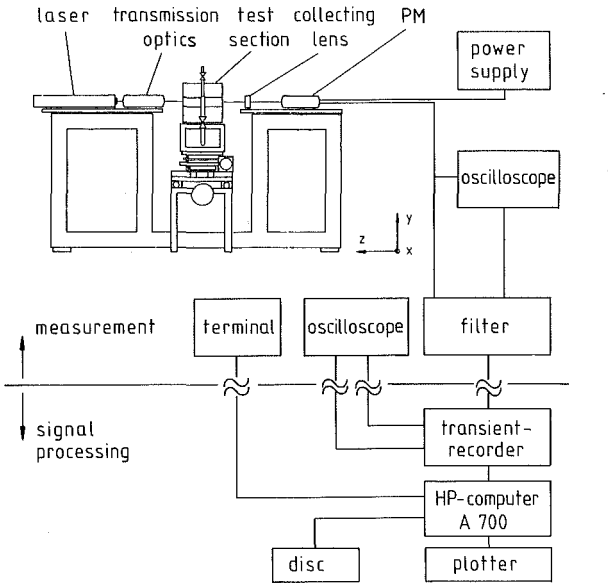

Fig. 1(*a*) Experimental set-up with laser-Doppler anemometer and evaluation electronics

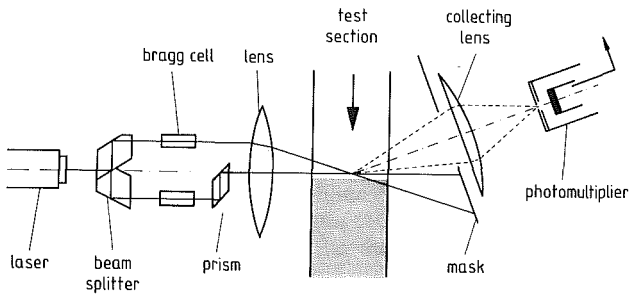

Fig. 1(*b*) Details of the employed LDA-optics

at each measurement point and their mean frequency was computed to yield the local mean velocity. Entire mean velocity profiles were obtained by traversing the test section relatively to the spatially fixed measuring point of the LDA-system.

For the experimental data presented in this paper, uncertainty estimates were performed taking into account all parameters uncertainties of the experiment. These can be given as follows. The dimensions of the test channel showed a manufacturing tolerance of ± 0.02 mm in all directions. The Reynolds number could be kept constant for each test run within $\Delta \mathrm{Re} = \pm 0.5$ percent. This is due to the highly constant fluid temperature of $\Delta T = \pm 0.1°\mathrm{C}$ and the small pump speed fluctuations of $\Delta n = \pm 0.5$ percent. The evidence of a constant mass flux during an entire test run is demonstrated in Table 1 given as an example for the experimental records at Reynolds number Re = 426. The tabulated values for the mass flux were obtained by integrating each measured velocity profile (see Fig. 4) and multiplying the resultant flow rate with the fluid density ρ at the actual test temperature, which was in this case $T = 20.4°\mathrm{C}$. The LDA-velocity measurements itself had a maximum uncertainty in $\Delta U = \pm 0.5$ percent, mainly influenced by the manufacturing tolerance of the transmission lens. The uncertainty in the relative horizontal x-positioning and the relative vertical y-positioning of the measuring volume was ± 50 μm, that means $X/D = \pm 0.005$ in Figs. 4 and 8.

3 Fluid Flow Equations and Computer Program

3.1 Fluid Flow Equations. In the present research work, the experimental investigations by means of laser-Doppler anemometry were complemented by numerical studies carried out by means of finite difference solution procedure for the governing equation of fluid flows. A set-up computer program was available for these studies and applying it, the flow was assumed to be laminar, steady and two-dimensional. Under these conditions the continuity and momentum equations solved in the employed computer program read as follows:

Table 1 Mass fluxes of each velocity profile for Reynolds number Re = 426 at $T = 20.4°\mathrm{C}$ (see Fig. 4)

Location of velocity profiles X/D	mass flux g/s
−0.8	42.54
−0.5	42.34
−0.3	42.56
−0.2	42.40
−0.15	42.33
−0.1	42.41
−0.075	42.26
−0.005	41.91
±0	40.59
+0.02	40.79
+0.05	42.83
+0.075	43.23
+0.1	43.07
+0.15	42.95
+0.2	42.84
+0.3	42.85
+0.5	42.81
+0.8	43.03

Continuity Equation:

$$\frac{\partial}{\partial x}(\rho U)+\frac{\partial}{\partial y}(\rho V)=0$$

Momentum Equation:

$$\frac{\partial}{\partial x}(\rho UU)+\frac{\partial}{\partial y}(\rho VU)=-\frac{\partial P}{\partial x}+\mu\left[\frac{\partial^2 U}{\partial x^2}+\frac{\partial^2 U}{\partial y^2}\right]$$

$$\frac{\partial}{\partial x}(\rho UV)+\frac{\partial}{\partial y}(\rho VV)=-\frac{\partial P}{\partial y}+\mu\left[\frac{\partial^2 V}{\partial x^2}+\frac{\partial^2 V}{\partial y^2}\right]$$

In these equations U, V are the velocity components in x- and y-direction, respectively. ρ is the density of the fluid, μ its dynamic viscosity and P the static pressure.

As the flow is plane and symmetric to the duct axis, the present computations were only carried out for one half of the channel and for two sets of boundary conditions. Along the inflow plane the inlet velocity U was prescribed as a parabolic profile. Along the walls no-slip flow conditions were applied. At the downstream end the employed boundary condition was:

$$\frac{\partial U}{\partial x}=\frac{\partial V}{\partial x}=0$$

The latter implies that the outlet is taken at a sufficiently large distance from the contraction to allow fully developed flow conditions to exist. In the present case this distance was assumed to be 1.5 times the duct height D of the inlet test section. Increasing the distance would require additional grid points to be available downstream of the test section, what corresponds to a coarser grid in the region of the step change of cross-sectional area and in a decrease of computational accuracy.

Regarding the boundary conditions along the symmetric axis, zero gradient conditions were used for the U-velocity and the V-velocity was set equal to zero. Hence, the experimentally found symmetry of the flow over the entire Reynolds number range was fully accounted for in the present predictions.

3.2 Computer Program for Flow Predictions. The set of governing fluid flow equations, discussed in the last chapter, was solved for the given boundary conditions using the computer program TEACH described by Gosman and Ideriah [4]. In this computer program, the conservation equations for mass and momentum are solved for primitive variables U, V, and P using equations derived by integrations of the terms of the partial differential equations in Section 3.1 over finite control volumes. This practice ensures a conservative discretization for mass and momentum. For the actual solution procedure the primitive variables are computed in the node points of a staggered grid, where the scalar values, like for instance the pressure P, are stored in the main grid nodes and the velocities U and V are stored at displaced locations.

The solution algorithm of the computer program TEACH employs a finite difference formulation for the convective terms in the partial differential equations for fluid flows which is usually referred to as the Hybrid Finite Difference Scheme, e.g., see Patankar [5]. This scheme utilizes a combination of the central and the upwind finite difference formulation of the gradient terms in the expressions of the convective transport terms of the equation and one formulation or the other is employed at a point in the flow field depending on the local grid Peclet number. For $-2 \leq \mathrm{Pe} \leq 2$ the Central Finite Difference Formulation is employed but otherwise Upwind Finite Differencing is used. In this way a stable solution procedure results and this characterizes the computer code TEACH.

To obtain grid-independent solutions the calculation domain was covered with a numerical grid consisting of N grid nodes in each coordinate direction. The grid was non-uniform in both directions but the distribution of grid nodes differed in the x- and y-direction. A large number of grid points was placed in regions where large changes in velocity and pressure occurred. Figure 2 shows the distribution of the grid nodes along the streamwise coordinate X/D and the normal coordinate Y/D for $N = 50$, respectively. The contraction is located at $X/D = 0$. The wall is indicated at $Y/D = 0.5$, the lip at $Y/D = 0.25$ and the axis of the flow field at $Y/D = 0$.

In order to assure numerical reliability of the predictions, computations were performed to check the grid independence of the final results. Figure 3 shows a comparison that was performed for various numbers of grid nodes. The figure provides information on the predicted extension in the y-direction of the upstream separation region computed for a Reynolds number of Re = 1326. The present study showed that, for a given number of grid nodes, grid-independence of the numerical solutions exists for lower Reynolds numbers, if it is assured at the highest Reynolds number of the present study.

The results in Fig. 3 show the somewhat typical behavior of the flow property dependence on the number of grid nodes used in the computations. Increasing the grid number results in a maximum of the y-extension of the upstream separation region followed by a decrease and an approach to an asymptotic value. The location of the maximum depends somewhat on the chosen grid distribution but the asymptotic value does not. Hence, the grid number has to be chosen in such a way to yield the asymptotic flow field indicated in Fig. 3. In the present study, all computations were performed for $N = 50$ in the x- and y-directions.

4 Experimental and Numerical Results

4.1 Mean Velocity Field. The experimental and numerical means described in Sections 2 and 3 were complementarily employed to study in detail the flow field in the vicinity of the forward facing double step formed by a sym-

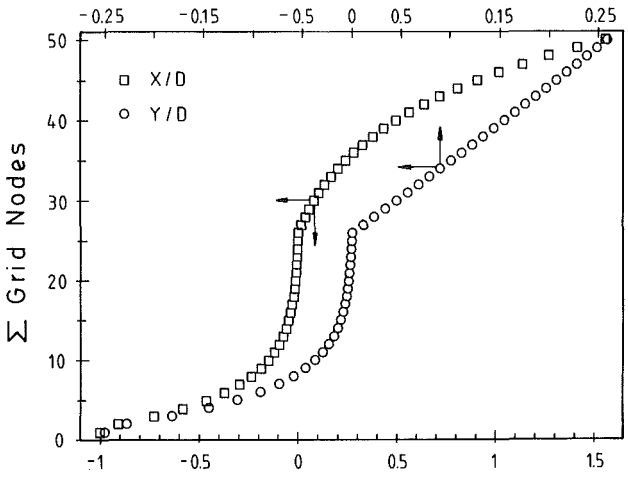

Fig. 2 Grid node distribution in Y/D- and X/D-coordinates

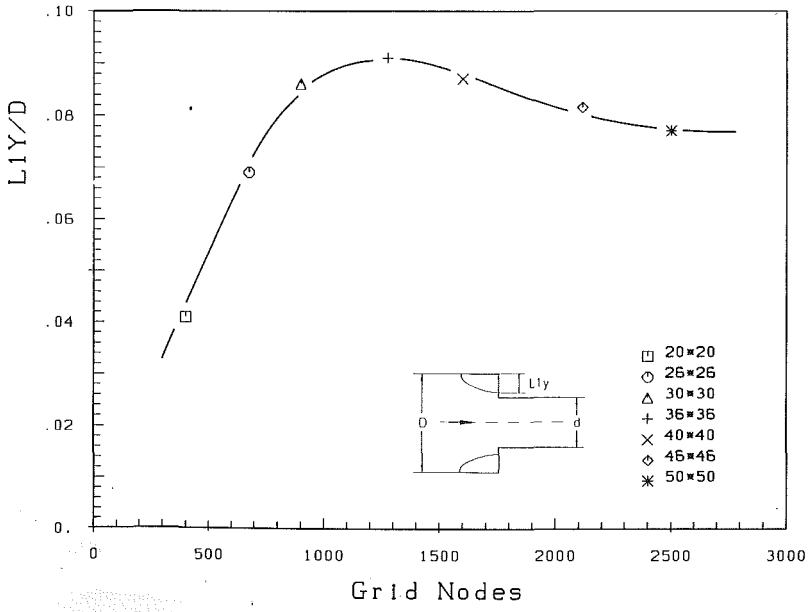

Fig. 3 Upstream separation height as a function of grid nodes for Re = 1326

metric sudden contraction of the cross-sectional area located in a two-dimensional duct. The experimental measurements and the flow predictions were carried out at identical Reynolds numbers so that both measurements and predictions could be checked against each other. Due to the spatial limitations of the LDA-system, experimental results could not be obtained over the entire flow regime with the required spatial resolution. In those regions of the flow where no detailed experimental data were obtainable, information concerning the physics of the flow was extracted from numerical results. This information was only accepted as reliable if good agreement between experiments and numerical predictions existed in those parts of the flow, where numerical as well as experimental results were available and agreed. In this way, both the experimental and the numerical techniques were checked against each other and at the same time used to yield complementary information on the physics of the flow. This approach has proven to be successful in studies on flows near axisymmetric sudden contractions reported by Durst and Loy [2].

It turned out to be not practical to prescribe the fully developed flow boundary condition far downstream of the step, where the flow has physically turned back into a parabolic profile. Especially for the higher Reynolds numbers this would have taken up too large a number of grid points and would have prevented accurate predictions close to the sudden contraction. Because of this, the computations were performed with a parabolic outlet velocity profile at 1.5 D downstream of the step.

One of the parameters that was varied in the investigations was the Reynolds number of the flow. In Fig. 4 examples of the experimental and numerical results are shown for a Reynolds number of Re = 426. The figure exhibits good agreement between the experiments and the numerical investigations in the entire flow field. The incoming flow remains parabolic up to approximately 1.5 step heights in front of the step and it has turned again into a parabolic profile at about two step heights after the contraction for the smallest Reynolds number flow. As the experiments revealed the redeveloping length for the highest Reynolds number laid far outside the plotted region. With increasing Reynolds number, the velocity profiles at the step become increasingly flat yielding close to a top hat velocity inlet profile at the contraction which then redevelops into the parabolic profile, characteristic for fully developed, two-dimensional duct flows. This general behavior of the flow is confirmed both by the experiments and also by the numerical results. Plots and data for all the investigated Reynolds numbers are provided in reference [6].

A large scale presentation of experimental and numerical velocity profiles in the region $X/D = \pm 0.1$ is shown in Fig. 5. In this figure the continuous line represents the prediction. Differences between the computations and the measurements occur in the near vicinity of the contraction. For the measurements one possible reason may be the uncertainty of the accurate horizontal and vertical positioning of the control volume relatively to the plane of contraction (see chapter 2.2). Since the flow varies very rapidly in this part of the flow and since the highest velocity gradients appear near the plane of the contraction, small deviations in the absolute x- and y-positioning can easily cause differences in the local velocity profiles obtained by measurements and predictions. Nevertheless, in spite of this location problem, the deviations were largely smaller than 5 percent.

The comparatively small deviations between experiments and predictions justified the usage of the numerical program to extract further information not available through the laser-Doppler measurements. In this way, it was also possible to extract information on the extension of the separation region just upstream of the forward facing step. For the major dimensions of this region previous results have been published in reference [7]. The authors' computation results are given in Fig. 6 where the extensions in the longitudinal and cross flow direction are shown, respectively. At very low Reynolds numbers, good agreement between the authors' computations and those available in literature are obtained. For higher Reynolds numbers the variation of the dimensions with Reynolds number differ from the asymptotic solution proposed by Dennis and Smith [7]. The authors are convinced that their results can be considered as grid independent solutions of the equations given in Section 2 up to Re = 1326.

Extensive studies were also performed to yield information on the separation region just downstream of the lip of the step where separation regions should form on each side of the smaller test channel. Computing the extension of this separation region yields the dependence of this quantity on the Reynolds number given in Fig. 7.

The separation regions appear the first time for Re > 400 and their dimensions increase as the Reynolds number increases. Hence, for very high Reynolds numbers the extension of those regions seems to approach a limiting value. Generally, the height of these separation regions and the resultant constriction of the flow are made responsible for increased pressure losses at sudden contractions in the cross sectional area, see reference [8]. However, the present investigation proves this height to be so small that no distinct flow constriction exists, what contradicts the commonly made explanations.

The predictions also provided information on the march of pressure, showing strong pressure variations in cross sectional area especially in the vicinity of the sudden contraction. These pressure variations have to be considered, if an integral treatment of the flow is attempted. For further details see reference [6].

In order to see the influence of the contraction ratios on the

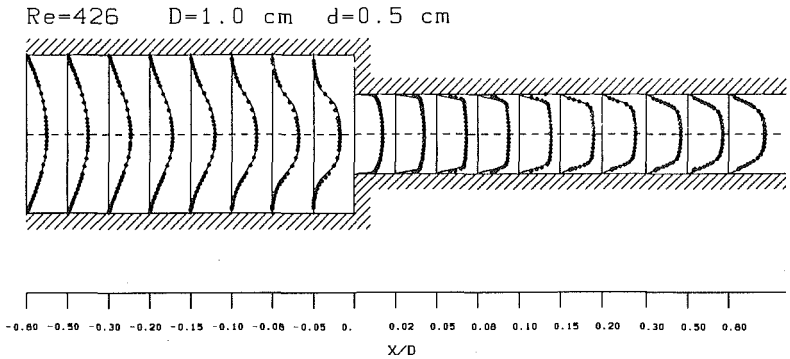

Fig. 4 Velocity profiles of various X/D-locations for contraction ratio 2:1 (——) prediction, (o o o o o o) measurement

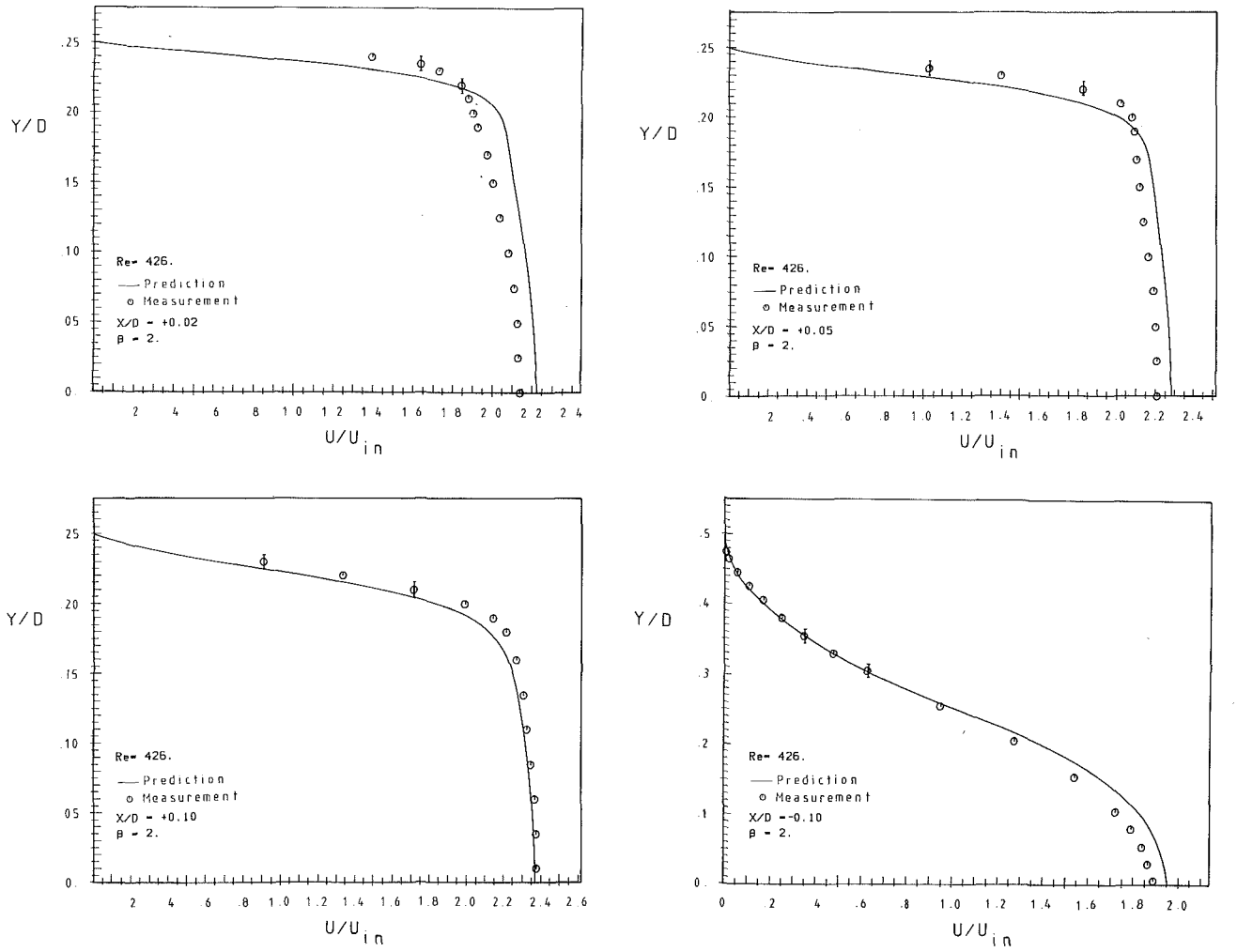

Fig. 5 Large-scale presentation of velocity profiles in the region $X/D = \pm 0.1$

flow field, computations and measurements were also carried out for higher contraction ratios than 2:1. An example of the resultant mean velocity profiles is shown in Fig. 8 for a contraction ratio of 4:1. For the higher contraction ratio, the profile at the inlet of the smaller part of the duct is flatter than for the duct with smaller contraction ratio. At high Reynolds numbers velocity overshoots occur just downstream of the plane of contraction close to the walls. To prove that the occurrence of these velocity peaks was not due to a three-dimensional flow field, various velocity profiles were measured in spanwise direction at a distance of 30 mm from the middle of the channel. As Fig. 9 indicates the verified profiles proved both the existence of the overshoots as well as the two-dimensionality of the flow field. Velocity maxima were also predicted in the present computations, however, they were much smaller and less distinct than in the experiments. Numerical diffusion might prevent the overshoot to be correctly predicted.

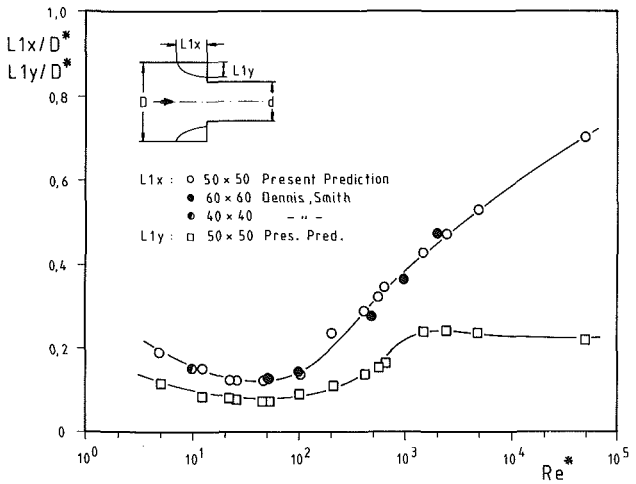

Fig. 6 Separation region in front of the contraction in x-direction and y-direction and comparison between present data and literature data

4.2 Elongation and Shear Strain Rates. As already mentioned in the introduction, internal flows of dilute polymer solutions or solutions of surfactants experience high pressure increases when forced to flow, at high flow rates, through channels with sudden contractions in cross sectional area. If flows are attempted, however, at low flow rates, the solutions behave just like Newtonian fluids. It is assumed that non-Newtonian behaviors are due to the flow field showing elongational and/or shear strain rates larger than a so-called onset value charcterizing the "dynamic behavior" of the molecules in solution. The present studies were extended to provide information on local elongation and shear strain rates in the vicinity of the plane of contraction where two-dimensional flow was maintained. Under these conditions, the strain tensor reduces to:

$$\epsilon_{ij} = \frac{1}{2}\begin{bmatrix} 2\frac{\partial U}{\partial x} & \frac{\partial U}{\partial y}+\frac{\partial V}{\partial x} \\ \frac{\partial V}{\partial x}+\frac{\partial U}{\partial y} & 2\frac{\partial V}{\partial y} \end{bmatrix}$$

where the term $\partial U/\partial x$ describes the local strain rate and the term $(\partial U/\partial y + \partial V/\partial x)$ the local shear rate, respectively.

Along the axis of the channel, the terms are equal to:

$$\frac{\partial U}{\partial y} = \frac{\partial V}{\partial x} = 0$$

Hence, on the symmetry axis of the channel, the shear stress terms disappear and only the elongational strain rate maintains. This quantity was measured and computed and examples of measurements and computations are given in reference [6].

The center line velocities along the streamwise x-coordinate in Fig. 10 reveal that the region of high elongational strain rates is restricted to 2 mm upstream and 2 mm downstream of the plane of contraction. In this region good agreement between the predictions and experiments could be obtained.

Computer results for the entire elongational strain rate field are shown in Fig. 11(a) for a Reynolds number of Re = 1326. In this figure, the gradient $\partial U/\partial x$ is normalized with the highest positive gradient occurring in the flow field. X/D describes the dimensionless channel length, with $X/D = 0$ being the position of the plane of contraction. Y/D describes the channel height with $Y/D = 0$ being the axis of symmetry.

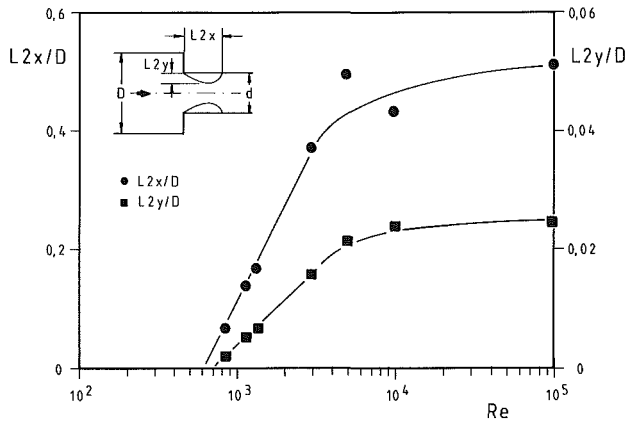

Fig. 7 Separation region downstream the contraction; extension in x-direction and y-direction

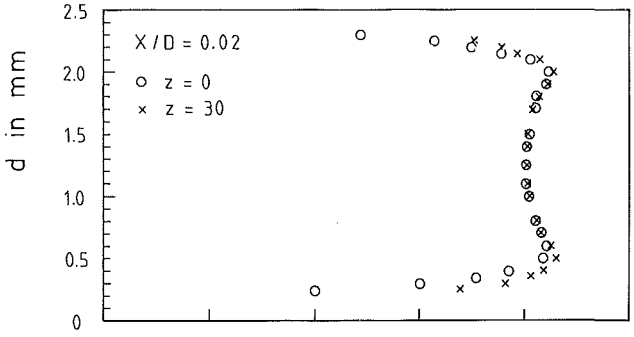

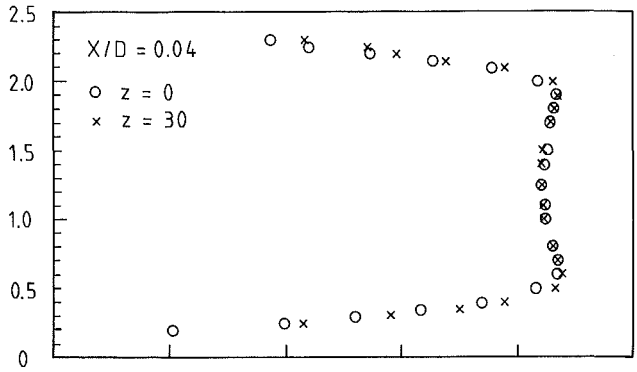

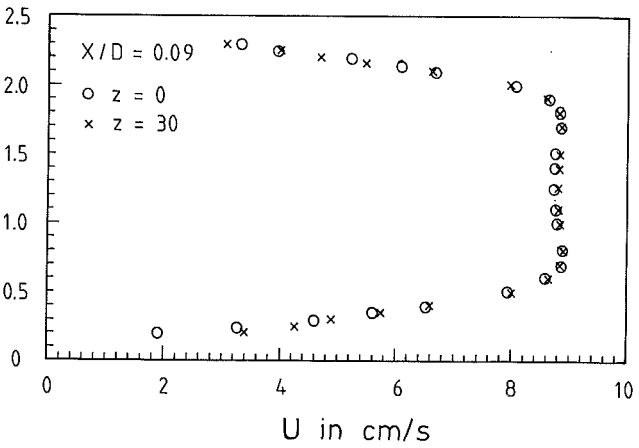

Fig. 9 Proof of the velocity overshoots and of the two-dimensionality of the flow field (z = spanwise coordinate in mm)

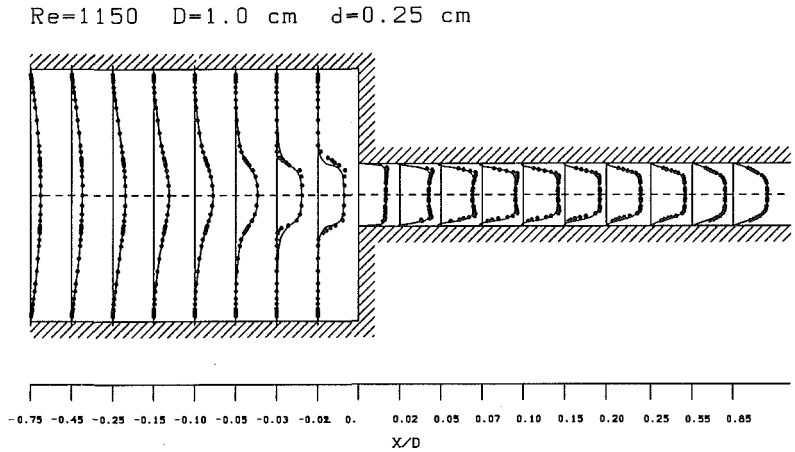

Fig. 8 Velocity profiles of various X/D-locations for contraction ratio 4:1 (——) prediction, (o o o o o o) measurement

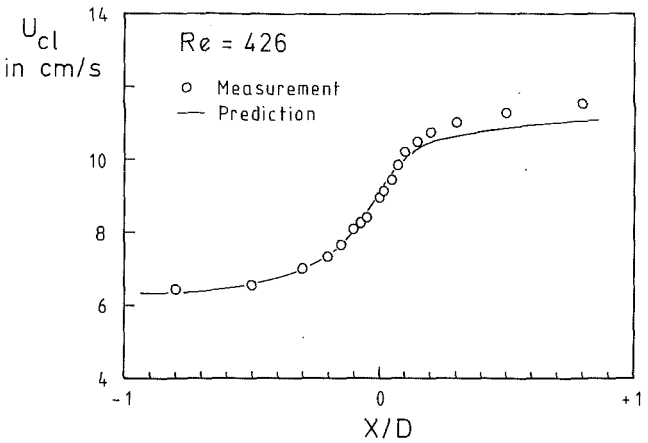

Fig. 10 Comparison of experimental and numerical center line velocities

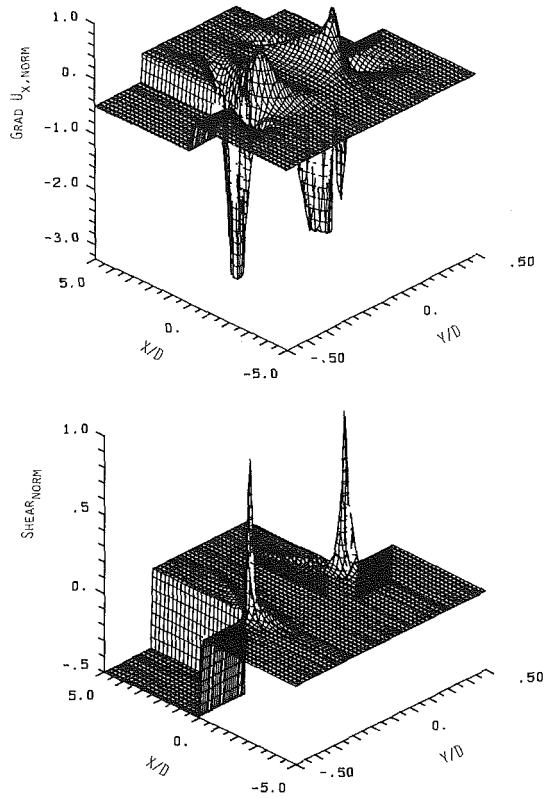

Figs. 11 Elongational strain distribution; (a) and shear strain distribution; (b) in the vicinity of the step

Figure 11(*a*) indicates that there are regions with zero axial velocity gradients for the inlet and outlet of the channel flow in accordance with a fully developed flow. Negative axial velocity gradients occur in front of the contraction, more precisely just in front of the step, which is due to the deceleration of the fluid. The largest negative gradients are present immediately downstream of the contraction very close to the wall. They are caused by the strong elongation of the fluid elements due to the redevelopment of the parabolic laminar profile from the more rectangular inlet profile in the plane of the contraction. These gradients can be several times the maximum positive gradient. Approaching the middle of the channel the gradient decreases very rapidly.

In Fig. 11(*b*) the shear strain rate is displayed for a flow of Reynolds number Re = 1326. The gradients are normalized with the maximum value occurring in the flow and this causes well known peaks to exist very close to the lip of the step but downstream of the step. Hence, the region of high elongational strain rates and high shear strain are close to each other.

5 Conclusions and Final Remarks

The present paper considers the flow around the plane of contraction of a two-dimensional duct with a sudden change in cross sectional area. Experimental and numerical investigations are carried out and reveal that two separation regions exist upstream and just downstream of the plane of contraction. The dimensions of these separation regions are given as a function of Reynolds number. Information is also provided on velocity profiles describing the entire flow field in the vicinity of the plane of contraction. Experimental and numerical results are compared and show good agreement. Because of this experiments and computations are employed to yield information on the physics of the flow in a complementary manner.

The experimental data were partially obtained to provide test data for development of computer codes to predict flows with regions of separation. To facilitate such comparitative investigations, the experimental data are available in forms of tables in [6].

Acknowledgments

Financial support for this work was provided by the Deutsche Forschungsgemeinschaft. This support is gratefully acknowledged. The authors are grateful to Miss M. Laternik, Miss A. Messner and Mrs. B. Spinnler for the expert typing of the manuscript.

References

1 Boger, D. V., "Circular Entry Flows of Inelastic and Viscoelastic Fluids," *Advances in Transport Processes*, Vol. II, Wiley Eastern Ltd., 1982.

2 Durst, F., and Loy, T., "Investigations of Laminar Flow in a Pipe with Sudden Contraction of Cross Sectional Area," *Computer and Fluids*, Vol. 13, No. 1, 1985, pp. 15-36.

3 Durst, F., Melling, A., and Whitelaw, J. H., *Principles and Practice of Laser-Doppler Anemometry*, Academic Press, 2nd Edition, 1981.

4 Gosman, A. D., and Ideriah, F. J. K., "TEACH-2E: A General Computer Program For Two-Dimensional, Turbulent, Recirculating Flows," Department of Mechanical Engineering, Imperial College, London S.W.7, 1976.

5 Patankar, S. V., *Numerical Heat Transfer and Fluid Flow*, McGraw-Hill, 1980.

6 Durst, F., Schierholz, W. F., and Wunderlich, A. M., "Experimental and Numerical Investigations of Plane Duct Flows With Sudden Contraction," Technical Report No. LSTM 93/EN/85, Lehrstuhl für Strömungsmechanik, University of Erlangen-Nürnberg.

7 Dennis, S. C. R., and Smith, F. T., "Steady Flow through a Channel with a Symmetrical Constriction in the Form of a Step," *Proceedings of the Royal Society*, London, Series A 372, 1980.

8 Truckenbrodt, E., *Fluidmechanik*, Band 1, Springer-Verlag, pp. 269ff.

M. S. Ingber

A. K. Mitra

Department of Engineering Science and Mechanics,
Iowa State University,
Ames, Iowa 50011

Numerical Solution of Stratified Flow Into a Sink: A Criterion for Selective Withdrawal

Steady flow of an inviscid, stratified fluid into a line sink is analyzed numerically using a finite difference scheme. A criterion is proposed to determine the critical Froude number below which selective withdrawal is possible for arbitrary sink position and upstream density profile. For the case of selective withdrawal, a method to determine the withdrawal layer thickness is developed.

Introduction

In the flow of a stably stratified fluid into a sink, vertical motions are inhibited because of buoyancy forces. It is possible in some cases to withdraw a horizontal layer at the level of the sink, leaving the rest of the fluid intact. This general process is known as selective withdrawal. Selective withdrawal has been in use in the hydroelectric industry since the 1950s and has also found widespread application in the area of water quality control. Density stratification in lakes and reservoirs can be caused by a variety of reasons including heating and cooling, variable concentration of solvents, suspended solids, and inflows and outflows. Therefore, a wide variety of stratifications is possible.

Selective withdrawal from reservoirs is often accomplished by placing slit-like outlets at different levels in a dam. In other cases, the withdrawal from the reservoir is obtained through a canal with a skimmer wall. (See, e.g., Wood and Lai, 1972 and Jirka, 1979.) In both cases, the flow field can be approximated two-dimensionally. Imberger, Thompson, and Fandry (1976) show, for flows with Reynolds numbers greater than one, that the primary balance in the selective withdrawal process from a line sink is performed between the inertial forces and the buoyancy forces. In most applications, the Reynolds number is much greater than one; hence, an inviscid model is appropriate.

The analysis of the flow of a stratified fluid into a horizontal line sink was first performed by Yih (1958). Assuming a linear density profile and that the product of density and velocity head was constant upstream, he obtained exact steady-state solutions for densimetric Froude numbers greater than $1/\pi$. He was able to determine steady-state solutions for Froude numbers less than $1/\pi$, but these soltuions had waves upstream from the sink. Debler (1959) then showed experimentally that the Froude number approximately equal to $1/\pi$ was critical in the sense that uniform upstream conditions were impossible for Froude numbers below critical because of the formation of a withdrawal layer. The works of Koh (1966), Imberger (1972), and Pao and Kao (1974) helped to establish the foundations of the selective withdrawal processes. Two very good review articles are provided by Brooks and Koh (1969) and Imberger (1980).

This paper considers the steady flow of an inviscid, stratified fluid into a line sink. A finite difference scheme is developed to handle a wide range of density stratifications as well as arbitrary sink locations. For a given density profile and sink position, there is a critical sink strength characterized by a critical Froude number above which selective withdrawal is impossible. From a numerical point of view, the determination of this critical Froude number using a steady-state analysis appears to lead to a circular argument. The reason is that in order to determine the steady-state solution, boundary conditions must be assumed upstream. But this presumes the existence or nonexistence of a withdrawal layer—the very presence one is trying to determine. If, however, the assumed upstream boundary conditions lead to an unrealistic flow pattern, as in the case with Yih's analytic solutions for Froude numbers less that $1/\pi$ as described above, it must be because the boundary conditions themselves are unrealistic. This is the basis for the authors' criterion for determining the critical Froude number. Assuming uniform flow upstream for a given sink position and density stratification, at large Froude numbers, the flow remains parallel upstream. However, as the Froude number is decreased, a critical Froude number is reached at which the calculated flow no longer remains parallel upstream but becomes wavy. This type of flow has never been noted in nature or experimentally. The authors contend that this is the critical Froude number at which the withdrawal layer forms; that is, uniform flow is no longer possible upstream. This criterion is supported by comparisons of the present numerical results with experimental and analytic studies.

Mathematical Formulation and Numerical Solution

Consider the two-dimensional steady flow of an incompressible, inviscid, stratified fluid. Using the transformation of variables (Yih, 1958),

$$(u', w') = \sqrt{\frac{\rho}{\rho_0}}(u, w) \tag{1}$$

Contributed by the Fluids Engineering Division and presented at the Winter Annual Meeting, Boston, Mass., December 13–18, 1987 of THE AMERICAN SOCIETY OF MECHANICAL ENGINEERS. Manuscript received by the Fluids Engineering Division January 27, 1986.

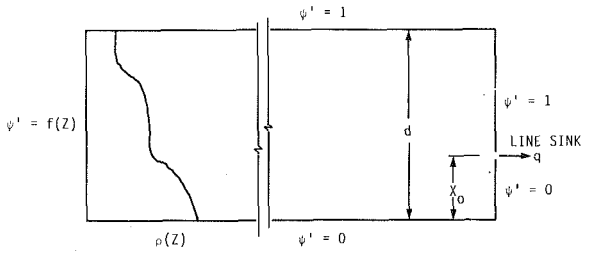

Fig. 1 Problem geometry

where ρ_0 is the reference density, it is easy to show that the equation of continuity is

$$\frac{\partial u'}{\partial x}+\frac{\partial w'}{\partial z}=0. \tag{2}$$

Thus, the stream function ψ' may be defined and the components of velocity may be written

$$u'=\frac{\partial \psi'}{\partial z},\ w'=-\frac{\partial \psi'}{\partial x}. \tag{3}$$

The streamlines of the flow coincide with lines of constant ψ'. The governing equation in terms of ψ' can be written (Yih, 1958)

$$\nabla^2\psi'+\frac{gz}{\rho_0}\frac{d\rho}{d\psi'}=\frac{1}{\rho_0}\frac{dH}{d\psi'}, \tag{4}$$

where H is the Bernoulli quantity defined by

$$H=p+\frac{\rho(u^2+w^2)}{2}+\rho gz. \tag{5}$$

Both H and ρ are constant along lines of constant ψ'. Therefore, if the upstream conditions are known, the particular forms of $d\rho/d\psi'$ and $dH/d\psi'$ may be determined. The problem becomes well-posed by specifying Dirichlet boundary conditions. However, without the knowledge of the development of the flow, it is difficult to determine the appropriate boundary conditions, especially the upstream conditions. In particular, for the case of flow into a sink, the phenomenon of blocking may occur; that is, stagnation zones may occur upstream.

Consider the geometry illustrated in Fig. 1. The value of ψ' is set to 1 along the portion of the boundary consisting of the top of the channel and the vertical portion of the boundary above the sink. The value of ψ' is set to 0 on the bottom of the channel and the vertical portion of the boundary below the sink. The sink is positioned a distance X_0 from the bottom and is simulated by ψ' changing from 0 to 1. The values of ψ' along the left-hand boundary will be allowed to vary from problem to problem. Further, should a withdrawal layer form, the top and bottom boundaries will be allowed to be repositioned in order to outline the withdrawal layer.

When the boundaries are repositioned to outline the withdrawal layer, the domain of computation is no longer rectangular and has curved boundaries. In this case, the Laplacian in equation (4) is approximated by a five-point finite difference formula with variable spacing. For the mesh arrangement in Fig. 2, it can be shown that

$$\nabla^2\psi'=\alpha_1\psi_1'+\alpha_2\psi_2'+\alpha_3\psi_3'+\alpha_4\psi_4'-\alpha_0\psi_0'+\epsilon, \tag{6}$$

where

$$\alpha_0=2\left[\frac{1}{S_1S_3k^2}+\frac{1}{S_2S_4k^2}\right],$$

$$\alpha_1=\frac{2}{S_1k[S_1k+S_3k]},$$

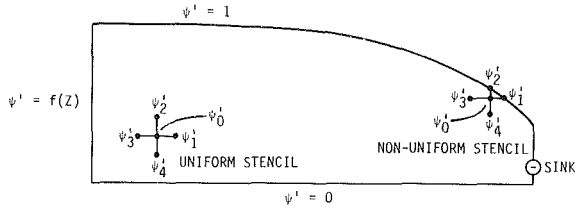

Fig. 2 Finite difference stencil in regions of uniform and nonuniform spacing

$$\alpha_2=\frac{2}{S_2k[S_2k+S_4k]},$$

$$\alpha_3=\frac{2}{S_3k[S_1k+S_3k]},$$

$$\alpha_4=\frac{2}{S_4k[S_2k+S_4k]},$$

and ϵ represents the local truncation error. Here, k is the typical grid spacing; S_1, S_2, S_3, and S_3 are fractions in regions where spacing is variable and are all unity for equal spacing. The first two terms in ϵ are

$$\frac{1}{6}\frac{\partial^3\psi'}{\partial z^3}\left[\alpha_2(S_2k)^3-\alpha_4(S_4k)^3\right]$$

$$+\frac{1}{6}\frac{\partial^3\psi'}{\partial x^3}\left[\alpha_1(S_1k)^3-\alpha_3(S_3k)^3\right].$$

When the α's are inserted, it is clear that local truncation error is $0(k)$. In the case of equal spacing the truncation error is $0(k^2)$. Because of this first-order truncation error, a smaller k has been used for computation in nonrectangular domains.

For the cases considered here, equation (1), when written in terms of the dimensionless variables and an appropriately defined Froude number, is Helmholtz type. Thus, the finite difference approximation leads to a pentadiagonal coefficient matrix. A typical run took five CPU seconds on a VAX/VMS system.

The Linear Stratification

The linear density stratification is used as a model problem since both analytic and experimental results are available for comparison. For the case of the linear upstream density profile and constant upstream velocity U', the governing equation (4) becomes linear and may be written

$$\nabla^2\psi+F^{-2}\psi=F^{-2}\eta, \tag{7}$$

where

$$\psi=\frac{\psi'}{U'd},\ \nabla^2=\frac{2}{\partial\zeta^2}+\frac{2}{\partial\eta^2},\ (\zeta,\eta)=\left(\frac{x}{d},\frac{y}{d}\right),\ \text{and}$$

$$F=U'\Big/\left(\frac{-gd}{\rho_0}\frac{d\rho}{d\psi}\right)^{1/2}$$

The nature of the solution is dependent on the magnitude of the Froude number F. For demonstration purposes, consider the case in which the sink is placed on the bottom of the channel. For Froude numbers much larger than $1/\pi$, the flow is characterized by nearly uniform flow toward the sink (Fig. 3(*a*)). As the Froude number approaches $1/\pi$ from above, an eddy develops in the corner above the sink (Fig. 3(*b*)). As the Froude number decreases further toward $1/\pi$, the eddy grows, suggesting a withdrawal layer (Fig. 3(*c*)). The steady-state solution changes dramatically for Froude numbers less than $1/\pi$. This solution is characterized by the appearance of waves

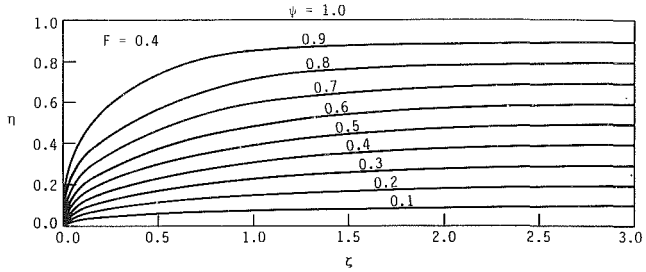

Fig. 3(*a*) $F = 0.4$

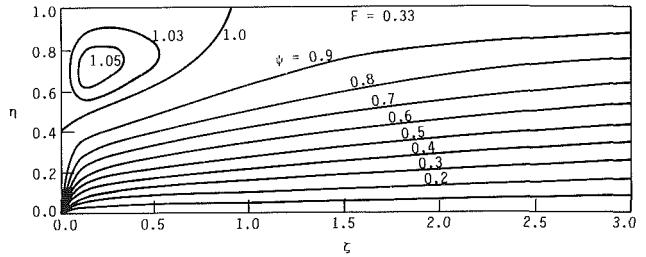

Fig. 3(*b*) $F = 0.33$

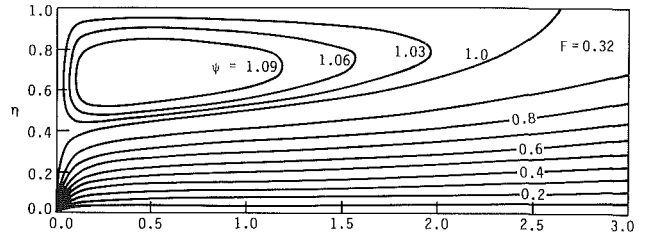

Fig. 3(*c*) $F = 0.32$

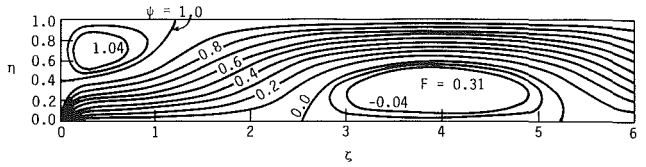

Fig. 3(*d*) $F = 0.31$

Fig. 3 Two-dimensional stratified flow into a sink with constant upstream density gradient and constant upstream U':

upstream from the sink along with an alternating pattern of eddies (Fig. 3(*d*)).

The critical Froude number that divides the wavy from the nonwavy cases as determined by the finite difference solutions is given by F = 0.313. The critical Froude number was easy to detect through numerical experiment. For Froude numbers above 0.314, the flow field was essentially horizontal upstream. For Froude numbers less than or equal to 0.313, the flow field was not horizontal upstream and the oscillatory nature of the streamlines was immediately apparent. The effect of imposing a parallel flow condition upstream as opposed to uniform flow was also considered. The results were essentially unaltered. It was determined that for computational domains of length greater than 10 compared to a height of 1 that the length of the computational domain had less than 1/10th of 1 percent effect on the critical Froude number. The length of the computational domain used to produce Fig. 3 was 10 in units of the normalized channel height. Finally, in all cases convergence tests were performed to insure that the mesh was fine enough to resolve the solution accurately.

Yih (1958) solved this problem analytically. His solutions were essentially the same as those shown in Fig. 3. The critical Froude number that divides the wavy from nonwavy cases for the finite difference solutions given by F = 0.313 compares favorably to the analytic result, $F = 1/\pi = 0.318$. The wave length of oscillation in Fig. 3(*d*) is 8.2 in units of channel depth. The analytic solution gives a wave length of 8.6. The Froude number $F = 1/\pi$ is critical in the sense that since no one has observed wavy solutions, it is most probable that below this value blocking occurs. This blocking would imply that the imposed boundary conditions are incorrect. That is, for Froude numbers below critical, a withdrawal layer exists, thus making uniform flow upstream impossible. In the next section a method is outlined to determine solutions at Froude numbers below critical with a withdrawal layer. This critical Froude number was determined to be insensitive to the location of the sink for the linear stratification.

Formation of a Withdrawal Layer

For Froude numbers below critical, solutions with withdrawal layers (nonwavy solutions) may be obtained provided the streamlines, $\psi = 0$ and $\psi = 1$, are allowed to align themselves with the withdrawal layer. As an example case, again consider the linear density profile with constant velocity U' upstream within the withdrawal layer and the sink placed at the bottom of the channel.

If the fluid is assumed to be stagnant above the withdrawal layer, the pressure distribution is hydrostatic on the dividing streamline. The linear density distribution is given by

$$\rho = \rho_0 - (\rho_0 - \rho_1)\frac{y}{d} \tag{8}$$

where d is now defined to be the height of the withdrawal layer upstream. Hence, the hydrostatic pressure is given by

$$P = P_A - \left[\rho_0 y - (\rho_0 - \rho_1)\frac{y^2}{2d}\right]g \tag{9}$$

where P_A is the pressure along the dividing streamline far upstream.

Since ρ is constant along lines of constant ψ, Bernoulli's equation along the dividing streamline demands

$$-\rho_0 g y + (\rho_0 - \rho_1)g\frac{y^2}{2d} + \frac{\rho_1(u^2 + w^2)}{2} + \rho_1 g y = \text{constant} \tag{10}$$

Setting $\eta = y/d$ and dividing equation (10) by $\rho(U')^2$ yields

$$\frac{gd}{(U')^2}\left[-\eta + \left(1 - \frac{\rho_1}{\rho_0}\right)\frac{\eta^2}{2}\right] + \frac{1}{2}\frac{\rho_1}{\rho_0}\left[\left(\frac{u}{U'}\right)^2 + \left(\frac{w}{U'}\right)^2\right] + \frac{gd}{(U')^2}\frac{\rho_1}{\rho_0}\eta = \text{constant} \tag{11}$$

Note that the second summand in equation (11) represents one half of the square of the transformed velocities (see equation (1)) normalized by U'. Note that further from the definition of the Froude number,

$$F^{-2} = \frac{gd}{(U')^2}\frac{\rho_1 - \rho_2}{\rho_0}$$

Therefore, by rearranging terms, equation (11) can be rewritten

$$\mathrm{F}^{-2}\eta = \mathrm{F}^{-2}\frac{\eta^2}{2} - \frac{(u')^2 + (w')^2}{2} = \text{constant} \tag{12}$$

The above form of the dynamic boundary condition can be used in an algorithm to determine the position of the dividing streamline. Although the equation is predicated on the linear density profile, the algorithm itself is quite general. For different density profiles, the hydrostatic pressure distribution can still be determined by integrating the density distribution, and the proper form of Bernoulli's equation can be determined analogously to equation (12). In practice, the upper

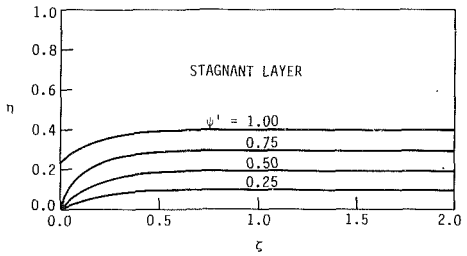

Fig. 4 Withdrawal layer shape, $F = 0.3$, with constant upstream density gradient

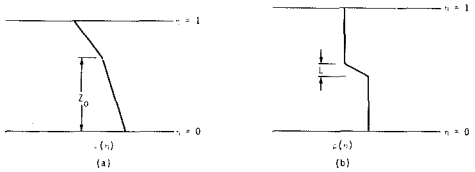

Fig. 5 Upstream density profiles

fluid is not entirely stagnant but recirculates slowly. Further, it can be expected that the linear density profile will be somewhat perturbed in the upper layer above the sink. However, these influences will have only minor effect on equation (12) and even less effect on the shape of the withdrawal layer.

The algorithm to determine the position of the dividing streamline is as follows. First, the location of the dividing streamline is assumed. Next, the finite difference program is run and the velocities in the flowing region at the interface are calculated. Bernoulli's condition (equation (12)) along the dividing streamline is in general not satisfied for the assumed position. The dividing streamline is then repositioned so that Bernoulli's condition is satisfied. With the new position of the dividing streamline, the procedure is repeated until the dividing streamline converges to its proper position.

For the example case of the linear density profile it appeared that the corner eddy approached a thickness of $\eta = 0.6$ as the Froude number approached critical from above (see Fig. 3). Thus, the initial position of $\Psi = 1$ was set uniformly to $\eta = 0.4$. The algorithm worked well except for the two nodes on the dividing streamline nearest the sink. These nodes were repositioned by trial and error. Five iterations were performed allowing the values of the Bernoulli constant along the interface to be within 3 percent of each other.

The shape of the withdrawal layer for a Froude number F = 0.3 is illustrated in Fig. 4. Far from the sink, the dividing streamline assumed the height given by $\eta = 0.38$. In test cases, the height of the dividing streamline decreased with decreasing Froude number.

Arbitrary Stratifications

The true versatility of the numerical method is that arbitrary density stratification may be handled with relative ease. The two density profiles shown in Fig. 5 are considered. The critical Froude number is determined as before; that is, the critical Froude number is the smallest possible before the steady-state solutions develop waves upstream from the sink.

For the density profile of Fig. 5(*a*), the density gradient in the region $z_0 < z < 1$ is twice as large as in the region $0 < z < z_0$. The Froude number is based on the smaller density gradient. The critical Froude number is, as in the case of constant gradient, insensitive to the position of the sink. The critical Froude number as a function of z_0 is shown in Fig. 6. For $z_0 = 1$, the value F = 0.313 from the constant slope case is retained. Similarly, for $z_0 = 0$, F = 0.626, which is twice the old value because of the way in which the Froude number is defined. In the region $0.6 < z_0 < 1$, the critical Froude numbers

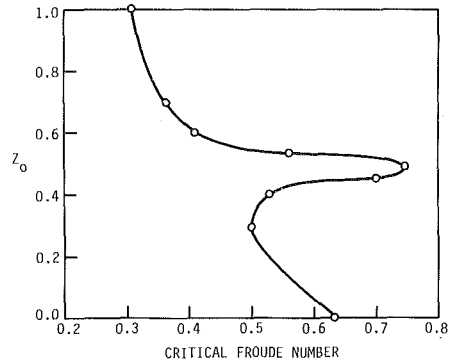

Fig. 6 The relationship between Z_0 and the critical Froude number for the piecewise linear upstream density profile

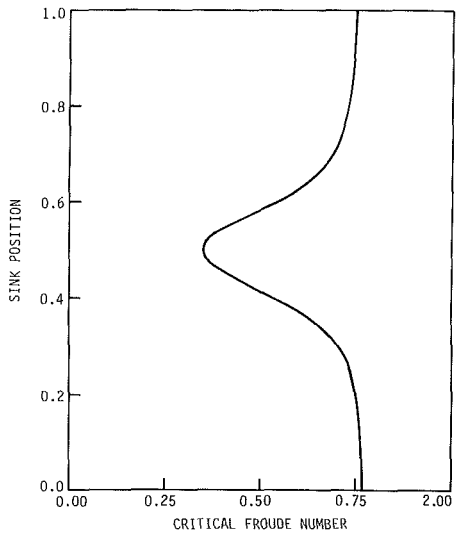

Fig. 7 The relationship between sink location and the critical Froude number for the layered upstream density profile

are very close to those that would be determined simply by rescaling the problem. For example, if $z_0 = 0.6$ was considered as a solid surface, so that the total depth of the channel was 0.60 and the density gradient was constant, the critical Froude number would be given by 0.40 as compared to 0.41 as shown on the graph. Similarly, in the region $0 < z_0 < 0.3$, the critical Froude numbers can be determined by rescaling the constant density gradient case. Thus, for a large range of z_0's, the criterion for selective withdrawal is dominated by the "larger layer." This is probably not an intuitive result, because it might be conjectured that the layer with the largest density gradient would be the critical one for determining the possibility of a withdrawal layer. However, as a layer shrinks in size, the formation and growth of the corner eddy is restricted, thus inhibiting the formation of the withdrawal layer. This is why in the middle region, $0.3 < z_0 < 0.6$, the formation of the withdrawal layer is delayed until larger Froude numbers, and the critical Froude number cannot be predicted simply by a rescaling argument.

The density profile depicted in Fig. 5(*b*) is not unlike what might occur in a thermally polluted lake. Since $d\rho/d\psi'$ is variable in this case, it is convenient to redefine the Froude number as follows

$$\mathrm{F} = \frac{U'}{\sqrt{g \dfrac{\rho_2 - \rho_1}{\rho_2} \dfrac{d}{2}}}$$

where d is the total depth of the channel, ρ_1 is the density

above the pycnocline, and ρ_2 is the density below the pycnocline. The pycnocline itself is centered in the channel. The relationship between critical Froude number and sink position is graphed in Fig. 7. It is seen that the critical Froude number is highly dependent in this case on the sink position. This is to be expected since for sink placement near the center, it is more difficult to withdraw from only one layer. In the limiting case of two superimposed layers of constant density and the sink placed on the interface, selective withdrawal from one layer would be impossible.

Comparisons With Analytic and Experimental Results

The numerical results for the linear stratification are essentially the same as those determined analytically by Yih (1958). The critical Froude number, F = 0.24, determined experimentally by Debler (1959) is reasonably approximated by the numerical value of F = 0.313, especially considering that viscous effects were neglected.

Kao (1976) considered the selective withdrawal problem for stratified, inviscid fluids with arbitrary stratification. He developed the criterion that if the steady-state velocity induced by the sink, that is, the sink strength divided by the fluid depth, was greater than the greatest internal-wave velocity, selective withdrawal would be impossible. The reasoning for this criterion is that the withdrawal layer is formed by columnar disturbances traveling upstream. This would be impossible if the upstream velocity was greater than the wave speed. For the density stratification shown in Fig. 5(*a*) with $z_0 = 0.5$, Kao determines a critical Froude number of 0.78. This compares favorably with the critical Froude number of 0.76 of the present analysis.

In the limiting case, $L \to 0$, the stratification shown in Fig. 5(*b*) approaches the two-layer discrete stratification. Jirka and Katavola (1979) have shown experimentally for a point sink that the parameter L is a secondary measure of geometric effects and that results obtained with the diffuse interface (Fig. 5(b)) can be compared to results obtained for the discrete stratification. The first study of the discrete two-layer system was performed by Craya (1949), who used Richardson's method to estimate a critical Froude number of 0.75 for the case of the sink placed at the bottom of the channel. This result was verified experimentally by Gariél (1949). Kao (1976), using the criterion mentioned above, determined a critical Froude number of 0.71. However, in his analysis, no attention was given to the position of the sink. In the present analysis, the critical Froude number is strongly dependent on the sink position. For the sink placed at the bottom of the channel, the present result yields a critical Froude number of 0.76, which compares very well with the previous results.

Discussion

A criterion has been outlined to determine numerically the critical Froude number below which selective withdrawal is possible from a line sink for an arbitrary upstream density profile. The criterion itself arose in response to a problem that has long plagued numerical analysts, namely, what boundary conditions are appropriate in the steady state. Given a set of boundary conditions, the selective withdrawal problem is well posed and a steady-state solution can be calculated. If the resulting steady-state solution is not realistic, then the boundary conditions must be in error. Since only two types of boundary conditions have been observed, it seems reasonable that if the assumption of parallel flow upstream leads to a wavy flow pattern, then the correct boundary conditions must reflect the existence of a withdrawal layer. The results of the present study compare favorably with previous analytical and experimental studies, reinforcing the validity of the criterion. Because of the wide range of natural conditions, it is desirable to be able to estimate the critical Froude number and withdrawal layer thickness for arbitrary density stratifications and sink placements. This can be accomplished inexpensively with the present numerical scheme.

Acknowledgments

This work is supported through the Engineering Research Institute of Iowa State University.

References

Brooks, N. H., and Koh, R. C. Y., 1969, "Selective Withdrawal From Density-Stratified Reservoirs," *J. Hydr. Div.*, ASCE, Vol. 95, pp. 1369–1400.

Debler, W. R., 1959, "Stratified Flow into a Line Sink," *J. Eng. Mech. Div.*, ASCE, Vol. 85, pp. 51–65.

Craya, A., 1949, "Recherches theoriques sur l'écoulement de couches superposées de fluides de densités differentes," La Houille Blanche, pp. 44–55.

Gariél, P., 1949, "Recherches experimentales sur l'écoulement de couches superposées de fluides de densités differentes," La Houille Blanche, pp. 56–64.

Imberger, J., 1972, "Two-Dimensional Sink Flow of a Stratified Fluid Contained in a Duct," *J. Fluid Mech.*, Vol. 78, No. 3, pp. 329–349.

Imberger, J., 1980, "Selective Withdrawal: A Review," *Second International Symposium on Stratified Flows*, Trondheim, Norway, pp. 381–400.

Imberger, J., Thompson, R. O. R. Y., and Fandry, C., 1976, "Selective Withdrawal From a Finite Rectangular Tank," *J. Fluid Mech.*, Vol. 78, Part 3, pp. 489–512.

Jirka, G. H., 1979, "Supercritical Withdrawal From Two-Layered Fluid Systems. Part 1: Two Dimensional Skimmer Wall," *J. Hydr. Research*, Vol. 17, pp. 43–52.

Jirka, G. H., and Katavola, D. S., 1979, "Supercritical Withdrawal From Two-Layered Fluid Systems," *J. of Hyd. Res.*, Vol. 17, No. 1, pp. 53–62.

Kao, T. W., 1976, "Selective Withdrawal Criteria of Stratified Fluids," *J. Hydr. Div.*, ASCE, Vol. 102, pp. 717–729.

Koh, R. C. Y., 1966, "Viscous Stratified Flow Towards a Sink," *J. Fluid Mech.*, Vol. 24, No. 3, pp. 555–575.

Pao, H. P., and Kao, T. W., 1974, "Dynamics of Establishment of Selective Withdrawal of a Stratified Fluid From a Line Sink. Part 1: Theory," *J. Fluid Mech.*, Vol. 65, pp. 657–688.

Wood, I. R., and Lai, K. K., 1972, "Selective Withdrawal From a Two-Layered Fluid," *J. Hydr. Research*, Vol. 10, pp. 475–496.

Yih, C. S., 1958, "On the Flow of a Stratified Fluid," *Proc. 3rd, U.S. Nat. Congr. Appl. Mech.*, pp. 857–861.

Air Flow Resistance of Wire Nettings in Natural Convection

M. Ishizuka
Researcher,
Mechanical Engineering Laboratory,
Research and Development Center,
Toshiba Corp.,
Kawasaki, 210, Japan

This paper describes some experimental values for flow resistance of wire nettings in low Reynolds number flows, such as natural air convection, providing basic thermal data necessary for designing electronic equipment casings. The experiment was designed to evaluate the wire netting resistance coefficient in natural air convection. As a result, the relationships among the resistance coefficient for wire netting, Reynolds number, and porosity coefficient were obtained in useful form.

1 Introduction

Measures for cooling electronic equipment have become increasingly important. To determine appropriate measures, predicting the air flow resistance for the equipment casing is indispensable. One typical resistance element for a casing is the porous plate used at a casing ventilation intake and outlet. However, resistance data for the ventilation netting in natural air convection can scarcely be found. Therefore, the standard practice has been to use available data, which have been obtained by several researchers [1–8] in forced air convection of relatively low Reynolds number.

For wire netting data at low Reynolds numbers (Re $<$ 100), a small amount of data was obtained by other researchers [9–11] and correlated by Cornel [12] with high Reynolds number data. However, data for practical use in electronic equipment cooling are scarce.

This paper describes a new method of obtaining resistance data for wire netting and also presents data on their correlation with a function of the porosity coefficient and Reynolds number.

2 Evaluation Method for Air Flow Resistance Coefficient

A ventilation model, shown in Fig. 1, is considered. Assuming a uniform temperature distribution and one-dimensional steady flow, two expressions can be written, one for overall energy balance and the other for balance between aerodynamic resistance and buoyancy force, as follows:

$$Q=\rho CpuA\Delta T \tag{1}$$

$$(\rho_\infty-\rho)gh=K_T\rho u^2/2 \tag{2}$$

where, h is the distance between the heater and wire netting and K_T is the flow resistance coefficient for the total system.

Assuming that the pressure is constant and the air is a perfect gas, the following relation is obtained:

$$(\rho_\infty-\rho)/\rho=\Delta T/T_\infty \tag{3}$$

Then, the equation for K_T is obtained from equations (1), (2), and (3) as follows:

$$K_T=2\,g\,h\Delta T^3/(T_\infty(\rho CpA/Q)^2) \tag{4}$$

This relation shows one important feature, which is that coefficient K_T can be evaluated, even when only dissipated power and temperature rise is known. In addition, these two quantities are relatively easy to measure. By taking advantage of this relation, it is possible to evaluate the pressure loss coefficient for a wire netting without measuring any pressure drop.

Next, K_T is divided into two parts; $K0$ and K. $K0$ is the coefficient for the system without a wire netting. $K0$ can be easily obtained by using equation (4) and making the same measurements as for K_T, but without a wire netting.

The net coefficient K for the wire netting is easily obtained by simply subtracting $K0$ from K_T, as follows:

$$K=K_T-K0 \tag{5}$$

3 Experimental Devices

Figure 2 illustrates the measurement system for realizing the ventilation model shown in Fig. 1. The system consists of inner and outer ducts. The inner duct has an input power heater at its bottom and a wire netting on its top. The power heater is shown in Fig. 3. Its electric resistance value was 31.5 ohms. The shape of the spiral heater was determined experimentally

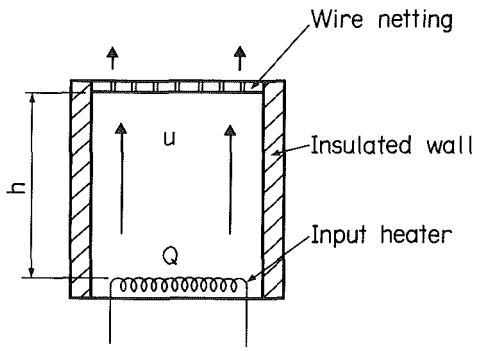

Fig. 1 Ventilation model

Contributed by the Fluids Engineering Division for publication in the JOURNAL OF FLUIDS ENGINEERING. Manuscript received by the Fluids Engineering Division February 22, 1986.

to obtain an even in-duct temperature distribution, with only a slight obstruction to the upward flow.

In order to minimize the heat loss from the inner duct, auxiliary ribbon heaters were wound around its outer wall. By adjusting the voltage values for these ribbon heaters, little difference between wall temperature Tw and air temperature at the center Tc was achieved so as to satisfy the following criterion.

$$(Tc - Tw)/Tc \leqq 0.02 \tag{6}$$

Thermocouples (copper-constantan thermocouples having 0.1 mm wire diameter) were installed within the duct at three positions (wall, slightly apart from wall, center of duct) for each of the upper, middle and lower levels. These thermocouples were bonded to the wall with heat conductive epoxy bonding material and tape. Actually, temperature T in this study was the average temperature inside the duct. Temperatures were monitored using a thermometer with 0.1 K accuracy.
The wattmeter accuracy was 0.01 watt. The experiments were carried out under the condition of $T_\infty = 298.5$ K.

The ratio of height to diameter in this particular set-up was set at 5.7. The reason was as follows:

First, $K0$ measurements were made without a wire netting. A linear relationship was obtained between $K0$ and H/D from those measurements as shown in Fig. 4. The 5.7 H/D ratio is at about the middle of the straight line which was obtained. Also, it was taken into account that, for a higher duct, it is more difficult to realize an isothermal condition inside the duct.

For this particular H/D ratio, $K0$ becomes a function of the Reynolds number, based on duct diameter D, as shown in Fig. 5. The relation was obtained as follows:

$$K0 = 2300/\mathrm{Re},D \tag{7}$$

Here, the air velocity u used to obtain Re, D is the value obtained from equation (1). It was found that laminar flow existed during this study, because Re, $D < 2000$.

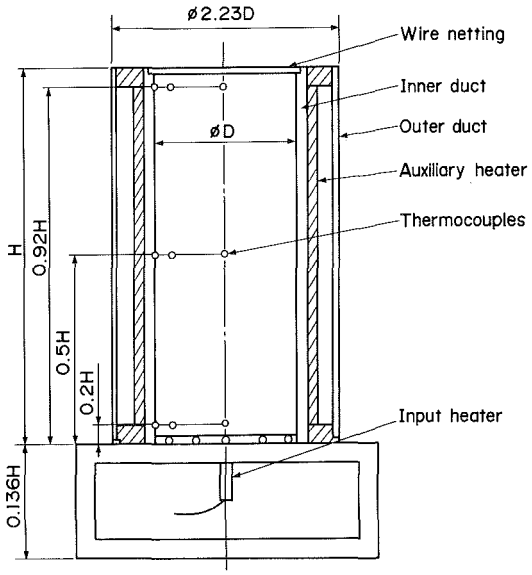

Fig. 2 Experimental device

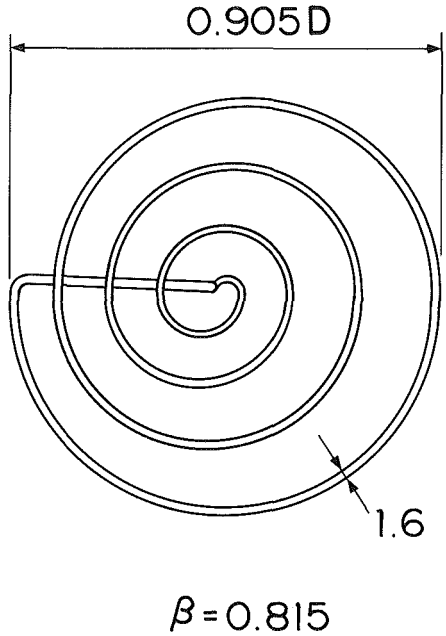

Fig. 3 Input power heater

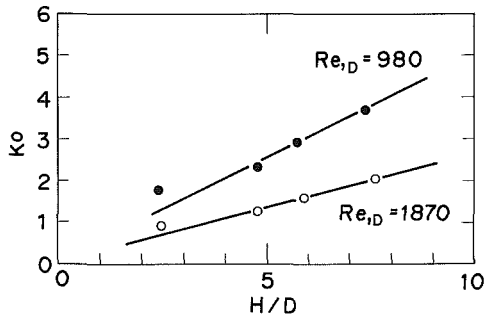

Fig. 4 Relationship between resistance coefficient $K0$ and duct height H

Nomenclature

A = duct sectional area
Cp = specific heat of air at constant pressure
$C1$ = constant
$C2$ = constant
D = duct diameter
d = wire diameter
g = gravitational acceleration speed
h = distance from heater to vent
H = duct height
K = resistance coefficient for wire netting
K_T = resistance coefficient for total system
$K0$ = resistance coefficient for total system without wire netting
M = mesh number
Q = input power value
r = radius from center of duct
$r0$ = duct radius
Re = Reynolds number for wire, $u\,d/\nu$
Re,D = Reynolds number for duct, $u\,D/\nu$
Re,s = Reynolds number for wire spacing, $u\,s/\nu$
s = wire to wire interval
T = temperature
ΔT = temperature rise
u = air flow average velocity
y = distance from duct bottom
β = porosity coefficient for wire netting
ρ = air density
λ = friction coefficient
ν = dynamic coefficient of viscosity for air

Subscript

0 = without wire netting
c = duct center
w = duct wall
∞ = ambient

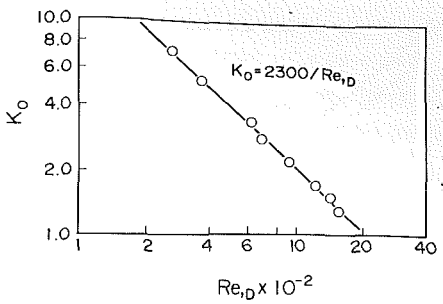

Fig. 5 Relationship between resistance coefficient K0 and Reynolds number $Re_{,D}$

Figure 6 shows in-duct temperature distributions at upper and lower areas of the duct, when power was input and when power was not input to the auxiliary ribbon heaters. For the middle area, temperatures were between those for the upper and lower areas. The distributions shown here are for $\beta = 0.778$, which is for a comparatively large porosity coefficient. Temperature control, in the case of large height, was generally difficult, because of the large heat emission through the upper area. The *Tw* value, with no power applied to the ribbon heaters, was considerably low, with respect to the *Tc* value. Temperature distribution was not uniform at all in this case. However, very good uniform distribution was obtained when power was applied to the ribbon heaters.

Air flow uniformity in the duct height direction was also obtained, since the ribbon heaters were divided into upper, middle, and lower sections, to each of which power was applied individually. Also note that this power input control was considerably difficult.

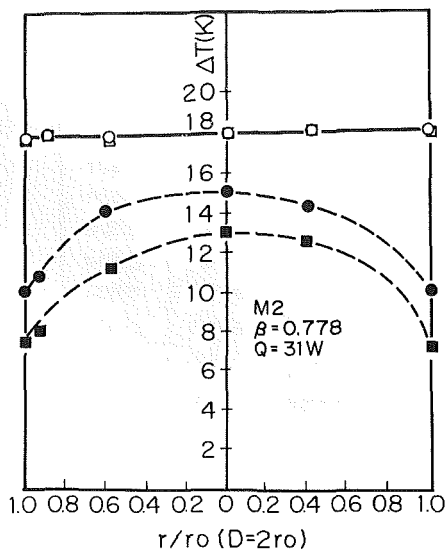

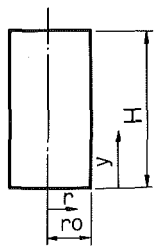

Symbol	y/H	Auxiliary Heater
—○—	0.92	on
--●--	0.92	off
—□—	0.20	on
--■--	0.20	off

Fig. 6 In-duct temperature distribution

4 Experimental Results

4.1 Wire Netting Used in This Study. The shape and mesh size (nine in total) of the wire nettings used for this measurement are shown in Fig. 7 and Table 1, respectively. Figure 7 shows that individual wire nettings were put into stainless steel frame rings. Wire nettings were also made of stainless steel. The nettings were spot-welded in place, so that even tension was applied to the entire wire netting. Symbol M in Table 1 shows the mesh number. M2 shows that two wires exist within an inch, for example. Wire nettings in Table 1 all have a squared grid. Therefore, the porosity coefficient β for a wire netting will be

$$\beta = (1 - d/(s+d))^2 \tag{8}$$

where, *s* is wire to wire interval.

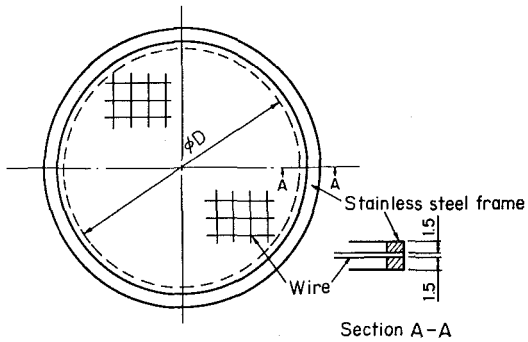

Fig. 7 Wire netting shape

4.2 Relation Between Resistance Coefficient *K* and Reynolds Number Re. Figure 8 shows, for each wire netting, the plotting of evaluated *K* against its Reynolds number Re. Re values were less than 100 and the relationships were on straight lines, each having an inclination of -0.85. However, it was confirmed that the *K* values were strongly affected by the porosity coefficient and Reynolds number. In Fig. 8, finite-length lines are indicators for uncertainty bands of the measured values with 20:1 odds.

A detailed discussion on uncertainty in this study will be made later.

4.3 Relations Among Resistance Coefficient *K*, Reynolds Number Re, and Porosity Coefficient. Figure 9 shows the relationships among evaluated *K* data for a group of two parameters, Reynolds number Re and porosity coefficient β. If the two variables are grouped as shown in Fig. 9, all the data become well correlated. The following empirical expression can then be drawn from the best fit to the measured data.

$$K = 28(\mathrm{Re}\ \beta^2/(1-\beta))^{-0.95} \tag{9}$$

The Re range in above the equation is $0.4 < \mathrm{Re} < 95.0$. The four data points, represented by double circles in Fig. 9, are those obtained by MacPhail [9] and applied to the relational expression (9). These data closely support the relation in Expression (9). Therefore, Expression (9) is considered to be sufficiently useful, provided that the Re value is not greater than 100, and that the expression is used for practical purposes only. As a result, the range for these experimental data are as follows.

$$2.3K \leq T \leqq 87.5K$$
$$2.1 \text{ watts} \leqq Q \leqq 57.5 \text{ watts} \tag{10}$$

5 Discussion on Results

In the previous section, the Reynolds number and porosity coefficient were grouped together to correlate them to the data obtained for the resistance coefficient *K*. In this section, it is shown how the group was derived to correlate all the data.

Collar [1] derived the following expression by assuming that

Table 1 Wire netting sizes

Screen No.	d (mm)	ℓ (mm)	β
M2	1.5	12.70	0.778
M3	1.5	8.47	0.677
M5	1.1	5.08	0.614
M14	0.5	1.82	0.526
M25	0.29	1.00	0.504
M30	0.23	0.870	0.541
M35	0.23	0.720	0.463
M100	0.10	0.256	0.371
M200	0.046	0.128	0.410

the resistance is proportional to the area of the wire netting and to the square of the air flow speed through the wire spacing which is inversely proportional to the porosity coefficient.

$$K = C1(1-\beta)/\beta^2 \tag{11}$$

where $C1$ is a constant.

However, $C1$ is actually considered to be a function of the Reynolds number in the low Reynolds number range. Now, it was assumed here that the flow through the wire spacings is similar to laminar duct flow, namely, the constant $C1$ for the wire netting can be represented as friction drag, as follows:

$$C1 = \lambda d/s \tag{12}$$

where λ is friction coefficient.

In a laminar duct flow, it is well known that the friction coefficient can be written as follows:

$$\lambda = C2/\mathrm{Re}, s \tag{13}$$

where, Re, s based on the wire interval s is used, and $C2$ is constant.

Then, the expression for the resistance coefficient K can be written from equations (11), (12), and (13) in the following way, since $\mathrm{Re} = d/s \cdot \mathrm{Re}, s$.

$$K = C2(d/s)^2\,(\mathrm{Re}\cdot\beta^2/(1-\beta))^{-1.0} \tag{14}$$

The right side of equation (14) includes the parameter group for Re and β used in equation (9). The results of equation (9) show that the above derived assumptions are reasonable, because the exponents in the power-law representation are slightly different for equation (9) and equation (14), respectively, being -0.95 and -1.0.

It may be considered that the combined aerodynamic resistance caused by the pressure drag due to the wake flow behind the wires and that by the friction between air flow and wires can be represented by the parameter group used in equation (9) at the low Reynolds number range.

6 Comparison Between Present Data and Other Data

For $\mathrm{Re} < 100$, the following expressions for wire nettings were proposed by Wieghart [10] and MacDougall [11], respectively.

$$K = 6\cdot\frac{(1-\beta)}{\beta^2}(\mathrm{Re})^{-1/3},\quad 60 < \mathrm{Re} < 1000 \tag{15}$$

$$K = \frac{33.93}{\mathrm{Re}}\,\frac{(1-\beta)\cdot\beta^{1.27}}{1+\beta^{1/2}},\quad 0.006 < \mathrm{Re} < 20 \tag{16}$$

Figure 10 shows numerical comparisons among equations (9), (15), and (16). It may be seen that equation (9) supports equation (16) by MacDougall very closely, but the K values by equation (15) are somewhat smaller than the others. The reason seems to be that equation (15) covers a wide Reynolds number range. Therefore, it is not necessarily appropriate for a small Reynolds number range, such as $\mathrm{Re} < 100$. However, since equation (9) is very close to MacDougall's values for $\mathrm{Re} < 20$, and it widens the applicable range to $\mathrm{Re} < 100$. It is considered to be the most useful, provided that $\mathrm{Re} < 100$.

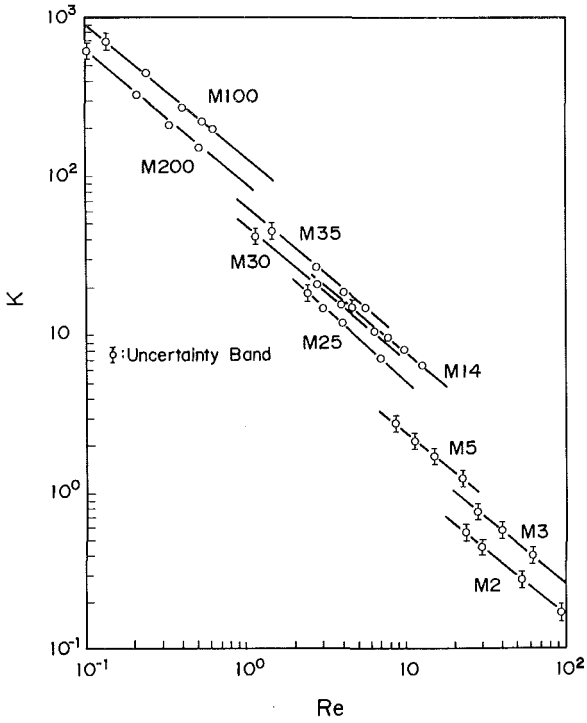

Fig. 8 Relationship between resistance coefficient K and Reynolds number Re

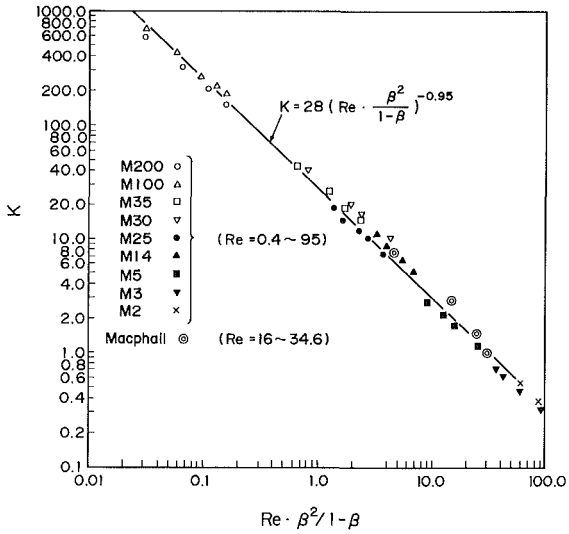

Fig. 9 Relationship among resistance coefficient K, Reynolds number Re and porosity coefficient β

7 Experimental Uncertainty

Uncertainty analysis was conducted by taking into account the two major uncertainties in the measurements; one for temperature rise, which was estimated as being 0.5 Kelvin, and the other for heat input, where 0.1 watt heat loss was estimated at most.

The uncertainty bands were calculated using the propagation equations, as shown by Kline [13], assuming that the uncertainty effects of heat flow Q and temperature rise ΔT on

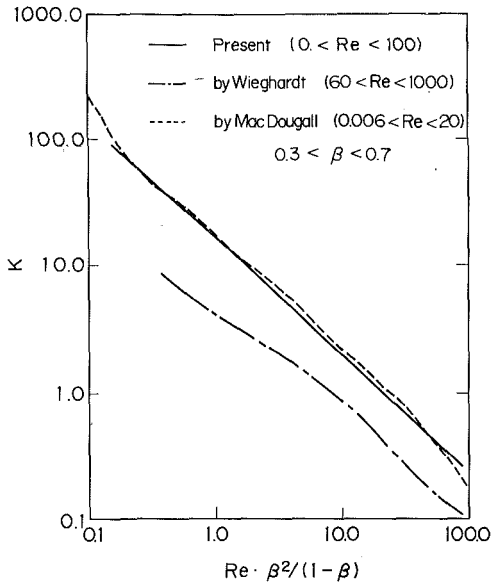

Fig. 10 Author's data compared with others

the uncertainty of the resistance coefficient K and air velocity u were dominant and those of other parameters were negligible. The equations used to obtain the K and u value uncertainty bands, respectively, were as follows:

$$|dK/K| = \{9(d\Delta T/\Delta T)^2 + 4(dQ/Q)^2\}^{1/2} \quad (17)$$

$$|du/u| = \{(dQ/Q)^2 + (d\Delta T/\Delta T)^2\}^{1/2} \quad (18)$$

The heat loss was estimated by considering that the downward heat loss by radiative heat transfer from the input heater was 0.08 watts at most, by assuming that the surface temperature was 150 degrees and that the emitted heat loss, caused by natural and radiative heat transfer from the heated wire netting, was 0.02 watts at most, because the maximum temperature rise was 85k. The heat loss from the duct wall was negligible because, as previously mentioned, the difference between the wall temperature and the air temperature at the center of the duct was adjusted to be within 2 percent.

The maximum total uncertainty obtained was 25 percent, when β was 0.63, due to the small temperature rise. In case β was less than 0.614, the maximum uncertainty bands, from equations (17) and (18), were 12 percent for the K value and 16 percent for the Re value. However, when β was more than or equal to 0.614, these maximum uncertainty bands became 65 percent for the K values and 22 percent for the Re values. The reason is that, when β is large, the temperature rise for the duct air becomes very small and the K value will be extremely small.

Considering a single wire, the uncertainty bands varied widely, due to Reynolds number change. As an example, for 200 mesh wire, the uncertainty bands for K and Re were 4.1 percent and 16 percent, respectively, at the lowest Reynolds number point, while the values were 0.5 percent and 0.18 percent for the highest Reynolds number, in the present experiments.

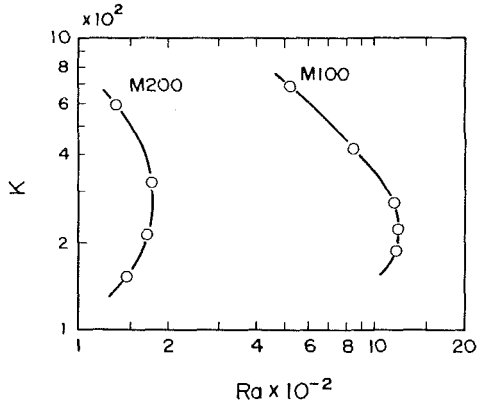

Fig. 11 Relation between resistance coefficient K and Rayleigh number Ra

8 Conclusion

A method for obtaining the resistance coefficients for wire nettings in natural air convection was designed and the resistance coefficients for wire nettings were correlated to the Reynolds number and porosity coefficient, as follows:

$$K = 28(\mathrm{Re}\cdot\beta^2/(1-\beta))^{-0.95}$$

This correlation and designed method are useful applying natural air cooling technology to electronic equipment.

References

1 Collar, A. R., "The Effect of a Gauze on the Velocity Distribution in a Uniform Duct," Brit. Aero. Res. Coun., Rep. and Mem. 1867, Feb. 1939.

2 Schubauer, G. B., Spangenberg, W. G., and Klebanoff, P. S., "Aerodynamic Characteristics of Damping Screens," N.A.C.A. Tech. Note. 2001, Jan. 1950.

3 Schubauer, G. B., and Spangenberg, W. G., "The Effect of Screens in Wide-angle Diffusers," N.A.C.A. Tech. Note. 1610, June 1947.

4 Simmons, L. F., and Cowdrey, C. F., "Measurements of the Aerodynamic Forces Acting on Porous Screens," Brit. Aero. Res. Coun., Rep. and Mem. 2276, Aug. 1945.

5 Eckert, B., and Pfluger, F., "Resistance Coefficients of Commercial Round Wire Grids," N.A.C.A., Tech. Memo. 1003, Jan. 1942.

6 Taylor, G. I., and Davies, R. M., "The Aerodynamics of Porous Sheets," R. & M. 2237, Apr. 1944.

7 Taylor, G. I., and Batchelor, G. K., "The Effect of Wire Gauze on Small Disturbances in a Uniform Stream," *Quarterly Journal of Mechanics and Applied Mathematics*, Vol. 2, 1949, pp. 1–45.

8 Annand, W. J. D., "The Resistance to Air Flow of Wire Gauzes," *Journal of the Royal Aeronautical Society*, Vol. 57, Mar. 1953, pp. 141–146.

9 MacPhail, D. C., "Experiments on Turning Vanes at an Expansion," Brit. Aero. Res. Coun., Rep. and Mem. 1876, 1939.

10 Wieghardt, K. E. G., "On the Resistance of Screens," *The Aeronautical Quarterly*, Vol. 4, Feb. 1953, pp. 186–192.

11 MacDougall, D. A., "Pressure Drop Through Screens," MS Thesis, Ohio State University, Columbus, Ohio, 1953.

12 Cornel, W. G., "Losses in Flow Normal to Plane Screens," TRANS ASME, May 1958, pp. 791–799.

13 Kline, S. J., "The Purposes of Uncertainty Analysis," ASME JOURNAL OF FLUIDS ENGINEERING, Vol. 107, June 1985, pp. 153–163.

Unsteady Viscous Flow Between Parallel Disks With a Time-Varying Gap Width and a Central Fluid Source

S. Ishizawa
Chief Researcher,
Mechanical Engineering Research Laboratory,
Hitachi Ltd.,
Tsuchiura, 300, Japan

Tooru Watanabe
Rheon Automatic Machinery Co., Ltd.,
Utsunomiya, 320, Japan

Koji Takahashi
Professor,
Department of Mechanical Engineering,
Sophia University,
Tokyo, 102, Japan

A theoretical analysis is presented for the unsteady laminar flow of an incompressible fluid between parallel disks with a time-varying gap width and a central fluid source of constant flow rate. New series solutions to the Navier-Stokes equations are obtained, on the basis of asymptotic series expansion in the radial direction and a new theory of "multifold series expansion" with respect to the time variable. The solutions cover the general case of arbitrarily time-varying gap width. Moreover, it can describe precisely the complicated non-linear interaction between the two coexisting flows due to the gap-width variation and to the central fluid source. Experiments were carried out for the case of sinusoidally oscillating gap-width variation, and it has been confirmed that the present solutions agree well with the experiments, even in severe cases that an approximate superposition theory neglecting the aforementioned interaction effect produces a remarkable error.

1 Introduction

The unsteady laminar flow of an incompressible viscous fluid between two parallel disks, where the gap width is varying arbitrarily with time and concurrently fluid is flowing out of a hole made in the central part of either of the two disks, is a fundamental type of unsteady fluid flow which is met frequently in many hodrodynamical machines and apparatus. This flow may be considered as a phenomenon in which two different types of flow coexist, one due to the gap-width variation, and the other due to the central fluid source.

In the case of a single flow phenomenon which is due either to the gap-width variation only or to the central fluid source only (in this latter case the gap width is retained unchanged), problem is simplified considerably, and many theoretical and experimental investigations have been made to date. For the flow due to the gap-width variation, there have been many reports (Hayasaka, 1944; Jones and Wilson, 1975; Hamza and MacDonald, 1981; Elkouh, 1976; Hashimoto and Tsuji, 1975 and so forth). In addition Ishizawa (1966b, 1984) has developed a new theory of "multifold series expansion," which has succeeded in solving the Navier-Stokes equations under the comprehensive conditions covering arbitrary time-variations of the gap-width and sufficiently high Reynolds numbers. For the flow due to the central fluid source (that is, the radial outward flow between parallel disks), also much work has been done (Hagiwara, 1962; Savage, 1964; Woolard, 1957; Ishizawa, 1965 and 1966a; Wilson, 1972; Raal, 1978 and so on), and complicated flow behaviour including separation and reattachment at Reynolds numbers larger than some critical value has been predicted by theoretical analyses (Ishizawa, 1965 and 1966a; Wilson, 1972; Raal, 1978).

However, for the present flow phenomenon where the two types of flow due to the gap-width variation and the central fluid source coexist, the problem becomes so difficult that, as far as the authors know, neither any precise theoretical analysis nor detailed experimental investigation has been presented to date. The only existing theory (Hashimoto and Tsuji, 1975) is an approximate one in which a solution to the flow caused by the gap-width variation only is superposed linearly on another solution to the flow caused by the central fluid source only. In the latter solution the time-variation of the gap-width is treated as if it were changing extremely slowly, that is, quasi-statically.

When the aforementioned two types of flow coexist, they are essentially inconsistent with each other since the flow due to the gap-width variation is of the form $\bar{u} \propto r$ whereas that due to the central fluid source is of the form $\bar{u} \propto 1/r$, where $\bar{u}$ and r are the mean radial flow velocity and the radial coordinate respectively. And, as the Reynolds numbers of the two coexisting flows increase together, they interact in a complicated manner through the non-linear convective inertial forces. As a result, there does arise a phenomenon which can not be described by means of the approximate superposition theory (Hashimoto and Tsuji, 1975). This point will be the most important problem remaining untreated and awaiting solution in the analysis for the present unsteady flow.

At the start of the theoretical analysis, we shall set up the following restrictive conditions for simplicity of analysis.

First, we assume that the outer radius r_e of the disks is sufficiently large as compared with the inner radius r_0 of the central fluid-source pipe ($r_e/r_0 \gg 1$), and the gap width h is suf-

Contributed by the Fluids Engineering Division for publication in the JOURNAL OF FLUIDS ENGINEERING. Manuscript received by the Fluids Engineering Division October 29, 1986.

ficiently small compared with the disk sizes r_e and r_0 (h/r_e, $h/r_0 \ll 1$).

Secondly, we consider the case when the Reynolds numbers of the two coexisting flows are not too large, though they are not so small as the non-linear convective inertia effect can be neglected. In such a case, the inlet region of the radial source flow is usually limited to a narrow range close to the entrance of the gap, so that we may neglect it and carry out a precise analysis, throughout the whole flow field, by means of a method of asymptotic series expansion for large r, as will be shown later in Section 2.1.

And lastly, we treat the case when the rate of flow from the central source is retained unchanged throughout the time-variation of the gap-width. This case may be considered as a typical, fundamental model of the present flow phenomenon, since in practical applications this condition is often realized almost perfectly when the radial source flow is fed, for example, from a positive-displacement pump with a steep pressure-flow characteristic, or from a high-pressure fluid-reservoir through a high-resistance flow-control valve, and so forth.

In the present research, under the above-mentioned conditions, we develop a precise theoretical analysis based on the Navier-Stokes equations for the general case of arbitrarily time-varying gap width, by applying partly the theory of "multifold series expansion" (Ishizawa, 1982a, 1982b, 1983 and 1984) which has been developed chiefly for the steady, laminar boundary layers under arbitrary mainstream velocity distribution. And, at the same time, an experimental investigation was performed for the case of gap-width variation of reciprocating sinusoidal oscillation, from which we have been able to verify the validity and applicability of the theory.

2 Theoretical Analysis

2.1 Navier-Stokes Equations and Their Asymptotic Series Expansion. Let two parallel disks be in arbitrary motion normal to their own surfaces, where one of the two disks has a fluid-source pipe in its central portion. For simplicity, we assume here that only one disk, say the upper one, is in motion and the other (the lower one) is at rest, though similar analysis can be performed for the general case when both the disks are in motion independent of each other.

We introduce a system of stationary cylindrical coordinates (r, θ, y) as shown in Fig. 1. The Navier-Stokes equations and the equation of continuity for an axisymmetric and radial flow of an incompressible viscous fluid without extraneous force are,

$$\frac{\partial u}{\partial t}+u\frac{\partial u}{\partial r}+v\frac{\partial u}{\partial y}=-\frac{1}{\rho}\frac{\partial p}{\partial r}+\nu\left(\frac{\partial^2 u}{\partial r^2}+\frac{1}{r}\frac{\partial u}{\partial r}-\frac{u}{r^2}+\frac{\partial^2 u}{\partial y^2}\right) \tag{1a}$$

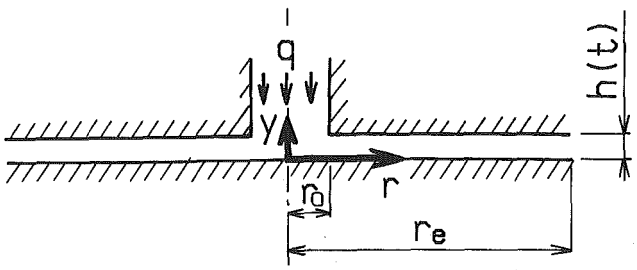

Fig. 1 Flow geometry and coordinate system

$$\frac{\partial v}{\partial t}+u\frac{\partial v}{\partial r}+v\frac{\partial v}{\partial y}=-\frac{1}{\rho}\frac{\partial p}{\partial y}+\nu\left(\frac{\partial^2 v}{\partial r^2}+\frac{1}{r}\frac{\partial v}{\partial r}+\frac{\partial^2 v}{\partial y^2}\right) \tag{1b}$$

$$\frac{\partial (ru)}{\partial r}+\frac{\partial (rv)}{\partial y}=0 \tag{1c}$$

where (u, v) are the velocity components in the (r, y) directions, respectively, p the pressure, ρ the density, and ν is the kinematic viscosity.

The boundary conditions are, with the arbitrarily varying gap-width denoted by $h(t) \geqq 0$,

$$u=v=0 \text{ at } y=0 \tag{2a}$$

$$u=0,\ v=dh/dt \text{ at } y=h(t) \tag{2b}$$

In the present problem, in addition to the conditions (2*a*) and (2*b*), we must simultaneously take into consideration the existence of a radial source flow at a constant flow rate (say q).

In the present research, taking these conditions into account, we have found out an original form of asymptotic series expansion with respect to r, which is valid in the region where r is sufficiently large. The basic idea of the expansion is as follows. It is known from many previous researches that the single flow caused by the gap-width variation can be expressed in the form $u = rf(y, t)$ provided that $(r_e/h) \gg 1$, while, in the single flow due to the central fluid source, u can be expanded for sufficiently large r in the following form of asymptotic series expansion:

$$u=a_1(y)/r+a_3(y)/r^3+a_5(y)/r^5+\cdots.$$

In the present problem, these two flows coexist. Therefore, one may naturally have an idea of combining the above-mentioned two expressions. The former expression, $u = rf(y, t)$, is proportional to r, and the latter asymptotic series expansion has a leading term of order r^{-1} and a common term-ratio proportional to r^{-2}. Therefore, formally the former expression just corresponds, accidentally and fortunately, to the next lower-order extension of the latter asymptotic series expansion. Thus, the combination of the two expressions can be performed without any conflict with the governing Navier-Stokes equations. In the present problem, the flow is unsteady so that the coefficients $a_1, a_3, a_5, \cdots$ will naturally become functions of y and t.

On the basis of the above idea, defining the non-dimensional variable

$$\eta=y/h(t) \tag{3}$$

in place of y, and arranging under dimensional-analytic consideration, we may formulate the asymptotic series expansions for the present problem in the following form:

$$u=-\frac{1}{2}\frac{\nu r}{h^2}\frac{\partial \phi(\eta,t)}{\partial \eta}+\frac{q_s}{hr}\frac{\partial F(\eta,t)}{\partial \eta}+\frac{q_s^2}{\nu r^3}\frac{\partial G(\eta,t)}{\partial \eta}+\cdots \tag{4a}$$

$$v=\frac{\nu}{h}\phi(\eta,t)+0+\frac{2q_s^2 h}{\nu r^4}G(\eta,t)+\cdots \tag{4b}$$

$$\frac{p}{\rho}=K(t)+\frac{\nu^2}{h^2}P_0(\eta,t)+\frac{\nu^2 r^2}{h^4}P_1(\eta,t)+\frac{\nu q_s}{h^3}\log\left(\frac{r}{r_e}\right)\cdot P_2(\eta,t)+\frac{q_s^2}{h^2 r^2}P_3(\eta,t)+\cdots \tag{4c}$$

where $K(t)$ is a constant of integration with respect to r and y to be determined later, and

$$q = 2\pi q_s = 2\pi r \int_0^h \left(u + \frac{1}{2} \frac{\nu r}{h^2} \frac{\partial \phi}{\partial \eta} \right) dy \tag{4d}$$

As is clear from the above explanation, in the right-hand side of (4*a*) the first term corresponds to the flow caused by the gap-width variation, while the second and the subsequent terms to the flow due to the central fluid source. The flow rate q is relevant only to the latter flow, that is, the second and the subsequent terms in (4*a*), so that q is expressed as (4*d*). The series expansions for u and v, (4*a*) and (4*b*), are in form which automatically satisfies the equation of continuity (1*c*).

Now, substituting (4*a*), (4*b*), and (4*c*) into the Navier-Stokes equations (1*a*) and (1*b*), and equating each sum of the coefficients with equal power of r to zero, we obtain the relations

$$\left.\begin{aligned}
&\frac{\partial^2 \phi}{\partial \eta^2} - (\phi - \alpha\eta)\frac{\partial \phi}{\partial \eta} + \alpha\phi - \frac{h^2}{\nu}\frac{\partial \phi}{\partial t} = \frac{\partial P_0}{\partial \eta} \\
&\frac{\partial^3 \phi}{\partial \eta^3} - (\phi - \alpha\eta)\frac{\partial^2 \phi}{\partial \eta^2} + \frac{1}{2}\left(\frac{\partial \phi}{\partial \eta}\right)^2 + 2\alpha\frac{\partial \phi}{\partial \eta} - \frac{h^2}{\nu}\frac{\partial^2 \phi}{\partial \eta \partial t} = -4P_1 \\
&\frac{\partial^3 F}{\partial \eta^3} - (\phi - \alpha\eta)\frac{\partial^2 F}{\partial \eta^2} + \alpha\frac{\partial F}{\partial \eta} - \frac{h^2}{\nu}\frac{\partial^2 F}{\partial \eta \partial t} = P_2 \\
&\frac{\partial^3 G}{\partial \eta^3} - (\phi - \alpha\eta)\frac{\partial^2 G}{\partial \eta^2} - \frac{\partial \phi}{\partial \eta}\frac{\partial G}{\partial \eta} + \frac{\partial^2 \phi}{\partial \eta^2} G - \frac{h^2}{\nu}\frac{\partial^2 G}{\partial \eta \partial t} + \left(\frac{\partial F}{\partial \eta}\right)^2 = -2P_3 \\
&\frac{\partial P_i}{\partial \eta} \equiv 0 : P_i \equiv P_i(t), \ (i = 1,2,3)
\end{aligned}\right\} \tag{5}$$

where

$$\alpha(t) = \frac{h}{\nu}\frac{dh}{dt} \tag{6}$$

As can be seen from the last relation of (5), P_1, P_2, and P_3 are all functions of t only and not of η, though in (4*c*) we have written them in more generalized forms of $P_1(\eta,t)$ and the like. Hence, it is possible to eliminate these P_1, P_2, and P_3 from the second to fourth equations of (5) by differentiating them with respect to η, and finally we obtain the following partial differential equations for $\phi(\eta,t)$, $F(\eta,t)$, $G(\eta,t)$, · · ·:

$$\left.\begin{aligned}
&\frac{\partial^4 \phi}{\partial \eta^4} - (\phi - \alpha\eta)\frac{\partial^3 \phi}{\partial \eta^3} + 3\alpha\frac{\partial^2 \phi}{\partial \eta^2} = \frac{h^2}{\nu}\frac{\partial^3 \phi}{\partial \eta^2 \partial t} \\
&\frac{\partial^4 F}{\partial \eta^4} - (\phi - \alpha\eta)\frac{\partial^3 F}{\partial \eta^3} - \left(\frac{\partial \phi}{\partial \eta} - 2\alpha\right)\frac{\partial^2 F}{\partial \eta^2} = \frac{h^2}{\nu}\frac{\partial^3 F}{\partial \eta^2 \partial t} \\
&\frac{\partial^4 G}{\partial \eta^4} - (\phi - \alpha\eta)\frac{\partial^3 G}{\partial \eta^3} - \left(2\frac{\partial \phi}{\partial \eta} - \alpha\right)\frac{\partial^2 G}{\partial \eta^2} + \frac{\partial^3 \phi}{\partial \eta^3} G = \frac{h^2}{\nu}\frac{\partial^3 G}{\partial \eta^2 \partial t} - 2\frac{\partial F}{\partial \eta}\frac{\partial^2 F}{\partial \eta^2}
\end{aligned}\right\} \tag{7}$$

subject to the boundary conditions

$$\left.\begin{aligned}
&\phi = \frac{\partial \phi}{\partial \eta} = F = \frac{\partial F}{\partial \eta} = G = \frac{\partial G}{\partial \eta} = 0 \text{ at } \eta = 0 \\
&\phi = \alpha(t), \ F = 1, \ \frac{\partial \phi}{\partial \eta} = \frac{\partial F}{\partial \eta} = G = \frac{\partial G}{\partial \eta} = 0 \text{ at } \eta = 1
\end{aligned}\right\} \tag{8}$$

2.2 Application of the Theory of "Multifold Series Expansion." In (7), the first equation which determines the function $\phi(\eta, t)$ corresponds to the flow caused by the gap-width variation. Previously, the same equation has been derived by Ishizawa (1966b and 1984) in the theoretical analysis for the unsteady flow between parallel disks with time-varying gap width, and he has succeeded in solving this equation on the basis of a new theory of "multifold series expansion," under the comprehensive conditions covering arbitrary time-variations of the gap-width and sufficiently high Reynolds numbers.

Meanwhile, the second and the subsequent equations which determine the functions $F(\eta,t)$, $G(\eta,t)$, · · · correspond to the flow due to the central fluid source. Here, it is noted that the important phenomenon of interaction between the two coexisting flows is expressed, in these equations, in terms of the cross products between the function ϕ and the functions F, G, · · ·, that is, $(\phi - \alpha\eta)\partial^3 F/\partial\eta^3$, $(\partial^3\phi/\partial\eta^3)G$, and so forth. Formally, these equations for F, G, · · · are analogous to the first one for ϕ in the sense that they are similarly of parabolic type and at the same time include $\alpha(t)$, an arbitrary known-function of the principal-axis variable t. Hence, it is expected that the above-mentioned new theory of "multifold series expansion" may be applied also to these equations for F, G, · · ·, as well as to the first one.

In the first place, according to Ishizawa's (1984) paper we change the time-variable t into the following nondimensional variable ζ, by which the time-differential operation in (7), $(h^2/\nu)(\partial/\partial t)$, is transformed into a standardized form of $\zeta(\partial/\partial\zeta)$ where $\zeta \geqq 0$;

$$\zeta = \exp\left[\int_{t_a}^{t} \frac{\nu d\tau}{h^2(\tau)}\right] \tag{9}$$

in which t_a is an arbitrary constant value of t. Of the above-mentioned "multifold series expansion" analyses (Ishizawa, 1966b and 1984), the former one (1966b) has not applied this transformation (9), and it gives a solution essentially equivalent to that of conventional small-perturbation analysis. In contrast with this, the latter one (1984), which is based on this transformation (9), has been proved to give a mathematically better-natured solution of more rapid, and larger radius of, series-convergence than the former and the conventional small-perturbation analysis, particularly for the cases of periodic gap-width variation at high Reynolds numbers and the like (for details, refer to the related papers mentioned above).

Now, with this variable ζ, we define the following infinite number of variable parameters $\{S_k\}_1^\infty$:

$$\left\{S_1 = \alpha, \ S_2 = \zeta\frac{d\alpha}{d\zeta}, \ S_3 = \zeta^2\frac{d^2\alpha}{d\zeta^2}, \ \cdots\right\} \tag{10}$$

where $S_1 = \alpha = \dfrac{h}{\nu}\dfrac{dh}{dt}$, $S_2 = \zeta\dfrac{d\alpha}{d\zeta} = \dfrac{h^3}{\nu^2}\dfrac{d^2h}{dt^2} + \left(\dfrac{h}{\nu}\dfrac{dh}{dt}\right)^2$, · · · ·

Then, in (7), the differential operation with respect to t is

decomposed into those with respect to these variable parameters $\{S_k\}_1^\infty$ as

$$\frac{h^2}{\nu}\frac{\partial}{\partial t}=\zeta\frac{\partial}{\partial\zeta}=S_2\frac{\partial}{\partial S_1}+(S_3+S_2)\frac{\partial}{\partial S_2}+\cdots \tag{11}$$

and the original time-variable t and its function $h(t)$ vanish from the system (7) and (8) [here note that $\alpha(t)=S_1$]. This means that the functions $\phi, F, G, \cdots$ have been transformed from the functions of (η, t) into those of $(\eta; S_1, S_2, S_3, \cdots)$, and consequently we may solve the system (7) and (8) by expanding the functions $\phi, F, G, \cdots$ in the following forms of "multifold series" of the independent variable parameters $\{S_k\}_1^\infty$:

$$\left.\begin{aligned}\phi=\quad & S_1\phi_1(\eta)+S_1^2\phi_{11}(\eta)+\cdots\\ &+S_2\phi_2(\eta)+\cdots\\ &+\cdots\end{aligned}\right\} \tag{12a}$$

$$\left.\begin{aligned}F=F_0(\eta)+S_1f_1(\eta)+S_1^2f_{11}(\eta)+\cdots\\ +S_2f_2(\eta)+\cdots\\ +\cdots\end{aligned}\right\} \tag{12b}$$

$$\left.\begin{aligned}G=G_0(\eta)+S_1g_1(\eta)+S_1^2g_{11}(\eta)+\cdots\\ +S_2g_2(\eta)+\cdots\\ +\cdots\end{aligned}\right\} \tag{12c}$$

In these "multifold series," the S_1-term belongs to the first order column, the S_1^2- and S_2-terms to the second, the S_1^3-, S_1S_2- and S_3-terms to the third and so forth, and the series terms belonging to a column are all of the same order of magnitude.

Here, according to Ishizawa (1984), it is possible, by introducing an arbitrary constant parameter α_0 into the multifold series expansions (12) in the form $S_1=(\alpha-\alpha_0)$ and adjusting its value at every instant of the gap-width variation, to obtain a solution of best-controlled convergence and as the result high accuracy throughout a wide range of the flow conditions. However, so far as we confine ourselves within the restrictive conditions described in Section 1, we may obtain accurate enough solutions even if this α_0 is not introduced, and besides even if the series solutions are truncated considerably shortly. Therefore, in (10), for simplicity we have put $\alpha_0\equiv 0$ and defined as $S_1=\alpha$.

Now, substituting (11) and (12) into (7) and (8), and equating the coefficients with like forms of variable parameters to zero, we obtain the following system of ordinary differential equations which determines the functions $\phi_1, \cdots, F_0, \cdots$ and $G_0, \cdots$:

$$\left.\begin{aligned}\phi_1''''&=0\\ \phi_{11}''''&=(\phi_1-\eta)\phi_1'''-3\phi_1''\\ \phi_2''''-\phi_2''&=\phi_1''\\ &\cdots\cdots\end{aligned}\right\} \tag{13a}$$

$$\left.\begin{aligned}F_0''''&=0\\ f_1''''&=(\phi_1-\eta)F_0'''+(\phi_1'-2)F_0''\\ f_{11}''''&=\phi_{11}F_0'''+\phi_{11}'F_0''+(\phi_1-\eta)f_1'''+(\phi_1'-2)f_1''\\ f_2''''-f_2''&=\phi_2F_0'''+\phi_2'F_0''+f_1''\\ &\cdots\cdots\end{aligned}\right\} \tag{13b}$$

$$\left.\begin{aligned}G_0''''&=-2F_0'F_0''\\ g_1''''&=(\phi_1-\eta)G_0'''+(2\phi_1'-1)G_0''-\phi_1'''G_0\\ &\quad-2(F_0'f_1''+F_0''f_1')\\ g_{11}''''&=\phi_{11}G_0'''+2\phi_{11}'G_0''-\phi_{11}'''G_0+(\phi_1-\eta)g_1'''\\ &\quad+(2\phi_1'-1)g_1''-\phi_1'''g_1\\ &\quad-2(F_0'f_{11}''+F_0''f_{11}'+f_1'f_1'')\\ g_2''''-g_2''&=\phi_2G_0'''+2\phi_2'G_0''-\phi_2'''G_0\\ &\quad+g_1''-2(F_0'f_2''+F_0''f_2')\\ &\cdots\cdots\end{aligned}\right\} \tag{13c}$$

$$\left.\begin{aligned}&\phi_1=\phi_1'=F_0=F_0'=Y=Y'=0 \text{ at } \eta=0\\ &\phi_1=F_0=1,\ \phi_1'=F_0'=Y=Y'=0 \text{ at } \eta=1\end{aligned}\right\} \tag{14}$$

where Y represents every function except ϕ_1 and F_0.

As can be seen, $\phi_1, \cdots, F_0, \cdots$ and $G_0, \cdots$ are all functions of η alone, being free from any other factors related to the individual, actual flow conditions (hence we call them the "universal coefficient-functions"). Consequently, if once these equations have been solved, the results can be applied universally for all kinds of, and arbitrary, time-variations of the gap-width.

Although analytical solutions to the system (13) and (14) exist, their actual derivations are lengthy and laborious, especially for higher-order functions. Therefore, in the present research we have solved this system (13) and (14) numerically by means of Runge-Kutta-Gill's method. Fourteen places (decimal digits) in significant figure of arithmetic operation were retained throughout the computation, and the step size applied was 0.00025.

The important results are shown in Table 1 and Fig. 2. In Table 1, the notation Z represents every universal coefficient-function, and the relations $Z\eta\eta(0)=-Z\eta\eta(1)$ and $Z\eta\eta\eta(0)=Z\eta\eta\eta(1)$ result from the symmetry of the radial-flow velocity profile.

Here, to examine the accuracy of the above numerical solutions, we solved by hand analytically exactly a part of the equations in (13) and (14), that is, those for ϕ_1, F_0, f_1, G_0, and g_1: for example, the exact solution for g_1 is obtained as

$$g_1=\frac{1}{46200}\eta^2-\frac{1}{5775}\eta^3+\frac{1}{140}\eta^4-\frac{9}{350}\eta^5-\frac{1}{100}\eta^6$$
$$+\frac{33}{175}\eta^7-\frac{107}{280}\eta^8+\frac{149}{420}\eta^9-\frac{17}{105}\eta^{10}+\frac{34}{1155}\eta^{11}$$

Table 1 Universal numerical values related to the fundamental flow characteristics (the notation Z represents every universal coefficient-function)

Function	Value of the function	
	$Z\eta\eta(0)=-Z\eta\eta(1)$	$Z\eta\eta\eta(0)=Z\eta\eta\eta(1)$
ϕ_1	6.00000	-1.20000×10^{1}
ϕ_{11}	-2.71429×10^{-1}	3.34286
ϕ_2	9.92936×10^{-2}	-1.19859
F_0	6.00000	-1.20000×10^{1}
f_1	-8.57143×10^{-2}	1.37143
f_{11}	-5.90600×10^{-4}	5.94310×10^{-3}
f_2	4.72104×10^{-4}	-2.35710×10^{-3}
G_0	-1.71429×10^{-1}	1.54286
g_1	4.32900×10^{-5}	-1.03896×10^{-3}
g_{11}	-1.39316×10^{-6}	-6.24817×10^{-5}
g_2	2.14597×10^{-6}	1.27623×10^{-5}

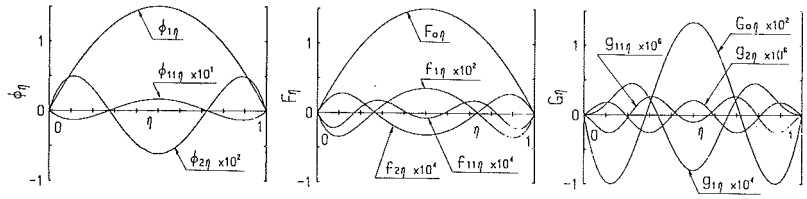

Fig. 2 Solutions of the universal coefficient-functions (1st order derivatives): (*a*) ϕ-family; (*b*) F-family; (*c*) G-family

and therefore $g_1''(0) = -g_1''(1) = 1/23100 = 4.3290043 \times 10^{-5}$ and $g_1'''(0) = g_1'''(1) = -2/1925 = -1.0389610 \times 10^{-3}$. The numerical results in Table 1 are in fine agreement with these exact values: the similar perfect agreements are also attained for other functions of ϕ_1, F_0, f_1 and G_0. From these results, it may be inferred that a satisfactorily high accuracy is retained throughout all the numerical solutions obtained in this research.

2.3 Solutions to the Fluid Pressure and the Hydrodynamical Force. In (4*c*), the coefficient functions P_0, P_1, P_2 and P_3 are determined, by applying (8) to the first to fourth equations of (5), as

$$\left.\begin{aligned} P_0(\eta,t) &= \left[\frac{\partial\phi}{\partial\eta} - \frac{1}{2}\phi^2 + \alpha\eta\phi - \frac{h^2}{\nu}\int_0^\eta \frac{\partial\phi}{\partial t}\,d\eta\right] \\ P_1(t) &= -\frac{1}{4}\left(\frac{\partial^3\phi}{\partial\eta^3}\right)_{\eta=0} = -\frac{1}{4}\left(\frac{\partial^3\phi}{\partial\eta^3}\right)_{\eta=1} \\ P_2(t) &= \left(\frac{\partial^3 F}{\partial\eta^3}\right)_{\eta=0} = \left(\frac{\partial^3 F}{\partial\eta^3}\right)_{\eta=1} \\ P_3(t) &= -\frac{1}{2}\left(\frac{\partial^3 G}{\partial\eta^3}\right)_{\eta=0} = -\frac{1}{2}\left(\frac{\partial^3 G}{\partial\eta^3}\right)_{\eta=1} \end{aligned}\right\} \quad (15)$$

Here, P_0 and P_1 are both determined by the function ϕ, and therefore they are of the same order of magnitude. However, comparison of magnitudes of the P_0- and P_1-terms in (4*c*) gives

$$\left[\frac{\nu^2 r^2}{h^4}P_1 \Big/ \frac{\nu^2}{h^2}P_0\right] = O\left[\left(\frac{r}{h}\right)^2\right]$$

so that the P_0-term becomes negligible in the region where $(r/h) \gg 1$. Accordingly, under the first restrictive condition presented in Section 1, it is permissible to disregard it throughout the whole flow field from $r = r_0$ to $r = r_e$.

Next, the integration constant $K(t)$ in (4*c*) may be determined under the following approximate boundary conditions at the outer edge of the disks (Ishizawa, 1966b), in which the drop of the static pressure at $r = r_e$, when the external fluid is inhaled into the gap, is taken into consideration.

$$\left.\begin{aligned} &p = p_e \text{ when } \bar{u}_e \geqq 0 \\ &p = p_e - \frac{1}{2}\rho\bar{u}_e^2 \text{ when } \bar{u}_e < 0 \end{aligned}\right\} \text{ at } r = r_e \quad (16)$$

where p_e denotes the pressure of the external uniform fluid at rest, and $\bar{u}_e$ is the mean radial flow velocity at $r = r_e$ and given by

$$\bar{u}_e = \frac{q_s}{r_e h} - \frac{1}{2}\frac{r_e}{h}\frac{dh}{dt} \quad (17)$$

From what is stated above, the pressure of fluid flow within the gap where $r_e \geqq r \geqq r_0$, say p_1, is given finally as

$$[p_1(r,t) - p_e] = \frac{\rho\nu^2 r_e^2}{h^4}\left(\frac{r^2}{r_e^2} - 1\right)P_1 + \frac{\rho\nu q_s}{h^3}\log\left(\frac{r}{r_e}\right)\cdot P_2 + \frac{\rho q_s^2}{h^2 r_e^2}\left(\frac{r_e^2}{r^2} - 1\right)P_3 - \frac{j}{2}\rho\bar{u}_e^2 \quad (18)$$

$$\text{where } j = \begin{cases} 0 \text{ when } \bar{u}_e \geqq 0 \\ 1 \text{ when } \bar{u}_e < 0 \end{cases}$$

For the fluid pressure acting on the disk surface in the central portion where $r_0 > r \geqq 0$, say p_2, we may estimate it approximately on the following assumptions:

(*a*) In the region where $r_0 > r \geqq 0$, since flow passage is much wider and therefore fluid motion is generally much slower and besides flow path is considerably shorter than those in the gap, the flow may be considered free from viscous friction.

(*b*) In the spatial domain (r, y) where $r_0 > r \geqq 0$ and $h(t) \geqq y \geqq 0$, the mean radial flow velocity is proportional to r.

(*c*) In the region where $r_0 > r \geqq 0$, the flow may be considered to be quasi-steady, so that the Bernoulli's equation for steady flow is applicable to it.

Generally speaking, these assumptions may be considered to hold with enough validity. Moreover, the error due to them, even if not negligible, does not affect so much the total hydrodynamical force acting on the disk surface, because the area of the central region relevant to these assumptions is, from the first restrictive condition in Section 1, $r_0 \ll r_e$, very small compared with that of the whole disk surface.

On the above-mentioned assumptions, we write the Bernoulli's equation as

$$p_0 + \frac{1}{2}\rho\bar{u}_0^2 \cong p_2 + \frac{1}{2}\rho\bar{u}_0^2\left(\frac{r}{r_0}\right)^2 \quad (19)$$

where p_0 and $\bar{u}_0$ denote, respectively, the pressure and the mean radial flow velocity at the inner edge of the disk, $r = r_0$. Here, p_0 is given by putting $r = r_0$ in (18), and $\bar{u}_0$ by replacing r_e with r_0 in (17). Finally, the pressure p_2 is given approximately as

$$p_2(r,t) \cong p_1(r_0,t) + \frac{\rho}{2}\left(\frac{q_s}{r_0 h} - \frac{1}{2}\frac{r_0}{h}\frac{dh}{dt}\right)^2\left(1 - \frac{r^2}{r_0^2}\right) \quad (20)$$

Next, the hydrodynamical force acting on the disk surface, W, is given by the formula

$$W = 2\pi\int_0^{r_e}(p - p_e)r\,dr \quad (21)$$

We divide this into two parts, W_1 for $r_e \geqq r \geqq r_0$ and W_2 for $r_0 > r \geqq 0$, corresponding to the fluid pressures p_1 and p_2. By substituting (18) into (21) in which the lower limit of the definite integral is replaced by r_0, W_1 is given as

$$W_1 = -\pi\rho\left(\frac{\nu^2 r_e^4}{2h^4}\sigma_1 P_1 + \frac{\nu q_s r_e^2}{2h^3}\sigma_2 P_2 + \frac{q_s^2}{h^2}\sigma_3 P_3 + \frac{j}{2}r_e^2\bar{u}_e^2\sigma_4\right) \quad (22)$$

$$\left.\begin{aligned}\sigma_1 &= 1-2(r_0/r_e)^2+(r_0/r_e)^4\\ \sigma_2 &= 1-(r_0/r_e)^2+2(r_0/r_e)^2\log(r_0/r_e)\\ \sigma_3 &= 1-(r_0/r_e)^2+2\log(r_0/r_e)\\ \sigma_4 &= 1-(r_0/r_e)^2\end{aligned}\right\}. \tag{23}$$

Similarly, W_2 is given as

$$W_2 \cong \pi r_0^2\left[\left(p_1(r_0,t)-p_e\right)+\frac{\rho}{4}\left(\frac{q_s}{r_0 h}-\frac{1}{2}\frac{r_0}{h}\frac{dh}{dt}\right)^2\right] \tag{24}$$

2.4 Nondimensional Expressions for the Pressures and the Hydrodynamical Forces. We define the nondimensional quantities for the fluid pressure p and the hydrodynamical force W, respectively, as

$$p_* = \frac{h_m^4(p-p_e)}{\rho\nu^2 r_e^2} \tag{25}$$

$$W_* = \left(\frac{h_m}{r_e}\right)^4 \frac{W}{\rho\nu^2} \tag{26}$$

where h_m denotes the representative gap-width. These forms may be considered most suitable for the present flow problem. In conformity with these definitions, the expressions (18), (20), (22), and (24) given in the preceding section are transformed respectively into the following nondimensional formulas.

$$p_{1*} = (r_*^2-1)\frac{P_1}{h_*^4}+R_q(\log r_*)\frac{P_2}{h_*^3} + R_q^2\left(\frac{1-r_*^2}{r_*^2}\right)\frac{P_3}{h_*^2}-\frac{j}{2h_*^2}\left(R_q-\frac{S_1}{2h_*}\right)^2 \tag{27a}$$

$$p_{2*} \cong p_{1*}\left(r_*=\frac{r_0}{r_e},t\right)+\left(\frac{r_e}{r_0}\right)^2\left(\frac{1}{2h_*^2}\right) \times\left\{R_q-\frac{1}{2}\left(\frac{r_0}{r_e}\right)^2\frac{S_1}{h_*}\right\}^2\left\{1-\left(\frac{r_e}{r_0}\right)^2 r_*^2\right\} \tag{27b}$$

$$W_{1*} = -\frac{\pi}{2}\left[\sigma_1\frac{P_1}{h_*^4}+R_q\sigma_2\frac{P_2}{h_*^3}+2R_q^2\sigma_3\frac{P_3}{h_*^2} +j\frac{\sigma_4}{h_*^2}\left(R_q-\frac{S_1}{2h_*}\right)^2\right] \tag{28a}$$

$$W_{2*} \cong \pi\left[\left(\frac{r_0}{r_e}\right)^2 p_{1*}\left(r_*=\frac{r_0}{r_e},t\right)+\frac{1}{4h_*^2}\cdot \times\left\{R_q-\frac{1}{2}\left(\frac{r_0}{r_e}\right)^2\frac{S_1}{h_*}\right\}^2\right] \tag{28b}$$

$$\text{where } j=\begin{cases}0 \text{ when } (S_1/2h_*)\leqq R_q\\ 1 \text{ when } (S_1/2h_*)>R_q\end{cases}$$

$$r_*=r/r_e,\ h_*=h/h_m,\ R_q=h_m q_s/\nu r_e^2$$

3 Discussion for the Interaction Phenomenon Between the Two Coexisting Flows

In the first place, we shall consider the two limit cases, one when $q = 0$ and the other when $h(t) \equiv$ const..

In the present solutions given above, when $q = 0$ and $h(t) \neq$ const., the terms related to the functions $F, G, \cdots$ all disappear, and only the term relevant to the function ϕ remains. As stated before, this condition corresponds to the flow caused by the gap-width variation only, that is, the flow between parallel disks with a time-varying gap width.

On the other hand, when $h(t) \equiv$ const. and $q \neq 0$, all the variable parameters $\{S_k\}_1^\infty$ defined in (10) become zero, and it follows from (12) that $\phi \equiv 0$, $F \equiv F_0(\eta)$, $G \equiv G_0(\eta)$, $\cdots$. This condition corresponds to the flow due to the central fluid source only, that is, the radial source flow between parallel disks with a constant (or quasi-statically, slowly varying) gap-width. An asymptotic series solution of the Navier-Stokes equations for this flow which is valid in the downstream region where $(r/h) \gg 1$ was first given by Savage (1964), and the present solution with $\phi \equiv 0$, $F \equiv F_0(\eta)$, $G \equiv G_0(\eta)$, $\cdots$ just coincides with it.

Now, consider the general case when $q \neq 0$ and simultaneously $h(t) \neq$ const.. In this case, all the universal coefficient-functions in the present multifold series solutions (12), that is, $\{\phi_1, \phi_{11}, \phi_2, \cdots\}$, $\{F_0, f_1, f_{11}, f_2, \cdots\}$, $\{G_0, g_1, g_{11}, g_2, \cdots\}$ and so forth, become relevant to the flow characteristics.

In the meantime, the approximate "superposition theory" explained in Section 1 gives a solution to this general case by combining linearly the aforementioned two limit cases. This is essentially equivalent to taking up, in the present series solutions, the unversal coefficient-functions of $\{\phi_1, \phi_{11}, \phi_2, \cdots\}$, $\{F_0\}$, $\{G_0\}$, $\cdots$, and to neglecting those of $\{f_1, f_{11}, f_2, \cdots\}$, $\{g_1, g_{11}, g_2, \cdots\}$, $\cdots$, as can be seen from what is stated above. This immediately means that the interaction phenomenon between the two coexisting flows is represented in terms of the universal coefficient-functions $\{f_1, f_{11}, f_2, \cdots\}$, $\{g_1, g_{11}, g_2, \cdots\}$, $\cdots$.

Thus, we have succeeded in solving analytically the important interaction problem, which has not been clarified to date, in most general form which is constructed with the universal coefficient-functions and the variable parameters $\{S_k\}_1^\infty$, where $\{S_k\}_1^\infty$ totally include information about the flow conditions and the way the gap-width changes. From the form of the present solution itself, we can understand and forecast with good visibility the essential mechanism of the flow phenomenon and the variation of the flow characteristics corresponding to the change in flow conditions. This is an important merit of the present analytical approach which can not be achieved by any numerical method.

Next, we shall examine quantitatively the difference between the results given by the approximate superposition and the present theories.

From a hydrodynamical point of view, the interaction phenomenon may be considered to grow stronger and stronger as the two kinds of the Reynolds numbers corresponding to the two coexisting flows increase together, under the condition that the two flows are kept in a balance of comparable strength. From the expression for mean radial flow velocity in the gap

$$\bar{u} = -\frac{1}{2}\frac{r}{h}\frac{dh}{dt}+\frac{q_s}{hr} \tag{29}$$

it follows that the two coexisting flows are of comparable strength when

$$\frac{1}{2}\frac{r}{h}\left|\frac{dh}{dt}\right| \cong \frac{q_s}{hr},\ \therefore\ \frac{1}{2}\frac{r_*^2}{h_*}\left|S_1\right| \cong R_q \tag{30}$$

Now, as a concrete example we consider the case of sinusoidally oscillating gap-width variation:

$$h(t) = h_m(1+a\sin\omega t) \tag{31}$$

where ω is the angular frequency and $1 > a \geqq 0$. Upon substituting (31) into (10), it can be seen that the flow characteristics in this case are governed by the following three parameters; that is, two kinds of the Reynolds numbers

$$R_\omega = h_m^2 \omega / \nu \tag{32}$$

$$R_q = h_m q_s / \nu r_e^2 \tag{33}$$

and the nondimensional amplitude a. And, in (30), $|S_1| = O(aR_\omega)$; the time-mean of h_* is unity; and the mean value of r_* may be considered to be approximately $1/\sqrt{2}$ since this radial position divides the disk surface into two (inner and outer) parts of equal areas. Consequently, the condition of comparable strength of the two coexisting flows, (30), becomes in this case as

$$\frac{1}{4}(aR_\omega) \cong R_q \tag{34}$$

Taking this (34) into account, typically we put $a = 0.4$ and set the following three couples of the values $\{R_\omega, R_q\}$:

(a) $(aR_\omega)/4 > R_q$: $\{R_\omega = 25,\ R_q = 0.5\}$

(b) $(aR_\omega)/4 = R_q$: $\{R_\omega = 25,\ R_q = 2.5\}$

(c) $(aR_\omega)/4 < R_q$: $\{R_\omega = 5,\ R_q = 2.5\}$

And, with these values we evaluate the two solutions, the present series solution itself (say "present solution") and the other (say "simple solution") in which the terms involving the functions $\{f_1, f_{11}, f_2, \cdots\}$, $\{g_1, g_{11}, g_2, \cdots\}$, $\cdots$ are ignored. From what is stated before, this "simple solution" is essentially equivalent to that given by the approximate superposition theory explained in Section 1. The difference between these two solutions indicates directly the effect of the interaction between the two coexisting flows. The results for the hydrodynamical force W_* are shown in Figs. 3(a), (b), and (c).

As can be seen from these figures, the difference between the two solutions becomes most remarkable in Fig. 3(b), that is, when $(aR_\omega)/4 = R_q$. This fact justifies the conjecture described above.

Next, in Fig. 3(d), a result obtained from the experimental investigation which will be described in detail in the next chapter is shown, for a case of $(aR_\omega)/4 \cong R_q$, together with the theoretical results of the two solutions.

As can be seen, while the simple solution which does not take account of the interaction produces a remarkable error, the present solution which takes it into consideration agrees very well with the experimental result. This fact just demonstrates the validity of the present theory.

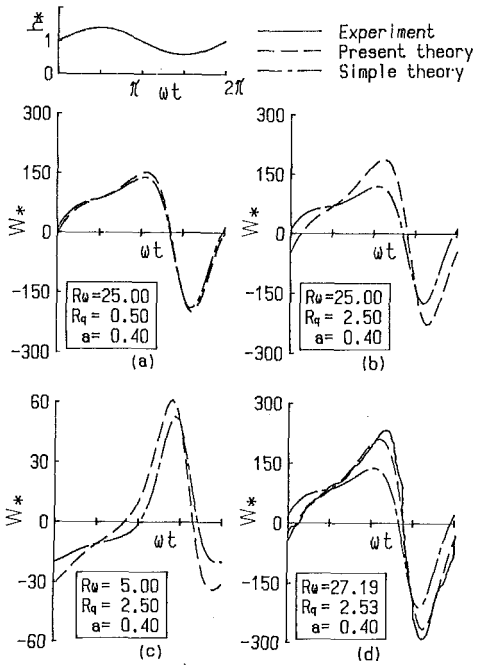

Fig. 3 Comparison between the present and the approximate superposition theories: the results of the nondimensional force W_* for the case of sinusoidally oscillating gap-width variation [in (d) an experimental result is shown together]

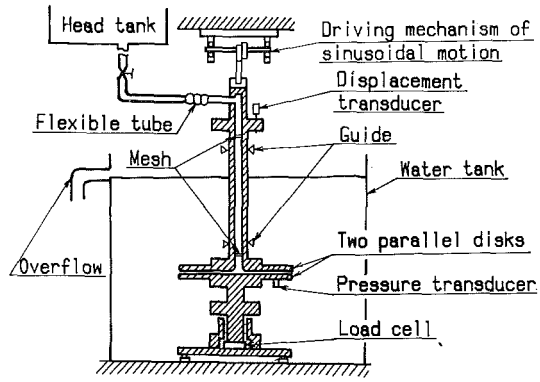

Fig. 4 Schematic diagram of the experimental setup

4 Experimental Investigation

The new theory developed in Section 2 covers the general case that the gap width $h(t)$ changes arbitrarily with time, providing that $h(t)$ is infinitely differentiable and the restrictive conditions described in Section 1 are satisfied. In this chapter, as a typical example we consider the particular case of sinusoidally oscillating gap-width variation, a fundamental type of flow in practical applications. Experiments for measurements of the fluid pressures and the hydrodynamical force acting on the disk surface were performed, and the validity of the new theory was examined and confirmed by comparing the theory with the experimental results.

4.1 Experimental Apparatus and Methods. The experimental setup used in the present research is shown schematically in Fig. 4. The working fluid, water, was supplied from a head-tank through a flow-control valve and two fine wire-screens into a test section formed by two parallel disks. The test section was set submerged within a water-tank. The water levels of the head-tank and the water-tank were kept constant respectively by overflow devices, and the difference head between the both levels was 12m. In this fluid-supply system, since the resistance of the flow-control valve installed in the flow passage was extremely higher than that of the test section, the rate of radial source flow between the parallel disks could be retained almost perfectly constant, not being affected by the gap-width variation.

A mechanism converting rotation into reciprocating motion, which was driven by a variable-speed electric motor, was used to oscillate sinusoidally the upper disk of the test section.

The two circular disks, which formed the test section, were made of 15mm-thick transparent plastic plates with 300mm outer diameter ($2r_e$). The upper disk had in its central portion a fluid-source pipe with 30mm inner diameter ($2r_0$). Therefore, in the present experiments $r_0/r_e = 0.1$, which fulfills the first restrictive condition in Section 1. Sharp edge at the central opening in the upper disk was rounded off in 2mm radius, in order to keep off flow separation from there. The water-tank, in which the above-mentioned test section was set submerged, was of 670 mm water-depth and 700 mm × 700 mm bottom sizes and sufficiently larger than the test section, so that the fluid flow within the test section was almost completely unaffected by the existence of the water-tank walls.

The time-varying gap width between the two disks, the fluid pressures and the hydrodynamical force acting on the lower-

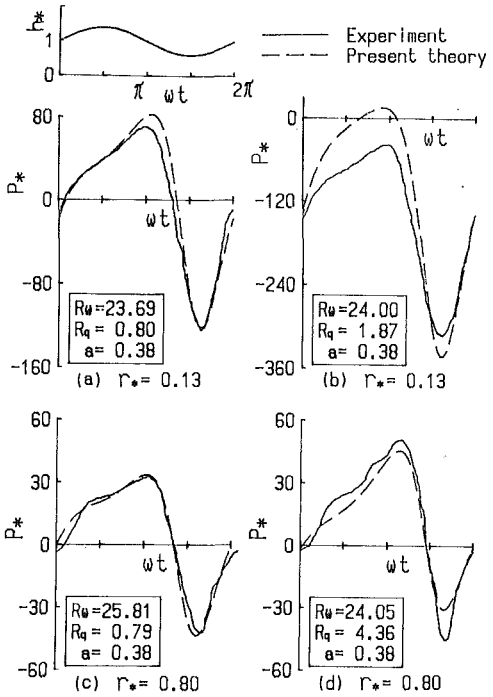

Fig. 5 Theoretical and experimental results of the fluid pressures for the case of sinusoidally oscillating gap-width variation: (*a*) and (*b*) $r_* = 0.13$; (*c*) and (*d*) $r_* = 0.80$

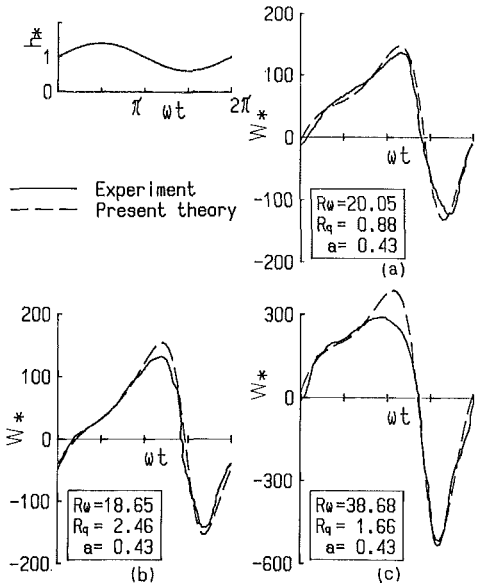

Fig. 6 Theoretical and experimental results of the hydrodynamical forces for the case of sinusoidally oscillating gap-width variation

disk surface, were measured respectively by a displacement transducer (capacitor type), pressure transducers (waterproofed, strain-gauge type; capacity of 0.02 MPa) and a load cell (waterproofed, strain-gauge type; capacity of 490 N). The outputs from these transducers were amplified and, after low-pass-filtered to cut off high-frequency noises from the electric motor and other disturbing sources, recorded on a data recorder and then fed to a pen recorder to obtain final results. The load cell was supported and protected by a precisely-made sliding guide, which was sufficiently low resistant for axial forces to be measured but extremely high rigid for any other possible lateral forces. The fluid pressures were measured on the lower-disk surface at five positions of r = 20, 30, 50, 80, and 120 mm, the respective positions being on different radial rays at angular intervals of 60 deg. In this experimental study, the mean gap-width h_m was varied between 1 and 2 mm, the amplitude ah_m between 0.5 and 1.0 mm and the frequency $(\omega/2\pi)$ between 0.5 and 3.0 Hz.

Uncertainty of the present experimental data mainly depends upon the measuring accuracy of the gap width, fluid pressure, force and flow rate. From an uncertainty analysis, the measured nondimemsional flow-characteristic quantities shown in Figs. 3(*d*), 5, 6, and 7, that is, W_*, p_*, h_*, R_q, and R_ω, are estimated to have the uncertainties less than ± 5 percent, ± 11 percent, ± 3 percent, ± 2 percent, and ± 2 percent respectively.

4.2 Experimental Results and Comparison With the Theory. The sinusoidally oscillating gap-width $h(t)$ is expressed as (31). As has already been pointed out, the flow characteristics in this case are governed by the three parameters, that is, two kinds of the Reynolds numbers R_ω and R_q defined respectively by (32) and (33) and the non-dimensional amplitude a.

In the present research, measurements were carried out for various sets of values of these parameters (R_ω, R_q, a). Some representative results are shown in Fig. 5 for the fluid pressures and in Figs. 6 and 3(*d*) for the hydrodynamical forces. In the figures, the theoretical results of the new series solutions given in Section 2 are also displayed.

It can be seen from examination that the present new series solutions agree very well with the experimental results over the range in which the series solutions are rapidly convergent. Namely, in the cases of Figs. 3, 5(*a*), 5(*c*), 6(*a*), and 6(*b*), the solutions are rapidly convergent and really good agreements are attained between the theory and the experiments. On the other hand, in the cases of Figs. 5(*b*), 5(*d*), and 6(*c*), the solutions are found to be no longer rapidly convergent and correspondingly some disagreements begin to appear.

Thus, there is naturally a finite range of applicability for the present finitely-truncated series solutions. Therefore, for the convenience of application, we have provided a practical guide which indicates roughly the range of applicability, by comparing the theory with the many experimental results obtained through this experimental investigation. Some examples are shown in Fig. 7.

4.3 Discussion for Convergence and Validity of the Solutions. In the present case of sinusoidally oscillating gap-width variation, the magnitudes of the variable parameters (10) are $|S_k| = O(aR_\omega{}^k)$, so that, in the multifold series expansions (12), the ratio of the neighbouring two columns is generally proportional to $O(R_\omega)$. Accordingly, the rate of convergence of these multifold series expansions lowers as R_ω increases. Meanwhile, in the asymptotic series expansions (4), the ratio of the neighbouring two terms is proportional to $O(R_q/r_*^2)$, except those involving the special irregular terms, that is, the terms with the function $\phi[=O(\alpha)]$, the second (null) term in (4*b*) and the P_0- and P_2-terms in (4*c*). Therefore, as a general rule the rate of convergence of these asymptotic expansions lowers as (R_q/r_*^2) increases, or, in other words, as r_* decreases under a condition of constant R_q.

In the region of small r_*, the above-mentioned tendency of series-convergence with respect to (R_q/r_*^2) does not necessarily correspond directly to the degree of agreement of theory with experiment, because in the present theory the existence of the inlet region of radial outward flow has not been taken into consideration: however, at least qualitatively this tendency can be observed actually in the results presented in the preceding section. For example, in comparison of Figs. 5(*b*) and 5(*d*), the difference between theory and experiment in Fig. 5(*b*) where $r_* = 0.13$ is larger than that in Fig. 5(*d*) where $r_* = 0.80$, though R_q in Fig. 5(*b*) is lower than that in Fig. 5(*d*). Also, in Fig. 7(*a*), the range of R_q in which the theory is valid reduces with decreasing r_*.

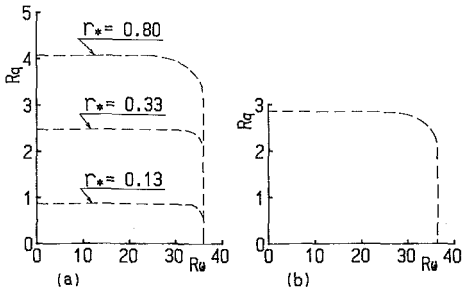

Fig. 7 Range of applicability of the solutions for the case of sinusoidally oscillating gap-width variation: (a) pressure (a = 0.38); (b) force (a = 0.43)

Next, in Fig. 7, in the R_ω-direction the range of applicability can be expanded widely by extending the multifold series expansions (12) to higher orders, or/and, following Ishizawa's new concept (1984), by introducing an adjustable parameter α_0 into the multifold series expansions (12) in the form $S_1 = (\alpha - \alpha_0)$, the parameter α_0 which by adjusting its own value forces the series to converge always as rapidly as possible. Meanwhile, in the R_q-direction the range of applicability may also be expanded to a certain degree by extending the asymptotic expansions (4) to higher orders, but for this much effect can not be expected because in the present theory the entrance-flow near the gap-inlet has not been taken into consideration to begin with. More precise analysis for the flow near the gap-inlet will be an important future problem awaiting solution.

5 Conclusions

A theoretical analysis and experimental results have been presented for the unsteady laminar flow of an incompressible fluid between parallel disks with a time-varying gap width and a central fluid source of constant flow-rate.

New series solutions to the Navier-Stokes equations are obtained, making use of a technique of asymptotic series expansion in the radial direction and on the basis of a new theory of "multifold series expansion" (Ishizawa, 1982a, 1982b, 1983, 1984) with respect to the time variable. The solutions cover the general case of arbitrarily time-varying gap width $h(t)$ even at high Reynolds numbers, provided that $h(t)$ is infinitely differentiable and the restrictive conditions described in Section 1 are satisfied. Moreover, the solutions can describe precisely the important interaction phenomenon between the two coexisting flows, one caused by the gap-width variation and the other due to the central fluid source. This interaction phenomenon is produced through the non-linear convective inertial forces, and its complicated characteristics have not been made clear up to date: the present theory is the first to throw light upon it.

Next, as a typical example, the particular case of sinusoidally oscillating gap-width variation was taken up, and the experiments for measurements of the fluid pressures and the hydrodynamical force acting on the disk surface were carried out. From comparison of the theory with the experiments, the validity of the new theory has been verified. The solutions given by the new theory agree well with the experimental results even in severe cases when the approximate "superposition theory" explained in Section 1 which neglects the interaction effect produces a remarkable error.

Finally, in connection with the present research, it will be an important problem to perform a more precise analysis for the flow in the region of small radii $r_*(= r/r_e)$. Also, another possible extension of the present work will be to analyze the more complicated case that the radial source-flow rate q varies arbitrarily with time, as well as the gap width between the two disks.

Acknowledgment

The authors thank Messrs. M. Ashino and T. Hattori for their efforts to construct the experimental setup, and also Messrs. Y. Nishimura and I. Katagiri for their assistance in carrying out the experiments.

References

Elkouh, A. F., 1976, "Fluid Inertia Effects in Non-Newtonian Squeeze Films," ASME *Journal of Lubrication Technology*, Vol. 98, pp. 409–411.

Hagiwara, T., 1962, "Studies on the Characteristics of Radial Flow Nozzle (1st/2nd/3rd/4th Report)," *Bulletin of the JSME*, Vol. 5, pp. 656–663/663–668/668–675/676–683.

Hamza, E. A., and MacDonald, D. A., 1981, "A Fluid Film Squeezed Between Two Parallel Plane Surfaces," *Journal of Fluid Mechanics*, Vol. 109, pp. 147–160.

Hashimoto, K., and Tsuji, S., 1975, *Transactions of the JSME*, Vol. 41, pp. 210–221 (in Japanese).

Hayasaka, H., 1944, Researches of the NTT (Japan telephone and telegraph) Electrotechnical Laboratory, Report No. 467.

Ishizawa, S., 1965, "The Axi-Symmetric Laminar Flow in an Arbitrarily Shaped Narrow Gap (1st Report)," *Bulletin of the JSME*, Vol. 8, pp. 353–367.

Ishizawa, S., 1966a, "The Axi-Symmetric Laminar Flow in an Arbitrarily Shaped Narrow Gap (2nd Report)," *Bulletin of the JSME*, Vol. 9, pp. 86–103.

Ishizawa, S., 1966b, "The Unsteady Laminar Flow Between Two Parallel Discs with Arbitrarily Varying Gap Width," *Bulletin of the JSME*, Vol. 9, pp. 533–550.

Ishizawa, S., 1982a, "A New Multifold Series General Solution of the Steady, Laminar Boundary Layers (1st Report)," *Bulletin of the JSME*, Vol. 25, pp. 1703–1716.

Ishizawa, S., 1982b, "A New Multifold Series General Solution of the Steady, Laminar Boundary Layers (2nd Report)," *Bulletin of the JSME*, Vol. 25, pp. 1717–1728.

Ishizawa, S., 1983, "A New Multifold Series General Solution of the Steady, Laminar Boundary Layers (3rd Report)," *Bulletin of the JSME*, Vol. 26, pp. 2081–2090.

Ishizawa, S., 1984, "A New Theory and its Extensive Application of the Multifold Series Expansion Analysis for the Boundary Layer Equations," *Bulletin of the JSME*, Vol. 27, pp. 432–442.

Jones, A. F., and Wilson, S. D. R., 1975, "On the Failure of Lubrication Theory in Squeezing Flows," ASME *Journal of Lubrication Technology*, Vol. 97, pp. 101–104.

Raal, J. D., 1978, "Radial Source Flow Between Parallel Disks," *Journal of Fluid Mechanics*, Vol. 85, pp. 401–416.

Savage, S. B., 1964, "Laminar Radial Flow Between Parallel Plates," ASME *Journal of Applied Mechanics*, Vol. 31, pp. 594–596.

Wilson, S. D. R., 1972, "A Note on Laminar Radial Flow Between Parallel Plates," *Applied Science Research*, Vol. 25, pp. 349–354.

Woolard, H. W., 1957, "A Theoretical Analysis of the Viscous Flow in a Narrowly Spaced Radial Diffuser," ASME *Journal of Applied Mechanics*, Vol. 24, pp. 9–15.

Turbulent Separated and Reattached Flow Over a Curved Surface

J. M. Serpa
Graduate Research Assistant.

R. C. Lessmann
Professor Mechanical Engineering.

W. M. Hagist
Professor Mechanical Engineering.

University of Rhode Island,
Kingston, RI

An experimental investigation of two-dimensional separated and reattached turbulent flow has been carried out in a wind tunnel. The test surface consisted of a five to one, length to height, polynomial curve having zero slope and curvature at both ends. Data were taken at reference speeds of 9.1 m/s (30 f/s) and 15.2 m/s (50 f/s). Surface mean pressure distributions and fluctuations were measured. The pressure coefficient was found to agree with a potential flow prediction up to 40 percent of the chord. Significant pressure fluctuations were observed well upstream of separation. Velocity profiles, profile scaling parameters, and integral thickness variations were also measured. Intermittency measurements, i.e., the fraction of time that reversed flow existed at a place, showed that both the separation point and reattachment point wandered over about 30 percent of the chord. Nowhere in the separated region was the intermittency found to be 100 percent. Wall shear stress distributions were measured from upstream of separation to downstream of reattachment.

Introduction

Flow separation is an inevitable consequence whenever a momentum deficient boundary layer encounters a sufficiently large pressure gradient. This is a very common situation in flows of real engineering interest and phenomena associated with it often dominate the flow field and its interaction with material objects.

New contributions in this field are continually appearing both on the analytical/numerical side and from experimental studies. Examples of recent theoretical work are the study of Whitfield et al. [1] and the dissertation by D. Das [2]. Whitfield et al. developed a finite difference based method where the viscous near surface calculations are coupled to an inviscid description of the outer stream. These authors employed an empirical correlation between the energy and momentum shape factors as a closure for their computational scheme. The profile data from this study compares well with their correlation.

In contrast, Das used an integral analysis based on a velocity profile model composed of an inner law-of-the-wall and an outer polynomial wake. These were scaled with the local skin friction in such a way that the profiles can exhibit reversed flow.

Two recent experimental studies are by Kline et al. [3] and Buckles et al. [4]. Kline examined a significant body of available data for turbulent separation and concluded that, unlike in the laminar case, turbulent flows separate over a broad region of the surface and show a high degree of intermittency. From the collected data, they developed a correlation between shape factor and displacement thickness for the point of incipient separation. Buckles et al. used a laser doppler anemometer to study turbulent separated and reattached flow over a large-amplitude wavey surface.

The most comprehensive body of experimental information on this problem is contained in the series of papers published by Simpson and his coworkers from the mid 70s to the early 1980s [5–10]. This basic work was done in a wind tunnel whose test section dimensions were comparable to those used in the present study. A principal difference is that these earlier investigations focussed only on boundary layer separation and an appropriate test flow was achieved by contouring the upper wall of their wind tunnel which imposed a pressure gradient on the flat bottom wall where measurements were taken. In this study, which also includes data through reattachment, measurement were taken on a curved surface as required by the projects sponsor. Another difference is that Simpson's flow was tripped by a step at the leading edge of his test surface while here the turbulent boundary layer was grown naturally.

Simpson et al. measured mean flow characteristics but were primarily interested in the turbulent structure of separating flows. They measured turbulent shear stress, eddy speeds, turbulent spectra, dissipation lengths, bursting frequencies and the spanwise variations of such turbulent quantities [5, 6]. They also investigated higher order turbulence correlations [7], transverse velocity variations [8], effects of free stream unsteadiness [9], and frequency effects on periodic unsteady free stream flows [10].

The work reported here was conducted over a period of twelve months on a very limited budget. The specifically man-

Contributed by the Fluids Engineering Division of THE AMERICAN SOCIETY OF MECHANICAL ENGINEERS and presented at the AIAA/ASME Fluids Engineering Meeting, Atlanta, Ga., May 1986. Manuscript received by the Fluids Engineering Division May 23, 1986.

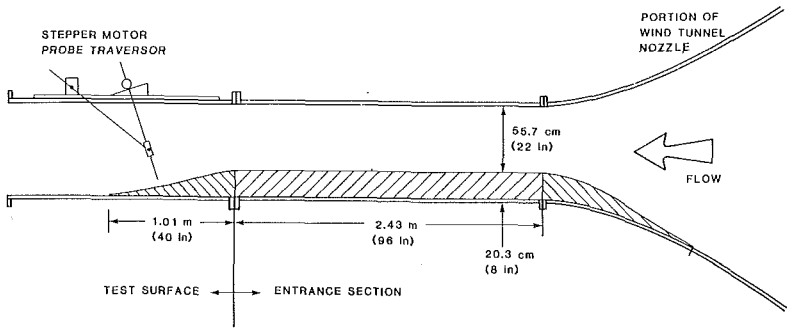

Fig. 1 Schematic representation of wind tunnel and test surface

dated goals of the project were to obtain mean velocity data and directly measured surface shear stress values starting upstream of separation and proceeding downstream through the reattachment point. Simpson et al. used a two channel laser anemometer for most of their measurements. This type of instrumentation was not available to the present project so a new, simplier and less expensive approach was needed to retrieve the required data from the highly intermittent separated flow region. Standard hot wire anemometers and surface hot films, which were available, could not be directly employed because they are normally incapable of detecting flow direction. These problems were solved by the development of a specially designed dual port pressure probe used to measure both velocity profiles and flow directional intermittency. Such an instrument, if used with a conventional manometer would not be adequate or reliable. However by coupling it to a differential electronic pressure transducer and monitoring the output with an on-line microcomputer an instrumentation system with a sufficiently high frequency response and sensitivity was achieved. The capabilities of the differential pressure probe and micro computer were also used to interpret the sign to be assigned to the output of an inexpensive glue-on surface hot film, calibrated in a separate pipe flow facility, to give fluctuating surface shear stress.

Experimental Setup and Procedure

The experiment was conducted in a low speed, open circuit wind tunnel, consisting of a fifteen to one contraction ratio entrance nozzle, followed by a 4.27m (14f) of 0.775 m (30.5 in) square test section, a transition section and an axial flow, speed-controlled, fan. This wind tunnel was modified as shown in Fig. 1. The false floor, upstream fairing in the entrance nozzle and test surface were all made of 3.175 mm (1/8 in.) thick PVC sheet. The contour of the test surface, which was 1.02 m (40 in) along the base and 20.3 cm (8 in) high, is given by the equation

$$y/H = 1 - 0.08(X/H)^3 + 0.24(X/H)^4 - 0.00192(X/H)^5$$

The surface slope and curvature of the test surface were zero at both ends.

Surface pressure ports were located 5.1 cm (2 in.) apart in the test surface and the downstream floor, and 6.2 cm (2.44 in.) apart in the upstream section. These pressure ports consisted of faced off lengths of 1.37 mm (0.054 in.) ID, 1.83 mm (0.072 in.) OD stainless steel tubing, pressed into predrilled holes. Measurements were made using a 100 Torr Barocel-Datametrics electronic manometer connected to these pressure ports through a 23 port Scanivalve pressure switch, via Tygon tubing. An on-line Apple IIe computer was used to sample the analog output voltage from the manometer.

Mean velocity profiles were made with a dual port pressure probe. This probe consisted of two lengths of 1.83 mm (0.072 in.) OD tubing, silver soldered together and sealed at one end. Holes 0.406 mm (0.016 in.) in diameter were drilled in each tube 0.305 mm (0.012 in.) from the sealed end. These holes were positioned such that, in the final assembly, they were 180 degrees apart and oriented in line with the flow (see insert Fig. 2). Positioning of the probe was done with a DISA 52B01 sweep drive unit and a 52C01 stepping motor system that gives a positional accuracy of 0.1 mm (0.0039 in.). In operation, the upstream tap sees a higher pressure than the downstream tap. This allowed for the determination of both speed and flow direction. Because of the flow pattern around the probe, neither the upstream nor the downstream port measures the real stagnation or static pressure, making it necessary to calibrate the probe against a standard Pitot Tube.

Figure 2 shows the probe calibration curve. The least

Nomenclature

C_p = pressure coefficient, $(P-P_0)/(\rho U^2/2)$
f = pipe friction factor
H = initial height of test surface
H_c = energy shape factor Θ^*/Θ
H_m = momentum shape factor δ^*/θ
I = intermittency
L = base length of test surface
n = number of samples
P = pressure
Re = pipe Reynolds number
S_P = standard deviation of wall pressure
U = velocity
X = distance along base of test surface
Y = position in boundary layer, perpendicular to test surface
y = local height of test surface
Δ = difference
δ = boundary layer thickness
δ^* = boundary layer displacement thickness

$$\delta^* = \delta \int_0^1 (1 - U/U_e)dy/\delta$$

Θ = boundary layer momentum thickness

$$\Theta = \delta \int_0^1 U/U_e(1 - U/U_e)dy/\delta$$

Θ^* = boundary layer energy thickness

$$\Theta^* = \delta \int_0^1 U/U_e(1 - (U/U_e)^2)dy/\delta$$

τ = shear stress

Subscripts

0 = reference value at start of test surface
c = position halfway between test surface and top of wind tunnel
e = edge of boundary layer

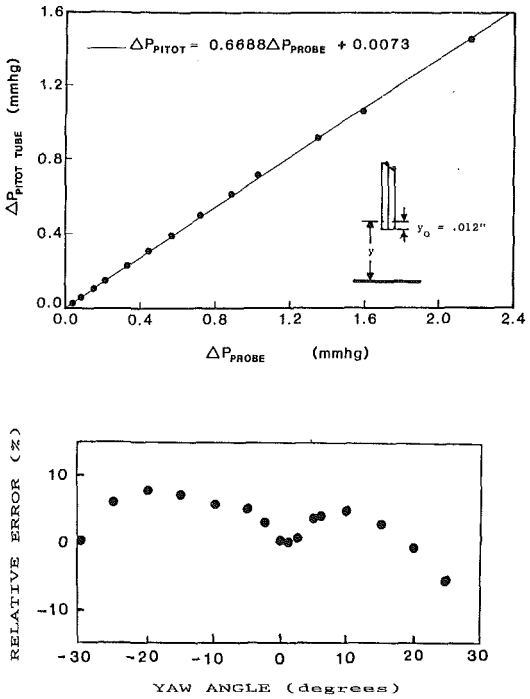

Fig. 2 Calibration data for dual port pressure probe and yaw angle misalignment error

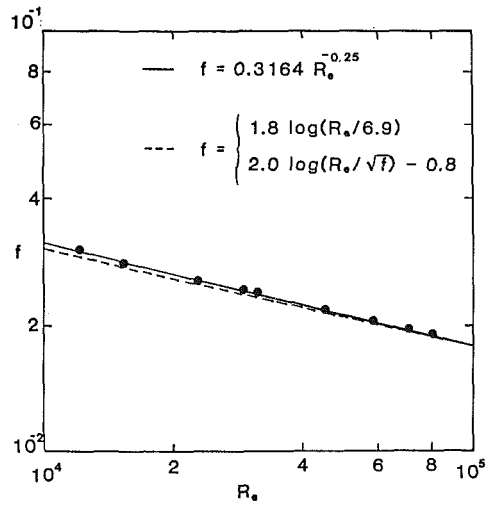

Fig. 3 Measured friction factors in calibration pipe compared to standard Reynolds number correlations

squares regression line has a correlation coefficient of 0.9997. Uncertainty in calculating a velocity using this result is less than 0.2 percent due primarily to uncertainties in measured values of atmospheric temperature and pressure. This figure also shows the relative error possible due to probe yaw angle misalignment which is less than 5 percent for angles within 10 deg of the flow direction. Surface proximity also has an influence on the probes reading. By measuring a number of velocity profiles in a fully developed turbulent boundary layer it was found that such effects cause consistent deviations above the law of the wall for $y+$ values less than 50. If necessary this can be accounted for by methods similar to those used to correct near wall hot wire measurements.

Details of this calibration are given in [11]. For both the experiment as well as the calibration runs, data was gathered with the same manometer – micro computer set up as described previously. Velocity fluctuations were measured directly during the experiment by calculating the speed corresponding to each sampled pressure difference and then treating the resulting set of velocity samples statistically.

Shear stress measurements along the surface were made with calibrated DISA R47 glue – on hot film probes. These consist of 0.5 micrometer thick, 1 mm long and 0.2 mm wide nickel sensors, mounted on a plastic film with attached copper leads. Measurements were made with a DISA 55D01 anemometer unit connected to the on-line micro computer.

As pointed out by both Sandborn [12] and Ramaprian et al. [13] nonlinear averaging error complicates the calibration and use of flush mounted hot film gages. This was compensated for by a new and simpler approach than used previously by these other investigators. Details of this, together with full documentation on the design of the pipe flow facility used to calibrate the hot films can be found in [11]. Verification data from this facility which are presented as Fig. 3 showed that it produced friction factors which were within 2 percent of standard correlations.

Care must be taken when interpreting the output of a surface mounted hot film sensor in separated flows since these devices are insensitive to flow direction. In this experiment a sign was attached to each shear stress measurement depending upon the flow direction deduced from the velocity probe. For this purpose, the probe was placed so that its tip was in the same transverse plane as the film sensor but displaced 1.27 cm (0.5 in.) spanwise. Switching between input channels to the microcomputer was fast enough to make the two successive readings essentially simultaneous. In this way, the proper sign could be given to each measured shear stress before the sample was averaged. Samples of 2000 values were collected with a sampling frequency of 20 hertz. Data for flow intermittency were obtained simultaneously. Intermittency is defined as the fraction of time, at a given position, that the flow direction is opposite to the free stream and was determined from knowledge of the sign of the pressure difference from the velocity probe.

It is always difficult to prove that a flow is essentially two-dimensional when in reality it is being created in a three-dimensional duct such as a wind tunnel. This question was addressed in the present study to the extent that time and the available instrumentation permitted. In addition to the primary set of surface pressure taps located on the center line of the test surface several arrays of span wise taps both upstream of separation and in the separation zone were installed. Negligible differences were observed between data from these and the centerline measurements over the central 30 percent of the test surface. Off centerline velocity profiles were also taken at these locations and agreed with the centerline profiles within the precision error of the instrumentation. Also the surface was fitted with an array of woolen thread tufts. These clearly showed the separation and reattachment zones to be in qualitative agreement with the measured intermittency profile and did not reveal the presence of any large three-dimensional flow effects. Since the primary emphasis of this study was on time average properties of a separating and reattaching boundary layer these were taken to be a sufficient indication of two-dimensionality. In addition the geometric characteristics of the tunnels test section is similar to that used in other two dimensional studies such as by Simpson et al. [5].

Experimental Results and Discussion

Surface Pressure Variation. The variation of the pressure coefficient along the surface for both reference speeds is shown in Fig. 4. Also shown is the result of a theoretical prediction of the pressure variation obtained from a boundary-element potential flow code [14]. Since potential

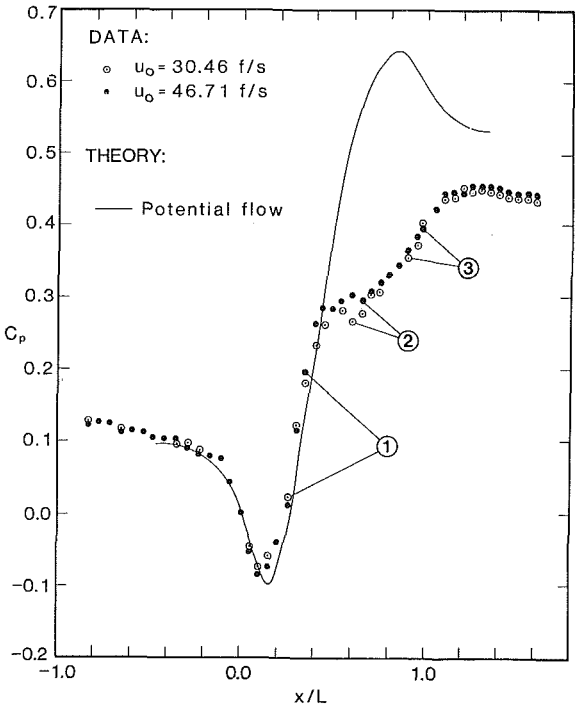

Fig. 4 Variation of surface pressure coefficient (relative uncertainty in $C_p = 0.8$ percent at 20:1 odds)

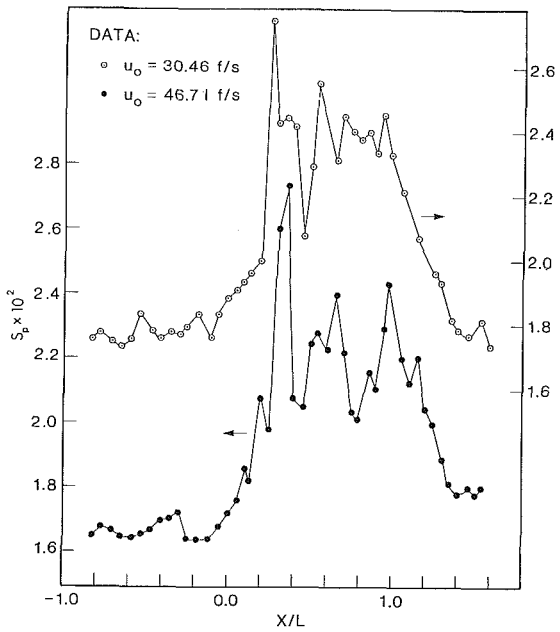

Fig. 5 Standard deviation of pressure coefficient data

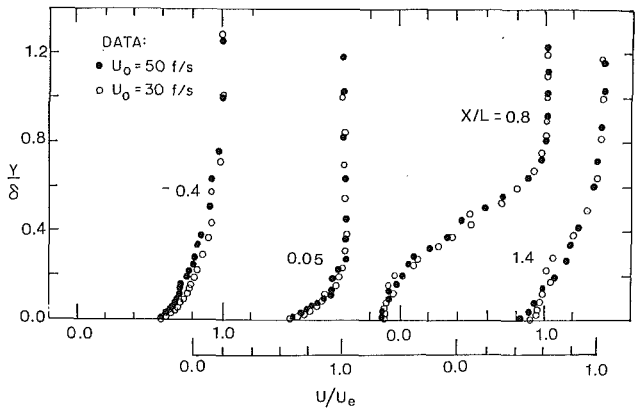

Fig. 6 Velocity profile development (relative uncertainty in $U = 5$ percent, in δ between 5 and 10 percent, in $y \pm 0.2$ mm at 20:1 odds)

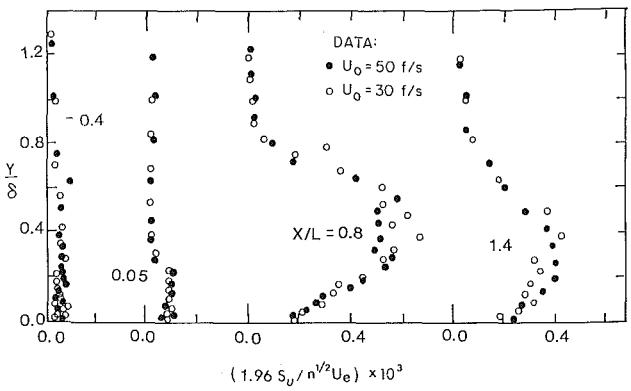

Fig. 7 Standard error of velocity profile data

flow cannot predict the frictional pressure drop in the constant area entrance section of the wind tunnel, the theoretical results were arbitarily matched to the data at the start of the test surface ($X/L = 0.0$). The agreement between the theoretical prediction and the data is extremely good between about $X/L = -0.4$ to $X/L = 0.45$.

Just before the start of the test surface, at an X/L of about -0.1, both the data and the theory show a marked decrease in pressure, corresponding to a sharp near-wall acceleration of the flow. The agreement in this region between the data and the potential flow theory indicates that such accelerations are purely a kinematic and geometric effect, independent of either viscous or turbulent boundary layer interactions.

At an X/L of about 0.15 the opening up of the area cross section of the wind tunnel begins to effect the flow. To satisfy mass conservation the average velocity begins to decrease while the surface pressure rises sharply. The data agree well with the potential flow theory up to about $X/L = 0.45$. Observation of woolen tufts taped to the surface showed the flow starting to separate at about this point. Downstream of this, after a small decrease, the pressure rises linearly up to about $X/L = 0.95$. The surface mounted tufts showed this point to be slightly downstream of the reattachment point for either speed. Beyond X/L of 1.0, the pressure continues to rise until about $x/L = 1.3$, after which, due to viscous effects in the exit duct, it begins to fall.

This pressure signature in the separated region is typical of two dimensional separated flows, and has been observed on blunt flat plates [15], rectangular cylinders [16, 17], and in the flow over a wavy surface [4].

Figure 5 displays the standard deviation of the surface pressure measurements and shows essentially identical patterns of unsteadiness for both speeds, leading to the conclusion that these are real effects of the flow rather than random influences or precision errors. For either speed, the fluctuation level is rather small and essentially constant in the entrance section. Once the flow reached the test surface, the fluctuation level increased dramatically, peaking at an X/L of approximately 0.30. The pressure coefficients that correspond to these first peaks in the standard deviation are labeled with a 1 on Fig. 2. As can be seen, these points are well upstream of the point where the average pressure shows any significant departure from the potential flow predictions.

This "early" activity in the boundary layer is indicative of

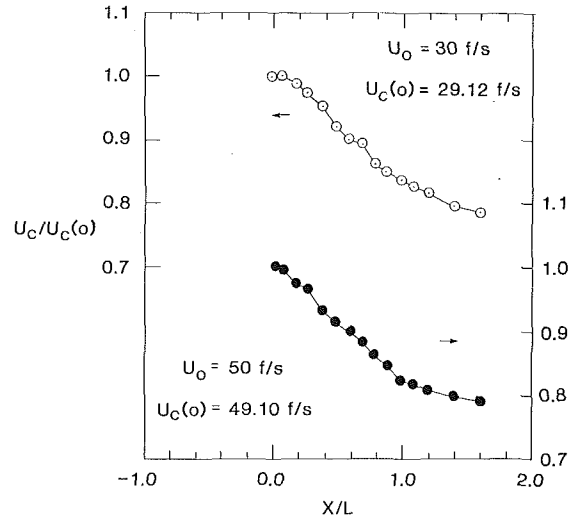

Fig. 8 Normalized free stream velocity variation (relative uncertainty in $U_c \approx 5$ percent at 20:1 odds)

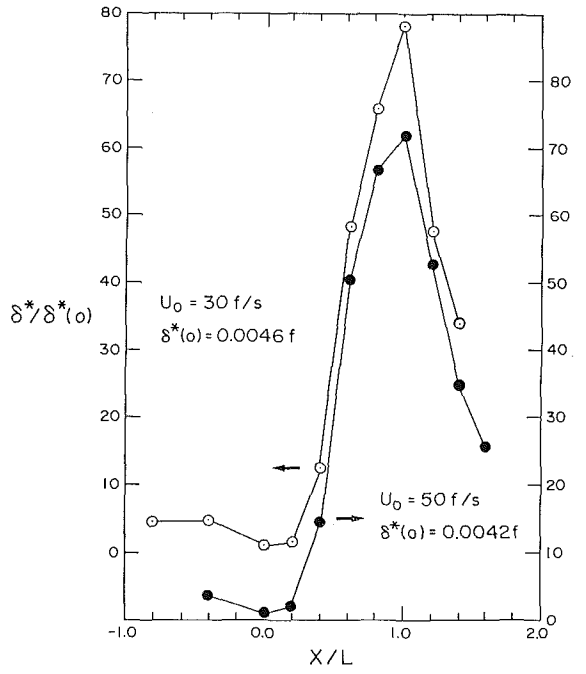

Fig. 9 Variation of boundary layer displacement thickness (relative uncertainty in δ^* between 5.5 percent and 11.2 percent at 20:1 odds)

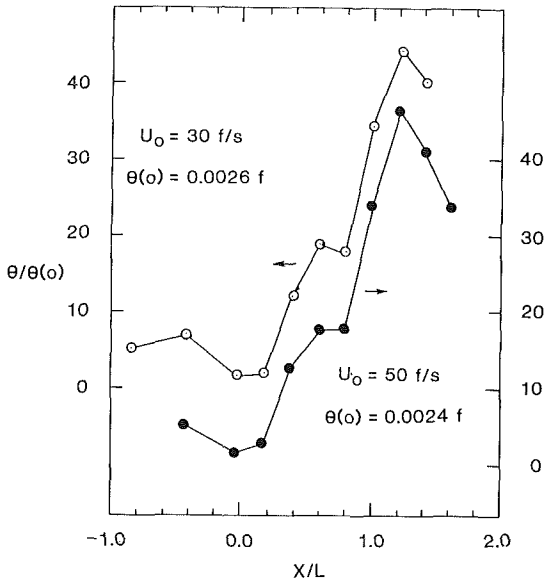

Fig. 10 Variation of boundary layer momentum thickness (relative uncertainty in θ between 5.5 percent and 11.2 percent at 20:1 odds)

the fact that turbulent separation is a process, extending over some considerable chord length of the surface [3-5] unlike the sharp local nature of laminar separation. For each reference velocity, two additional peaks in the unsteadiness of the surface pressure coefficient are recognizable on Fig. 3. These peaks occur at an X/L of around 0.6 and 1.0 and the corresponding pressure coefficients are labeled with a 2 and a 3 on Fig. 4. These three points will be referred to again when discussing the results for intermittency.

Velocity Profiles. Velocity profiles were measured at positions ranging from $X/L = -0.8$ to $X/L = 1.6$ for the two reference speeds. Figures 6 and 7 show a progression of the velocity profiles and their associated standard errors. The standard error is a 95 percent confidence limit equal to 1.96 times the standard deviation divided by the square root of the size of the data sample (here 2000 points).

The first profile, at $X/L = -0.4$, shows the typical shape of the profiles as the flow approaches the test surface. The level of velocity fluctuations, as indicated by the associated standard error, is almost constant throughout the boundary layer, finally dropping at the free stream. The next profile, at $X/L = 0.05$, shows the acceleration of the near wall flow. At $X/L = 0.8$, a recirculation bubble has been established. The level of velocity fluctuations shows an almost eight fold increase compared to those associated with the first profile. The last profile at $X/L = 1.4$, shows the flow once again fully reattached. A turbulent boundary layer is being reestablished and the shear layer, as seen from the standard error profile, is slowly disappearing. Additional profile data are included in [11].

Figure 8 shows the variation of the velocity midway between the test surface and the top of the wind tunnel for both reference speeds.

Figures 9 and 10, show the variation of the normalized boundary layer displacement thickness and momentum thicknesses, respectively. The normalized boundary layer energy thickness varied in much the same way as the momentum thickness ratio being 10 percent lower on the average.

The displacement thickness falls slightly in the accelerating flow near the start of the test surface and then rises dramatically throughout the separated flow peaking at nearly eighty times its initial value at reattachment. It then falls precipitously in the exit duct. The momentum and energy thicknesses also fall initially and then rise through separation plateauing in the middle of the separation bubble. They then rise to reattachment reaching forty times their initial value before falling again.

Further validation for these profile measurements and integral thickness calculations is provided on Fig. 11. This figure compares the correlation between the boundary layer energy and momentum shape factors as adopted by Whitfield et al. [1] with the present data. Agreement is seen to be excellent except for the two points representing the reattachment profiles ($x/L = 1.0$) for both test speeds. These data are extremely sensitive to profile details near the free-stream since reattaching profiles have zero slope and an inflection point near the surface. It turns out that in both these cases profile data taking was terminated before actually reaching the free-stream. As these profiles were at the end of the test surface where it meets

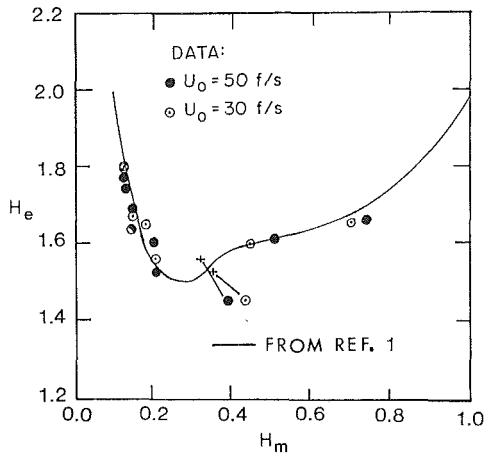

Fig. 11 Correlation between boundary layer energy and momentum shape factors

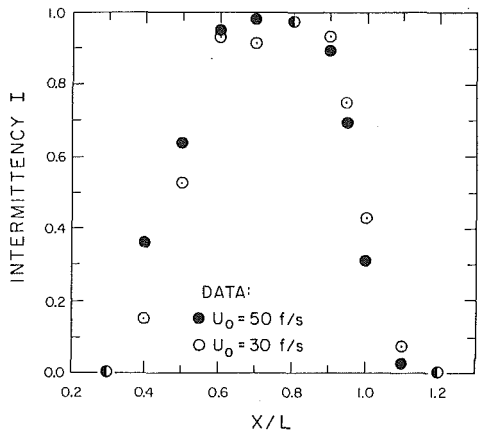

Fig. 12 Intermittency variation

the bottom of the wind tunnel, the tunnel half width and centerline velocities where added to the profile data sets as a correction. This fully explains the discrepancy as it moves the data in question to the positions marked with crosses on Fig. 9.

Surface Shear Stress Variation and Intermittency. Intermittency, I, is defined as the fraction of time at a certain surface position that the local flow is opposite to that in the free stream. Therefore, intermittency in an attached flow is zero; it rises during the process of separation and approaches one in a fully separated flow region. Figure 12 displays the intermittency data for both reference speeds. Upstream of $X/L = 0.3$ the flow is fully attached in both cases. From this point to X/L approximately 0.6, intermittency steadily increases reaching a value in the vicinity of 0.95. Intermittency remains essentially constant at this value up to $X/L = 0.8$, at which point it starts steadily decreasing, reaching zero again at $X/L = 1.2$. The fact that the intermittency never reaches 1.0 indicates that nowhere in the separated region is the flow in the reversed direction one hundred percent of the time. This result has also been observed by other investigators [4, 5], and is indicative of the unsteady nature of turbulent flow separation.

A precise meaning can now be given to the terms separation and reattachment. They will be taken to be the points where intermittency is exactly 0.5, or where the flow is in the reverse direction exactly half the time. These points have been estimated from the data shown on Fig. 12. Separation and reattachment occur at $X/L = 0.49$ and 0.99, respectively, for

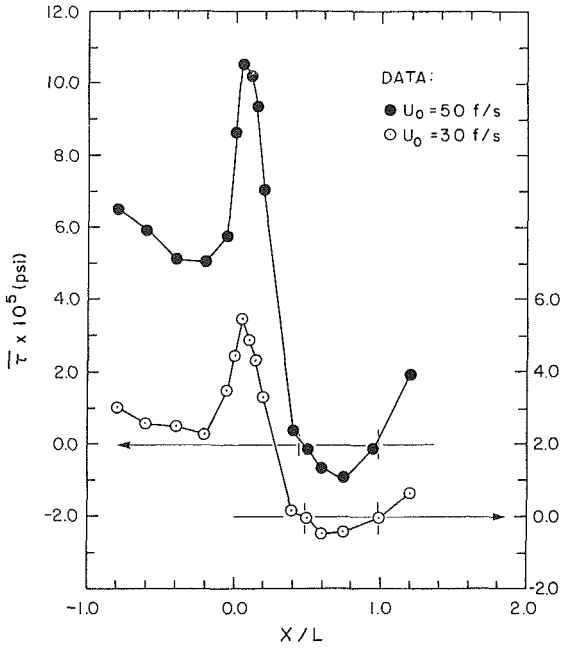

Fig. 13 Variation of surface shear stress (relative uncertainty in τ between 2 percent and 8 percent at 20:1 odds)

the 9.1 m/s (30 f/s) reference speed and at $X/L = 0.44$ and 0.97 for the 15.2 m/s (50 f/s) data.

It is interesting to note that the first peak in the fluctuations of the surface pressure coefficient, the point labeled 1 on Fig. 4, correspond approximately to the place where intermittency first deviates from zero. The second peaks on the same graph, labeled with a 2, correspond to the place where intermittency first reaches the plateau value of 0.95. Finally, the third peaks occur around the reattachment point.

Surface shear stress data is presented in Fig. 13. As can be seen, the shear stress distribution follows the same pattern for both flow velocities, those at 15.2 m/s (50 f/s) being, generally, double those at 9.1 m/s (30 f/s). In both cases, the wall shear stress falls in the entrance section up to $X/L = -0.2$. This is the place at which the near wall flow first experiences a favorable pressure gradient and begins to accelerate. Correspondingly, the local shear stress rises sharply, peaking at $X/L = 0.0$. This is somewhat upstream of the minimum in the pressure coefficient curve and flow at this place is still accelerating. From $X/L = 0.0$ the shear stress falls sharply toward separation, becomes negative, reaches a minimum and then rises again through reattachment.

As a rough verification of these results, shear stresses for $X/L = -0.40$ were calculated from the velocity profiles using a Clauser plot. The results obtained were 8 percent lower for the reference velocity of 9.1 m/s (30 f/s), and 6 percent higher for 15.2 m/s (50 f/s). For both sets of data, on Fig. 13 the ratio of the maximum negative stress to the maximum positive stress is about 1 to 10. The estimated positions of separation and reattachment from the intermittency data are also shown on Fig. 13. These are seen to be in very close agreement with the points of zero mean shear.

Error Analysis

The relative error for the surface pressure coefficient was estimated by propagating the instrumentation manufacturer's claimed accuracy of 0.25 percent for a pressure measurement. The result is a general uncertainty of less than plus or minus 0.8 percent. The surface pressure precision uncertainty calculated from the measured data samples and proportional to the standard deviation plotted on Fig. 3 was found to be negligible by comparison.

The source of maximum possible error for the velocity probe was found to be due to probe misalignment. For a probe yaw of less than 10 degrees, the error was experimentally shown to be less than plus or minus 5 percent as shown on Fig. 2. Again precision errors were negligible by comparison. These are equal to the standard errors shown on Fig. 5.

The maximum relative error for the boundary layer thickness was estimated to be less than plus or minus 5 percent for profiles made in the recirculation region, and less than plus or minus 10 percent for the ones made in the remaining regions. This error was estimated based on half the distance between the two last data points in the boundary layer profile, the error being smaller for the recirculation region because of better resolution in these profiles near the edge of the boundary layer.

Errors in the displacement, momentum and energy thicknesses, when nondimensionalized with the boundary layer thickness, were calculated by integrating the standard error for the velocity measurements to be between 2.5 and 5 percent, respectively. Combining this with the estimated uncertainty in the boundary layer thickness gives an overall uncertainty of between 5.5 percent and 11.2 percent.

Finally, errors for the surface shear stresses were estimated to be no worse than 8 percent based on the Clauser plot comparison and probably closer to 2 percent based on the calibration facility verification shown on Fig. 3.

Conclusions

1. Surface pressure coefficients are shown to agree well with theoretically calculated potential flow pressure distributions up to about 40 percent of the chord of the test surface. A reasonably clear and well defined departure from the potential flow prediction is evidenced by the data.

2. The early activity in the surface pressure measurements as well as the intermittency measurements indicate that turbulent separation is a process, extending over some considerable length of the surface, unlike the sharp local nature of laminar separation. Exceptionally high levels of surface pressure fluctuations were observed at places where the intermittency began to change value, i.e., where it first became nonzero indicating incipient separation, where it first leveled off in the separation bubble and where it began to fall indicating the onset of reattachment.

3. Intermittency results show turbulent flow separation to be very unsteady. Both the separation and reattachment points wondered over about 30 percent of the chord of the test surface. Nowhere in the separated region was the flow in the reversed direction one hundred percent of the time.

4. Displacement thickness increases steadily throughout the separating and separated flow peaking at reattachment at slightly less than eighty times its initial value. The momentum and energy thicknesses also show an increase through separation but plateau near the middle of the separation bubble. They then increase sharply, peaking downstream of reattachment at better than forty times their initial value. These data agreed well with a previously published empirical correlation between the energy and momentum shape factors.

5 The maximum shear stress occurred at the beginning of the test surface, in the region of accelerated near wall flow, and the minimum shear stress occurred approximately in the middle of the recirculation zone. The ratio between the absolute values of these two quantities was found to be 10 to 1.

References

1 Whitfield, D. L., Swafford, T. W., and Jacobs, J. L., "Calculations of Turbulent Boundary Layers with Separation and Viscous-Inviscid Interaction," *AIAA Journal*, Vol. 19, No. 10, Oct. 1981.

2 Das, D. K., "An Integral Method for Analyzing Incompressible Two-Dimensional Turbulent Boundary Layers with Separation," Doctoral Dissertation, University of Rhode Island, Dept. of Mech. Engin., 1983.

3 Kline, S. J., Bardina, J., and Strawn, R., "Detachment and Reattachment of Turbulent Boundary Layers on Two-Dimensional Faired Surfaces," AIAA Paper 81-1220, 1981.

4 Buckles, J., Hanratty, T. J., and Adrian, R. J., "Turbulent Flow over Large-Amplitude Wavy Surfaces," *Journal of Fluid Mechanics*, Vol. 104, 1984, pp. 27–44.

5 Simpson, R. L., Strickland, J. H., and Barr, P. W., "Features of a Separating Turbulent Boundary Layer in the Vicinity of Separation," *Journal of Fluid Mechanics*, Vol. 79, 1977, pp. 553–594.

6 Simpson, R. L., Chew, Y. T., and Shivaprasad, B. G., "The Structure of a Separating Turbulent Boundary Layer. Part 1, Mean Flow and Reynolds Stresses," *Journal of Fluid Mechanics*, Vol. 113, 1981, pp. 23–51.

7 Simpson, R. L., Chew, Y. T., Shivaprasad, B. G., "The Structure of a Separating Turbulent Boundary Layer," Part 2, Higher Order Turbulence Results," *Journal of Fluid Mechanics*, Vol. 113, 1981, pp. 53–73.

8 Shiloh, K., Shivaprasad, B. G., and Simpson, R. L., "The Structure of a Separating Turbulent Boundary Layer, Part 3, Transverse Velocity Measurements," *Journal of Fluid Mechanics*, Vol. 113, 1981, pp. 75–90.

9 Simpson, R. L., Shiva, B. G., and Chew, Y. T., "The Structure of a Separating Turbulent Boundary Layer. Part 4, Effects of Periodic Free-Stream Unsteadiness," *Journal of Flud Mechanics*, Vol. 127, 1983, pp. 219–261.

10 Simpson, R. L., Shiva, B. G., "The Structure of a Separating Turbulent Boundary Layer. Part 5, Frequency Effects on Periodic Unsteady Free-Stream Flows," *Journal of Fluid Mechanics*, Vol. 131, 1983, pp. 319–339.

11 Serpa, J. M., "Separation and Reattachment of Turbulent Flow on a Curved Surface," Master's Thesis, University of Rhode Island, Dept. of Mech. Engin., 1985.

12 Sandborn, V. A., "Evaluation of the Time Dependent Surface Shear Stress in Turbulent Flows," ASME paper 79-WA/FE-17, 1979.

13 Ramaprian, B. R., and Tu, S. W., "Calibration of a Heat Flux Gage for Skin Friction Measurements," ASME *Journal of Fluids Engineering*, Dec. 1983, pp. 455–457.

14 Archibald, T. E., and Sadd, M., "Shape-A Laplace Equation Solver Using the Boundary Element Method," Dept. of Mech. Engin. Technical Report, Univ. of Rhode Island, May 1984.

15 Ota, T., and Itaska, M., "A Separated and Reattached Flow on a Blunt Flat Plate," ASME JOURNAL OF FLUIDS ENGINEERING, Mar. 1976, pp. 79–86.

16 Sam, R. G., Lessman, R. C., and Test, F. L., "An Experimental Study of Flow Over a Rectangular Body," ASME JOURNAL OF FLUIDS ENGINEERING, Dec. 1979, pp. 443–448.

17 McCormick, D., Lessmann, R. C., and Test, F. L., "Heat Transfer to Separated Flow Regions from a Rectangular Prism in a Cross-Stream," ASME *Journal of Heat Transfer*, Vol. 106, No. 2, May 1984, pp. 276–283.

D. R. Poling*

D. P. Telionis

Virginia Polytechnic Institute and State University, Dept. of Engineering Science and Mechanics, Blacksburg, Virginia 24061

The Trailing Edge of a Pitching Airfoil at High Reduced Frequencies

Trailing edge flows are visualized for a pitching airfoil. The validity of the quasi-steady and an extension to an unsteady Kutta condition, namely the Giesing-Maskell condition are examined. A new dynamic similarity parameter is proposed. Earlier work and the present results are re-evaluated in terms of this parameter. A range is identified in which no Kutta-type condition may apply.

Introduction

Today numerical solutions of the Navier-Stokes equations can provide realistic answers that can be used in the design of aerodynamic elements. However, such methods are confined to certain classes of problems. For complex problems involving unsteady and/or three-dimensional flows, free shear layers interacting with solid bodies and large separated regions, Navier-Stokes solutions fail to predict accurately the phenomena involved. In such cases, approximate methods are still valuable design tools. Sharp corner flows, as for example flows over airfoil trailing edges, have been traditionally handled by models such as the Kutta condition. Such models are based on physical arguments but their validity is not rigorously justified. The study of such models provides necessary conditions for the solution of inviscid flow equations. Moreover, such studies provide benchmark information for comparison of numerical Navier-Stokes solutions, as well as physical insight into the physics of the phenomena involved.

The validity of the Kutta condition in unsteady flow has been the topic of recent work as discussed in references [1] and [2]. The classical Kutta condition is often expressed as a requirement that the rear point of stagnation is at the trailing edge. However, for non-cusped trailing edges in unsteady flow this is not sufficient to render a numerical inviscid solution unique [2]. Most investigators examine the static pressure near the edge of the airfoil [3–7]. However, more reliable information can be obtained by measuring the velocity vectors in this region.

Laser-Doppler Velocimetry data [2] indicate that for large reduced frequencies, the streamline emanating from the trailing edge aligns with one of the two sides of the airfoil. This is depicted schematically in Fig. 1. The controlling parameter is the sign of the time derivative of the airfoil circulation. This condition is essentially an unsteady Kutta condition and was termed in reference [2] the Giesing-Maskell condition. The reader is also referred to reference [8] for more discussion. In the present paper we present flow visualization data in support of this condition for the range of reduced frequencies between 0.8 and 1.2. We go further to prove that this condition as well is violated beyond a reduced frequency of about 2.4.

Facilities and Instrumentation

Tests were conducted in a water tunnel with a test section cross section of 25 cm × 30 cm, at speeds of 10 to 29 cm/s. For a description of the facility, the reader is referred to references [9] and [10]. An NACA 0012 airfoil with a 10 cm chord was oscillated in pitch about its quarter chord. To prevent transferring external forces on the test section, the airfoil was driven via a four-bar linkage. The arrangement is depicted schematically in Fig. 2. The reader will find more details in reference [2]. In the work presented here Laser-Doppler Velocimetry measurements were obtained only upstream to monitor the flow.

An 8 mm-wide sheet of light in a plane parallel to the tunnel walls was generated to illuminate the midplane of the two-dimensional field. This was achieved by positioning two Tungsten-Hallogen 1000 Watt lamps above and below the test section and guiding the light through ducts of 8 mm width.

The flow was visualized by particles. Koromilas and Telionis [9] describe in detail a method of visualizing the flow by dispersion of neutrally buoyant, light-reflecting particles (PLIOLITE). Such particles populate uniformly the entire flowfield. Dyes were also released from the upper and lower surface of the airfoil at a distance of 0.2 chordlengths from the trailing edge. Particle paths were recorded by photographic time exposure. With a dark background, the particle images produce streaks on the photographic film which are aligned with the images of the velocity vectors and are proportional approximately to their magnitude. In this way we can essentially produce instantaneous shots of the entire velocity field.

Of great importance here is the frame of reference. Traditionally, the flowfield is recorded by measurement or flow visualization in terms of a fixed frame of reference. However, in the present case it is of great interest to view the flow from a frame of reference mounted on the moving airfoil. This is because the unsteady Kutta condition is expressed in terms of such a frame [2, 8]. To study the trailing edge velocity field,

Present address: Boeing Vertol Co., Philadelphia, Pa., 19142.

Contributed by the Fluids Engineering Division and presented at the Forum on Unsteady Flow, Winter Annual Meeting, Miami Beach, Fla., November 17–22, 1985 for THE AMERICAN SOCIETY OF MECHANICAL ENGINEERS. Manuscript received by the Fluids Engineering Division August 5, 1986.

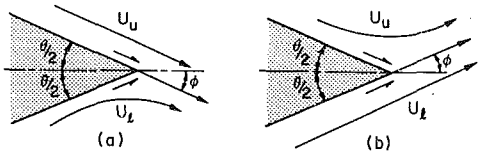

Fig. 1 Schematic configuration of streamline pattern in the vicinity of a moving trailing edge according to the Giesing-Maskell criterion. (*a*)upward motion, (*b*)downward motion. Here θ is the airfoil wedge angle and ϕ is the streamline slope. The Giesing Maskell conditon requires $\phi = \theta/2$.

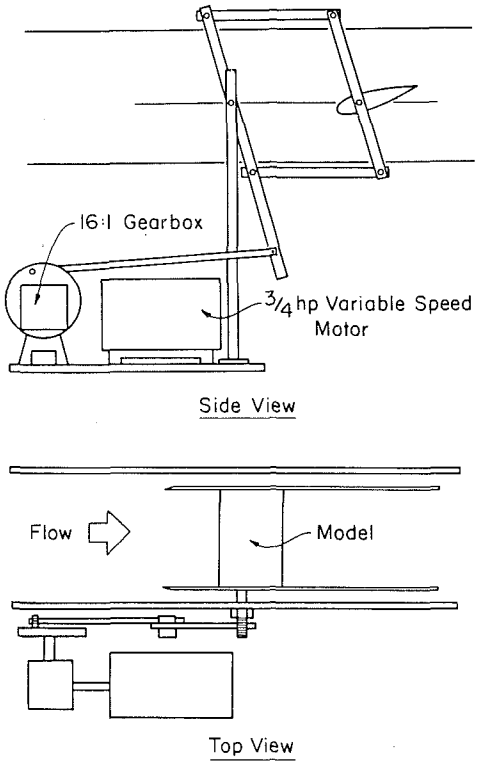

Fig. 2 Test section model and the driving four-bar linkage

the camera (NIKON F-3.5 MACRO lens) was mounted on the four-bar linkage and therefore was fixed on the frame of the pitching airfoil.

For periodic flows it is necessary to record the phase within the period. To this end, a signal from a LED sensor on the flywheel of the disturbing mechanism was used to zero a digital clock. In this was the clock always displayed the time elapsed from a fixed point in the period. Alternatively, the instantaneous angle of attack was marked on a strip and visualized by a pointer. The clock or the pointer were viewed by the camera via a small mirror. A schematic of this rig is shown in Fig. 3. In this way, a small section of the photographic film was devoted to the recording of the phase of the periodic phenomenon.

Experimental Results

Experiments were conducted at 4 reduced frequencies, $k = 0.8$, 1.2, 2.4 and 3.9 where k is defined as $k = \omega C/2U_\infty$ with ω the frequency of the periodic motion, C the chord length and U_∞ the freestream velocity. The amplitude of the angle of attack, α, was 10 deg, and the motion was very nearly sinusoidal. Related calibration curves are included in reference [10]. The lowest frequency tested actually represents a moderate frequency for some practical applications. Our findings here indicate that at $k = 0.8$, the quasi-steady Kutta

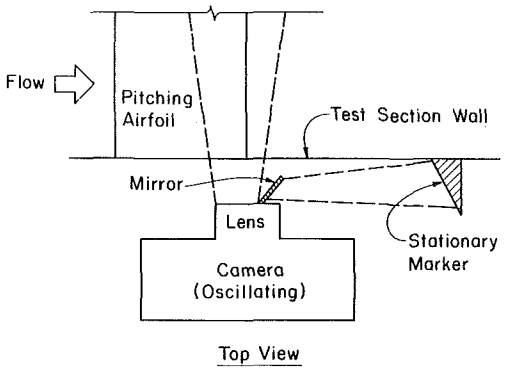

Fig. 3 Mounting of the camera on the frame of the airfoil

Fig. 4 Instantaneous flow visualization for $k = 0.8$, U_∞ cm/s, $\mathrm{Re} = 10^4$, $k = 0.8$, $\alpha = -10$ deg

Fig. 5 Instantaneous flow visualization for $k = 1.2$, $U_\infty = 20$ cm/s, $\mathrm{Re} = 2 \times 10^4$, $k = 1.2$, $\alpha = -50$, downstroke

condition does not hold, in agreement with the measurements we reported in reference [2] as well as the findings of reference [1] but in contrast to reference [6].

Typical flow visualization results are shown in Figs. 4, 5, 6, 7, and 8 for $k = 0.8$, 1.2, 2.4, 2.4 and 3.9, respectively. In these figures we display only the aft 20 percent portion of the airfoil chord. The boundary-layer thickness near the edge of the airfoil is on the order of 0.03 to 0.5 chordlengths. In all cases it is clear that the streamlines near the edge of the airfoil are not aligned with the bisector of the airfoil trailing wedge angle.

Fig. 6 Instantaneous flow visualization for $k=2.4$, $U_\infty=10$ cm/s, $Re=10^4$, $\alpha=-0$ upstroke

Fig. 7 Instantaneous flow visualization for $k=2.4$, $U_\infty=10$ cm/s, $Re=10^4$, $\alpha=0$ deg upstroke

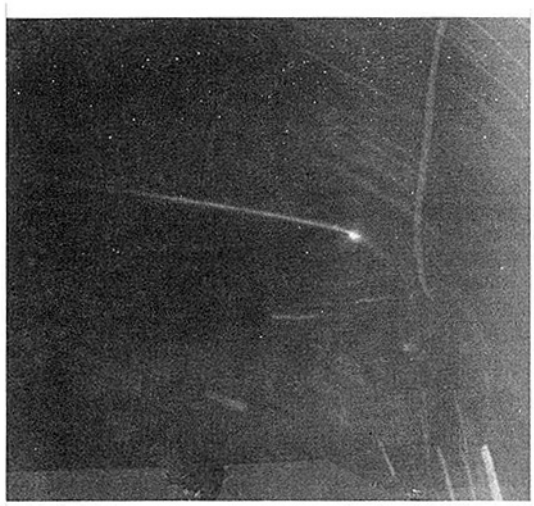

Fig. 8 Instantaneous flow visualization for $k=3.9$, $U_\infty=10$ cm/s, $Re=10^4$, $\alpha=-0$ deg downstroke

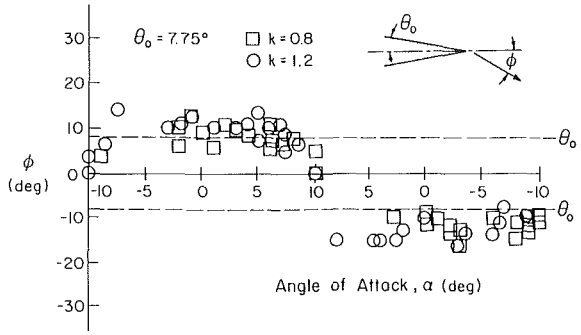

Fig. 9 Slope of streamlines at the trailing edge for $k=0.8$ and 1.2

The classical Kutta condition is therefore violated. The velocity vectors appear to be rather aligned with the one side of the airfoil. In fact, at distances larger than a few hundreds of the chord length from the edge, the streamlines may have inclinations even larger than the advancing side of the airfoil.

A large number of frames like those of Figs. 4–8 were obtained. For each one of these frames, the slope of the streamline on the advancing side of the trailing edge was measured at a distance approximately $0.01C$ above the airfoil. This often required averaging over a distance of $\pm 0.02C$ upstream and downstream of the edge. The data thus obtained are displayed in Figs. 9 and 10. It should be noted that the quasi-steady Kutta condition should require that all such points collapse on the horizontal axis. Since the trailing edge wedge angle of the NACA 0012 is approximately 15.5 deg, the Giesing Maskell criterion, would require that data fall on $\phi=8$ deg and $\phi=-8$ deg for the upstroke and the downstroke motion, respectively. Deviation of the data beyond $\phi=\pm 8$ implies that neither of the conditions is valid. The error in the calculation of the instantaneous angle of attack was estimated at ± 0.5 deg whereas the error in the inclination of the streamline from a single particle segment was approximately ± 1 deg. However, the error involved in averaging over different particles to obtain the predominant slope in the neighborhood of the trailing edge was about ± 2 deg and at higher frequencies perhaps even ± 3 deg.

A careful examination of Figs. 9 and 10 also reveals that the data are not antisymmetric about $\alpha=10$ deg. This discrepancy may be attributed to small errors of adjusting the angle $\alpha=0$ deg of the airfoil at the midpoint of the oscillating mechanism.

Discussion and Conclusions

The flow at a trailing edge is dominated by viscous effects. However, for very large Reynolds numbers and therefore very thin boundary layers, it is possible to avoid solving viscous flow equation and render solutions of inviscid flow equations unique by assuming a Kutta-type condition. The idea is that across the streamline emanating from the trailing edge, the pressure cannot jump and this is quite true, as long as the boundary-layer approximation holds. Pressure gradients across a boundary layer or a free shear layer are negligible, if the curvature of the streamlines within the viscous region is very small. It is important to emphasize here that assessing the validity of a Kutta-type condition in the potential flow should actually be determined by the behavior of the flow at the edge of the boundary layer and not at the solid surface itself.

In the present study the flow visualizations for $k \leq 1.2$ indicate that the velocity vectors across the boundary layer thickness and into the outer flow are parallel on the advancing side. Here the results were obtained from the visual data within the thickness of the boundary layer, but approximately at the edge of the displacement thickness. There is one more justification for this practice. Triple-deck theory has indicated that for axial distances of the order of $Re^{-3/8}$, viscous effects are confined to the lower deck which has a thickness of order $Re^{-5/8}$. In other words, for small axial distances, about 0.02 C

upstream and downstream of the trailing edge, the boundary layer responds in an inviscid manner in the middle deck. Viscous effects are contained in the lower deck whose thickness is less than the displacement thickness.

The present visual data indicate that for the range of $0.8 \leq k \leq 1.2$ the Giesing-Maskell criterion is valid for the entire period of the oscillation. Indeed, with very good accurcy we may assume that the trailing-edge streamline instantly adjusts itself to become tangent to the side of the airfoil which leads the pitching motion. This observation therefore makes this criterion a useful practical tool for calculating unsteady airfoil flows at high frequencies.

For reduced frequencies larger than 1.2, all models break down. However, the flow is still attached on both sides of the airfoil. It may be argued that the situation in Fig. 8 is identical to Figs. 4–7, except that the curvature of the free shear layer is larger very close to the airfoil edge. Our thesis here is that at higher frequencies, sharp turning occurs within the viscous layer. Similar conclusions were reported in reference [2] but for a different configuration. At the edge of the boundary layer where one would expect an inviscid model to be valid, the velocity slopes more than the model surface. The unsteady Kutta condition proposed in reference [2] is thus violated.

If sharp turning occurs within the viscous layer, then the boundary layer approximation is also violated. In other words, gradients normal to the wall and notably, the pressure gradient across the boundary layer are not small. There is a considerable change of pressure across the trailing edge, or, in the more established terminology, the trailing edge is loaded.

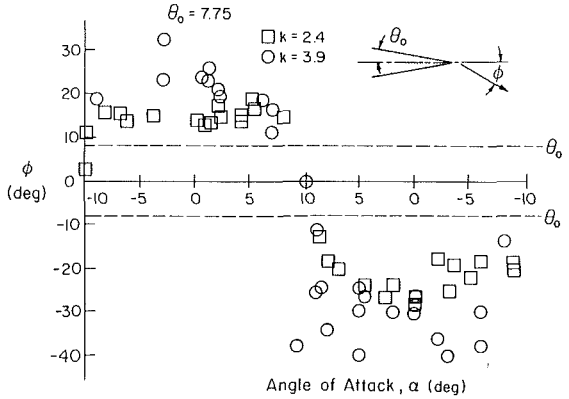

Fig. 10 Slope of streamlines at the trailing edge for $k = 2.4$ and 3.9

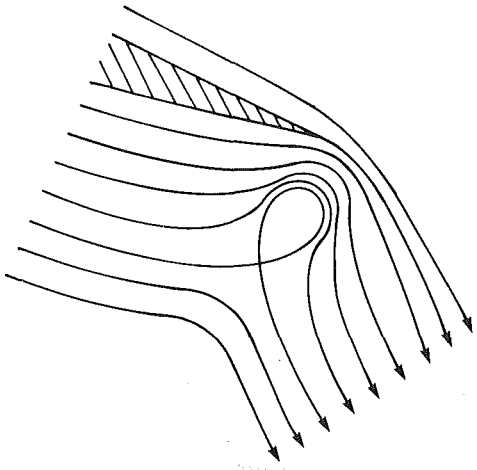

Fig. 11 Schematic sketch of the streamline pattern of Figs. 6 and 7

In the range of frequencies $k \geq 2.4$, no inviscid model can be defined.

A remark on the technique of deriving quantitative results form the flow visualization is pertinenet here. The technique is valid if the exposure time is much less then the time scale of the developing unsteady phenomenon. In our experiments, the camera speed was 1/15 and the range of disturbing frequencies were at most 2 Hz. It appears therefore that the condition is satisfied. Yet, for the largest frequencies, the velocity around the trailing edge increases sharply. In fact the visualized paths are actually particle paths and not streamlines. It was observed though that for about 80 percent of the period of the motion, these curves are almost frozen and therefore, in the frame of the moving airfoil the flow is steady. Particle paths therefore nearly coincide with streamlines. Nevertheless, this observation which was actually pointed out by a reviewer adds one more element of uncertainty to the data for high reduced frequencies.

In flow visualizations of high reduced frequencies, the free shear layer quickly rolls into a strong vortex very close to the trailing edge. The flow stagnates near, but not on the retreating side of the airfoil as shown in the flow visualization of Fig. 8. The corresponding streamline pattern is illustrated schematically in Fig. 11. The streakline geometry for the same field is displayed in Fig. 12 which is very similar with the sketch included in reference [11]. In this figure we have captured both a dye trace as well as short particle paths. Such streakline patterns may be very deceiving, as Ohashi and Ishikawa [11] point out. The vortex may be mistaken for a region of separation. Our findings are therefore in agreement with those of Ohashi and Ishikawa who indicate that even for the highest reduced frequency they tested, the flow stays attached on both sides of the airfoil.

One more point must be clarifield here. It was argued in reference [2] that the reduced frequency is not a good dynamic simlarity parameter for the comparison of experimental data. A more proper criterion should include the amplitude of the oscillation. We suggest here that a good parameter could be the ratio of the maximum velocity of the trailing edge to the velocity of the free stream. For a pitching oscillation this works out to be $\ell = r\omega\alpha_0/U_\infty$ with r the distance from the pivot to the trailing edge, while for a plunging airfoil, this becomes $\sigma = h_0\omega/U_\infty$, where h_0 is the linear amplitude of the oscillation. A hint towards a similar parameter was given by McCroskey [12] with regard to his Fig. 30. This is again the ratio of the tip velocity over the freestream velocity. However, McCroskey is using this quantity as a variable to mark the phase of the oscillation.

The range of the number ℓ for our experiments is 0.104 to 0.513 whereas for the experiments of reference [1] it is 0.016 to 0.320. A value of about $\ell = 0.1$ appears then to be in both references a limit above which the quasi-steady criterion is not

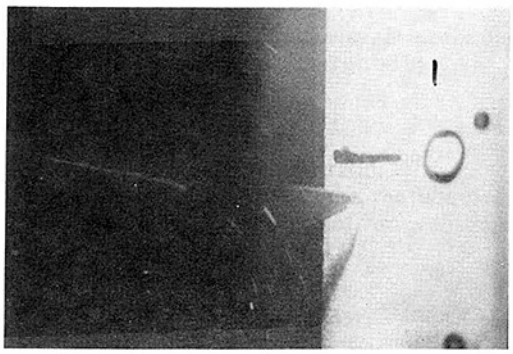

Fig. 12 Instantaneous flow visualization for $k = 3.9$, $U_\infty = 10$ cm/s, $Re = 10^4$, $\alpha = 5$ deg downstroke

valid. In reference [6] all values of ℓ are below 0.015705, and therefore all their experiments were conducted well below the limit of the validity of the quasi-steady criterion.

Recapitulating, we find that for all reduced frequencies tested, the stagnation point is fixed at the trailing edge. This does not imply that the classical Kutta condition is met, becasue the stagnation streamline is inclined with respect to the bisector of the airfoil. The unsteady Kutta condition is valid up until $\ell \simeq 0.32$ but is violated at $\ell = 0.511$. For the highest values of the parameter ℓ, a vortex rolls up very close to the trailing edge and may be erroneously interpreted as separation.

Acknowledgment

The monitors of this NASA grant (NGT-47-004-801), Dr. E. C. Yates and later Dr. W. J. McCroskey, have contributed substantially to this work by their support and criticism. Drs. L. W. Carr and W. J. McAlister have also made many helpful suggestions.

References

1 Ho, C. M., and Chen, S. H., "Unsteady Kutta Condition of a Plunging Airfoil," in *Unsteady Turbulent Shear Flows*, Eds. R. Michel, J. Cousteix and R. Houdeville, pp. 197–200, May 1981, Springer, Berlin, Heidelberg.

2 Poling, D. R., and Telionis, D. P., "The Response of Airfoils to Periodic Disturbances—The Unsteady Kutta Condition," *AIAA Journal*, Vol. 24, 1986, pp. 193–199.

3 Achibald, F. S., "Unsteady Kutta Condition at High Values of the Reduced Frequency Parameter," *Journal of Aircraft*, Vol. 12, 1975, pp. 545–550.

4 Ostdiek, F. R., "A Cascade in Unsteady Flow," *Unsteady Phenomena in Turbomachinery*, AGARD CP 177, 1975, pp. 26-1 - 26-13.

5 Commerford, G. L., and Carta, F. O., "Unsteady Aerodynamic Response of a Two Dimensional Airfoil at High Reduced Frequency," *AIAA Journal*, Vol. 12, 1974, pp. 43–48.

6 Satyanarayana, B., and Davis, S., "Experimental Studies of Unsteady Trailing Edge Conditions," *AIAA Journal*, Vol. 16, Feb. 1978, pp. 125–129.

7 Fleeter, S., "Trailing Edge Conditions for Unsteady Flows at High Reduced Frequency," AIAA Paper 79-0152, 1979.

8 Basu, B. C., and Hancock, G. J., "The Unsteady Motion of a Two-Dimensional Aerofoil in Incompressible Inviscid Flow," *Journal of Fluid Mechanics*, Vol. 87, 1987, pp. 159–178.

9 Koromilas, C. A., and Telionis, D. P., "Unsteady Laminar Separation: An Experimental Study," *Journal Fluid Mechanics*, Vol. 97, 1980, pp. 347–384.

10 Poling, D., "Airfoil Response to Periodic Disturbances - The Unsteady Kutta Condition," Ph.D. Dissertation, Virginia Polytechnic Institute & State Univ., Blacksburg, VA, Aug. 1985.

11 Ohashi, H., and Ishikawa, N., "Visualization Study of Flow Near the Trailing Edge of an Oscillating Airfoil," *Bulletin of the J.S.M.E.*, Vol. 15, 1972, pp. 840–847.

12 McCroskey, W. J., "Some Current Research in Unsteady Fluid Dynamics - The 1976 Freeman Scholar Lecture," TRANS. ASME JOURNAL OF FLUIDS ENGINEERING, Vol. 99, 1977, pp. 8–38.

S. S. Chen
Fellow ASME

J. A. Jendrzejczyk

Argonne National Laboratory,
Argonne, Ill. 60439

Fluid Excitation Forces Acting on a Square Tube Array

Fluid forces acting on a tube array are important in the assessment of vibration of system components consisting of multiple circular cylinders. This paper presents test results for a square tube array with the pitch-to-diameter ratio of 1.75 subject to turbulent flow. The fluctuating drag and lift forces are measured as a function of Reynolds number, incoming flow conditions, and tube location in an array.

I Introduction

When a fluid flows across a tube array, a fraction of the fluid energy is transmitted to the tubes, resulting in tube vibration. Crossflow-induced vibration of tube arrays is caused by one or more of the following mechanisms: turbulent excitation, vortex-induced oscillations, acoustic excitation, and fluidelastic instability. This study is directed toward the first two mechanisms. Previous works in the subject area are briefly reviewed.

Flow Field. The flow characteristics across a single tube depend on Reynolds number, Re. The major identifiable regions are presented by Lienhard [1]. Reviews of the fluid dynamics of a single cylinder can be found in Morkovin [2], Mair and Maull [3], Marris [4], and Berger and Wille [5] and reviews of a pair of tubes were reported by Zdravkovich [6, 7] and Chen [8].

Flow patterns for a flow across tube arrays depend on tube arrangement as well as Reynolds number, and tube spacing is an important parameter. Flow visualization of flow development in in-line and staggered tube arrays were reported by Weaver and Abd-Rabbo [9] and Abd-Rabbo and Weaver [10]. Detailed classification of flow patterns remains a subject of current research. Based on limited data [11, 12], flow patterns for in-line and staggered tube arrays can be classified in, at least, five regimes. The flow pattern is the same within a range of tube pitches, and an abrupt change can be observed at some values of tube spacing.

Pressure distribution around a tube in an array is very complex, and depends on the incoming-flow properties and tube arrangements. Only limited data are available, but these data are important in understanding the flow field as well as obtaining the necessary force coefficients for response calculations. Zdravkovich and Namork [13] reported the fluctuating and time-average pressure distribution around a tube located in different rows of a triangular array having a transverse pitch to tube diameter ratio (T/D) of 1.375 for $\mathrm{Re} = 1.1 \times 10^5$ and free-stream turbulent intensity of 2 percent. Measurements for staggered arrays were also reported by other investigators [14–17].

The turbulence intensity depends on the location of the tube. Turbulence measurements were made by Price et al. within a rotated square tube array [18]. A test by Sandifer and Bailey [19] shows that turbulence intensity starts at a low level (about 4 percent) at the entrance to the array and gradually increases to about 23 percent in the middle of the array. At a particular location of a tube array, the turbulence intensity is fairly constant with increasing gap velocity. In addition, the power spectrum of turbulence excitation does not change significantly through the tube array at a particular gap velocity.

Flow Excitation Force Coefficients. Depending on tube spacings, as well as other system parameters, vortex shedding may or may not exist in a tube array. Early studies on vibration of tube arrays proceeded on the assumption that vortex shedding was the dominant mechanism. Therefore, the main objective was to determine the vortex shedding frequency. Unfortunately, there are multiple vortex shedding frequencies and the frequencies may be different in different parts of the array [18]. Precise determination of vortex shedding in a tube array proved complicated. Even at subcritical Reynolds numbers, it is not possible to give a precise value of Strouhal number for each tube arrangement. However, based on the available experimental data, Strouhal numbers have been compiled by several investigators [20, 21]. For tube arrays, the Strouhal number, St, is defined the same way as that for a single tube; i.e.,

$$\mathrm{St} = \frac{f_s D}{U}, \tag{1}$$

where f_s is the vortex shedding frequency, D is tube diameter, and U is the gap flow velocity, which is given by

$$U = \frac{U_{\text{approach velocity}}}{1 - D/T}. \tag{2}$$

T is the transverse pitch-to-diameter ratio.

Each time a vortex is shed from a tube, the tube experiences a time-varying force at the frequency of vortex shedding. The periodic fluctuating force components are

$$g = \frac{1}{2}\rho U^2 D C_D' \sin(\Omega_D t) \quad \text{and} \qquad h = \frac{1}{2}\rho U^2 D C_L' \sin(\Omega_L t). \tag{3}$$

Contributed by the Fluids Engineering Division for publication in the JOURNAL OF FLUID ENGINEERING. Manuscript received by the Fluids Engineering Division August 23, 1986.

Ω_L is equal to the Strouhal frequency and Ω_D is equal to twice the Strouhal frequency. The drag and lift coefficients, obtained from equation (3), are referred to as fluctuating drag and lift coefficients. When the excitation is not at a discrete frequency, the coefficients of fluctuating drag and lift are defined by the root mean square value of the drag and lift fluctuations as obtained from an integration of the corresponding frequency specta, viz.,

$$C_D' = \frac{\text{RMS value of fluctuating drag force per unit length}}{1/2\rho U^2 D} \tag{4}$$

and

$$C_L' = \frac{\text{RMS value of fluctuating lift force per unit length}}{1/2\rho U^2 D}.$$

The coefficients obtained in this manner are referred to as RMS fluctuating drag and lift coefficients.

The fluctuating force coefficients C_D' and C_L' depend on different parameters:

$$C_D' = C_D'(\text{Re, turbulence characteristics, surface characteristics, tube pitches}) \tag{5}$$

and

$$C_L' = C_L'(\text{Re, turbulence characteristics, surface characteristics, tube pitches}).$$

Measurements of fluid excitation force coefficients are very limited for general tube arrays. There have been few systematic studies to measure those coefficients. The fluctuating lift coefficients for various tube arrays are presented by Chen [22] and Pettigrew and Ko [23] for application to heat exchanger tubes. Some of the coefficients are deduced from tube response, not from force measurements. Note that resonance is more likely and more severe in upstream tubes, and highly nonuniform flow or gross turbulence can prevent the formation of correlated periodic wake shedding.

Fluctuating fluid coefficients C_L' and C_D' for equilateral staggered arrays and square pitch in-line arrays were measured by Savkar and Litzinger [24] for different pitch ratios ($T/D = 1.2$, 1.5, and 1.71) and upstream turbulence intensity (0.5 and 8.5 percent). The flow patterns between the two types of arrays were considerably different. Flow through the staggered array followed a zig-zag path with the wakes more or less closed, while flow through the in-line arrays was channeled in the open lanes [9, 10].

The steady drag and lift forces acting on a tube in the middle of an array were obtained using the measured pressure for several different arrangements by Zdravkovich et al. [25]. The transverse pitch was 1.66, and the coefficients were based on the free stream velocity. Steady drag coefficients also were measured by Morsy [14] for a staggered array (30 deg) with a pitch ratio of 1.5 in a wind tunnel. The first row offered the highest form resistance to flow. This is expected, due to the severe circumferential pressure gradients measured on this row of tubes and the big difference between the pressures on the front and rear halves of its tubes. The drag coefficient for the first row of tubes is about 4.5 times the values recorded for a single tube in crossflow.

Both steady and unsteady drag and lift coefficients based on the gap velocity were obtained by Heinecke and Mohr [17] for square arrays in a range of Reynolds numbers $10^4 \le \text{Re} \le 10^5$. Heinecke and Mohr showed that (1) the unsteady lift coefficient is almost independent of Reynolds number and the coefficient for the second row is larger than the first row; and (2) for different spacings the pressure distribution around the circumference is asymmetric.

The turbulence pressure field for tube arrays is not well characterized. A complete description of the pressure for application to vibration theory requires power spectral density of pressure at different locations and the correlation. There is no complete set of data for any tube array. However, several forms of approximation have been suggested to render the turbulence pressure field practicable for simple use.

Pettigrew and Gorman [26] assumed that the random force field is homogeneous and spatially correlated. The power spectral density of the random force acting on a tube is expressed

$$\Phi = \left(\frac{1}{2} C_R \rho U^2 D\right)^2, \tag{6}$$

where C_R is called the random turbulence excitation coefficient. Values of C_R from the results of different experiments show that the random force field depends on the location of the tube in an array.

Blevins, Gibert, and Villard [27] measured both power spectral density and correlation of coherence along the axis of the tube in a wind tunnel for an in-line array. The turbulence rises from the inlet to a maximum value about six rows back; this turbulence level then persists to the back of the arrays and is consistent with the results by Sandifer and Bailey [19].

The correlation length for the first row is about 3.4 tube diameters, which is comparable to the values obtained for a single tulbe [28]. The correlation drops within the tube array and increases sharply with tube vibration.

Effects of Different System Parameters. The response of a tube in crossflow is affected by different system parameters: high Reynolds number, turbulence, yawed flow, blockage effect, surface roughness, etc. Some of the effects of these parameters are still not well understood.

High Reynolds Number. Vibrations at high Reynolds numbers are of particular interest with respect to the vibration of some structural components. Full-scale data on crossflow response of tubes are quite limited because large-amplitude motions lead to failure within a short time of the onset of oscillations. The response of a single tube at high Reynolds number is not well documented. Based on the limited available data, some general observations are valuable in the assessment of the structural response.

- In contrast to stationary tubes there is no discernible Reynolds number effect on the Strouhal number for Re from 3×10^5 to 1.4×10^6 obtained from a full-scale experiment with a 30 in. diameter pipe [29].
- The universal wake Strouhal number St* presented by Griffin [30] spans five decades of the Reynolds number from 10^2 to 10^7. St* collapses the characteristic wake scales onto a single curve.

The fluid-force data for tube arrays in the high Reynolds number range are not available. This is one of the areas that requires more experimental studies.

Surface Roughness. A comprehensive study of the effect of surface roughness on steady drag was made by Miller [31] for the case of isolated stationary tubes. However, there are very limited data for the fluid force coefficients on roughed tubes. More tests are needed to quantify the effect of roughness of tube response in different flow regions.

Yawed Flow. If a tube is yawed to the flow direction with an angle ϕ, both the effective fluid force and the reduced flow velocity are reduced:

$$g = \frac{1}{2}\rho D[C_D(U\cos\phi)^2 + C_D'(U\cos\phi)^2\cos(\Omega_D t)],$$

$$h = \frac{1}{2}\rho D[C_L(U\cos\phi)^2 + C_L'(U\cos\phi)^2\cos(\Omega_L t),$$

and

Table 1 Grid and turbulence characteristics*

Grid	X_m, cm	TI, %	L_x, cm	a, cm	b, %
A	42.3	1-3	4-8.5	0.476	49
B	42.3	4-5	1.2-1.4	1.74	58
C	42.3	10-11	2.3-2.7	2.76	75

*Source: Ref. 34.

X_m is the distance between downstream surface of the grid and the center of the test section,
a is the hole diameter,
b is the blockage ratio,
TI is the turbulence intensity, and
L_x is the length scale.

Table 2 Experimental uncertainty

Convection Velocity $U_c/U = \pm 3\%$
Drag and Lift Force (g and h) = $\pm 5\%$
Fluid Force Coefficients (C'_D and C'_L) = $\pm 7\%$
Flow Velocity (U) = $\pm 3\%$
Frequency (f) = $\pm 1\%$
Linear Dimension = $\pm 1\%$
Power Spectral Density (Φ) = $\pm 10\%$
Reynolds Number (Re) = $\pm 3\%$
Strouhal Number (St) = $\pm 3\%$
Time Delay = $\pm 1\%$

$$U_r = \frac{U\cos\phi}{fD}. \tag{7}$$

This is based on the assumption that the normal component of the flow velocity can be taken as the effective flow velocity on a yawed tube; the use of the normal component of velocity is called the independence principle. Studies have verified the validity of the principle (e.g., references [32 and 33]).

Turbulence. In an ideal crossflow, periodic drag and lift forces are the two excitation force components. In a turbulent crossflow, the frequency spectra of the lift and drag force components consist of a component in a narrow band of frequencies due to organized vortex shedding, and a component covering a wide band of frequencies predominantly below the vortex shedding frequency due to flow turbulence in the coming flow stream and in the wake. The roles of these two components depend on Re and turbulence of the flow stream.

The turbulence in the flow stream can have significant effects on the fluid force characteristics acting on a tube. It is generally known that the effect of introducing turbulence into the flow is to produce a change in effective Reynolds number in the measuremnt of drag. This corresponds to the shift in the transitional region to a lower Reynolds number range.

II Experimental Setup

The experiment was performed in the Flow Induced Vibration Test Facility (FIVTF). The primary system of the loop is filled with demineralized water and consists of four pumps arranged in parallel, feeding a closed accumulator of 30 m^3 (8000 gal). By using a combination of pumps and valves, the flowrate can be controlled from ~ 0.003 m^3/s (50 gpm) to a maximum of 0.5 m^3/s (8000 gpm). From the closed accumulator, water is valved to one of the several test leg branches and returned to a common supply tank of 38 m^3 (10,000 gal). The quality of the water is maintained using water conditioning equipment installed in the supply tank.

The test section is a square flow channel with a flow area of 30 cm × 30 cm (11-3/4 in. × 11-3/4 in.) connected to one of the test leg branches, which is a 46 cm (18.1 in.) pipe. A 30 cm (11.75 in.) square liner is inserted in the pipe to form a square flow channel upstream and downstream of the test section. The diameter of the tubes for the tests is 2.54 cm (1 in.). The

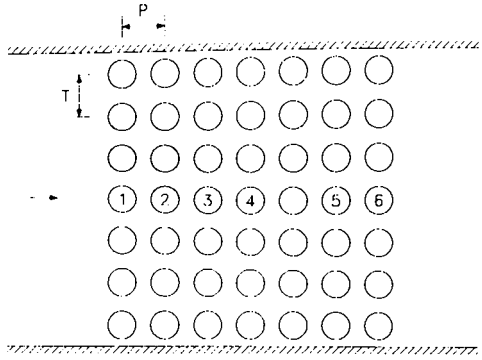

Fig. 1 Tube arrangement

minimum Reynolds number based on the gap flow velocity is $\sim 1.5 \times 10^4$. With a maximum gap flow velocity of 13.7 m/s, a Reynolds number of $\sim 3.5 \times 10^5$ can be reached.

Fluid-force components depend on the upstream turbulence. Different grids were placed upstream to vary the flow field. Tests were conducted for three grids—grid A, grid B, and grid C. Grid A a perforated plate 0.159 cm (0.0625 in.) thick with 0.476 cm (0.1875 in.) diameter holes. Grids B and C were constructed by drilling holes uniformly in a closely-packed array through 2.86 cm (1-1/8 in.) thick plates. The grid and turbulence characteristics are given in Table 1 [34].

The test section consists of seven rows of tubes. The pitch to diameter ratios are 1.75 ($P/D = T/D = 1.75$), as shown in Fig. 1. To measure fluctuating fluid forces, two piezoelectric three-axial transducers (one at each end of the test tube) were used. The active length is the channel width 30 cm (11.75 in.). The location of the test tube in the test section is shown in Fig. 1.

III Test Procedures and Data Analyses

In each test, fluid pressure, flow velocity, and fluid forces acting on the tubes were measured. The total flowrate was measured by turbine flow-meters. The mean flow velocity was obtained by dividing the flowrate by the net flow area. All calculations are based on the gap flow velocity. The experimental uncertainty of various parameters is given in Table 2.

In each test run, the flow velocity was increased by small intervals. At each flow velocity, the flulid force components in the lift and drag directions were recorded on a magnetic tape for several minutes for subsequent analysis. A fast Fourier transform analyzer was used to determine fluid force characteristics. Low-pass filters were used to filter out the transducer tube resonant frequency ($f = 240$ Hz).

Fluid excitation forces acting on the tubes are

$$g_j = \frac{1}{2}\rho U^2 D C_{Dj} + \frac{1}{2}\rho U^2 D C'_{Dj}\sin(\Omega_{Dj}t + \phi_{Dj}) + g'_j$$

and (8)

$$h_j = \frac{1}{2}\rho U^2 D C_{Lj} + \frac{1}{2}\rho U^2 D C'_{Lj}\sin(\Omega_{Lj}t + \phi_{Lj}) + h'_j,$$

where C_{Dj} (C_{Lj}) is the steady drag (lift) coefficient, C'_{DJ} (C'_{Lj}) is the fluctuating drag (lift) coefficient, Ω_{Dj} (Ω_{Lj}) is the circular frequency of periodic flow excitation in the drag (lift) direction and ϕ_{Dj} (ϕ_{Lj}) the corresponding phase angle, and g'_j (h'_j) is the random fluctuating drag (lift) force. The steady drag and lift forces cannot be measured with piezoelectric transducers. In this paper, RMS fluctuating drag and lift coefficients are given:

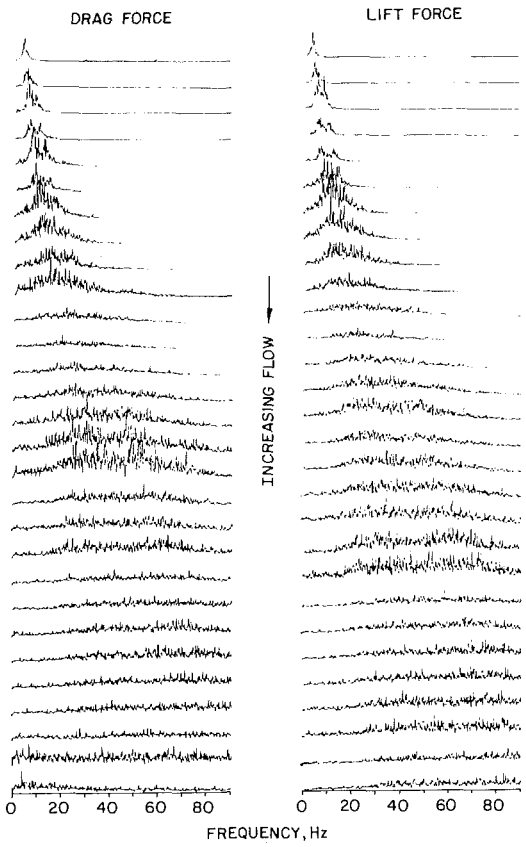

Fig. 2 Frequency spectra of drag and lift forces for tube 4 with grid A

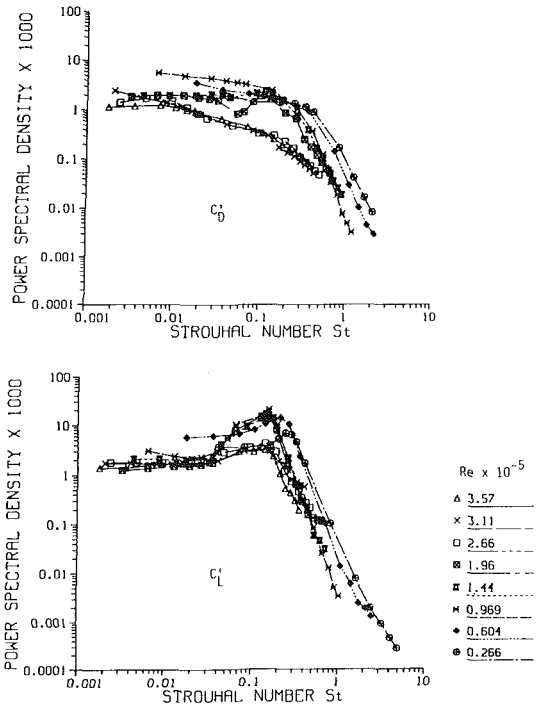

Fig. 3 Normalized fluid-force power spectra for tube 2 with grid A

$$\bar{C}'_{Dj} = <C'_{Dj}\sin(\Omega_{Dj}+\phi_{Dj}) + \frac{2}{\rho U^2 D} g'_j>^{1/2}$$

and (9)

$$\bar{C}'_{Lj} = <C'_{Lj}\sin(\Omega_{Lj}+\phi_{Lj}) + \frac{2}{\rho U^2 D} h'_j>^{1/2},$$

where $<>$ denotes mean square value of the argument.

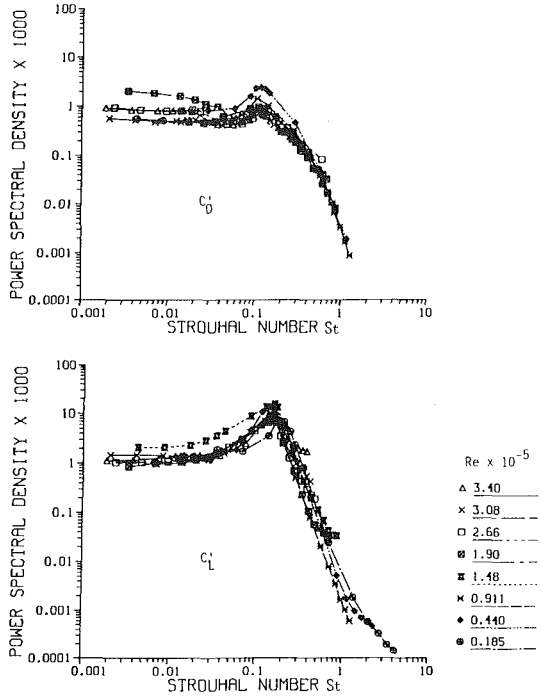

Fig. 4 Normalized fluid-force power spectra for tube 2 with grid C

Tubes located at different positions were measured. In each test run, two tubes were measured simultaneously (see Fig. 1):

Run 1 – tubes 1 and 4.
Run 2 – tubes 2 and 3.
Run 3 – tubes 5 and 6.

In each test run, fluid forces acting on two tubes were measured simultaneously. The correlations from these fluid forces can be calculated. Broad-band and narrow-band correlations using different pairs of tubes were obtained for tubes 2 and 3 and tubes 5 and 6. From the correlations, the convection velocity of the excitation can be calculated.

IV Experimental Results

The measurements were taken from subcritical to transition regions. The gap flow velocity, calculated from the flow rate divided by the gap flow area, is about $0.61\ \text{m/s} < U < 13.7\ \text{m/s}$. The results are presented based on the gap flow velocity.

Figure 2 shows typical frequency spectra of the lift and drag forces as a function of flow velocity. The characteristics of the fluid excitation forces depend on the location of the tubes and the incoming flow conditions. At low flow velocities, the dominant frequencies are associated with the vortex excitations. At higher flow velocities, the frequency spectra for tube 1 are different with different grids. With grid A, the dominant contribution is attributed to the low frequency while with grid C, the dominant frequency increases with flow velocity. In contrast, the downstream tube is insensitive to the upstream flow conditions; the frequency spectra of the lift forces with grids A and C are similar. Once the fluid has passed the first few rows, the fluid forces are insensitive to the location of the tubes. For example, the lift-force spectra for tube 6 with grid A and grid C are similar. The turbulence in the incoming flow is modified by the tubes; i.e., the flow going through the tube array is conditioned by the tubes, regardless of the incoming flow characteristics. This result is consistent with the turbulence measurements by Sandifer and Bailey [19], who show that the turbulence intensity starts at a low level at the entrance to the bundle (4 percent) and gradually increases up to about 23 percent after the third row.

Figure 2 shows the frequency spectra $\Phi(f)$ of the drag and lift forces for an interior tube with grid A. The frequency spectra in the lift and drag directions are similar. This agrees with the measurements by Savkar [35]. However, for the upstream tubes, there are some differences between the lift and drag spectra.

To characterize the fluid excitation forces, a normalization of the fluid forces was made. Figures 3 and 4 show the normalized power spectral density $\bar{\Phi}$ of the lift and drag forces of Tube 2 with grids A and C as a function of $S(=fD/U)$. The spectral density of force $\Phi(f)$ is normalized by the dynamic pressure head multiplied by tube length and tube diameter [27]; i.e.,

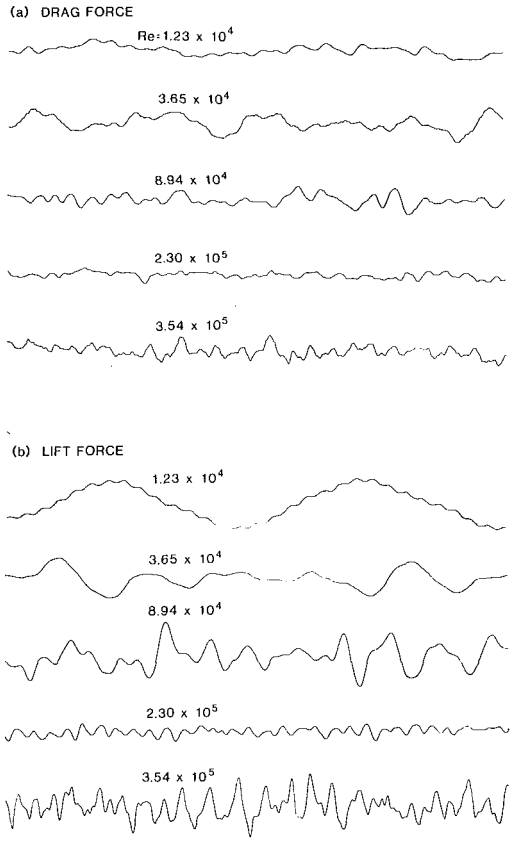

Fig. 5 Drag and lift forces of tube 6 with grid A

$$\bar{\Phi}(s) = \frac{\Phi(f)}{\left(\frac{1}{2}\rho U^2 D\ell\right)^2} \times \frac{U}{D} \tag{10}$$

where ℓ is tube length. From Figs. 3 and 4 and other PSD curves, several features are noted:

- For small St, the curves are fairly flat. There is a peak at the Strouhal frequency in some cases. For St > 0.2, the power spectral density decreases drastically.
- The power spectral density is insensitive to Re for most of the curves.
- The general shapes of the power spectral density curves for drag and lift forces are qualitatively similar.
- The Strouhal frequency peak in the spectrum increases with the increase of the tube row.
- Comparing Figs. 3 and 4 shows that the upstream turbulence does not affect the general shape of the spectral density curves significantly.
- The power spectral density curves are similar to those of an isolated tube in crossflow [34].

Figure 5 shows the fluctuating lift and drag forces for tube 6 with grid A for five representative Re to illustrate the changing nature of the force. At $\mathrm{Re} = 1.23 \times 10^4$, the fluctuating lift is periodic. With the increase of Re, the lift force changes from highly organized to random. The organized nature of the lift force is indicative of the orderly alternate vortex shedding. At higher Re, the shed vortices would no longer have a distinct frequency. These characteristics are basically the same as those for an isolated tube.

In the subcritical flow velocity range, some of the dominant frequencies increase with flow velocity. These frequency peaks are believed to be vortex shedding frequencies. The Strouhal numbers determined from the frequency peaks are given in Table 3. There are no detectable peaks for tube 1 except the lift force with grid C. Similarly, for tube 2, the frequency peaks are not well defined for grids A and B. For tubes 4, 5, and 6 the Strouhal number calculated from the drag force frequency peaks is 0.11, while from the lift force, two values are obtained, 0.11 and 0.17 ~ 0.19. If the Strouhal numbers are calculated based on the approach flow velocity, the Strouhal numbers are 0.26 and 0.40 ~ 0.45, respectively. The value of 0.26 compares well with those by Chen [21] and Fitz-Hugh [20].

Figures 6 to 8 show the RMS values of the lift and drag coefficients, $\bar{C}'_L$ and $\bar{C}'_D$, for the six tubes for three different tur-

Table 3 Strouhal number

Tube number	Lift force			Drag force		
	Grid A	Grid B	Grid C	Grid A	Grid B	Grid C
1	None	None	0.16	None	None	None
2	None	0.11 0.18	0.16	None	None	0.11
3	0.11 0.18	0.11 0.18	0.16	0.11	0.11	0.11
4	0.11 0.18	0.11 0.17	0.10 0.17	0.11	0.11	0.11
5	0.11 0.18	0.11 0.17	0.10 0.17	0.11	0.11	0.11
6	0.11 0.19	0.11 0.19	0.10 0.17	0.11	0.11	0.11

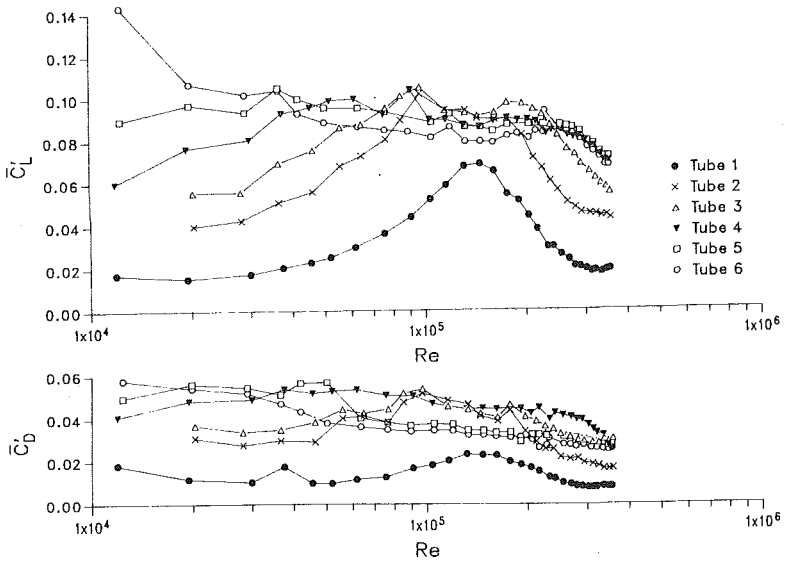

Fig. 6 RMS fluctuating drag and lift coefficients with grid A

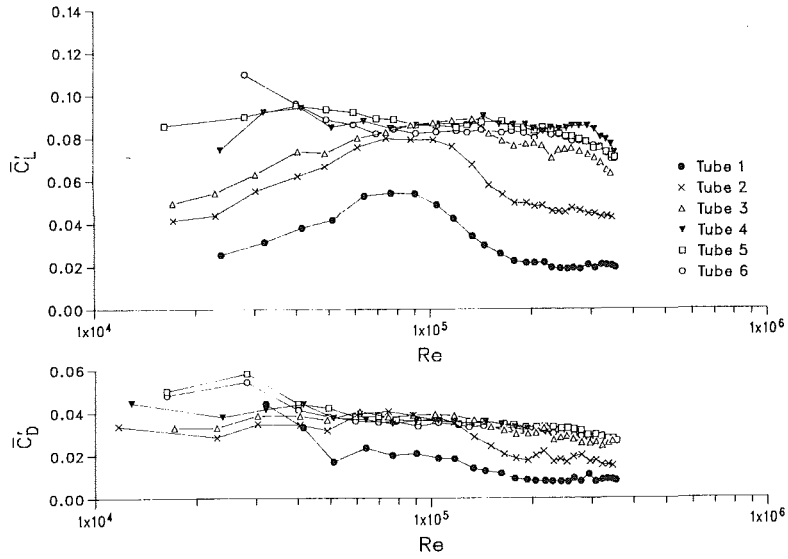

Fig. 7 RMS fluctuating drag and lift coefficients with grid B

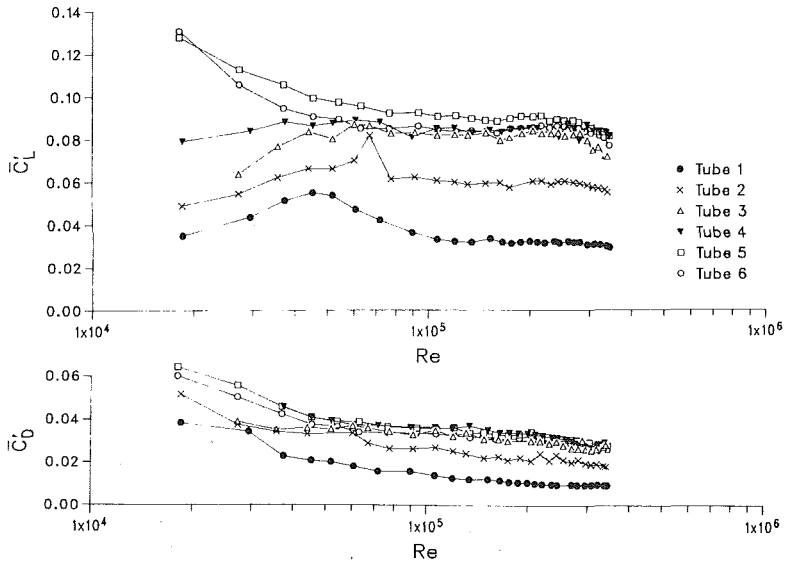

Fig. 8 RMS fluctuating drag and lift coefficients with grid C

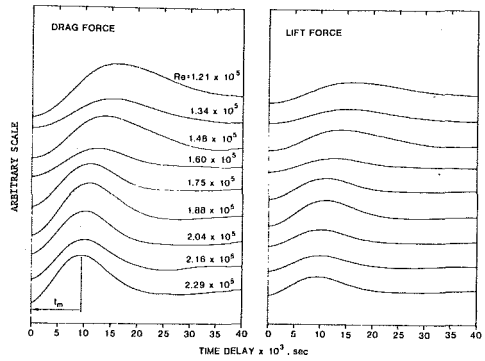

Fig. 9 Correlation function of drag and lift forces for tubes 5 and 6 with grid C

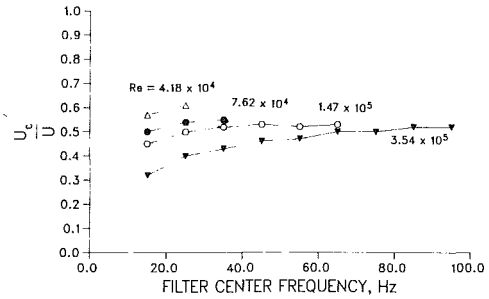

Fig. 10 Ratio of U_c/U as a function of filter center frequency

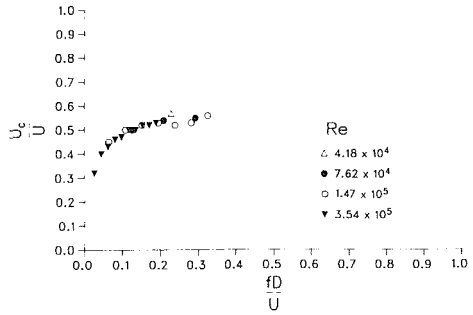

Fig. 11 Ratio of convection velocity to gap velocity as a function of the reduced frequency

bulence intensities. Several features of these data are worth noting:

- The lift coefficient $\bar{C}'_L$ is always larger than the drag coefficient $\bar{C}'_D$ for all six tubes for three turbulence intensities and at all flow velocities (Re) except that for tube 1 with grids B and C and $\text{Re} < 3 \times 10^4$. The larger values of $\bar{C}'_L$ are attributed partly to the contribution of vortex shedding.
- The progression of the measured $\bar{C}'_L$ and $\bar{C}'_D$ as a function of the row was more or less monotonic for the first four rows. The values of these coefficients for tubes beyond the fourth row are approximately constant.
- There is a peak in the fluid force coefficients for tube 1. The peak occurs at $\text{Re} = 1.5 \times 10^5$ for grid A, 8×10^4 for grid B, and 4.5×10^4 for grid C. The peak becomes smaller as the turbulence in the incoming flow increases.
- The variation of $\bar{C}'_L$ with Re for the tubes beyond the third row is the same as those for $\bar{C}'_D$. This in conjunction with the frequency spectra suggests that the fluctuations measured are probably in the gross flow field. This is consistent with the measurements by Savkar [35].
- For the interior tubes (tubes beyond the third row), the amplitude of $\bar{C}'_D$ is about 40 percent of $\bar{C}'_L$. This is comparable with the 50–60 percent obtained by Savkar [35] for a pitch ratio of 1.71.

The fluctuating drag and lift coefficients are much smaller than those obtained by Savkar [35]. This is attributed to two causes:

- The gap flow velocity is used in computing the force coefficient; this will reduce the magnitude in proportion to $(T-D)^2/T^2$.
- The resultant force acting on the tube is measured; the effective length is the channel width. In the experiments by Savkar, the active length is smaller.

Typical correlation plots for the lift and drag forces for tubes 5 and 6 are given in Fig. 9 for a series of flow velocities. The curves are plotted as a function of time delay. As can be seen from Fig. 9, the individual correlation curves peak at a given value of time delay. The peaking of the correlation curves is associated with the convection of the excitation forces and a convection velocity is defined as

$$U_c = P/t_m, \tag{11}$$

where P is the longitudinal tube pitch and t_m is the time delay of the maximum correlation of the fluid forces acting on the two tubes. From equation (11), U_c can be calculated. The convection velocity represents the speed at which the fluid excitation force is transported downstream.

Figure 10 shows the values of U_c/U as a function of filter center frequency with a bandwidth of 10 Hz for the lift forces on tubes 5 and 6 with grid A, where U is the gap flow velocity. The value of U_c/U depends on Re and center filter frequency; it decreases with Re and increases slightly with the center frequency. This illustrates that the lower-frequency excitations propagate at a lower speed.

Figure 11 shows the value of U_c/U as a function of the reduced frequency for tubes 5 and 6. All data for different frequency and Reynolds number collapse in one curve. U_c/U increases with fD/U. This is contrary to the case for turbulent wall-pressure fluctuation on a plate or a body of revolution, in which U_c/U decreases with reduced flow velocity [36, 37].

Figure 12 shows the ratio of U_c and U as a function of Re for tubes 2 and 3 and tubes 5 and 6. The convection velocity of the excitation force relative to the gap flow velocity is not very sensitive to the change of Re. It decreases slightly with the increase of Re.

The convection velocity for the drag force is higher than that for the lift force. This implies that the flow noises contributing to the lift and drag forces are not the same.

The convection velocity is expected to depend on other system parameters. For example, the effective length of the tube can affect the convection velocity.

The convection information is useful for prediction of tube response. In addition, it can be used to estimate the gap flow velocity U in the tube array. The gap flow velocity is difficult to measure. Once the convection velocity of the fluid excitation forces is known, U can be calculated.

The experimental data have illustrated the general characteristics of flow across a tube array. As the flow passes through each row of tubes, the fluid is subjected to resistance, the effect of which is to convert some of the fluid pressure energy to turbulence energy. In the first few rows, the transformation of energy occurs in a more orderly manner. As the flow reaches the interior tubes, unsteadiness of the flow increases and, usually, a randomness of the flow and its pressure fluctuation exists in the flow field.

V Discussion and Conclusions

One of the objectives of studying the fluid excitation forces

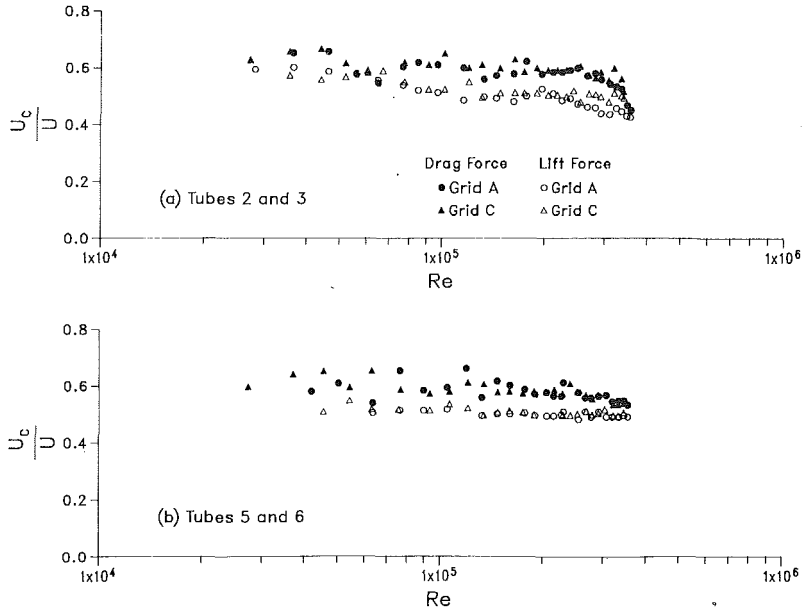

Fig. 12 Convection velocity as a function of Reynolds number

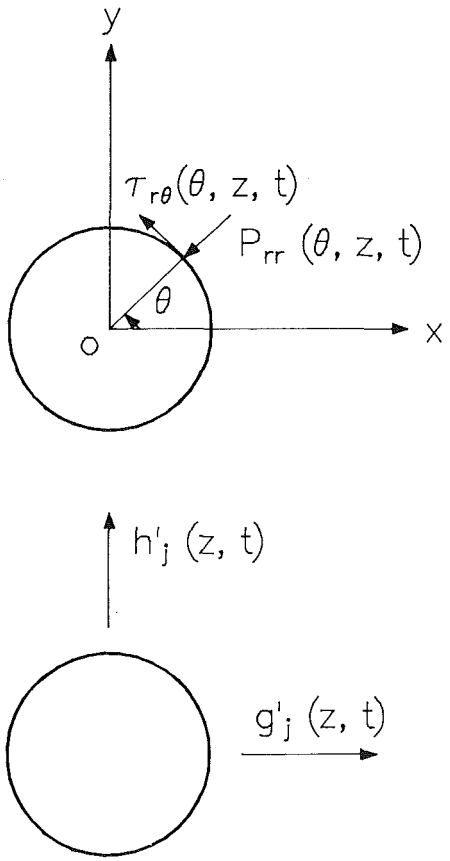

Fig. 13 Fluid excitation force components

is to predict tube response to turbulent buffeting. The general procedures for analysis of tube response to various excitations are given in reference [38].

Turbulent buffeting is attributed to the fluid excitation forces $g_j(z, t)$ and $h_j(z, t)$, which, in turn, depend on the pressure p_{rr} and shear stresses $\tau_{r\theta}$ on the surface of the tube (see Fig. 13).

$$g_j(z, t) = -\int_0^{2\pi} R_j p_{rr}(\theta, z, t)\cos\theta \, d\theta - \int_0^{2\pi} R_j \tau_{r\theta}(\theta, z, t)\sin\theta \, d\theta$$

and (12)

$$h_j(z, t) = -\int_0^{2\pi} R_j p_{rr}(\theta, z, t)\sin\theta \, d\theta + \int_0^{2\pi} R_j \tau_{r\theta}(\theta, z, t)\cos\theta \, d\theta,$$

where R_j is the radius of tube j. To predict tube response to turbulent buffeting, it is necessary to know the fluid pressure and shear stress acting on the tube surface.

In this study, the resultant fluid forces $G_j(t)$ and $H_j(t)$ are measured; i.e.,

$$G_j(t) = \int_0^{\ell} g_j(z, t)dz$$

and (13)

$$H_j(t) = \int_0^{\ell} h_j(z, t)dz,$$

where ℓ is the effective tube length. In the test section, the flow is uniform; therefore

$$G_j(t) = \ell g_j(t)$$

and (14)

$$H_j(t) = \ell h_j(t).$$

Based on the measured $G_j(t)$ and $H_j(t)$, the tube response can be calculated.

The analysis is straightforward. However, practical applications to most system components encounter some difficulties: First, many system components are subjected to turbulent flow at high Reynolds number. As shown in the published data and the fluid force coefficients obtained in this test, the fluid forces depend on Reynolds number. To obtain the precise fluid excitation forces, simulation of Re is required.

Second, the characteristics of the incoming flow field are important; these include turbulence intensities and scales and flow velocity distribution along the tube axis. In the test, the

flow is uniform. The detailed flow characteristics in the incoming flow generally are highly turbulent and are not uniform. Without the incoming flow characteristics, it will be difficult to predict tube response.

Third, turbulent buffeting is random. Random vibration theory is more appropriate to describe the tube response. To complete such an analysis, it is necessary to have the power spectra of the fluid forces and correlations in the axial direction and among different tubes. This information is not available at this time.

In spite of the difficulty in predicting the tube response in the practical environment, the experimental data presented in this paper provide additional insights into the turbulent excitation forces acting on a tube array in crossflow.

- The fluid forces acting on the first few rows depend on the incoming flow conditions. Once the flow has passed through 3 to 4 rows, the flow and its excitation on the tubes reach a steady-state condition.
- In the square array tested, the RMS values of the lift coefficients are larger than the drag coefficients for $10^4 < \mathrm{Re} < 3.5 \times 10^5$.
- As the flow passes through a tube array, the turbulence intensity increases and the resulting fluid excitation forces increase.
- The power spectral densities of the fluid excitation forces are fairly flat for $U/fD < 0.1$; a peak occurs at the Strouhal frequency and then decreases drastically with increasing U/fD.
- The convection velocity for drag force is higher than that for lift force. The convection velocity varies from 0.5 to 0.7 of the gap flow velocity and it increases with U/fD.

To predict practical system response, further work should be done in two areas: measurements of fluid forces in full-scale model, and simplified mathematical models. The first will provide the necessary excitation forces and the second will facilitate analysis using random vibration theory. Results from these studies will be useful in applications components consisting of tube arrays.

Acknowledgments

This work was performed under the sponsorship of NASA-Lewis Research Center. The authors gratefully acknowledge the interest of Drs. Lou Povinelli, Jeffrey Haas, and John Schwab.

References

1 Lienhard, J. H., "Synopsis of Lift, Drag and Vortex Frequency Data for Rigid Circular Cylinders," Washington State University, College of Eng. Research Division Bulletin 300, 1966.

2 Morkovin, M. V., "Flow Around Circular Cylinders. A Kaleidoscope of Challenging Fluid Phenomena," *ASME Symposium on Fully Separated Flows*, Philadelphia, Pa., 1964, pp. 102–118.

3 Mair, W. A., and Maull, O. J., "Bluff Bodies and Vortex Shedding – A Report on Euromech 17," *J. Fluid Mech.*, Vol. 45, Part 2, 1971, pp. 209–224.

4 Marris, A. W., "A Review on Vortex Streets, Periodic Wakes and Induced Vibration Phenomena," ASME Journal of Basic Engineering, Vol. 86, 1964, pp. 185–196.

5 Berger, E., and Wille, R., "Periodic Flow Phenomena," *Ann. Rev. Fluid Mech.*, Vol. 4, 1972, pp. 313–340.

6 Zdravkovich, M. M., "Review of Flow Interference between Two Circular Cylinders in Various Arrangements," ASME JOURNAL OF FLUIDS ENGINEERING, Vol. 99, 1977, pp. 618–633.

7 Zdravkovich, M. M., "Classification of Flow-Induced Oscillations of Two Parallel Circular Cylinders in Various Arrangement," ASME *Sym. on Flow-Induced Vibration*, Vol. 2, 1984, p. 1–18.

8 Chen, S. S., "A Review of Flow-Induced Vibration of Two Circular Cylinders in Crossflow," ASME *J. Pressure Vessel Technology*, Vol. 108, 1986, pp. 382–393.

9 Weaver, D. S., and Abd-Rabbo, A., "A Flow Visualization Study of a Square Array of Tubes in Water Cross Flow," ASME JOURNAL OF FLUIDS ENGINEERING, Vol. 107, 1985, pp. 354–363.

10 Abd-Rabbo, A., and Weaver, D. S., "A Flow Visualization Study of Flow Development in a Staggered Tube Array," *J. Sound and Vibration*, Vol. 106, No. 2, 1986, pp. 241–256.

11 Ishigai, S., Nishikawa, E., Yagi, E., "Structures of Gas Flow and Vibration in Tube Banks with Tube Axes Normal to Flow," *Int. Sym. on Marine Engineering*, Tokyo, 1973, pp. 1-5–23 to 1-5–33.

12 Chen, Y. N., "The Sensitive Tube Spacing Region of Tube Bank Heat Exchangers for Fluid-Elastic Coupling in Cross Flow," Fluid Structure Interaction Phenomena in Pressure Vessel and Piping Systems, ASME PVP-PB-026, 1977, pp. 1–18.

13 Zdravkovich, M. M., and Namork, J. E., "Structure of Interstitial Flow Between Closely Spaced Tubes in Staggered Array," *Flow Induced Vibrations*, ASME Publication, 1979, pp. 41–46.

14 Morsy, M. G., "Skin Friction and Form Pressure Loss in Tube Bank Condensers," *Proc. Instn. Mech. Engr.*, Vol. 189, 49/75, 1975.

15 Aiba, S., Tsuchida, H., and Ota, T., "Heat Transfer Around Tubes in Staggered Tube Banks," *Bulletin of the JSME*, Vol. 25(204), 1982, pp. 927–933.

16 Aiba, S., Tsuchida, H., and Ota, T., "Heat Transfer Around Tubes in Inline Tube Banks," *Bulletin of the JSME*, Vol. 25(204), 1982, pp. 919–926.

17 Heinecke, E. P., and Mohr, K. H., "Investigations on Fluid Borne Forces in Heat Exchangers with Tubes in Cross Flow," *Proc. Int. Conf. on Vibration in Nuclear Plant*, Keswick, U.K., 1982.

18 Price, S. J., Paidoussis, M. P., Macdonald, R., and Mark, B., "The Flow-Induced Response of a Single Flexible Cylinder in an Array of Rigid Cylinders: A Comparison Between Air- and Water-Flow Tests," *Flow-Induced Vibration - 1986*, ASME PVP 104, 1986, pp. 107–117.

19 Sandifer, J. R., and Bailey, R. T., "Turbulent Buffeting of Tube Arrays in Liquid Crossflow," *Proc. ASME Sym. on Flow-Induced Vibrations*, Vol. 2, 1984, pp. 211–226.

20 Fitz-Hugh, J. S., "Flow-induced Vibration in Heat Exchangers," *Proc. Int. Sym. on Vibration Problems in Industry*, Keswick, U. K., Paper No. 427, 1973.

21 Chen, Y. N., "Flow-Induced Vibration and Noise in Tube Bank Heat Exchangers due to von Karman Streets," ASME *Journal of Engineering for Industry*, Vol. 90, 1986, pp. 134–146.

22 Chen, Y. N., "Fluctuating Lift Forces of the Karman Vortex Streets on Single Circular Cylinders and in Tube Bundles, Part 3 – Lift Forces in Tube Bundles," ASME *Journal of Engineering for Industry*, Vol. 94, 1972, pp. 603–628.

23 Pettigrew, M. J., and Ko, P. L., "A Comprehensive Approach to Avoid Vibration on Fretting in Shell and Tube Heat Exchangers," *Flow-Induced Vibration of Power Plant Components*, PVP-41, ASME, 1980, pp. 1–18.

24 Savkar, S. D., and Litzinger, T. A., "Buffeting Forces Induced by Cross Flow Through Staggered Arrays of Cylinders," General Electric CRD Report No. 82CRD238, 1982.

25 Zdravkovich, M. M., Singh, S., Nuttall, J. A., and Causon, D. M., "Flow Induced Vibration in Staggered Tube Banks," Sixth Thermodynamics and Fluid Mechanics Convention, University of Durham, Apr. 1976.

26 Pettigrew, M. J., and Gorman, D. J., "Vibration of Heat Exchanger Tube Bundles in Liquid and Two-Phase Cross-Flow," ASME Publication, *Flow-Induced Vibration Design Guidelines*, PVP Vol. 52, 1981, pp. 89–109.

27 Blevins, R. D., Gibert, R. J., and Villard, B., "Experiment on Vibration of Heat Exchanger Tube Arrays in Cross Flow," *Trans. 6th Int. Conf. on Structural Mechanics in Reactor Technology*, Paris, Paper No. B6/9, 1981.

28 Toebes, G. H., "The Unsteady Flow and Wake Near an Oscillating Cylinder," ASME *Journal of Basic Engineering*, Vol. 91, 1969, pp. 831–838.

29 Wootton, L. R., Warner, M. H., and Cooper, D. H., "Some Aspects of the Oscillations of Full-Scale Pipes," *Flow-Induced Structural Vibrations*, Ed. by E. Naudascher, Springer-Verlag, Berlin, 1974, pp. 587–601.

30 Griffin, O. M., "Universal Similarity in the Wakes of Stationary and Vibrating Bluff Structures," ASME JOURNAL OF FLUIDS ENGINEERING, Vol. 103, 1981, pp. 52–58.

31 Miller, B. L., "The Hydrodynamic Drag of Roughened Circular Cylinders," Paper 9, Roy. Instn. Nav. Arch., Spring Meeting, 1976.

32 King, R., "Vortex Excited Oscillations of Yawed Circular Cylinders," ASME JOURNAL OF FLUIDS ENGINEERING, Vol. 99, 1977, pp. 495–502.

33 Ramberg, S. E., "The Effects of Yaw and Finite Length Upon the Vortex Wakes of Stationary and Vibrating Circular Cylinders," *J. Fluid Mech.*, Vol. 128, 1983, pp. 81–107.

34 Mulcahy, T. M., "Design Guides for Single Circular Cylinder in Turbulent Crossflow," ANL – CT-82-7, Argonne National Laboratory, Argonne, IL, 1982.

35 Savkar, S. D., "Buffeting of Cylindrical Arrays in Crossflow," *Proc. Sym. on Flow-Induced Vibrations*, Vol. 2, 1984, pp. 195–210.

36 Schloemer, H. H., "Effects of Pressure Gradients on Turbulent-Boundary-Layer Wall-Pressure Fluctuations," *J. Acoust. Soc. Am.*, Vol. 42, 1967, pp. 93–113.

37 Bakewell, H. P., "Turbulent Wall-Pressure Fluctuations on a Body of Revolution," *J. Acoust. Soc. Am.*, Vol. 43, 1968, pp. 1358–1363.

38 Chen, S. S., "Dynamics of Heat Exchanger Tube Banks," ASME JOURNAL OF FLUIDS ENGINEERING, Vol. 99, No. (3), 1977, pp. 462–469.

Investigation of Third-Order Closure Model of Turbulence for the Computation of Incompressible Flows in a Channel With a Backward-Facing Step

R. S. Amano
Associate Professor.
Mem. ASME

P. Goel
Student.

Department of Mechanical Engineering,
University of Wisconsin—Milwaukee,
Milwaukee, Wis. 53201

To predict the diffusion process of the Reynolds stresses in reattaching shear flows, the transport model for the triple-velocity products has been developed and tested for the computation of the flow in a channel with a backward-facing step. Upon comparison of the results of uuv, uvv, and vvv with those obtained by using existing algebraic correlations, it was shown that the present model improved the prediction of the triple-velocity products.

Introduction

In the computation of turbulent shear flows, it has become common to use the second-order closure of turbulence. While modern computational techniques enable us to successfully predict complex turbulent shear flows, it is still difficult to accurately predict a reattaching shear flow which is accompanied by a flow recirculation. This is partly because the computation should be performed with an elliptic approach which requires a large amount of computer time and storage and partly because a universal turbulence model that can predict such a complex turbulent flow incuding a flow reattachment, a flow recirculation and a recovering boundary layer has not yet been completely developed for universal usage.

It has been observed by many experimenters that, after the separation of a flow at the edge of the step, a rapid decay of turbulence energy begins at the start of the unsteady reattachment region, one to two step heights upstream of the mean reattachment point. This decay is followed by a short plateau of very slowly decreasing turbulence intensity before a second region of rapid decay begins downstream of the reattachment point. A similar trend was observed also by Chandrsuda and Bradshaw [1] in the decay of the triple-velocity products of turbulence fluctuation.

In a previous paper of Amano and Goel [2], the Reynolds stresses were computed by solving the full Reynolds stress equations for the reattaching shear layer; the results in recirculating, reattaching, and redeveloping regions were compared with the computations using the $k\sim\epsilon$ model and the algebraic stress model. Upon comparison with experimental data, it was proven that the computations using the Reynolds stress model, which takes the convective action of u_iu_j into account, produced more accurate predictions of the behavior of the stresses than the predictions obtained using the algebraic stress model.

Since the flow over a backward-facing step possesses several additional features over boundary layers or free mixing layers, a standard approach with the second-order closure model cannot handle most of the transport processes of turbulence quantities such as the Reynolds stresses, turbulence energy, pressure-strain correlations, and triple-velocity correlations. In particular, the triple-velocity products change their profiles rapidly in the reattachment region due to the constraint of the mean velocities at the solid wall, resulting in distortion of the large eddies due to an irrotational mechanism. Since the turbulent transport by the triple-velocity products is a significant part of the Reynolds-stress balance in the shear flow region, it must be formulated with reasonable accuracy in the turbulence model that is to be used for the flow predictions.

To date, algebraic correlations have been proposed by several researchers: Daly and Harlow [3], Hanjalic and Launder [4], Shir [5], and Cormack et al. [6], etc. Each proposer determined the coefficient of the model based on experimental data for duct/pipe flows, wall jets, or mixing layers except Cormack et al. who performed complete modeling of a generalized data-fitting formulation. All these models were tested by Amano and Goel [7] for reattaching shear layers. As a result it was found that the computed levels of the triple-velocity products are generally much lower than experimental data. A similar discussion was also given by Smits et al. [8]. The implication of these results is that algebraic correlations between the triple-velocity products and the Reynolds stresses are likely to be inadequate for such flows that contain a strong convective effect on solid walls due to a reattachment, making it necessary to use transport equations for the triple-velocity products.

The present paper is concerned with the modeling of the

Contributed by the Fluids Engineering Division and presented at the Winter Annual Meeting, Boston, Mass., December 13-18, 1987 of THE AMERICAN SOCIETY OF MECHANICAL ENGINEERS. Manuscript received by the Fluids Engineering Division March 4, 1986.

triple-velocity products, $\overline{u_iu_ju_k}$, for better evaluation of the diffusion rate of the Reynolds stresses. In particular, the convective and generative effects of the triple-velocity product, $u_iu_ju_k$, are investigated by formulating and solving the transport equations for the triple-velocity products in a channel with a backward-facing step. The results are compared with the computations using the algebraic correlations for the triple-velocity products, $u_iu_ju_k$, as well as the experimental data.

The Third-Order Closure Model

The transport equation for the kinematic Reynolds stress, $\overline{u_iu_j}$, can be written as

$$(U_k\overline{u_iu_j})_{,k} = -(\overline{u_ju_k}U_{i,k} + \overline{u_iu_k}U_{j,k}) - 2\nu\overline{u_{i,k}u_{j,k}} + \overline{(p/\rho)(u_{i,j}+u_{j,i})} - [\overline{u_iu_ju_k} - \nu(\overline{u_iu_j})_{,k} + \overline{(p/\rho)(\delta_{jk}u_i + \delta_{ik}u_j)}]_{,k} \quad (1)$$

In equation (1) the Reynolds stress tensor, $\overline{u_iu_j}$, is defined in terms of both the mean velocity field and the second and third-order correlations which are themselves unknown. The second and the third terms of equation (1) were closed only in terms of the second-order moments along with the turbulence energy, k, and the energy dissipation rate, ϵ (Daly and Harlow [3], and Naot et al. [9]).

The last bracketed term represents the diffusion of the Reynolds stresses due to turbulent velocity fluctuations, molecular viscosity, and pressure fluctuations. It has been shown by Irwin [10] that the diffusion due to viscosity and pressure fluctuations is negligibly small at large turbulence Reynolds numbers.[1] Thus the triple-velocity product is the most dominant diffusive agency for the kinematic Reynolds stresses.

The coefficients have been determined by respective originators by testing for relatively simple shear flows such as free jets or boundary layers. It was shown that, although all these models gave relatively low levels of the triple-velocity products, the model of Hanjalic and Launder [4] was the best for the prediction of backward-facing step flows because of its symmetric property in all directions. Indeed, agreement with the experimental data of Chandrsuda and Bradshaw [1] was the best for all three components, $\overline{uuv}$, $\overline{uvv}$, and $\overline{vvv}$. However, it was also discussed that since none of these models could take the convective and generative actions of the triple-velocity products into account for the reattaching shear flows, the levels predicted with these models were not high enough.

[1] These terms appear to be small in most circumstances since turbulence energy budgets balance, to within experimental error, even when these are neglected.

Table 1 Coefficients for α_i

α_1	α_2	α_3	α_4
-8.14×10^{-3}	-1.72×10^{-2}	-4.80×10^{-2}	-1.02×10^{-1}

The Existing Models. The models used for comparison with the transport equation are given as follows:

(i) The model of Daly and Harlow [3]

$$\overline{u_iu_ju_k} = -0.25\tau\overline{u_ku_l}(\overline{u_iu_j})_{,l} \quad (2)$$

(ii) The model of Hanjalic and Launder [4]

$$\overline{u_iu_ju_k} = -0.11\tau[\overline{u_lu_j}(\overline{u_iu_k})_{,l} + \overline{u_lu_i}(\overline{u_ju_k})_{,l} + \overline{u_lu_k}(\overline{u_iu_j})_{,l}] \quad (3)$$

(iii) The model of Shir [5]

$$\overline{u_iu_ju_k} = -0.04\tau k(\overline{u_iu_j})_{,k} \quad (4)$$

(iv) The model of Cormack et al. [6]

$$\overline{u_iu_ju_k} = 4\tau k\{2\alpha_1(\delta_{ij}\delta_{kl}+\delta_{ik}\delta_{jl}+\delta_{kj}\delta_{il})k_{,l} + \alpha_2(a_{ik,j}+a_{ij,k}+a_{kj,i})\} + 2\tau\{2\alpha_3(\delta_{ik}a_{jl}+\delta_{ij}a_{kl}+\delta_{jk}a_{il})k_{,l} + \alpha_4(a_{ik}a_{jl,l}+a_{ij}a_{kl,l}+a_{kj}a_{il,l})\} \quad (5)$$

where

$$a_{ij} = \overline{u_iu_j} - \frac{2}{3}\delta_{ij}k \quad (6)$$

and where the coefficients α_i are given in Table 1.

The Transport Equation for $\overline{u_iu_ju_k}$. The general transport equation for the triple-velocity product is derived by suitable multiplication of the exact equation for a single fluctuating velocity by unaveraged Reynolds stresses; then, after time averaging of the resultant equation, the following is obtained:

$$(U_l\overline{u_iu_ju_k})_{,l} = -(\overline{u_iu_ju_k}U_{k,l} + \overline{u_ju_ku_l}U_{i,l} + \overline{u_ku_iu_l}U_{j,l}) \quad \text{(I)}$$

$$+ [\overline{u_iu_j}(\overline{u_ku_l})_{,l} + \overline{u_ju_k}(\overline{u_iu_l})_{,l} + \overline{u_ku_i}(\overline{u_ju_l})_{,l}] \quad \text{(II)}$$

$$-[\overline{u_iu_ju_ku_l} + \overline{(p/\rho)(u_ju_k\delta_{il}+u_ku_i\delta_{jl}+u_iu_j\delta_{kl})} - \nu(\overline{u_iu_ju_k})]_{,l} \quad \text{(III)}$$

$$+ \overline{(p/\rho)[(u_ju_k)_{,i} + (u_ku_i)_{,j} + (u_iu_j)_{,k}]} \quad \text{(IV)}$$

$$-2\nu[\overline{u_iu_{j,l}u_{k,l}} + \overline{u_ju_{k,l}u_{i,l}} + \overline{u_ku_{i,l}u_{j,l}}] \quad \text{(V)} \quad (7)$$

In equation (7) term (I) represents the generation due to mean

Nomenclature

C_{ij} = coefficients for near-wall Reynolds stresses (used in equation (11))
C_γ = coefficient used in the transport equation for $u_iu_ju_k$
H = step height
k = turbulence kinetic energy ($=\overline{u_i^2}$)
p = pressure fluctuation
P = mean pressure
u = fluctuating velocity in x direction
U = mean velocity
U_{IN} = inlet stream velocity
v = fluctuating velocity in y direction
x, y = Cartesian coordinates
y^+ = dimensionless distance from the wall ($=\rho k^{1/2}y/\mu$)
Y_0 = width of the channel upstream of the step
$\alpha_1, \alpha_2, \alpha_3, \alpha_4$ = constants (used in equation (5))
δ_{ij} = Kronecker delta
ϵ = energy dissipation rate
μ = dynamic viscosity
ν = kinematic viscosity
ρ = density
τ = turbulence time scale ($=k/\epsilon$)
ω = turbulence frequency ($=\epsilon/k$)

Subscripts

i, j, k, l = tensor notations

Symbols

$-$ = time averaged quantity

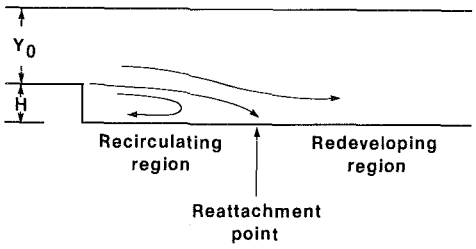

Fig. 1 Flow geometry

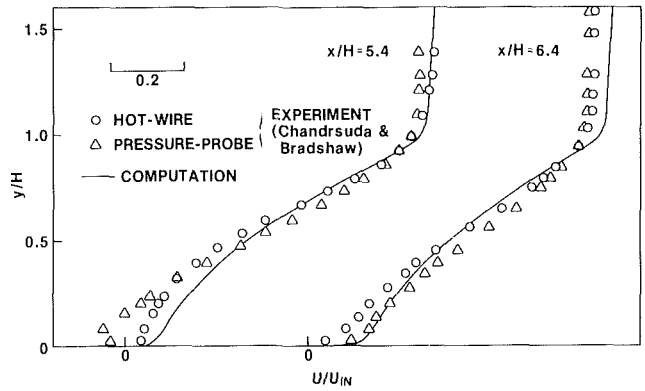

Fig. 2 Mean velocity profiles ($Y_0/H = 2.5$)

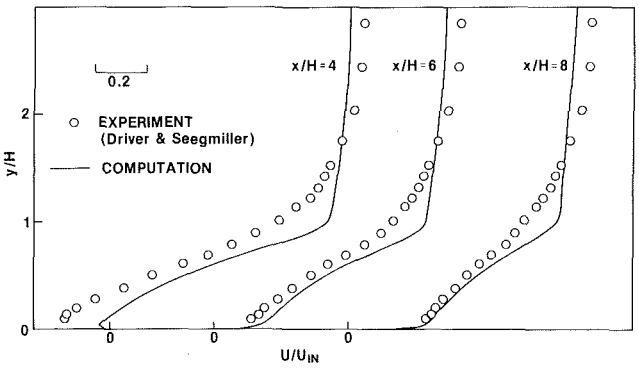

Fig. 3 Mean velocity profiles ($Y_0/H = 8.0$)

strains and term (II) corresponds to the generation due to turbulence stresses. Term (III) denotes the diffusion rate of the triple-velocity products. In the bracket the quadruple-velocity correlation is the most predominant one; the others make only a negligible contribution to the overall diffusive action of the third-moments. However, the last term in the bracket is kept in this research in order to account for the viscous effect. Here the quadruple-velocity product is approximated by assuming quasi-Gaussian following Hanjalic and Launder [4] as,

$$\overline{u_iu_ju_ku_l} = \overline{u_iu_j}\cdot\overline{u_ku_l} + \overline{u_iu_k}\cdot\overline{u_ju_l} + \overline{u_iu_l}\cdot\overline{u_ju_k} \tag{8}$$

Term (IV), which is the pressure-stress correlation, can be evaluated by the following approximation

$$(N) = -C_\gamma\omega\overline{u_iu_ju_k} \tag{9}$$

where the effect of the mean-strain contribution has been neglected. In fact, the mean-strain contribution, which corresponds to the "rapid" term for the second-order closure pressure-strain correlation, is not significant for the variation of the third-moments. This has been proven by the fact that term (I) of equation (7) is much smaller than term (II) in many shear layers.

The dissipation terms (term V) are neglected in the present study as was done by Hanjalic and Launder [4].

Table 2 Grid test

Mesh sizes	32×32 to 42×42	42×42 to 52×52	52×52 to 62×62
U	55.0%	40.0%	5.0%
u^2	75.0%	25.0%	1.0%
v^2	66.6%	33.4%	1.2%
uv	62.5%	37.5%	1.1%

The final form of equation (7) becomes

$$\begin{aligned} U_l(\overline{u_iu_ju_k})_{,l} = & \\ & -(\overline{u_iu_ju_l}U_{k,l} + \overline{u_ju_ku_l}U_{i,l} + \overline{u_ku_iu_l}U_{j,l}) \\ & -[\overline{u_ku_l}(\overline{u_iu_j})_{,l} + \overline{u_ju_l}(\overline{u_iu_k})_{,l} + \overline{u_iu_l}(\overline{u_ku_j})_{,l}] \\ & +[\nu(\overline{u_iu_ju_k})_{,l}]_{,l} - C_\gamma\omega\overline{u_iu_ju_k} \end{aligned} \tag{10}$$

The model introduced here is different from the model of Hanjalic and Launder for its possession of the convective terms which are considerably significant in separated shear layers. The viscous diffusion terms are also additional ones to the present model which accounts for viscous effects in the near-wall region. As was discussed in the introduction, it is known that the convective effect of the third-moments of turbulence through the separated shear layer becomes predominant when approaching the wall. In consequence, the model proposed here would more accurately predict the triple products of turbulence velocity fluctuations.

The Boundary Conditions. At the inlet of the channel, the triple-velocity products are evaluated using the model of Daly and Harlow (equation (2)). The outlet is located at 50 H downstream from the step where the continuative boundary condition is used; that is, the normal gradient of the triple-velocity products to the boundary is zero. Although the values of $\overline{u_iu_ju_k}$ at the wall are zero, these are evaluated using an algebraic model at the nodes next to the wall. Since the turbulence kinetic energy can be better defined with "the law of the wall" than with the Reynolds stresses in the near-wall region, the model of Shir, which has fewer terms with the Reynolds stresses than other models, was employed along with the so-called "near-wall Reynolds stresses" [2]. The near-wall Reynolds stresses are given as

$$\overline{u_iu_j} = C_{ij}k - (1-\delta_{ij})\frac{y}{\rho}\frac{dP}{dx} \tag{11}$$

where x is the streamwise coordinate and y is the normal coordinate to the wall. The coefficients are determined based on several experimental data as $c_{11} = 1.21$, $C_{22} = 0.24$, $C_{12} = 0.24$.

Results and Discussion

The Reynolds stresses, the mean velocities, the turbulence energy, the energy dissipation rate, and the triple-velocity products were computed in the flow field shown in Fig. 1. The method employed for these computations is based on the finite volume method which is the same as that used in [2]. Exploratory grid tests were attempted to achieve a grid-independent state for the mean velocities and the Reynolds stresses.

An example for this test is shown in Table 2. Here the percentile changes are shown when mesh sizes are increased. It is shown that there is no appreciable change from 52×52 to 62×62; thus, the case with 52×52 is chosen in the present study for both the cases of Chandrsuda and Bradshaw [1] and Driver and Seegmiller [11].

The dimensionless distance from a wall adjacent node to the wall varies from $y^+ = 6.7$ to 13.6 where the maximum y^+ occurs near the reattachment point and the minimum y^+ about 2H to 3H downstream therefrom.

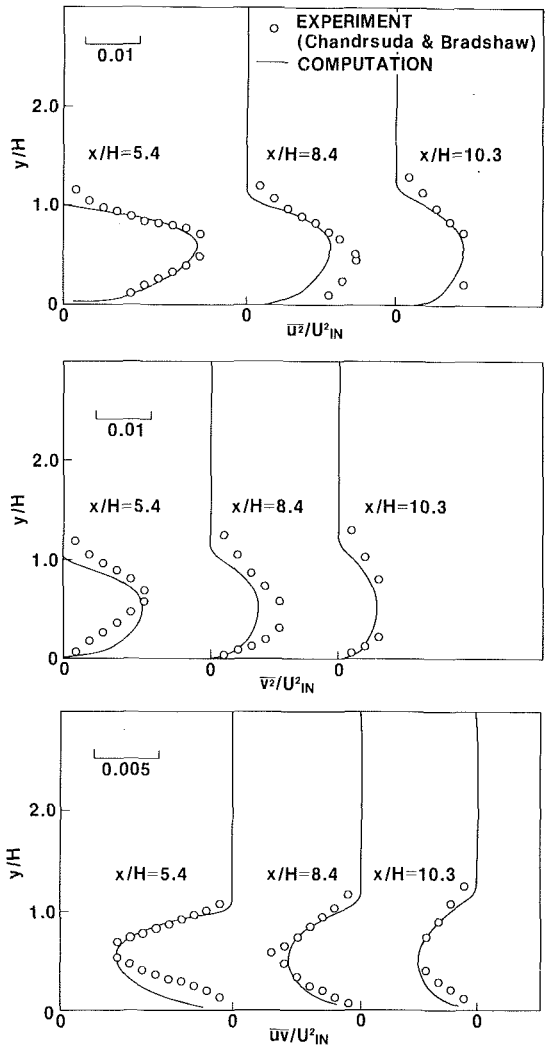

Fig. 4 Reynolds-stress profiles ($Y_0/H = 2.5$)

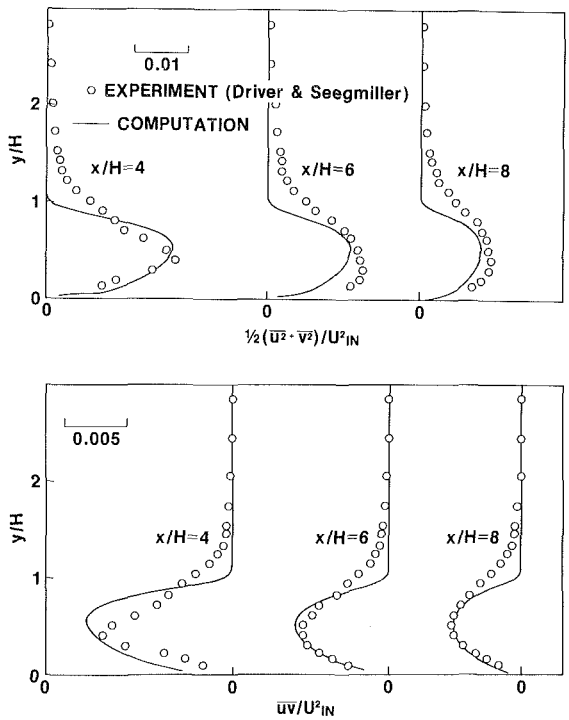

Fig. 5 Reynolds-stress profiles ($Y_0/H = 8.0$)

Figures 2 and 3 compare the mean velocity profiles with the experimental data near the reattachment point. In Fig. 2 two sets of experimental data are shown: one by a hot-wire and the other by a pressure-probe. Although a slight discrepancy is discernible, the trends are similar between measured data and computations. In the core of the shear flow, however, both data and the numerically determined profiles are in sufficient agreement.

Figures 4 and 5 show the Reynolds stress distributions at three different streamwise locations ranging between $x/H = 4$ and 10.3 which includes all recirculating, reattachment and recovering regions of the flow, and are compared with the experimental data of Chandrsuda and Bradshaw [1] and with that of Driver and Seegmiller [11], respectively. The computed results are in reasonable agreement with the experimental data.

Initially, the values of $\overline{u_i u_j u_k}$ were evaluated solving the model of Daly and Harlow [3]. Then equation (10) was solved with these initial values. Since equation (10) represents the transport equations of $\overline{uuu}$, $\overline{uuv}$, $\overline{uvv}$, and $\overline{vvv}$, and all four components are associated among themselves in their own equations, four transport equations were solved iteratively. The computations were terminated when the relative residual source of each triple-velocity product equation dropped below 3×10^{-12} which was typically attained after 50 iterations with CPU time of 7 minutes on a UNIVAC 1100.

After testing with different values of C_γ, the computation with $C_\gamma = 5.8$ was found to give the best agreement with the data of Chandrsuda and Bradshaw [1] and of Driver and Seegmiller [11]. This coefficient corresponds to an inverse coefficient $C_s = 1/C_\gamma = 0.17$ which is close to the value of $C_s = 0.11$ recommended for the Hanjalic and Launder model (see equation (3)). However, it may be premature to establish a fixed value for C_γ; this value can be finalized if more data are obtained for a variety of conditions.

Figures 6 and 7 compare the computations obtained using the present transport model (with $C_\gamma = 5.8$) with the results computed by using four algebraic models. It is observed that two peaks appear across the shear layer: one along the core of the separated shear layer, the other near the bottom wall. Although all the computations exhibit a similar trend to the experimental data, the predicted levels of $\overline{u_i u_j u_k}$ are fairly different. While the model of Shir gives the lowest levels for all three components, the model of Cormack et al. provides high levels for $\overline{uvv}$ and $\overline{vvv}$ but not for $\overline{uuv}$. Unlike the model of Cormack et al., the Daly-Harlow model gives high levels for only $\overline{uuv}$ and relatively low levels for both $\overline{uvv}$ and $\overline{vvv}$. Among the algebraic models the results with the Hanjalic-Launder model seem to be consistent showing nearly the same levels for all three components. This is because the Hanjalic-Launder model is the only one that has a symmetric property in all three directions.

Agreement between the present computations obtained using the transport equations and the experimental data is generally better than agreement found using the algebraic models for two reasons. First, the coefficient, C_γ, can be suitably adjusted whereas the algebraic models were tested for simpler shear flows and not for a reattaching shear layer. Second, the transport equations of $\overline{u_i u_j u_k}$ have a symmetric property in all three directions; thus, the predictions with the transport model are better for inhomogeneous flows as well as for homogeneous ones. However, the most important point we should note from Figs. 6 and 7 is that the location of the peak along the separated shear layer is predicted more accurately by using the transport equations than by using the algebraic models. This is primarily because the transport model takes both the convection and the generation due to mean strains into account; thus, the trail of energy propaga-

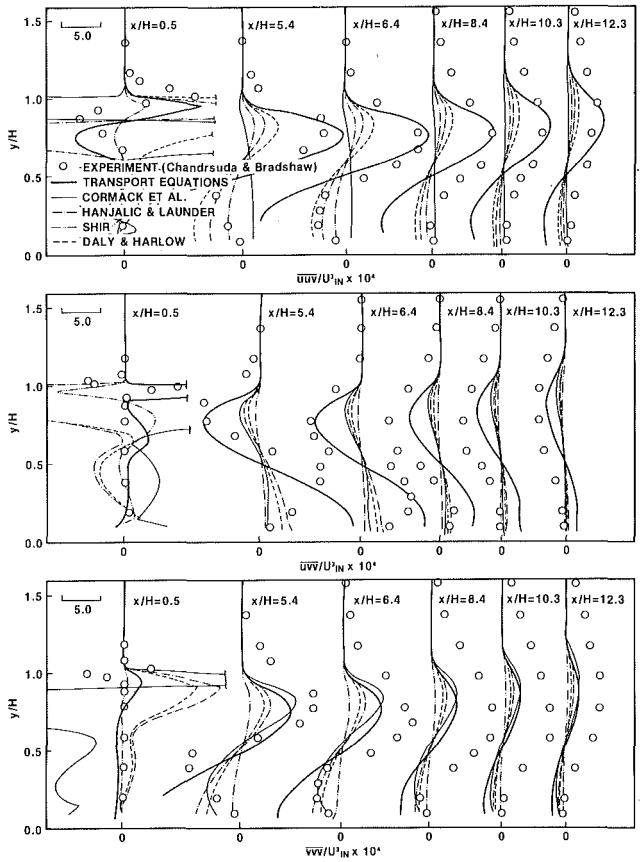

Fig. 6 Profiles of triple-velocity products ($Y_0/H = 2.5$)

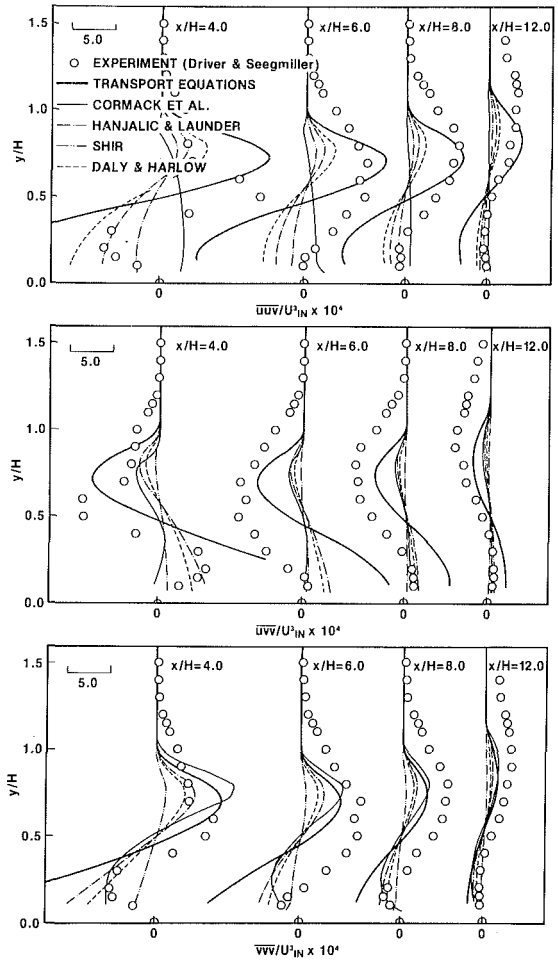

Fig. 7 Profiles of triple-velocity products ($Y_0/H = 8.0$)

tion for the triple-velocity products accords with the experimental data.

The results in Figs. 6 and 7 also suggest that the transport model needs to be improved to give better profiles near the wall. In the wall adjacent region the model must incorporate a low-Reynolds number effect, although the computations in the free shear flow region agree well with the data. The effect of the wall boundary condition on the profiles of $u_i u_j u_k$ near the wall was tested by adopting several other models for the numerical nodes next to the wall. However, the influence of the wall boundary condition was negligibly small. Therefore, to improve the prediction of the triple-velocity products in the near-wall region it is advisable to develop a low-Reynolds number model in order to take the viscous effect into account.

Conclusions

The transport model for $\overline{u_i u_j u_k}$ is developed and tested for the computations of the backward-facing step flow in a channel.

1. The transport model improves the prediction of the triple-velocity products in the separating shear layer region.
2. In the near-wall region a low-Reynolds number model must be devised for the transport equation of $\overline{u_i u_j u_k}$ in order to take the viscous effect into account.

Acknowledgment

This work is supported by NASA Lewis Research Center under Grant NAG 3-546, "A Study of Reynolds Stress Closure Model," monitored by Mr. Thomas VanOverbeke.

References

1 Chandrsuda, C., and Bradshaw, P., "Turbulence Structure of a Reattaching Mixing Layer," *Journal of Fluid Mechanics*, Vol. 110, 1981, pp. 171–194.

2 Amano, R. S., and Goel, P., "Computations of Turbulent Flow Beyond Backward-Facing Steps by Using Reynolds-Stress Closure," *AIAA Journal*, Vol. 23, No. 9, 1985, pp. 1356–1361 (Also AIAA Paper No. 84-1181.)

3 Daly, B. J., and Harlow, F. H., "Transport Equations in Turbulence," *The Physics of Fluids*, Vol. 13, No. 11, 1970, pp. 2634–2649.

4 Hanjalic, K., and Launder, B. E., "A Reynolds Stress Model of Turbulence and Its Application to Thin Shear Flows," *Journal of Fluid Mechanics*, Vol. 52, Part 4, 1972, pp. 609–638.

5 Shir, C. C., "A Preliminary Numerical Study of Atmospheric Turbulent Flows in the Idealized Planetary Boundary Layer," *Journal of Atmospheric Science*, Vol. 30, 1973, pp. 1327–1339.

6 Cormack, D. E., Leal, L. G., and Seinfeld, J. H., "An Evaluation of Mean Reynolds Stress Turbulence Models: The Triple-Velocity Correlation," ASME Journal of Fluids Engineering, Vol. 100, 1978, pp. 47–54.

7 Amano, R. S., and Goel, P., "A Study of Reynolds-Stress Closure Model," NASA CR-174342, 1985.

8 Smits, A. J., Young, S. T. B., and Bradshaw, P., "The Response of a Turbulent Boundary Layer to Lateral Divergence," *Journal of Fluid Mechanics*, Vol. 94, 1979, pp. 243–268.

9 Naot, D., Shavit, A., and Wolfshtein, M., "Two-Point Correlation Model and the Redistribution of Reynolds Stresses," *The Physics of Fluids*, Vol. 16, No. 6, 1973, pp. 738–743.

10 Irwin, H. P. A. H., "Measurements of a Self-Preserving Plane Wall Jet in a Positive Pressure Gradient," *Journal of Fluid Mechanics*, Vol. 61, 1973, pp. 33–63.

11 Driver, D. M., and Seegmiller, H. L., "Features of a Reattaching Turbulent Shear Layer Subject to an Adverse Pressure Gradient," *AIAA Journal*, Vol. 23, No. 2, 1985, pp. 163–171.

Noise and Erosion of Self-Resonating Cavitating Jets

G. L. Chahine
Principal Research Scientist,
Tracor Hydronautics, Inc.,
Laurel, Md.

P. Courbière
Commissariat a l'Energie Atomique
DRNR/STRS,
Saint Paul Lez-Durance, France

Self-resonating jets have been developed which take advantage of the natural tendency of a jet to organize in large structures. Tests have shown that these jets are both highly erosive and a source of a discrete frequency high level noise. Simultaneous investigations of the noise and erosion of these jets have been conducted and have shown a definite trend toward correlation. For instance, time evolution of volume removal rates of an impacted surface and rms readings of a pressure transducer have been found to be correlated. Similarly, shifts in the relative importance of the various frequencies have followed the advancement of erosion. These results could be of great advantage in the determination of the evolution of a jet cutting operation in progress. In this paper jet noise and erosion correlation tests will be described and the results analyzed.

Introduction

Cavitation is mainly known for its harmful effects, namely, loss of performance, erosion, and noise [1]. The usual procedure to prevent these deleterious effects is to avoid the phenomenon by proper design and by limiting the operating conditions. However, attempts to induce and harness cavitation for useful purposes have been increasingly successful. In high-pressure jets, cavitation has for some time now been purposely induced in order to increase their drilling, cutting, and cleaning capabilities [2–3]. The noise associated with cavitation is being used as a means of sensing cavitation when it becomes destructive and, hence, could allow for alleviating its damaging effects. More recently, a more direct utilization of cavitation noise in jets for sound generation was proposed and demonstrated [4–5].

The occurrence of cavitation in the high-volume flows of sodium in fast neutron reactors has prompted the French C.E.A. to undertake a large research program on cavitating sodium flows [6]. This was prompted primarily by the importance of the phenomena to the sodium pump development program. Because of the lack of sufficient understanding of cavitation erosion and its scaling laws in sodium, excessive safety margins are presently used for pump design. It is therefore highly desirable to develop techniques to discriminate between erosive and nonerosive cavitation events and flow conditions. Since optical detection of cavitation in sodium flowing at very high temperatures is not feasible, acoustic detection instrumentation (CANASTA) was developed at the Cadarache Nuclear Research Center, France.

Acoustic detectors and signal processing instrumentation (CANASTA) capable of handling the high-frequency signals created by cavitation has been developed at CEN/Cadarache. The ability of this instrumentation has been demonstrated using a liquid sodium test loop [7]. However, due to the extremely long time periods required to create measurable erosion in any traditional flow tunnel and therefore in the Cadarache sodium cavitation tunnel, test runs have been expensive and data collection somewhat difficult. In the work described here, erosion due to self-resonating cavitating jets is used to gather data which allows discrimination between the noise patterns created by erosive versus nonerosive cavitation. The high erosive capability of these jets which significantly shortens experimentation time relative to a cavitation tunnel was the incentive to conduct this investigation. In the work reported here, controlled erosion experiments on 316 stainless steel have been conducted. The time evolution of the erosion and the emitted noise were measured simultaneously. The objective was to evaluate the possibility of discrimination between erosive and nonerosive cavitation.

A significant amount of work was devoted earlier to the study of cavitation noise. An extensive review of these studies can be found in references [1, 8]. The efforts concentrated first on the noise of single bubbles [9, 10], then on the characterization of the noise of a hydrodynamic cavitating field [11, 12]. Later, the desire to correlate noise and erosion motivated additional studies, examples of which can be found in references [6, 7, 13–16]. The studies of De and Hammitt [13–15] have established, in particular flow configurations and for specific materials quantitative variation laws of noise and erosion. Our approach in this study, in continuation of our earlier single bubble dynamic study [17], aims at differentiating for the same flow and velocity conditions cavitation noise when in presence of erosive and nonerosive cavitation. The present investigation sugests an acoustic erosion detection method. The practical advantage of this method relative to earlier approaches is that it does not require quantitative evaluation of the noise or measurement of the relative variations between one velocity and another but is more simply based on the observation of a qualitative modifications with time of the detected acoustic signal for the same hydrodynamic conditions.

Contributed by the Fluids Engineering Division of THE AMERICAN SOCIETY OF MECHANICAL ENGINEERS and presented at the BHRA 8th International Symposium on Jet Cutting Technology, Durham, England, September 1986. Manuscript received by the Fluids Engineering Division May 6, 1986.

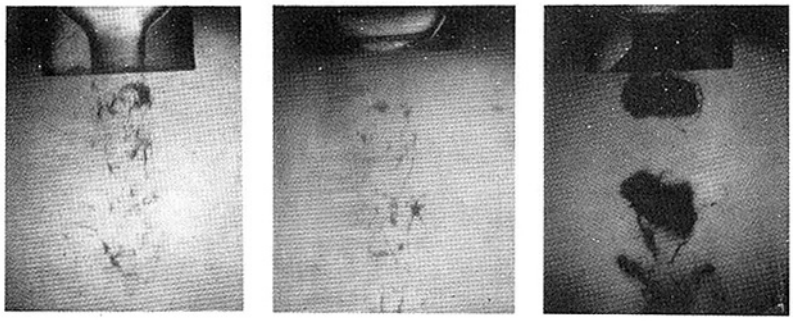

Fig. 1 Comparison of three types of nozzles at about the same cavitation number P_a ~ 28 psi, (*a*) $\Delta P \simeq 86$ psi, $\sigma \sim 0.33$, (*b*) $\Delta P \sim 98$ psi, $\sigma \simeq 0.29$, (c) $\Delta P \simeq 94$ psi, $\sigma \simeq 0.29$

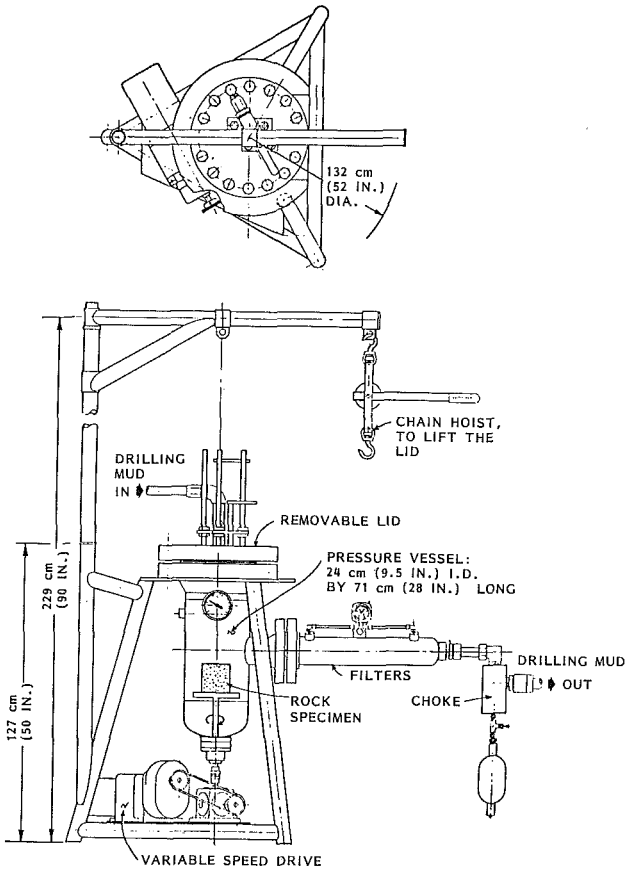

Fig. 2 High pressure cell for elevated ambient pressure studies of cavijet® nozzles

Self-Resonating Cavitating Jets

Experimental observations of submerged jets show the tendency of the turbulent eddies in their shear layer to organize in large structures. Excitation of an air jet with periodic acoustic signals produced upstream of the nozzle by transducers or loudspeakers shows a remarkable change of the jet structure into discrete ring vortices when the excitation frequency, f, matches the predominant natural frequencies of the nonexcited jet.

The potential of such a phenomenon for submerged water jets was recognized and a unique technology was developed related to achieving useful submerged jets having very high amplitude, periodic, oscillatory discharge without using moving parts in the supply system [2–5]. The passive excitation is obtained hydroacoustically and structures and shear layer of the jet into discrete, well defined ring vortices when the excitation frequency, f, matches the jet's preferred values. This can be obtained by (*a*) feeding the final jet-forming nozzle with various types of acoustic chambers (for example, Helmholtz chambers or organ-pipe tubes) tuned to resonate at the desired frequency; and (*b*) shaping the nozzle so as to feed back the pressure oscillations which occur at the exit. Such devices are forms of "whistles" which self-excite and thus are totally passive. These STRATOJETs have shown enhanced erosivity from increased cavitation activity.

While the vorticity in the shear layer of a nonexcited submerged jet is distributed into weak, randomly oriented vortices, it concentrates in strong equally spaced vortex ring structures when the jet is excited at its preferred frequency. When cavitation occurs these ring vortices fill up with vapor and appear as bubble rings (see Fig. 1). The large pressure oscillations associated with the intensification of cavitation, with resonance in the nozzle assembly, and with the production and disappearance of large vortical structures greatly improve the erosion and cleaning capabilities of the jet and make a very effective noise generator [4–5]. A summary of the dynamics and applications of these jets can be found in reference [3].

Experimental Setup

The tests described here were conducted in the Tracor Hydronautics High Pressure Cell (HPC). The pressure in this cell can be varied up to 207 bar with independent variation of the nozzle pressure up to 690 bar. Therefore, wide ranges of cavitation intensity and cavitation number can be achieved in this facility. When the jet is allowed to impact on surfaces, erosion can be obtained with various cavitation numbers in a controllable manner. By adjusting the standoff distance of the impacting jet, one is able to control the erosion intensity with a fixed erosive strength for the jet. Therefore, the potential discrimination of erosive versus nonerosive cavitation noise patterns can be investigated.

Detailed descriptions of the HPC can be found elsewhere [17]. A drawing of this cell is shown in Fig. 2. The flow into the cell enters through a removable lid which is bolted to the main cell and sealed with an O-ring. The ambient pressure within the cell is controlled by a valve. The cell rated pressure capacity is 207 bar. The main circulation pump used in these tests was a diesel-driven high-pressure pump, manufactured by American Aero. It has five plungers and is rated for 112kW and yields 1.27 *l/s* at 690 bar.

Two test plates made of 316 stainless steel were used as targets. Their dimensions were 16.9 × 16.9 × 1.9 cm. Two transducer holes were provided on each plate with dimensions of 3.1 cm and 5.6 cm in diameter. The position of these holes with respect to the jet impact joint is shown in Fig. 3.

Two types of pressure transducers were used in the test runs.

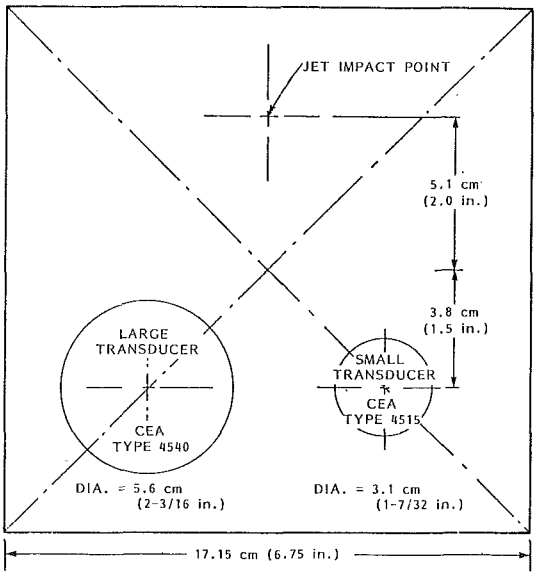

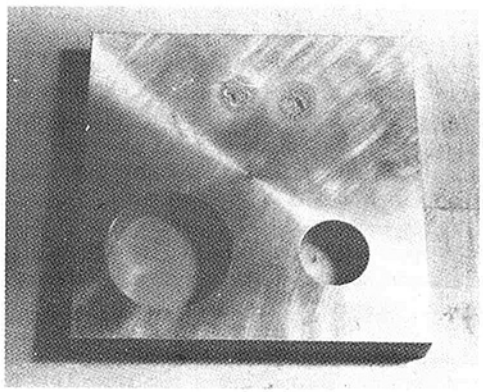

Fig. 3 Test plate used in noise/erosion tests

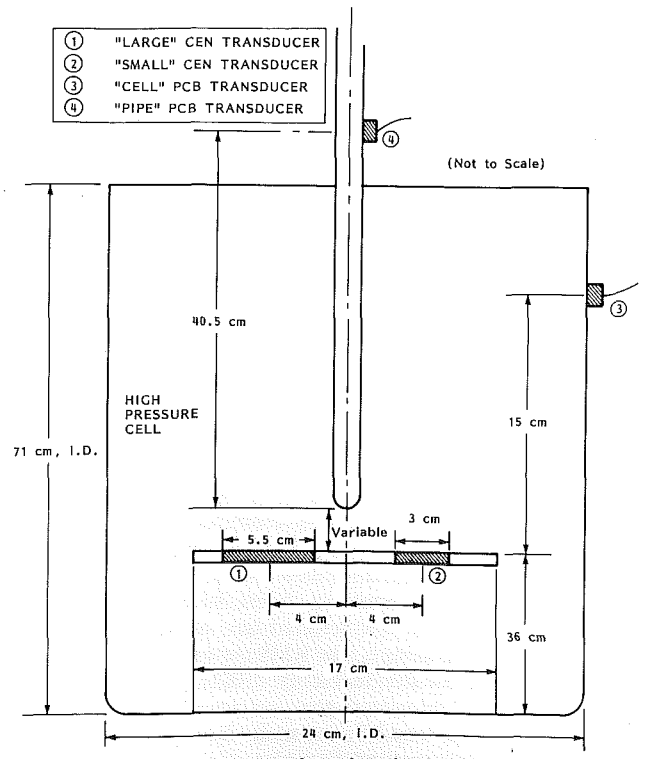

Fig. 4 Sketch of pressure transducer location in the high pressure cell

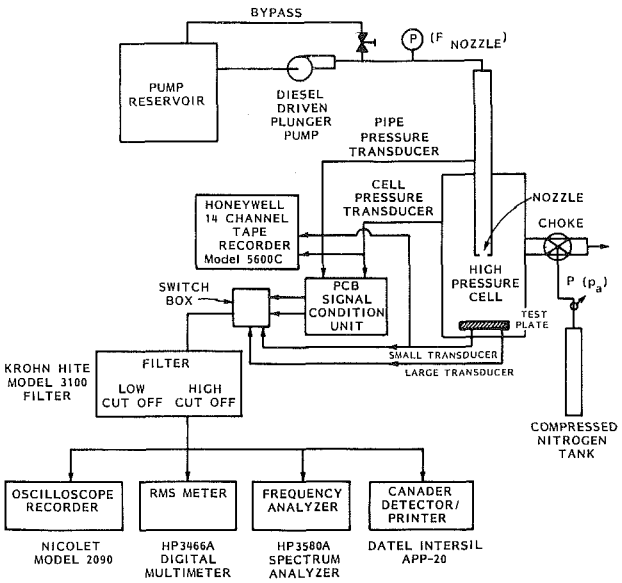

Fig. 5 Schematic of test facility and instrumentation

The transducers mounted in the test plate were provided by CEN/Cadarache. These were piezoelectric crystal transducers, and they had a large sensing area, about 3.1 cm and 5.6 cm in diameter, respectively. The large surface areas provided integrated signal over the surface. These transducers (Type 4540 and 4515) have been designed for withstanding high temperatures (up to 650°C), and their frequency range was up to 5 MHz. The third transducer, mounted on the wall of the high-pressure cell was a commercially available piezoelectric pressure transducer (PCB Model 101 M55). Its resonant frequency was 300 KHz, and the sensing area was 0.635 cm in diameter. This transducer provided the overall pressure fluctuations, and thus measured the noise inside the HPC. A similar transducer was positioned in the feed pipe leading to the nozzle. Figure 4 gives a sketch of the location during the tests of these four transducers.

The CANASTA system was provided by the CEN Cadarache and was used to analyze the output of the transducers. The system counts during a measurement cycle the number of pressure spikes whose amplitude exceeds an imposed threshold. This number is related to the number of strong cavitation bubble implosions. Another output of the system is information on the detected pulses' "total energy." It is proportional to the time integrals of all the detected pressure bursts.

The signals from the transducers were also captured on a Nicolet 2090 Digital Oscilloscope and then stored on floppy disks for later analysis. This oscilloscope had a maximum digitizing rate of 50 ns per point and a band-width of up to 7 MHz. A Digital Equipment Corp. VAX 11/750 computer was interfaced with the oscilloscope allowing the digitized pressure-time information to be analyzed with a Fast Fourier Transform. A root mean square voltmeter, RMS HP 3466A, was also used to obtain information on the generated overall noise level. Figure 5 shows a schematic of the test facility and instrumentation.

Tests and Procedures

In earlier tests the self resonating jet (STRATOJET) outperformed other jets. Very significant erosion depths were measured on commercial aluminum (up to 3 mm.) after five minutes of static impact. A pressure drop across the nozzle of 476 bar was used. Figure 6 shows comparative curves of mean depth of erosion versus ambient pressure for several types of nozzles. The STRATOJET nozzle of diameter 2.54 mm was

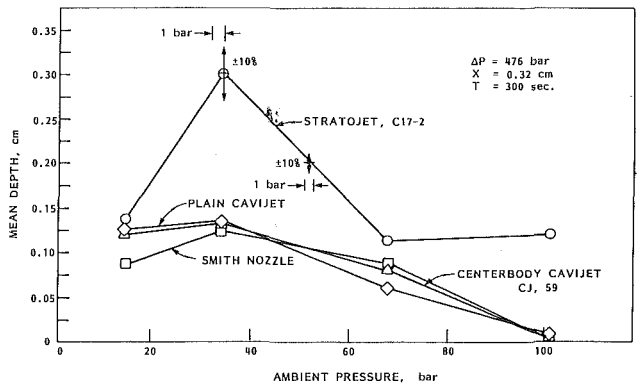

Fig. 6 Comparison of mean depth of erosion for four nozzles on aluminum

chosen for the present study. A CENTERBODY CAVIJET was also used for comparative purposes. Its diameter was 2.72 mm, and the center body cylinder diameter was 1.36 mm. From the earlier tests, it was concluded that pressures in the range 450 to 700 bar would produce measurable erosion imprints on stainless steel in a reasonable jetting time.

For the noise/erosion study reported here, the ambient pressure in the High Pressure Cell was fixed to 13.6 bar in order not to exceed the allowed maximum pressure of the CEA transducers' sealed elements. The pressue drop across the nozzles was 476 bar for one set of tests, and 680 bar for another set. The standoff distance between the nozzles and the plate was fixed at 9.5 mm when cavitation erosion was sought, and exceeded 90 mm in the nonerosion case.

Once the nozzle and the plate were positioned at the desired standoff distance, the ambient pressure in the cell was set to 13.6 bar, and the main pump was turned on to reach the required pressure: 476 bar or 680 bar. The following measurements were then taken during the jetting:

1. Sequential rms readings of the three transducers mentioned above, plus periodic rms readings of a fourth transducer located in the feed-pipe to the nozzle;
2. Sequential readings from the CANASTA for each of the three transducers.
3. Sequential high frequency recording of the transient signals from the three transducers on floppy discs of the Nicolet for later frequency analysis; and
4. Sequential frequency spectra of the three transducers' signals.

The following procedure was followed. The CANASTA system was allowed to integrate the signal of one transducer for fifteen seconds. Then, during a five-second intermission period the detection was shifted to the following transducer. While the CANASTA was integrating the signal of a given transducer, readouts were taken of the rms and frequency values of the signals from the other transducers. After a selected period, ΔT, was completed, jetting was stopped, the HPC lid was opened, and the plate was visually inspected. Measurements and photographs of the erosion pattern were then taken if a detectable change from the preceding testing increment was observed. ΔT was varied from 140 seconds up to 2180 seconds. Erosion quantification was achieved by measuring mean and maximum depth of erosion as well as an equivalent diameter of the eroded area. Mean depth and equivalent diameter were obtained from measurements of the erosion imprint using statistical averaging. When erosion became significant, volume removal was determined by using a graduated syringe and filling the eroded imprint with a liquid. For the purpose of this study, surface tension was reduced by the use of a surfactant but no additional effort was made to correct the surface tension effects in the pippete. The above described method of measuring erosion imprint is responsible for the relatively large errors in the volume removal rate computations ($\simeq \pm 20$ percent) shown on the figures below. However, this has no significant drawbacks, since we are only interested here in qualitative and comparative measurements. Recording of the transient signals on floppy discs was done at least once for each transducer during each ΔT period. These signals were then analyzed using the VAX 11/750 computer.

Results and Interpretation

A total of six tests using the method described above were run and the main results are summarized here using a typical example. Additional details can be found in reference [18]. Since the two CEN transducers were located symmetrically with respect to the jet, the differences in their signals reflected only differences in their sensitivities and frequency responses. This was not the case for the PCB transducer which was located much farther from the jet and therefore from the collapsing and eventually eroding bubbles. Differences between signals from this transducer and the two CEN transducers were therefore due not only to differences in their characteristics but also to differences in the actual pressure signals they observed from their different positions. The "large" transducer detected the highest number of spikes due to the large dimension of its sensitive area over which the pressure pulses are integrated. The "cell" transducer came in second position even though its sensitive area was much smaller and its distance to the sound source much larger. This was probably due to its very high sensitivity. Since the CANASTA responds to signals stronger than a trigger level fixed by the operator, a more sensitive transducer detects, for the same acoustic source and trigger level, a large number of spikes than a less sensitive transducer.

During the tests, the CANASTA trigger level was, for practical reasons, kept the same for the three transducers and maintained constant throughout a test run. This level was chosen such that a good response without saturation could be obtained for all transducers. Very good correlation between the CANASTA processed signals of the three transducers was observed as long as saturation did not occur. In the corresponding erosion tests volume removal from the target plate through erosion was either absent or moderate and therefore changes in the sound characteristics were moderate. However when erosion was intense and jetting time relatively long the trigger level became inadequate for the CEN transducers. No obvious correlation was then seen between the three signals. Another important reason for the absence of correlation comes from the phenomenon itself. Once an erosion pattern is imprinted on the surface of the target plate, the flow field on the plate is modified. This modification becomes very substantial when the imprint becomes deep. Secondary cavitation and erosion is generated, and a large separation region can be formed. For the transducers imbedded in the target plate, such an occurrence has a more dramatic effect than for the far-field transducer. This implies that these embedded sensors will not necessarily detect acoustic pressures for more intense erosion. The presence of separation bubbles or cavities could isolate these sensors from the noise sources or attenuate the incoming signals. All indications from the present tests are that this has occurred and that a location of the transducer far from the erosion region is preferred.

Figure 7 shows a comparison of the RMS readings of the three transducers for the selected set of tests. Since the readings were made using a true RMS meter on signals filtered only for the very low frequencies ($f < 60$Hz), they give a very good indication of the overall pressure sound level. This figure compares two tests A and B. In test B ($X = 90$ mm), the nozzle was far away from the target plate, hence no erosion was

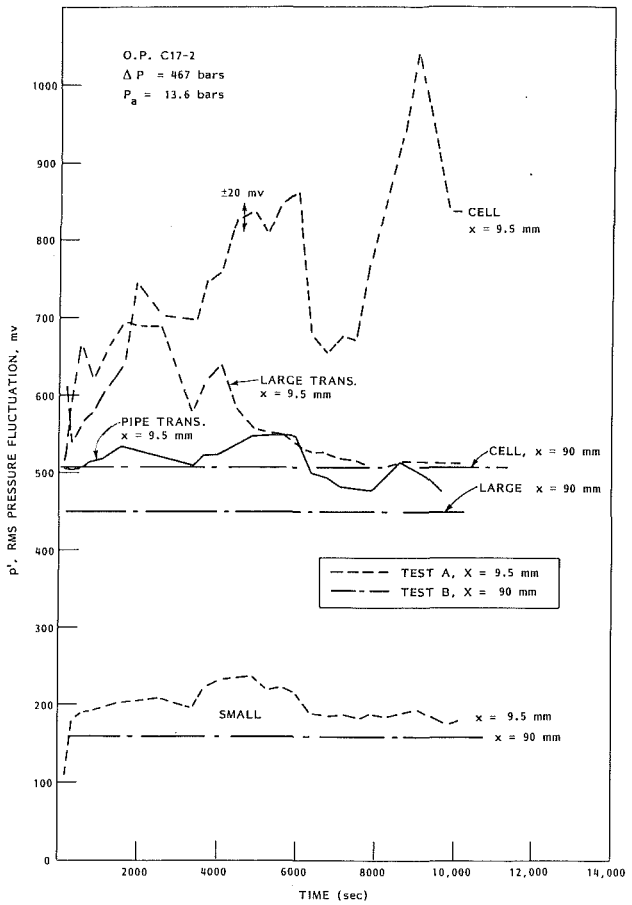

Fig. 7 Comparison of rms readings of three transducers. Tests A and B. Organ pipe stratojet, C17-2

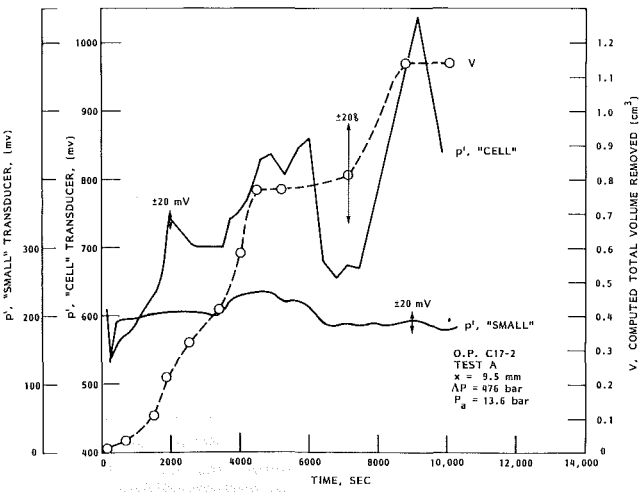

Fig. 8 Correlation between total volume removed and rms reading of "cell" and "small" transducers

occurring, and the three transducers detected no significant changes in the rms pressure levels as a function of time. However, large variations with time of the rms readings were seen during test A where $X = 9.5$ mm. All four transducers show corresponding peaks and valleys in the rms signals time histories. These "oscillations" are, however, most intense for the transducer located in the cell. These oscillations indicate acceleration and saturation periods of noise generation and, as we will see later, high rates of erosion followed by erosion saturation periods. The intensification of the rms readings

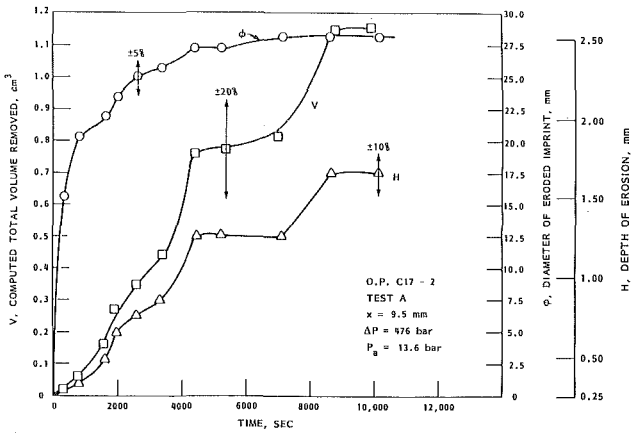

Fig. 9 Eroded imprint characteristics, test A stratojet nozzle

during the initial erosion phase and the tendency to return to the nonerosive value seem to indicate the generation of a separated region on the plate.

The time history of the signal of the large transducer has an overall trend quite different from the other transducers. As indicated also with the CANASTA signals a detrimental event has happened at $t \simeq 4000$ seconds. The rms signal of this transducer takes an overall continuous downslope which is not observed with the other transducers. This deterioration of the signal was confirmed at the end of the tests ($t \approx 10{,}000$ seconds) by the complete "death" of the transducer. This transducer was replaced by a second similar one for the following tests.

In Fig. 8, the time variation of the mean pressure fluctuations are compared with the evolution of the total volume removed from the target plate. The test corresponding to this figure, Test A, was conducted for a long enough period to observe significant erosion and noise modification. Figure 8 shows simultaneously the rms pressure fluctuations measured by the "small" CEN transducer and the PCB "cell" transducer. The volume removed was determined for this figure by measuring "mean" eroded diameters and depths (see Fig. 9). The qualitative agreement between the general trend of the total volume removed curve and the rms signal evolution of the cell transducer is very satisfactory. Additional information is provided in Fig. 10. In this figure, simultaneous representation of time variations of rms pressures, total volume removed, volume removal rate, and the CANASTA counts can be seen. The volume removal rate is obtained by fitting polynomial curves through portions of the curve of total volume removal versus time and by computing the time derivatives of these polynomials.

From these observations, we can tentatively say that following the initial incubation period, both rms pressure fluctuations and total volume removal increase with time until the first saturation period. The comparison between rate of volume removal and rms pressures is much more striking for this initial phase. When saturation of total volume removed and the saturation of rms readings were achieved, a very high erosion rate was attained and then terminated following a spike in the volume removal rate curve (e.g., $t \simeq 4500$ *s* and $t \simeq 9500$ s). Then, the rms reading has a maximum followed by a decline in value which follows with some delay that of the volume removal rate. One would have liked to be able to continue to observe continuously the erosion in a more monotonic fashion. . .probably a relatively large piece of metal was removed at that point, and a new incubation period restarted on the newly bared metal. This can be deduced from the sudden flattening in the total volume removal curve and by the sharp drop in the volume removal rate. The following phases

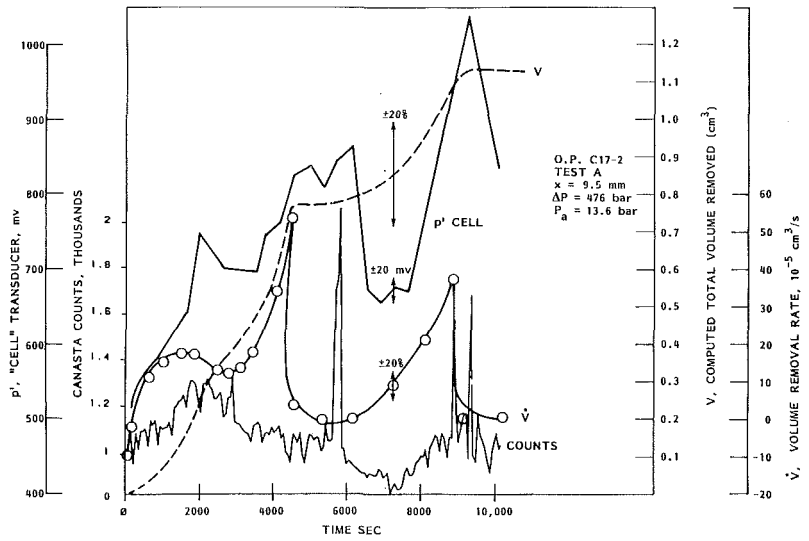

Fig. 10 Correlation between total volume removal, volume removal rate, rms acoustic pressure time variations, and number of canasta impact counts

look like periodic repeats of the initial phase. A lag between two successive periods is related to incubation periods for the newly bared surface metals. Drops in the rms pressure readings (Fig. 10, $t \geq 6000$ s), which are difficult to explain by considering the total volume removed, seem to be related to negative slopes in the volume removal rate.

Comparison of the CANASTA processed signal with the other signals shows that peaks and troughs do correspond, but the general trend of increasing rms pressure is not seen. The most correlated curve with the rms curve seems to be the volume removal rate curve. However, the shift between the spikes and mostly that between the peak at $t = 4000$ s observed in the removal rate curve and that at $t = 5500$ s observed in the CANASTA signal does not have a satisfactory explanation at this time. Errors in the evaluation of the volume removal rate as well as in the total volume measurement might explain these differences.

Frequency spectra of the signals detected by the transducers in eroding and noneroding cavitation conditions were analyzed. All the spectra were obtained by applying to the recorded signals a Fast Fourier Transform. Before erosion was significant, the only main frequency component was the self resonance frequency of the STRATOJET which is about 7.3 KHz. This was also the case when the plate was away form the nozzle. A second frequency (24.4 KHz) was also present but was less important. When erosion developed, the signal became much richer in frequency. For case A presented in this paper, after 5220 seconds the energy of the signal was mainly contained in the frequency band 7.3 to 24 KHz. Some other higher frequencies also appeared. However, the relative importance of the main frequency to the others changed significantly with erosion. The main indication of the erosive process seems to be reflected in all three transducers by the strong enforcement of the frequencies in the range 24 to 45 KHz. This is mostly reflected in the "cell" transducer. As we have seen in the preceding sections, this "cell" transducer gave the best correlation with erosion. Here, indications are given that this transducer, probably because of its size, location, and response was the most able to detect the frequency range most sensitive to erosion.

The analysis of the other tests shows similar trends to those presented here. However, the erosive process was not as intense for all tests as for the STRATOJET test selected for this paper and therefore, did not always show, over the testing period, as many regions of the time erosion curves as with the STRATOJET. Details of all the experimental observations can be found in reference [18].

Conclusions

We have investigated in this paper the correlation between noise and erosion of cavitating self-resonating jets. Comparisons between volume removal of 316 stainless steel and acoustic signal analysis of various transducers have produced the following preliminary conclusions. Some of these conclusions corroborate earlier results, but most of them need confirmation through additional testing and variation of the experimental configurations.

(*a*) The location of the noise detecting transducer is a key factor in a good noise-erosion correlation technique. A transducer distant from the eroded region seems to be significantly more sensitive to the erosion versus time variations.

(*b*) A tansducer of small size, high sensitivity, and flat frequency response is recommended for the correlations.

(*c*) The time variation of the root mean square values of the detected sound pressure seems to give the best correlation with the total volume removal.

(*d*) The frequency contents of the erosive and nonerosive cavitating conditions investigated here seem to be similar. The major influence of erosion is to shift the importance of the various frequencies. The main resonance frequency of the jet becomes of secondary importance when erosion is occurring.

(*e*) Significant acoustic pressure variations are only detectable when significant erosion is occurring. Volume removal has to take place and modification of the secondary flow over the erosion imprint is probably needed.

(*f*) RMS sound pressures and CANASTA readings increase with increasing volume removal rates and total volume removal rates and total volume removed. These readings decrease following saturation of material removal and a drop in the volume removal rates. The overall tendency of the noise to increase with the total volume removed is, however, only correlated with the rms readings.

The results of this study are very encouraging in showing the possibility of correlation between noise and erosion. They add a significant amount of data, information, and evidence to

earlier studies on the subject. An outcome of a reliable correlation between noise and erosion would be the detection of potential erosion in an installation and its control. An additional outcome, which shows more promise at this point in time, is the monitoring of the evolution of a jet cutting operation. The conclusions drawn above indicate that it is possible, when direct observation is difficult, to remotely assess the progress of erosion by observing the time evolution of the noise signal. This qualitative criterium can be compared to the classical qualitative acoustic or visual cavitation inception criterium.

Acknowledgments

The study described in this report was supported by the Commissariat a l'Energie Atomique CEN, Cadarache, France, under Contract No. C320243. We would like to thank many colleagues at Tracor Hydronautics, Inc. for their significant contributions.

References

1 Hammitt, F. G., *Cavitation and Multiphase Flow Phenomena*, McGraw-Hill International Company, 1980.

2 Johnson, V. E., Jr., Chahine, G. L., Lindenmuth, W. T., Conn, A. F., Frederick, G. S., and Giacchino, G. J., Jr., "Cavitating and Structured Jets for Mechanical Bits to Increase Drilling Rate," ASME *Journal of Energy Resources Technology*, Vol. 106, 1984, pp. 282–294.

3 Chahine, G. L., and Johnson, V. E., Jr., "Mechanics and Applications of Self-Resonating Cavitating Jets," *ASME International Symposium on Jets and Cavities*, Miami, Florida, Nov. 1985, pp. 21–35.

4 Chahine, G. L., Johnson, V. E., Jr., Lindenmuth, W. T., and Frederick, G. S., "The Use of Self-Resonating Cavitating Water Jets for Underwater Sound Generation," *Journal of the Acoustical Society of America*, Vol. 77, No. 1, Jan. 1985, pp. 113–126.

5 Chahine, G. L., Johnson, Jr., V. E., Frederick, G. S., and Watson, R. E., "Sound Enhancement and Modulation of Self-Resonating Cavitation Jets for Underwater Noise Generation," Tracor Hydronautics Technical Report 83005-2, 1985.

6 Courbière, P., "Cavitation Erosion in Sodium Flow. Sodium Cavitation Tunnel Testing," *ASME Cavitation Erosion in Fluid Systems*, Ed. W. L. Swift and R. A. Arndt, June 1981, pp. 105–118.

7 Courbière, P., "An Acoustic Method for Characterizing the Onset of Cavitation in Nozzles and Pumps," *ASME International Symposium on Cavitation Inception*, Dec. 1984, pp. 137–145.

8 Ross, D., *Mechanics of Underwater Noise*, Pergamon Press Inc., New York, 1976.

9 Harrisson, H., "An Experimental Study of Single Bubble Cavitation Noise," *Journal of the Acoustical Society of America*, Vol. 24, 1952, pp. 776–782.

10 Mellen, R. H., "An Experimental Study of the Collapse of a Spherical Cavity in Water," *Journal of the Acoustical Society of America*, Vol. 28, 1956, pp. 447–454.

11 Il'ichev, V. I., an Lesunovskii, N. P., "On the Noise Spectra Associated With Hydrodynamic Cavitation," *Soviet Physics Acoustics*, Vol. 9, 1963, p. 25.

12 Morozov, V. P., "Cavitation Noise as a Train Pulse Generated at Random Times," *Soviet Physics Acoustics*, Vol. 14, No. 3, 1969.

13 Hammitt, F. G., De, M. K., Elenz, J. J., and Hunt, J. W. Jr., "Venturi Cavitation Bubble Collapse Spectra and Observed Pits in Soft Aluminum," *ASME Cavitation and Polyphase Flow Forum*, June 1978, pp. 31–34.

14 De, M. K., "Acoustic Waves From Hydrodynamic Cavitation," PhD Thesis, University of Michigan, Report No. OMICH014456-2-T, 1980.

15 Hammitt, F. G., "Cavitation Damage Prediction," *ASME Cavitation and Multiphase Flow Forum*, 1983, pp. 12–14.

16 Chahine, G. L., Courbière, P., and Garnaud, P., "Correlation Between Noise and Dynamics of Cavitation Bubbles," *Proceedings Sixth International Conference on Fluid Machinery*, Budapest, Hungary, Sept. 1979, pp. 200–210.

17 Conn, A. F., Johnson, V. E., Jr., Liu, H. L., and Frederick, G. S., "Evaluation of CAVIJET® Cavitating Jets for Deep-Hole Rock Cutting," HYDRONAUTICS, Incorporated Technical Report 7821-1, Aug. 1979.

18 Chahine, G. L., Liu, H. L., Frederick, G. S., and Watson, R. E., "Correlation Between Cavitation Noise Using Cavitating Jets," Tracor Hydronautics Technical Report 83106, Apr. 1985.

An Experimental Study of Liquid Entrainment by Expanding Gas

M. J. Tan[1]

J. M. Delhaye

Centre d'Etudes Nucleaires de Grenoble,
Service d'Etudes Thermohydrauliques,
38041 Grenoble Cedex,
France

An experimental study of the hydrodynamic aspect of the expansion process in a hypothetical core disruptive accident (HCDA) by means of a shock-tube technique is described. The working fluid pair was water-air. Interface displacement data for shock strengths in the range 0.5–3.0 were obtained by means of high-speed photography. The displacement data are fitted into least-square polynomials in time, which are used to compute accelerations and entrainment velocities. The accelerations thus obtained, which are in the range 950 m/s²–15,000 m/s², are uniform in time. The entrainment velocities for experiments performed with the circular driven section are consistently higher than those for the experiments performed with the square driven section at the same accelerations. The difference is attributed to the entrainment velocity for the latter case being time-dependent. Furthermore, an upper bound on the rate of entrainment in an HCDA is proposed.

1 Introduction

One of the hypothetical core disruptive accidents (HCDA's) for the liquid-metal fast breeder reactors (LMFBR's) involves the development of a high pressure liquid-vapor two-phase mixture, consisting mainly of fuel and structural steel, in the disassembled reactor core. The two-phase mixture then expands through the undamaged core region into the upper coolant pool and in the process entrain some of the coolant. The bulk of the coolant, accelerated by the expanding two-phase mixture, can in turn smite the reactor vessel (Kocamustafaogullari and Chan, 1983). The expansion work of the two-phase mixture is thus a measure of the disruptive mechanical energy of this hypothetical accident. It has been suggested that the dynamic interactions between the main body of the coolant and the expanding two-phase mixture may result in a considerable reduction of the magnitude of the expansion work (Cho et al., 1974; Corradini et al., 1980; Tobin and Cagliostro, 1980).

The hydrodynamic aspect of the interactions is generally discussed in reference to the phenomenon of coolant entrainment. The experimental results of Tobin and Cagliostro (1980) suggested that Rayleigh-Taylor instability of the interface between the main body of the coolant and the expanding two-phase mixture be the dominant mechanism for coolant entrainment. The instability itself in the context of two fluids of different densities was described by Taylor (1950). In principle, when a heavier fluid is accelerated by a lighter fluid pushing against it, their interface is unstable and the growth rate for initially two-dimensional sinusoidal disturbances is exponential at the first instant. The experiments of Lewis (1950) and of Emmons et al. (1954) showed that after the initial exponential growth period the interface changes to the shape of broad round-ended columns (bubbles) of the lighter fluid penetrating into the heavier fluid which forms slender columns (spikes) between the lighter-fluid bubbles. Accordingly, the evolution of the interface in question would involve the formation of bubbles of the two-phase mixture rising through the coolant and spikes of the coolant falling into the two-phase mixture. Coolant entrainment then occurs as the spikes thus formed break up into droplets.

The experimental investigation described in this paper was conducted to study the hydrodynamic aspect of the expansion process in an HCDA without the complications of heat transfer and phase change. A shock tube capable of operation at driver pressures of up to 3.5 bar was used. The working fluid pair was water-air. The transient penetration of air into the water pool at accelerations in the range from 950 m/s² to 15,000 m/s², which are comparable to those that may appear in large-scale systems, was studied by means of high-speed photography. An empirical correlation on which estimation of the upper bound on the rate of entrainment may be based is proposed.

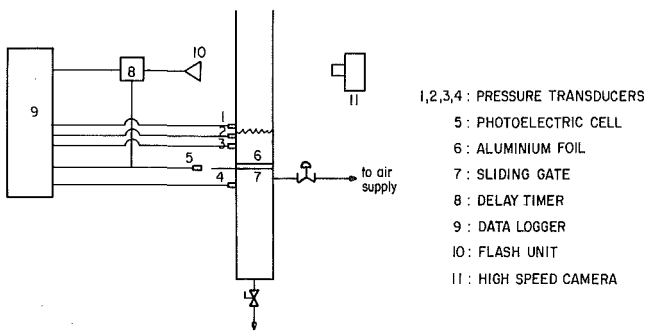

Fig. 1 Schematic diagram of the experimental setup

[1]Present address: Reactor Analysis and Safety Division, Argonne National Laboratory, Argonne, IL 60439.

Contributed by the Fluids Engineering Division for publication in the JOURNAL OF FLUIDS ENGINEERING. Manuscript received by the Fluids Engineering Division June 11, 1985.

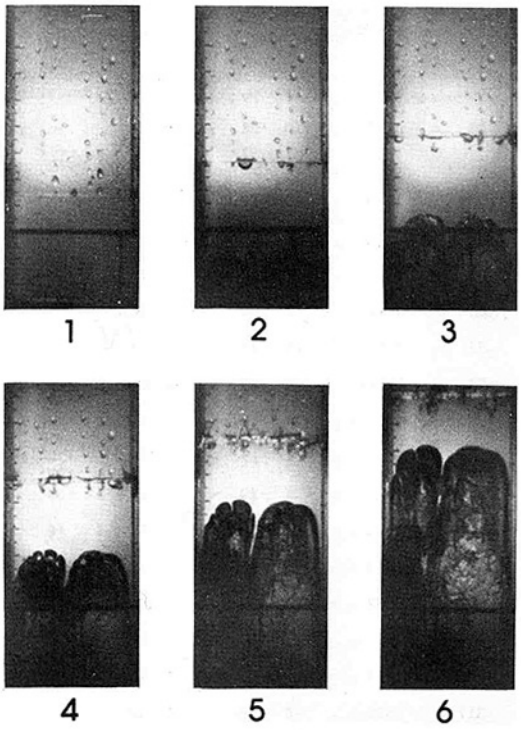

Fig. 2 Photographic sequence for experiment no. S5. Time from opening the sliding gate to the first frame shown is 6.58 ms. Time interval between frame (1) and frame (2) is 2.13 ms; between any other two consecutive frames is 1.06 ms. (Uncertainty in time is 0.05 ms at 20:1 odds.)

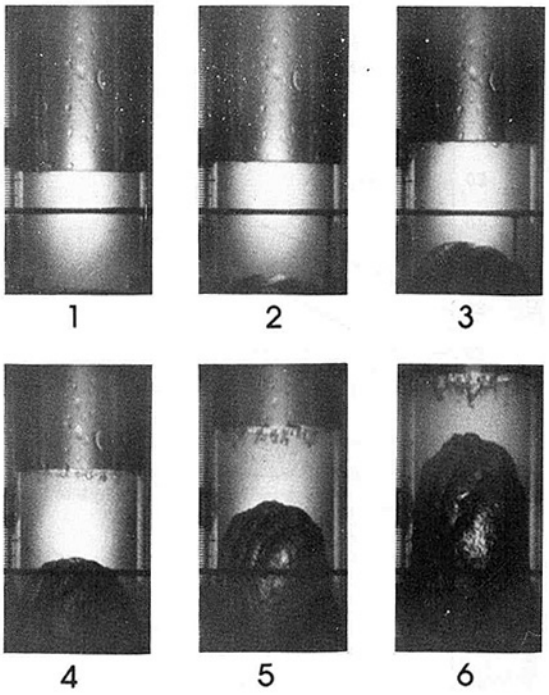

Fig. 3 Photographic sequence for experiment no. C7. Time from opening the sliding gate to the first frame shown is 7.58 ms. Time interval between two consecutive frames is 1.07 ms. (Uncertainty in time is 0.05 ms at 20:1 odds.)

2 Apparatus and Procedure

A schematic diagram of the experimental setup is shown in Fig. 1. All experiments were carried out using a vertical shock tube assembly which included an upper driven section and a lower driver section. In the first series of experiments a square test section of inside dimension of 50×50 mm was used as the driven section. In the second series of experiments a circular test section of inside diameter of 50 mm was used as the driven section. Both test sections were constructed of Plexiglas. The driver section was made of 50-mm ID steel pipe and was closed at its lower end. A spring-loaded sliding gate having a 50-mm diameter circular aperture was mounted horizontally on top of the driver section so that the driver section could be made airtight by loading the spring and thereby closing the sliding gate. The center of the aperture in the sliding gate lied on the axis of the driver section when the spring was in its unloaded position. A thin rod was synchronized with the sliding gate in such a way that the moment when the sliding gate was made barely open from its closed position could be determined by monitoring the position of the thin rod with a photoelectric cell.

For pressure measurements four quartz pressure transducers were flush mounted in the wall of the shock tube: the upper three were located 100 mm, 50 mm, and 20 mm, respectively, above the lower end of the driven section; the fourth one was located 150 mm below the sliding gate.

The data acquisition system consisted of a data logger (16k RAM, frequency range 0-100 kHz) and a drum-type high-speed camera (max. speed 35,000 frames per second) operating in conjunction with a flash unit (max. flash duration 10.8 ms).

At the start of each experimental run the spring was loaded and the sliding gate was held closed by means of a latch. The driven section was clamped to the frame of the sliding gate with a piece of aluminum foil in between. Water of predetermined volume was introduced into the driven section, which remained open to the atmosphere, and rested on top of the aluminum foil. The driver section was pressurized with compressed air to a predetermined pressure. The camera was brought up to speed and its shutter was opened. The sliding gate was then unlatched manually. Upon detecting the opening of the sliding gate, the photoelectric cell emitted a signal that triggered immediately the data logger and after a delay time the flash unit. In the meantime, the imposed impulsive pressure change caused the aluminum foil to rupture. The ensuing upward motion of the bulk of water was recorded into the film when the flash unit was activated. The pressure and the flash time histories were registered into the data logger.

3 Results and Discussion

The photographic sequences for two experiments are shown in Figs. 2 and 3, in which the sliding gate is at the bottom of each photograph and moves from right to left. It is seen that the upper interfaces remain virtually flat throughout, which is typical for all runs, and that the lower interfaces change their forms continuously. Indeed, the evolution of the lower interfaces can be broadly divided into two groups. In the first

Nomenclature

D = diameter or width of the driven section
g = effective acceleration
L = characteristic length used in equation (2)
t = time
v = entrainment velocity
x_L = position of the apex of the lower interface
x_U = position of the upper interface

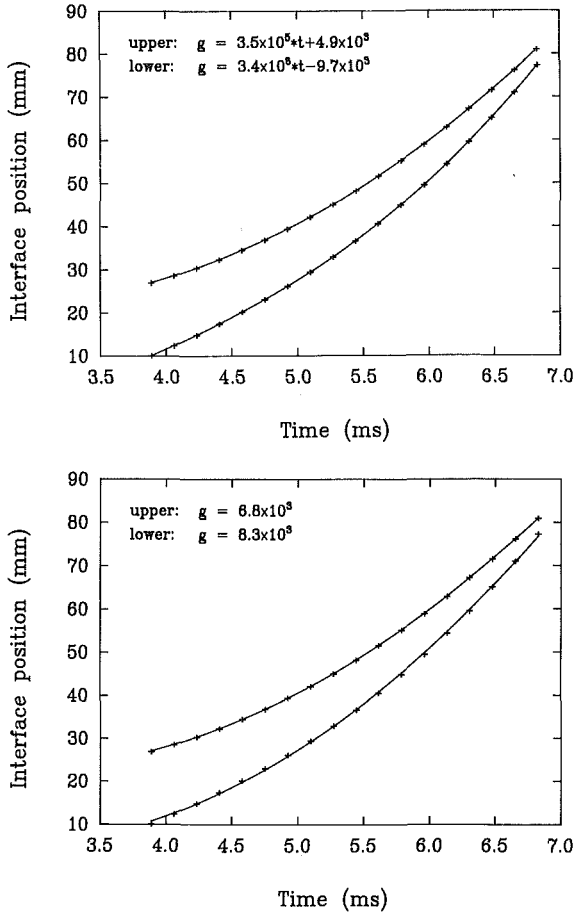

Fig. 4 Plots of time-position data for experiment no. S17. (*a*) Data are fitted with third-degree polynomials. (*b*) Data are fitted with second-degree polynomials. (Uncertainties in time and position are 0.05 ms and 0.5 mm respectively at 20:1 odds.)

group, which consists of most of the experiments performed with the square driven section, the profiles resemble that of two parallel and adjacent columns as typified by frames 4, 5, and 6 in Fig. 2; the penetration velocities of the two air columns differed from each other in some experiments. In the second group, which includes *all* of the experiments performed with the circular driven section, the profiles resemble that of a dome as shown in Fig. 3. The peripheral region of the profiles in both groups tapers down towards the base of the column in a similar fashion. The photographs at the first instant show that the apparent number of the dome-like air columns is to a large degree dependent upon the form of the aluminum foil at the moment of its rapture. We infer that the dissimilarity of the profiles of the lower interface is less a direct consequence of the dissimilar geometries of the driven sections than a manifestation of the effects of rather aleatory initial conditions.

It is also seen from Figs. 2 and 3 that the apparent volume of the main body of water decreases with time, which is due to the entrainment of water into the expanding air. For definiteness, the rate of entrainment in the present study is discussed in terms of an entrainment velocity v given by

$$v=\frac{d}{dt}(x_L-x_U) \tag{1}$$

where x_U and x_L denote the positions of the upper interface and the apex of the lower interface respectively. The rate of entrainment can thus be unambiguously determined from the two-dimensional photographs.

For each experiment the acceleration of the main body of water was established in the following manner. The time-position data of the upper interface were first fitted into a least-square third-degree polynomial, as illustrated by the example given in Fig. 4(*a*), to allow for time-dependent accelerations. It turned out that the variations of the accelerations during the time span of observation were generally small: an average of 13 percent for the experiments carried out with the square driven section and an average of 20 percent for the experiments carried out with the circular driven section. This observation led us to consider the accelerations of the main body of water as uniform throughout. The time-position data of the upper interface were then fitted into a least-square second-degree polynomial, as illustrated in Fig. 4(*b*). The values of the uniform acceleration thus obtained and the relative deviation are given for sixty experiments in Tables 1 and 2. The relative deviation is defined as the normalized difference between the extremum of the acceleration that would exist if the third-degree data-fitting polynomial were used and the value of the uniform acceleration that is obtained from a second-degree data-fitting polynomial. The smallness of the

Table 1 Calculated values of effective acceleration and entrainment velocity for experiments performed with the square driven section

experiment no.	g, m/s²	relative deviation, %		v, m/s	relative deviation, %	
S1	1149	+19	−21	2.11	+6	−1
S2	952	+21	−23	2.12	+62	−21
S3	2800	+20	−22	2.46	+24	−7
S4	2190	+4	−5	2.40	+13	−3
S5	2531	+11	−12	2.72	+6	−1
S6	2572	+7	−8	2.76	+6	−23
S7	2198	+15	−14	2.71	+25	−36
S8	2358	+2	−3	3.01	+2	−9
S9	4812	+20	−22	3.17	+16	−71
S10	5181	+17	−19	3.26	+38	−9
S11	4175	+18	−20	3.46	+50	−28
S12	4400	+10	−11	3.51	+8	−29
S13	4363	+5	−5	3.43	+36	−49
S14	3882	+2	−2	2.88	+24	−14
S15	3943	+13	−14	3.32	+23	−35
S16	5054	+11	−13	3.10	+18	−70
S17	6809	+8	−9	4.12	+115	−27
S18	5956	+20	−23	3.73	+51	−38
S19	5688	+8	−9	3.19	+75	−66
S20	6734	+5	−5	3.45	+42	−10
S21	7626	+3	−4	3.17	+27	−9
S22	9257	+8	−9	3.56	+76	−17
S23	8184	+12	−9	4.31	+31	−7
S24	6819	+5	−4	3.72	+8	−36
S25	7656	+1	−1	2.96	+31	−8
S26	10693	+7	−9	3.81	+7	−2
S27	12668	+11	−13	4.88	+9	−2
S28	14761	+21	−16	4.17	+63	−75
S29	13822	+1	−2	4.39	+17	−67
S30	12043	+11	−14	4.18	+13	−51

Table 2 Calculated values of effective acceleration and entrainment velocity for experiments performed with the circular driven section

experiment no.	g, m/s^2	relative deviation, %		v, m/s	relative deviation, %	
C1	1146	+13	-14	2.74	+30	-7
C2	1463	+14	-15	2.85	+9	-39
C3	1141	+8	-9	2.84	+30	-6
C4	3304	+16	-19	4.29	+55	-15
C5	2963	+33	-39	4.41	+21	-5
C6	2396	+10	-9	3.63	+22	-49
C7	2976	+3	-3	4.09	+26	-16
C8	2352	+3	-4	3.66	+5	-22
C9	2434	+2	-3	3.85	+43	-10
C10	5270	+27	-33	6.27	+28	-8
C11	6558	+15	-17	5.89	+17	-5
C12	4420	+14	-16	5.13	+45	-11
C13	4978	+19	-21	6.06	+24	-19
C14	4486	+15	-18	5.64	+7	-4
C15	4101	+13	-15	5.09	+1	-1
C16	6885	+10	-12	5.52	+54	-30
C17	8198	+20	-25	6.34	+25	-6
C18	7630	+23	-29	7.44	+17	-5
C19	7169	+16	-19	6.95	+4	-1
C20	6220	+8	-9	6.94	+22	-6
C21	9259	+15	-17	7.83	+32	-8
C22	6738	+22	-26	7.01	+3	-13
C23	9736	+17	-21	7.65	+43	-12
C24	7980	+16	-20	6.85	+35	-9
C25	9563	+23	-28	6.97	+23	-6
C26	5664	+25	-28	5.73	+44	-10
C27	7345	+20	-23	6.21	+52	-15
C28	9224	+8	-9	7.77	+49	-12
C29	9958	+15	-19	8.10	+19	-40
C30	9767	+21	-28	8.10	+11	-3

relative deviations indicates that the accelerations in our experiments are indeed uniform.

The accelerations of the lower interface calculated in a similar manner are mostly greater than those of the upper interface, as is illustrated by the example given in Fig. 4(*b*). This was to be expected since the time-position data for the lower interface were based on the apex. It should be noted, however, that the RMS average of the relative deviations of the accelerations of the lower interface from those of the upper interface is only 14 percent. In cases that the lower interface is accelerated at approximately the same rate as is the upper interface, the entrainment velocities would be approximately uniform in time. The calculations of such uniform entrainment velocities are illustrated by Figs. 5 and 6. The straight lines therein represent the least-square linear approximation to the data points. It is noticed that the deviations of the data points from the straight lines were generally larger for the experiments performed with the square driven section than for those performed with the circular driven section, as is shown in Figs. 5 and 6. In Tables 1 and 2 are also given for each of the sixty experiments the values of the entrainment velocity that is determined under the assumption of being uniform in time and the values of the relative deviation that is calculated in a manner analogous to that in which the relative deviation from uniform acceleration is calculated.

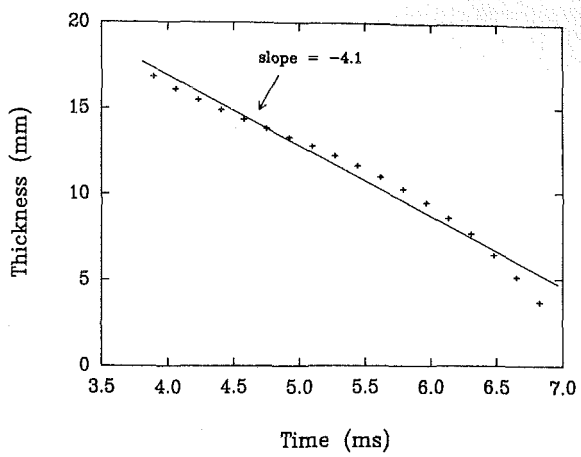

Fig. 5 Plot of $x_U - x_L$ versus time for experiment no. S17. (Uncertainties in time and position are 0.05 ms and 0.5 mm, respectively, at 20:1 odds.)

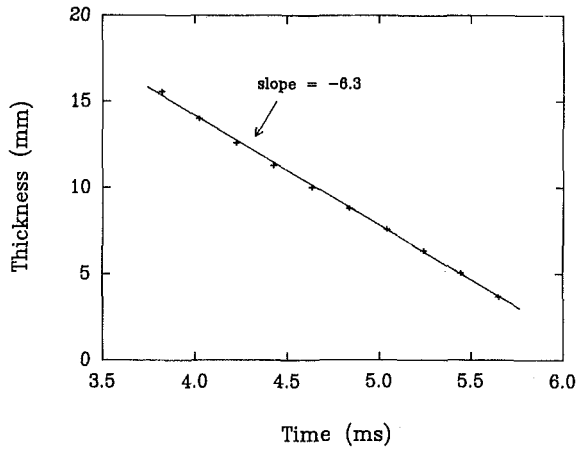

Fig. 6 Plot of $x_U - x_L$ versus time for experiment no. C17. (Uncertainties in time and position are 0.05 ms and 0.5 mm, respectively, at 20:1 odds.)

Previous experimental studies of the problem of Rayleigh-Taylor instability (Lewis, 1950; Emmons et al. 1954) showed that round-ended columns of the lighter fluid would penetrate into the heavier fluid at a uniform velocity and the relation between the uniform penetration velocity and the acceleration can be written as

$$v = C(gL)^{1/2} \tag{2}$$

where g is the effective acceleration, L is some characteristic length, and C is some constant.

Frames 4, 5, and 6 in Fig. 2 show that the lower interface is characterized by several small hemispherical protuberances, which bespeak the round-ended columns of the lighter fluid discussed for the later-stages development of Rayleigh-Taylor instability. Moreover, a remarkable feature of the profiles of the lower interface is that they resemble that of one or two large bubbles of irregular shape of the forward face rising in a vertical tube. In the light of this and the fact that the exact relation governing the steady motion of a large gas bubble rising in a vertical tube containing liquid depends only on the diameter of the tube and a shape factor (Batchelor 1967), it is expected that if the entrainment velocities are uniform in time, the physical dimension of the driven section would be the characteristic length used in a relation between entrainment velocity and effective acceleration. The entrainment velocity is

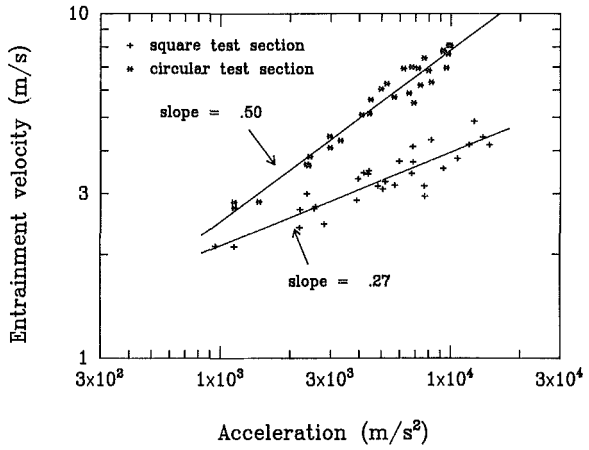

Fig. 7 Plot of entrainment velocity v versus acceleration g. (Uncertainties in v and g are given in terms of relative deviation in Tables 1 and 2.)

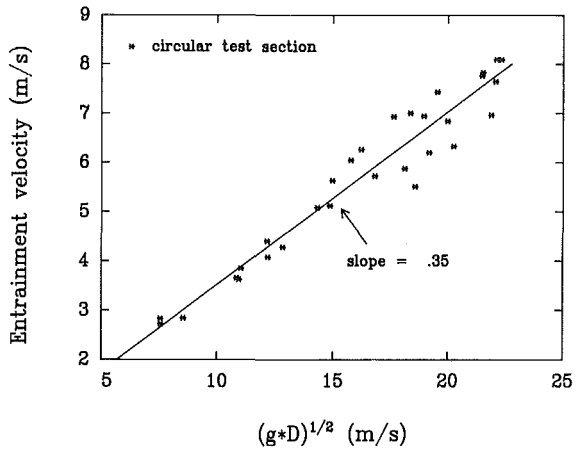

Fig. 8 Plot of v versus $(gD)^{1/2}$. $D = 50$ mm. (Uncertainties in v and g are given in terms of relative deviation in Table 2.)

thus related to the effective acceleration by an expression of the form

$$v = C_1 g^{1/2}. \tag{3}$$

On the other hand, it has been proposed by Corradini et al. (1980) that the critical Rayleigh-Taylor instability wavelength be used as the characteristic length. Since the critical Rayleigh-Taylor instability wavelength is proportional to $g^{-1/2}$ (Bellman and Pennington, 1954), equation (2) in this case would be reduced to

$$v = C_2 g^{1/4}. \tag{4}$$

Figure 7 is a plot of $\log(v)$ versus $\log(g)$ for the values of v and g given in Tables 1 and 2. It is evident that the points fall into two distinct groups: the ones corresponding to the experiments carried out with the circular driven section lie approximately on a least-square data-fitting straight line of slope 0.5, whereas those corresponding to the experiments carried out with the square driven section have a slightly larger spread and give a data-fitting straight line of slope 0.27. The discrepancy suggests that either the difference in the geometry of driven section entails different mechanisms for entrainment, as implied by the two length scales, or the entrainment velocity as given by equation (1) cannot be considered uniform in time in the case of square driven section.

In view of the operation procedures in our experiments it is doubtful that the entrainment mechanism depends to such a large degree upon the geometry of driven section. It can be shown that in the case of a large gas bubble rising *unsteadily* relative to the surrounding fluid in a vertical tube, a term which depends implicitly on acceleration, tube diameter, and time must be added to the right-hand side of equation (2) (Batchelor, 1967). Hence a relation between entrainment and acceleration of the form (2) is inadequate when the approximation of uniform entrainment velocity is poor, which is the case for some of the experiments carried out with the square driven section. It is thus inferred that the geometry of driven section per se does not have a bearing upon the entrainment mechanism. As a result, the rates of entrainment depend largely on system initial conditions, and when they are uniform in time, the larger length scale, i.e., the physical dimension of the driven section, should be used as the characteristic length in (2).

We set out to investigate experimentally the hydrodynamic aspect of the expansion process in an HCDA. Using a shock-tube technique, we found that at the same accelerations the entrainment velocities for the experiments performed with the circular driven section are consistently higher than those for the experiments performed with the square driven section. In view of the fact that a plethora of structural steel are present in the core region of LMFBR's, the space involved in entrainment in HCDA's would be finite. Therefore, the two simple geometries considered in the present work are not unrealistic. On the one hand, it has been shown (Tan, 1986) that the presence of rigid boundaries can introduce a stabilizing effect on the shape of the interface, thereby the rate of entrainment. On the other hand, the dynamic interactions such as heat transfer and phase transition between the bulk of coolant and the expanding two-phase mixture would certainly attenuate the rate of entrainment that is estimated from a purely hydrodynamic study. The implication is that a reasonable upper bound on the rate of entrainment could be obtained from the present work. With this in mind, it suffices to consider only the results of the experiments with the circular driven section insofar as providing the upper bound on the rate of entrainment is concerned. Figure 8 is a plot of v versus $(gD)^{1/2}$, where the values of v and g are given in Table 2 and D is the diameter of the circular driven section. It is seen that the data lie approximately on a straight line as expected. We thus propose the following correlation for estimating the *upper bound* on the rate of entrainment:

$$v = 0.35(gD)^{1/2}. \tag{5}$$

4 Conclusions

An experimental study of the hydrodynamic aspect of the expansion process in an HCDA by means of a shock-tube technique with water-air as the working fluid pair has been conducted. The results are summarized as follows:

(1) Under the conditions given Rayleigh-Taylor instability is the dominant mechanism for water entrainment.

(2) Accelerations obtained are uniform in time. Same operation conditions lead to approximately the same accelerations irrespective of the geometry of the driven section.

(3) At the same accelerations the entrainment velocities for the experiments performed with the circular driven section are higher than those for the experiments performed with the square driven section. The difference is probably due to the penetration velocity of the apex of the lower interface for the latter case being time-dependent.

(4) The upper bound of the rate on coolant entrainment during the expansion of the two-phase mixture in an HCDA may be estimated from the correlation between entrainment and acceleration based on the results of the experiments performed with the circular driven section.

References

Batchelor, G. K., 1967, *An Introduction to Fluid Dynamics*, Cambridge University Press, Great Britain, p. 474.

Bellman, R., and Pennington, R. H., 1954, "Effects of Surface Tension and Viscosity on Taylor Instability," *Quarterly of Applied Mathematics*, Vol. 12, pp. 151–162.

Cho, D. H., Epstein, M., and Fauske, H. K., 1974, "Work Potential Resulting from a Voided-Core Disassembly," *Transactions of the American Nuclear Society*, Vol. 18, p. 220.

Corradini, M. L., Rohsenow, W. H., and Todreas, N. E., 1980, "The Effects of Sodium Entrainment and Heat Transfer with Two-Phase UO_2 During a Hypothetical Core Disruptive Accident," *Nuclear Science and Engineering*, Vol. 73, pp. 242–258.

Emmons, H. W., Chang, C. T., and Watson, B. C., 1960, "Taylor Instability of Finite Surface Waves," *Journal of Fluid Mechanics*, Vol. 7, pp. 177–193.

Kocamustafaogullari, G., and Chan, S. H., 1983, "General Formulation of an HCDA Bubble Rising in a Sodium Pool and the Effect of Nonequilibrium on Fuel Transport," *Nuclear Technology*, Vol. 63, pp. 23–39.

Lewis, D. J., 1950, "The Instability of Liquid Surfaces When Accelerated in a Direction Perpendicular to Their Planes, II," *Proceedings of the Royal Society, Series A*, Vol. 202, pp. 81–96.

Tan, M. J., 1986, "On the Steady Solution of the Problem of Rayleigh-Taylor Instability," *Journal of Fluid Mechanics*, Vol. 170, pp. 339–353.

Taylor, G. I., 1950, "The Instability of Liquid Surfaces When Accelerated in a Direction Perpendicular to Their Planes, I," *Proceedings of the Royal Society*, Series A, Vol. 201, pp. 192–196.

Tobin, R. J., and Cagliostro, D. J., 1980, "Energetics of Simulated HCDA Bubble Expansions: Some Potential Attenuation Mechanisms," *Nuclear Engineering and Design*, Vol. 58, pp. 85–95.

A. Yamaguchi
Professor.

S. Shimizu
Research Associate.

Department of Mechanical Engineering,
Yokohama National University,
Yokohama, Japan

Erosion Due to Impingement of Cavitating Jet

Cavitation erosion produced by impingent of cavitating jet was experimentally studied with specimens of aluminum alloy in high water base fluid of chemical solution type and tap water. Furthermore, the behavior of impinging cavity clouds was observed through instantaneous photographs.

Introduction

Impingement of cavitating jet leads to serious erosion in valves and oil hydraulic equipment. On the other hand, cavitation erosion due to cavitating jet can sometimes be useful for jet cutting and underwater cleaning. In order to reduce the cavitation erosion in valves and oil hydraulic equipment or improve the performance of jet cutting and underwater cleaning, it is necessary to have an adequate knowledge about the mechanism of erosion due to impingement of cavitating jet. There are a number of reports about the erosion due to cavitating jet. Lichtarowicz [1–5] showed that a cavitating jet apparatus was useful for cavitation erosion testing of materials. Kleinbreuer [6–11], Berger [12, 13] and Backe et al. [14] used similar apparatus to Lichtarowicz's one and investigated cavitation erosion in oil hydraulic equipment. Conn et al. [15–17] indicated the feasibility of utilizing cavitation erosion to improve the performance of deep hole drilling bits by their rock erosion tests. They discussed the role of various parameters which affect the erosive action. However, there are still unclear points about the cavitation erosion due to cavitating jet.

In the present report, cavitation damage produced by the impingement of cavitating jet was experimentally studied with specimens of aluminum alloy in high water base fluid of chemical solution type and tap water. The effects of the upstream and the downstream pressures of the nozzle, the distance between the nozzle and the specimen, the diameter of the specimen and the geometry of the test cell, i.e., the diameter of the test cell and the configuration of the nozzle holder, were investigated. Furthermore, the behavior of impinging cavity clouds was observed through instantaneous photographs.

Experimental Apparatus

The experiments were conducted by using cavitation erosion apparatus shown in Fig. 1 and Table 1. The jet is supplied from a constant pressure source *Pu* through a nozzle. It discharges into a test cell at specified constant pressure *Pd* and impinges against a test specimen mounted coaxially with the jet. Most of the experiments were conducted at $Pu = 9.9$ MPa and *Pd* from 0.14 to 0.40 MPa. Stand-off distance *L* between the outlet edge of the nozzle and the specimen is adjusted by spacers. The inner diameters of the test cells are 40 mm for apparatus 1 and 80 mm for apparatus 2 and 3. Windows are provided on both sides on the test cell so that the cavitating jet can be observed. By attaching a jet impingement plate made of plexiglass instead of a specimen mount, impinging cavity clouds can be observed. The impingement plate has a diameter of 40 mm.

Table 1 Cavitating jet erosion apparatus

	Diameter of test cell	Liquid used
Apparatus 1	40 mm	HWBF
Apparatus 2	80 mm	HWBF
Apparatus 3	80 mm	tap water

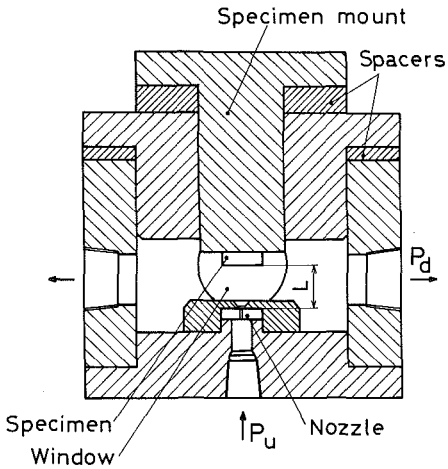

Fig. 1 Cavitating jet erosion apparatus

Nozzles of long orifice type were used in the experiments. The diameter and the thickness of the nozzle are 1.00 mm and 4.0 mm, respectively. The inlet edge of the nozzle is sufficiently sharp and the discharge coefficients of the tested three nozzles are in the range of $0.59 \sim 0.60$. The discharge coefficients did not change during the series of the experiments. Reynolds number based on the diameer of the nozzle is in the range of $1.2 \sim 1.5 \times 10^5$.

Two types of nozzle holder (Fig. 2) were used to investigate the effect of the configuration around the jet exit. The

Contributed by the Fluids Engineering Division for publication in the JOURNAL OF FLUIDS ENGINEERING. Manuscript received by the Fluids Engineering Division, February 27, 1986.

Table 2 Chemical composition of specimen

	Si	Fe	Cu	Mn	Mg	Cr	Ti
Aluminum alloy A5056BD	0.12	0.19	0.01	0.06	4.68	0.05	0.02

Table 3 Properties of test liquids

	Kimematic viscosity	Density
HWBF at 40°C	1.01±0.02 mm^2/s	1.00±0.01 g/cm^3
tap water 17°C	1.08±0.02 mm^2/s	1.00±0.01 g/cm^3
40°C	0.66±0.02 mm^2/s	0.99±0.01 g/cm^3

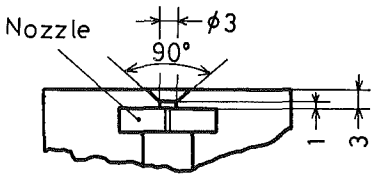

Nozzle holder A

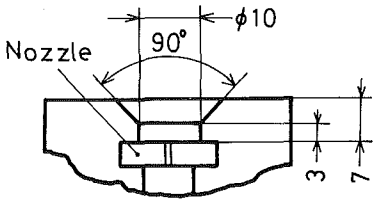

Nozzle holder B

Fig. 2 Configurations of nozzle holders

diameters of the jet exit holes are 3 mm for nozzle holder A and 10 mm for nozzle holder B. The outlet of the jet exit hole is enlarged and the total thicknesses are 3 mm for nozzle holder A and 7 mm for the nozzle holder B.

Circular speicmens of aluminum alloy (A5056BD) were used. The diameters of the specimens are 15 mm for specimen A and 28 mm for specimen B. Chemical composition of the specimens is shown in Table 2. Vickers hardness of the face of the specimens is in the range of 80~90. Masses of the specimens were measured before and at various intervals throughout the tests to an accuracy of 0.1 mg.

High water base fluid of chemical solution type (HWBF) and tap water were used as test liquids. HWBF contains the following components in terms of percentage by weight: water 96.95, polyalkylene glycol 1.5, fattyacid amine salt 1.25 and the rest 0.3. The rest contains vapor phase rust inhibitor (amine type), metal deactivator, anti-foam agent (alcohol type), antiseptic and coupling agent (glycol type). The properties of the test liquids are shown in Table 3.

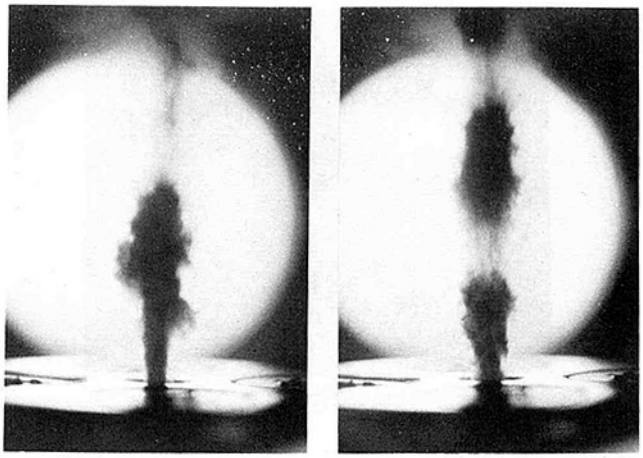

Fig. 3 Cavitating jet (apparatus 2 with nozzle holder A, HWBF, $Pu = 9.9$ MPa, $Pd = 0.20$ MPa)

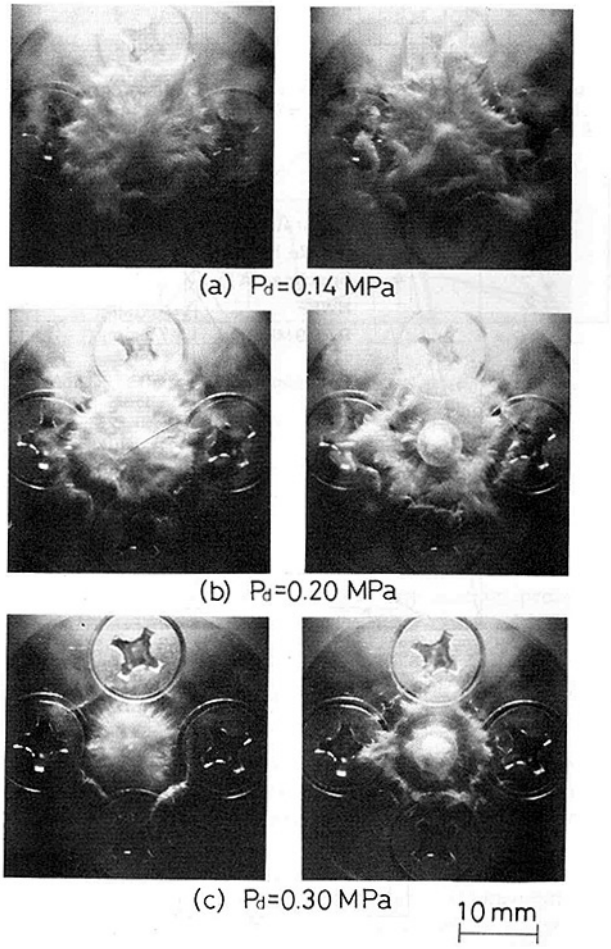

Fig. 4 Impinging cavity clouds (apparatus 2 with nozzle holder A, HWBF, $Pu = 9.9$ MPa, L = 10 mm)

Nomenclature

Cd = discharge coefficient of nozzle
D = erosion ring diameter
d = diameter of nozzle
de = effective jet diameter, $d\sqrt{Cd}$
L = distance between outlet edge of nozzle and specimen
l = distance between inlet edge of nozzle and specimen
M = mass loss
Pu = upstream pressure of nozzle
Pd = downstream pressure of nozzle
T = exposure time
σ = cavitation number, Pd/Pu

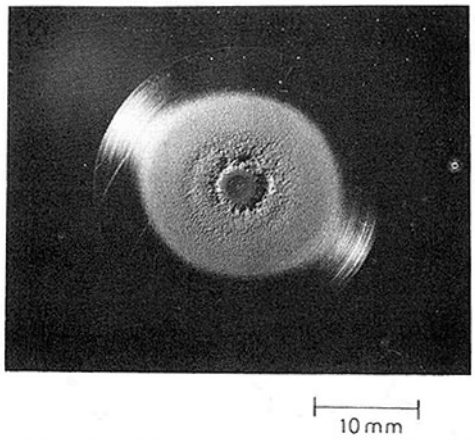

Fig. 5 Eroded specimen (apparatus 2 with nozzle holder A, HWBF, specimen B, Pu = 9.9 MPa, Pd = 0.14 MPa, L = 10 mm)

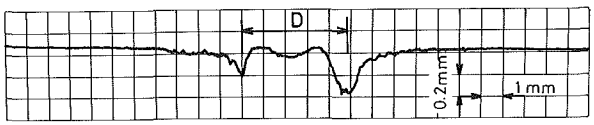

Fig. 6 Sectional curve of eroded specimen (apparatus 2 with nozzle holder A, HWBF, specimen B, Pu = 9.9 MPa, Pd = 0.14 MPa, L = 10 mm, 15 hours)

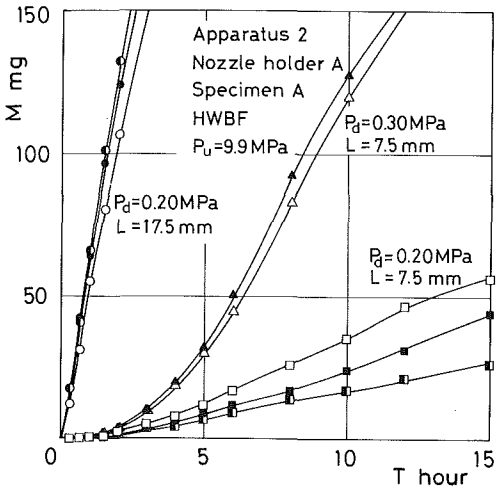

Fig. 7 Typical relationship between weight loss and exposure time

Apparatus 1 and 2 for HWBF are installed in parallel in a closed circuit. Supply to the nozzle was well filtered (3μm) so that the specimen would not damaged by particle erosion. The liquid temperature is measured at the exit from the test cell and the experiments were conducted at 40 ± 1°C. Apparatus 3 for tap water is installed in another circuit. The temperature of the water at the exit from the cell was 17 ± 3°C or 40 ± 1°C.

Experimental Results and Discussion

The following experiments were carried out by using HWBF as the test liquid unless otherwise specified. The uncertainties in the experimental conditions are as follows: the upstream pressure Pu ±0.2 MPa, the downstream pressure $Pd\pm0.01$ MPa and the standoff distance $L\pm0.1$ mm.

Figure 3 shows some examples of the photographs of the cavitating jet. The flow direction is upward. Since the jet was illuminated from back, the cavity clouds appear to be black. By attaching the jet impingement plate made of plexiglass instead of the specimen mount, impinging cavity clouds were

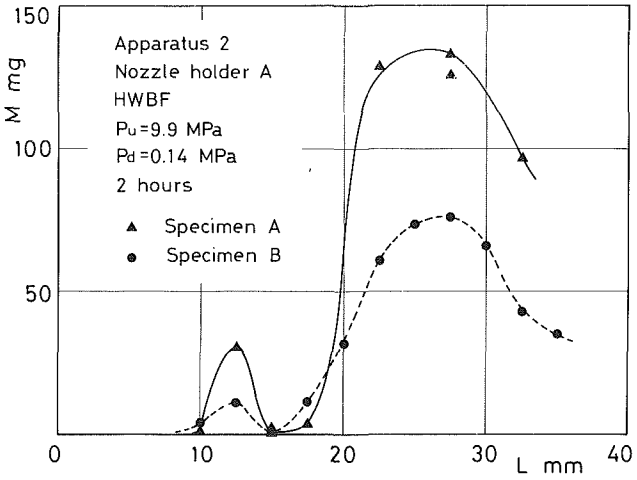

Fig. 8 Effect of specimen diameter on weight loss (diameter of specimen A is 15 mm and that of specimen B is 28 mm)

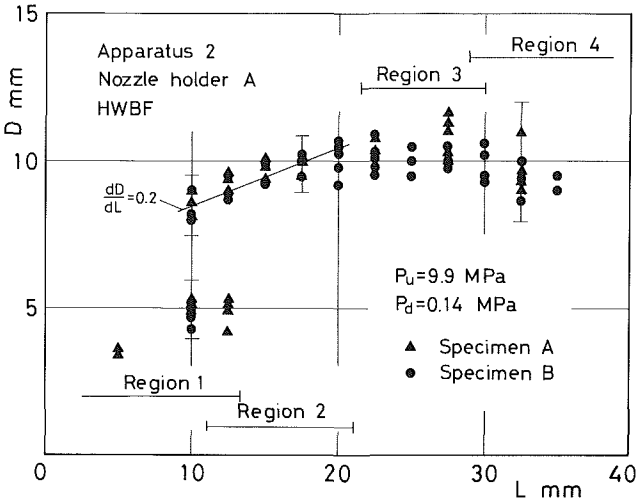

Fig. 9 Effect of specimen diameter on erosion ring diameter (diameter of specimen A is 15 mm and that of specimen B is 28 mm)

observed from the front. Figure 4 shows the photographs of the impinging cavity clouds. In the photographs, the cavity clouds appear to be white and the nozzle holder is visible behind the cavity clouds. The photographs in Figs. 3 and 4 were taken at unrelated intervals of time. The exposure time is approximately 20 μs. The cavity clouds appear to be continuous near the jet exit but separate and develop into lumps as they travel with the jet (Fig. 3). After the impingement, the cavity clouds splash radially (Fig. 4) and collapse of the cavities causes characteristic ring damage on the specimen as shown in Fig. 5. The specimen shown in Fig. 5 was eroded under the same conditions of the pressures and the stand-off distance as the photographs in Fig. 4(*a*). The cavity clouds spread far from the center but a deeply eroded ringlike valley is formed in the region relatively near the center. Outside the deeply eroded valley, a shallow eroded valley can be seen. Figure 6 shows the sectional curve of the eroded specimen shown in Fig. 5. The erosion ring diameter D is defined as shown in Fig. 6.

Some of the experiments were repeated under the same conditions to assure reproducibility of results. Figure 7 shows typical variations of mass loss M with the exposure time T. The scatter of M depends on the upstream pressure, the downstream pressure, the stand-off distance and the exposure time. The scatter of M in the case of $Pd=0.20$ MPa, $L=7.5$ mm at $T=15$ hours in Fig. 7 reaches about ±35 percent. In

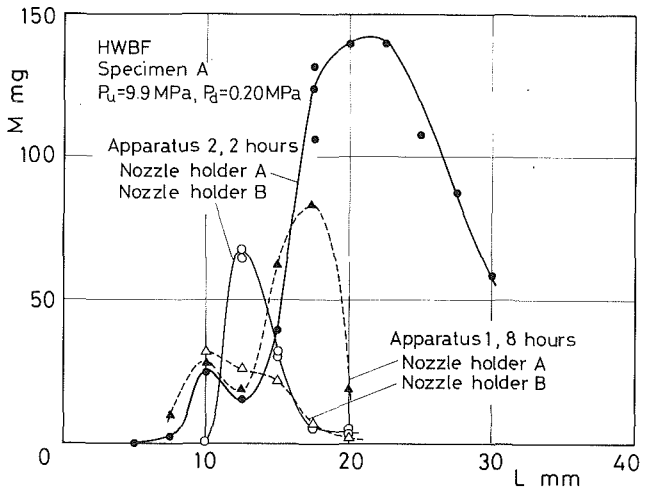

Fig. 10 Effect of test cell geometry on weight loss

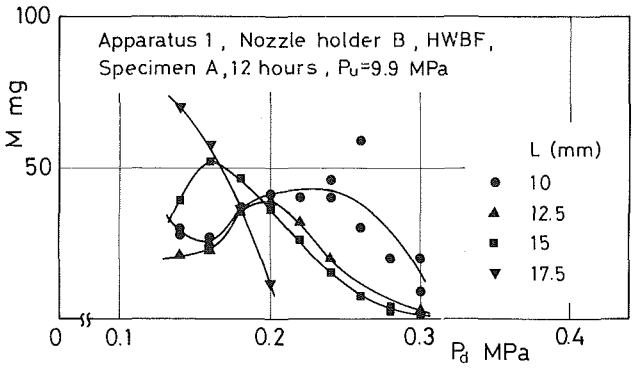

Fig. 11 Effect of downstream pressure on weight loss

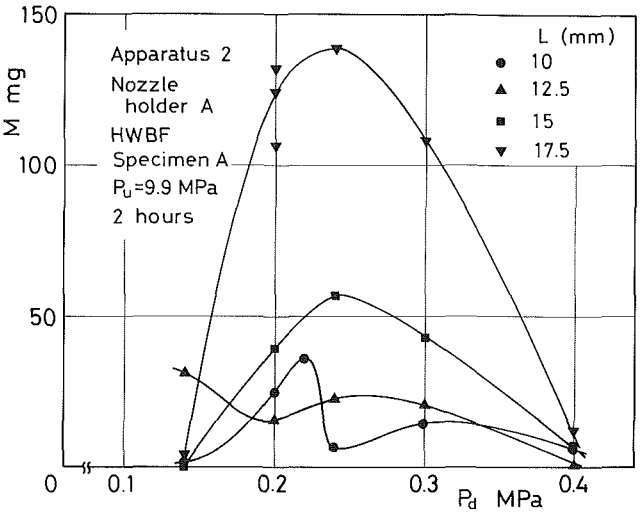

Fig. 12 Effect of downstream pressure on weight loss

the following results, for instance, in the case of $L = 10$ mm and $Pd = 0.26$ MPa in Fig. 11 and of $L = 10$ mm for 40°C tap water in Fig. 17, the scatters reach about ±30 percent. However, in the majority of cases, the scatters of M are less than ±15 percent.

The mass loss depends on the diameter of the specimen. Apparatus 2 with nozzle holder A was used to investigate the effect of the specimen diameter. Figures 8 and 9 show the variations of mass loss and erosion ring diameter with the stand-off distance for specimen A (diameter of 15 mm) and specimen B (diameter of 28 mm) at $Pd = 0.14$ MPa. In general, the mass loss of specimen A is larger than that of specimen B but the stand-off distances of specimen A to give the peak mass loss and the variation of D of specimen A are much the same as specimen B. In the case of $Pd = 0.20$ MPa, the mass loss of specimen A is larger than that of specimen B but the difference of the mass losses between specimens A and B is smaller than that of $Pd = 0.14$ MPa. Kleinbreuer [8] reported similar results about the effect of the specimen diameter from his experiments in hydraulic oil.

The mass loss also depends on the geometry of the test cell. Figure 10 shows the variations of mass loss with the stand-off distance by apparatus 1 and 2 with nozzle holder A or B. Apparatus 1 and 2 are installed in parallel in the circuit so that the liquid of the same condition is provided. Effects of the configuration around the jet exist was investigated by using nozzle holders A and B shown in Fig. 2. In general, the mass loss by apparatus 1 is considerably smaller than that by apparatus 2. The mass loss is also affected significantly by the configuration around the jet exit.

The variations of mass loss with downstream pressure are shown in Figs. 11 and 12 for apparatus 1 with nozzle holder B and apparatus 2 with nozzle holder A, respectively. As pointed out before, the mass loss by apparatus 2 with nozzle holder A is considerably larger than that by apparatus 1 with nozzle holder B. The mass loss tends to have two peaks for relatively short stand-off distanct and only one peak for long stand-off distance. The downstream pressure of apparatus 1 to give the maximum mass loss is larger than that of apparatus 2. For example, when L equals 15 mm, Pd to give the maximum mass loss of apparatus 1 is approximately 0.16 MPa, but that of apparatus 2 is approximately 0.24 MPa. Conn et al. [17] investigated the effect of the downstream pressure on erosion rate and obtained similiar curves to those at $L = 15$ mm and 17.5 mm in Figs. 11 and 12, namely low rate of erosion at low pressure speaking at some interim value, followed by a reduction of erosion as pressure continues to rise. The complicated behavior at $L = 10$ mm and 12.5 mm in Figs. 11 and 12 is connected to the fact that the mass loss has a peak at around $L = 10$ mm and the stand-off distance corresponding to the peak mass loss decreases with increasing the downstream pressure as shown in Fig. 13.

Figure 13 shows the variations of mass loss with the stand-off distance for various values of the downstream pressure. These are the results of specimen A by apparatus 2 with nozzle holder A. The mass losses for $Pd = 0.14$, 0.20, 0.30, and 0.40 MPa have maximums at $L = 25 \sim 27.5$ mm, $20 \sim 22.5$ mm, 20 mm and 17.5 mm, respectively. For $Pd = 0.14$ and 0.20 MPa, the mass losses have local maximums at $L = 12.5$ mm and 10 mm, respectively. The variations of erosion ring diameter with the stand-off distance for $Pd = 0.14$ MPa and 0.30 MPa are shown in Figs. 9 and 18, respectively. Figure 14 shows the sectional curves of the eroded specimens at various stages of erosion for $Pd = 0.20$ MPa at $L = 7.5$ mm, 10 mm and 15 mm. From Figs. 8, 9, 13, 14, and 18, the variation of erosion with the stand-off distance is divided into four regions.

Region 1: The stand-off distance is relatively small. Two or three eroded valleys are formed but the progress of erosion is slow and the mass loss is small. (Fig. 14 (a))

Region 2: The erosion ring diameter increases linearly with increasing the stand-off distance and its gradient is approximately 0.2, which agrees with that of circular jet diameter in fully developed flow region.

In region 1 especially near the boundary of regions 1 and 2, an outer erosion ring is formed in the early stage of erosion but as the erosion proceeds an inner erosion ring is formed rapidly (Fig. 14(b)). The mass loss tends to have a peak between

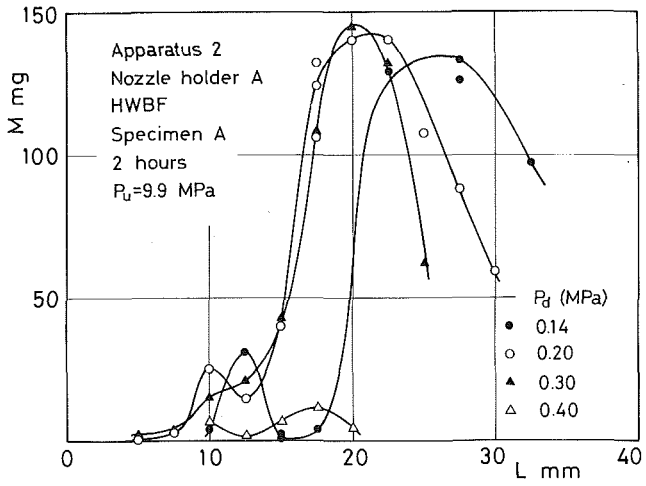

Fig. 13 Effect of downstream pressure on variation of weight loss with stand-off distance

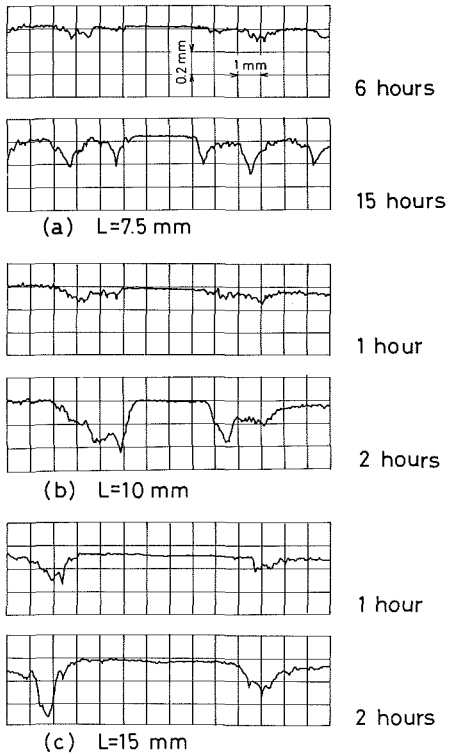

Fig. 14 Sectional curves of eroded specimen at various stages of erosion (apparatus 2 with nozzle holder A, HWBF, specimen A, $Pu = 9.9$ MPa, $Pd = 0.20$ MPa)

regions 1 and 2, where the deeply eroded valley seems to shift from the inner ring to the outer ring.

Region 3: There is not very much change of the erosion ring diameter. In the case of apparatus 2 with nozzle holder A, the mass loss has a maximum in this region.

Region 4: The erosion ring diameter and the mass loss decreases with increasing the stand-off distance.

From the experiments conducted at $L = 10 \sim 22.5$ mm by using apparatus 1 with nozzle holde B, similar results were obtained when the downstream pressure was relatively low. For example, the mass loss has a maximum at $L = 20$ mm and a local maximum at $L = 12.5$ mm for $Pd = 0.14$ MPa. When the downstream pressure is equal to or larger than 0.20 MPa, the

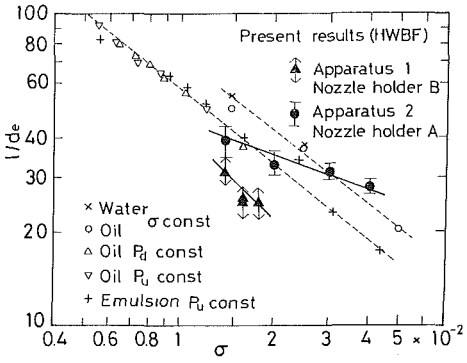

Fig. 15 Variations of optimum stand-off distance with cavitation number (Uncertainty in $\sigma \simeq \pm 0.2 \times 10^{-2}$)

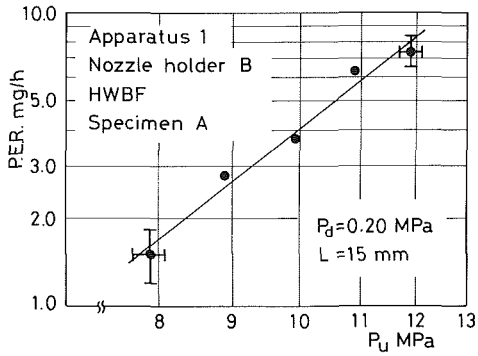

Fig. 16 Variation of P.E.R. with upstream pressure

mass loss has a maximum at $L = 10$ mm. Lichtarowicz [5] rearranged his own and other researchers' experimental results obtained with hydraulic oil, water and water-oil emulsion and found the relationship between optimum stand-off distance l and the cavitation number as follows;

$$l/de = a\sigma^{-m} \tag{1}$$

where the value of m is approximately 0.8. The optimum stand-off distance is defined as the distance between the inlet edge of the nozzle and the specimen to give a maximum cummulative erosion rate or a maximum mass loss for a fixed time. The effective jet diameter de is defined by

$$de = d\sqrt{Cd} \tag{2}$$

where d is the nozzle diameter and Cd is the discharge coefficient. The results by apparatus 1 with nozzle holder B and apparatus 2 with nozzle holder A are plotted on Lichtarowicz's figure as shown in Fig. 15. In this report the optimum stand-off distance is defined as the distance to give a maximum mass loss for a fixed time (12 hours for apparatus 1 and 2 hours for apparatus 2). The present results seem to satisfy the relationship given by equation (1). For apparatus 1 with nozzle holder B, the value of m is approximately 0.9 but the optimum stand-off distance is considerably smaller than that by apparatus 2 with nozzle holder A and other researchers' results. The value of m for apparatus 2 with nozzle holder A is approximately 0.3.

By using apparatus 1 with nozzle holder B, the effect of the upstream pressure was investigated. The experiments were conducted at $Pd = 0.20$ MPa and $L = 15$ mm. The cavitation number varies with Pu from 0.017 to 0.025. The mass loss increases with increasing the upstream pressure. Figure 16 shows the variation of peak erosion rate (P.E.R.) with the upstream pressure, where P.E.R stands for the peak value of increasing rate of mass loss defined by dM/dT. There exists the relationship between P.E.R. and Pu as

$$\text{P.E.R.} \propto Pu^n \tag{3}$$

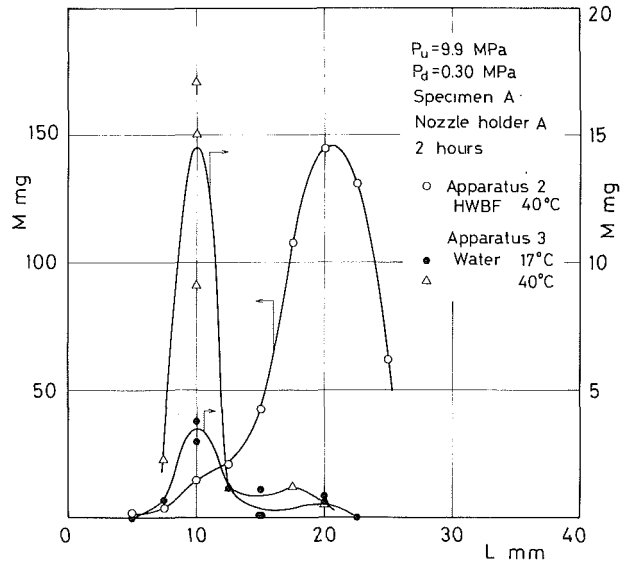

Fig. 17 Variations of weight loss with stand-off distance for HWBF and tap water

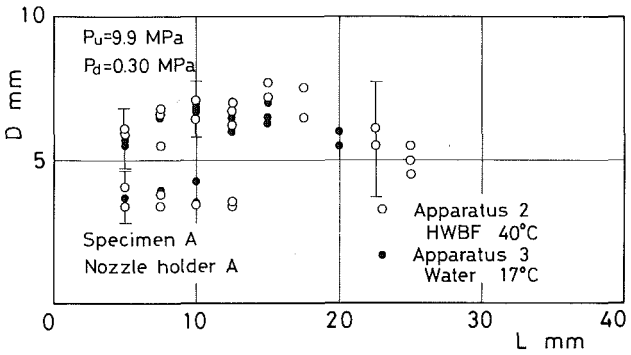

Fig. 18 Variations of erosion ring diameter with stand-off distance for HWBF and tap water

where $n = 4.0$. Similar results were reported by Lichtarowicz [4], Kleinbreuer [7] and Conn et al. [17]. Lichtarowicz indicated that the index was around 4 when the tests were carried out at constant cavitation number and at optimum stand-off distance. Kleinbreuer reported $n = 4.5$ for mass loss rates. Conn et al. obtained $n = 3$ from their CAVIJET erosion depth rate tests.

Figure 17 show the variations of mass loss with the stand-off distance in HWBF and tap water. The upstream and the downstream pressures are 9.9 MPa and 0.30 MPa, respectively. The mass losses in tap water are considerably smaller than those in HWBF except the result at $L = 10$ mm and 40°C where the mass loss is comparable to that in HWBF. The mass loss in HWBF has a point of inflection at $L = 10 \sim 12.5$ mm and a maximum at $L = 20$ mm. On the other hand, the mass loss in tap water has a maximum at $L = 10$ mm. The mass losses in water at 40°C larger than those at 17°C especially at $L = 10$ mm. Figure 18 shows the variations of erosion ring diameter with the stand-off distance. The variations in tap water at 17°C and HWBF at 40°C are about the same. There are a few reports about the effects of high weight polymer on cavitation erosion. Ashworth and Procter [18] reported the results of vibratory test in solutions of polyacryamid, where the cavitation erosion rate in increased. Kudin et al. [19] reported that underwater jet cutting was greatly enhanced by polymer additions to the jet fluid. Hoyt and Taylor [20] observed that the cavitation bubbles in drag reducing polymer solution appeared larger than those in pure water. They suggested that the large bubble size in polymer solution could offer a explanation on increased erosion compared with pure water.

Conclusions

Cavitation erosion due to impingement of cavitating jet was studied experimentally with specimens of aluminum alloy in high water base fluid of chemical solution type and tap water by using cavitation erosion apparatus. Futhermore, the behavior of cavitating jet and impinging cavity clouds were observed through instanteous photographs.

Impinging cavity clouds splash radially and collapse of the cavities causes ring damage on a specimen. When the stand-off distance is short, a deeply eroded ringlike valley is formed in the region relatively near the center compared with the extent of the cavity clouds.

Cavitation erosion is affected significantly by configuration of the test cell. The stand-off distance to give the maximum mass loss depends on the upstream pressure and the downstream pressure of the nozzle, configuration of test cell and test liquid.

In general, the mass loss in tap water is smaller than that in HWBF.

Acknowledgments

The authors wish to express their thanks to Mr. Hiroyasu Komatu for his cooperation in carrying out experiments.

References

1 Lichtarowicz, A., "Use of a Simple Cavitating Nozzle for Cavitation Erosion Testing and Cutting," *Nature; Physical Science*, Vol. 239, No. 91, 1972, pp. 63–64.

2 Lichtarowicz, A., "Cavitating Jet Apparatus for Cavitation Erosion Testing," ASTM STP 664, 1979.

3 Lichtarowicz, A., "Erosion Testing with Cavitating Jet," *Fluids Engng. Conf.*, Boulder, Col., 1981, ASME.

4 Lichtarowicz, A., and Scott, P. J., "Erosion Testing with Cavitating Jet," *Proc. 5th Int'l Conf. on Erosion by Solid and Liquid Impact*, Cambridge, 1979, pp. 69-1 to 69-8.

5 Lichtarowicz, A., and Kay, P., "Erosion Tesing with Cavitating Jets, *Proc. 6th Int'l. Conf. on Erosion by Liquid and Solid Impact*, Cambridge, 1983, pp. 15-1 to 15-4.

6 Kleinbreuer, W., "Werkstoffzertörung durch Kavitation in ölhydraulichen Systemem," *Industrie-Anzeiger*, Vol. 98, No. 61, 1976, pp. 1069–1100.

7 Kleinbreuer, W., "Kavitationserosion in hydraulischen Systemen," *Industrie-Anzeiger*, Vol. 99, No. 34, 1977, pp. 609–613.

8 Kleinbreuer, W., "Untersuchung der Werkstoffzerstörung durch Kavitation in ölhydraulischen Systemen," Disseration, TH. Aachen, 1979.

9 Kleinbreuer, W., "Anwendung eines Partikel-Maß-und Zählgerätes," *ölhydraulik und pneumatik*, Vol. 24, No. 2, 1980, pp. 89–93.

10 Kleinbreuer, W., "Maßnahmen zur Vermeidung bzw. Verminderung von Kavitationserosion in hydraulischen Systemem," *ölhydrulik und pneumatik*, Vol. 24, No. 6, 1980, pp. 455–460.

11 Kleinbreuer, W., and Pohl, M., "Vorgänge beim Materialabtrag durch Kavitation in ölhydraulischen Systemem," *ölhydraulik und pneumatik*, Vol. 25, No. 5, 1981, pp. 409–417.

12 Berger, J., "Untersuchung der Auswirkung von Kavitation beim Einstatz von HFA-Flüssighkeiten," *ölhydraulik und pneumatik*, Vol. 26, No. 6, 1982, pp. 441–451.

13 Berger, J., Pohl, M., and Sitnik, L., "Einflu der Werkstoffes und seines Oberflächenzustandes auf die Kavitationsbeständigkeit," *ölhydraulik und pneumatik*, Vol. 27, No. 10, 1983, pp. 714–718.

14 Backe, W., and Berger, J., "Kavitationserosion bei HFA-Flüssigkeiten," *ölhdraulic und pneumatik*, Vol. 28, No. 5, 1984, pp. 288–295.

15 Conn, A. F., "CAVIJET Augmented Deep-hole Drilling Bits," ASME *Journal of Pressure Vessel Technology*, Vol. 100, 1978, pp. 52–59.

16 Conn, A. F., "Elevated ambient pressure effects on rock cutting by cavitating fluid jets," *Proc. 5th Int'l. Conf. on Erosion by Solid and Liquid Impact*, 1979, pp. 68-1 to 68-8.

17 Conn, A. E., and Johnson, V. E., Jr., "The Fluid Dynamics of Submerged Cavitating Jet Cutting," *Proc. 5th Int'l. Symp. on Jet Cutting Tech.*, 1980, pp. 1–14.

18 Ashworth, V., and Proctor, R. P. M., "Cavitation Damage in Dilute Solution," *Nature*, Vol. 258, 1975, pp. 64–66.

19 Kudin, A. M., Barenblatt, G. I., Kalashnikov, V. N., Vlasov, S. A., and Belkon, V. S., "Destruction of Metric Obstacles by a Jet of Dilute Polymer Solution," *Nature; Physical Science*, Vol. 245, 1973, pp. 95–96.

20 Hoyt, J. W., and Talyor, J. J., "A Photographic Study of Cavitation in Jet Flow," ASME JOURNAL OF FLUIDS ENGINEERING, Vol. 103, 1981, pp. 14–18.

Journal of Fluids Engineering

Technical Briefs

On the Development of Laminar Internal Flows With Mass Injection and Extraction

C. A. Busse[1]

Logical criteria are presented for determining the effects of channel shape, viscous force, and mass injection/extraction on axisymmetric and planar velocity profiles.

Nomenclature

- A = cross-sectional area of flow channel
- c = velocity of sound in the fluid
- F_μ, F_r = defined by (17), (18) or (25), (26)
- g_r, g_z = inertia force density in axial direction, contribution from radial and axial transport of axial momentum, respectively
- h = coordinate normal to symmetry plane of two flat plates
- H = half width of flow channel
- Ma = Mach number
- P = pressure of fluid
- r = radial coordinate
- R = radius of flow channel
- Re = axial Reynolds number
- Re_r = wall Reynolds number
- S = circumference of flow channel
- u = radial velocity
- v = suction velocity at the wall
- w = axial velocity
- z = axial coordinate
- δ = variation
- ϵ = half angle of flow channel
- μ = viscosity of fluid
- ρ = density of fluid

Subscripts

- o = center ($r=0$ or $h=0$)
- 1 = wall ($r/R = 1$ or $h/H=1$)
- in = inlet

Superscripts

- $'$ = partial differentiation with respect to r/R or h/H
- $\bar{}$ = average over the cross-section of the flow channel

[1]Thermodynamics Division Head, Commission of the European Communities, Joint Research Centre - Ispra Establishment, 21020 Ispra (VA) - Italy.

Contributed by the Fluids Engineering Division of The American Society of Mechanical Engineers. Manuscript received by the Fluids Engineering Division July 31, 1986.

Introduction

Injection and extraction of mass have a significant influence on the development of a flow. For external laminar flows, this influence is well known and can qualitatively be described by a simple rule: extraction of mass tends to produce full velocity profiles, while injection promotes the development of separation profiles characterized by an inflexion point and back flow at the wall. A practical consequence of this rule is that mass extraction stabilizes an external flow (for a comprehensive literature review see [1]).

Internal flows are more complicated and less well understood. Although the flows can be computed, no general rules for the development of the velocity profile have been identified yet. Some analyses (e.g. [2-5]) show that the influence of injection and extraction of mass on the profile development is just opposite to external flows, i.e., mass extraction promotes flow separation. The computations of Bankston and Smith [6] indicate that this may not always be the case. Van Ooijen and Hoogendoorn [7], for example, predict for a condensing flow between parallel plates the occurrence of both types of influence. In the upstream region the mass extraction makes the profile steeper at the wall, similar to an external flow. Further downstream the opposite trend occurs and leads to flow separation. The reason for this change is unknown.

In the present paper a local criterion is derived for axisymmetric internal flows, which indicates whether a given velocity profile has the tendency to develop towards a separation profile or not, and from which some general rules for the profile development are deduced.

2 Basic equations and profile shapes

The general frame of the analysis is steady laminar compressible flow with injection or extraction of mass and small variations of the channel cross-section. The following restrictive assumptions are made. The flow is subsonic and has axial symmetry. The cross-section varies with a constant half angle, ϵ. The normal velocity at the wall, v, is constant. The radial velocity component, u, is small with respect to the average axial velocity component, $\bar{w}$, so that Prandtl's boundary layer approximation of the Navier-Stokes equation can be used [1]. This implies specifically that $v << \bar{w}$ and that the tube has only a slight divergence or convergence. The equation of momentum then is

$$\frac{dP}{dz} = -\rho\left(u\frac{\partial w}{\partial r} + w\frac{\partial w}{\partial z}\right) + \mu\left(\frac{1}{r}\frac{\partial w}{\partial r} + \frac{\partial^2 w}{\partial r^2}\right) \quad (1)$$

Mass conservation requires

$$\frac{\partial}{\partial r}(r\rho u) + r\frac{\partial}{\partial z}(\rho w) = 0 \quad (2)$$

The fluid is assumed to be a perfect isothermal gas. The equation of the state is

$$\frac{P}{\rho} = \text{const.} = c^2 \tag{3}$$

The assumption of isothermal flow simplifies the analysis considerably. It is well suited for gases with a specific heat ratio c_p/c_v close to 1, such as organic vapors with high molecular weight, and a rather uniform inlet temperature. In other cases it is a reasonable first approximation because the temperature variation in subsonic flows is in general relatively small.

The boundary conditions for the radial and axial velocity component at the wall, u_1, w_1 are (see Fig. 1)

$$u_1 = v \cos \epsilon \tag{4}$$

$$w_1 = -v \sin \epsilon \tag{5}$$

To define the flow completely, the upstream initial profile of the axial velocity, $w(r, z=0)$ has to be specified.

Figure 2 shows a typical set of numerical solutions of the foregoing equations which give an idea of the kind of velocity profile variations to be discussed. The solutions were obtained by the method described in [8, 9]. They show the development of a flow in a cylindrical tube ($\epsilon = 0$) with injection or extraction of mass at the wall. The initial velocity profile is assumed as parabolic with a centerline Mach number

$$\text{Ma}_o = \frac{w_o}{c} \tag{6}$$

of 0.6. The curve parameter is the ratio of the axial mass flow to the initial axial mass flow, which can be expressed by the corresponding ratio of the Reynolds numbers Re/Re_{in}, where

$$\text{Re} = \frac{2R\rho\bar{w}}{\mu} \tag{7}$$

The wall velocity v corresponds to a wall Reynolds number

$$Re_r = \frac{R\rho v}{\mu} \tag{8}$$

of $+10$ (for injection) and -10 (for extraction), respectively. The diagram illustrates the two main types of profile deformation: profile flattening characterized by a decrease of the normalized centerline velocity

$$\frac{d}{dz}\frac{w_o}{\bar{w}} < 0 \tag{9}$$

and the opposite profile "extrusion," which leads to flow separation.

3 The Mechanism of Velocity Profile Deformation by Mass Extraction

The striking difference between external and internal flows is that, for example, mass extraction in the first case always tends to deform the profile in the same way, but not in the second case. This can easily be understood. Let us consider a flow in a cylindrical tube. Extraction of mass at the wall creates a radial mass flow towards the wall and decreases the axial mass flow. These two processes are coupled with a change of the density of axial momentum. The resulting densities of axial force are given by the two inertia terms of the momentum equation (1)

$$g_r = -\rho u \frac{\partial w}{\partial r} \tag{10}$$

$$g_z = -\rho w \frac{\partial w}{\partial z} \tag{11}$$

They represent the net delivery of axial momentum per unit volume by the radial mass flow, ρu, and the axial mass flow, ρw, respectively.

Let us assume a velocity profile with $\partial w/\partial r \leqq 0$. A mass transfer in radial direction, $u > 0$, then carries particles with high axial velocity into regions of low axial velocity. The result is an accelerating force $g_r > 0$ is z-direction. Taking into account that ρ is constant in the radial direction (because of (3)) and that u and $\partial w/\partial r$ are zero on the axis and finite at the wall, it follows from (10) that g_r is small near the centerline and relatively large at the wall.

Also g_z is positive, since the flow is slowed down. But at the wall w and, therefore, also $\partial w/\partial z$ are zero because of the no-slip condition, while they are finite in the center. It follows from (11) that g_z is small near the wall and relatively large in the center.

The consequence of the different radial variation of g_r and g_z is that g_r accelerates preferentially the peripheral part of the flow and g_z the central part, i.e., the radial mass flow tends to flatten the normalized velocity profile while the simultaneous decrease of the axial mass flow tends to extrude the profile. The net outcome depends on which of these counteracting effects dominates. This is the basic reason for the ambivalent character of extraction or injection of mass in the case of internal flows.

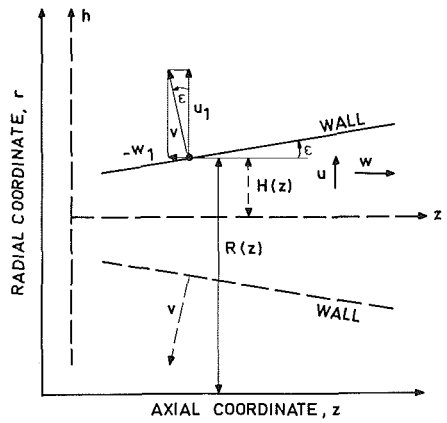

Fig. 1 Coordinate system for axisymmetric flow (r, z). Dashed: planar duct flow (h, z).

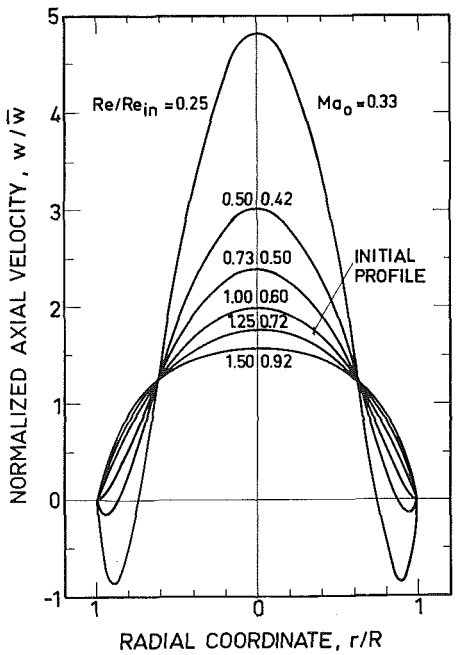

Fig. 2. Development of an axisymmetric flow in a cylindrical tube with injection or extraction of mass at the wall ($\text{Re}_r = \pm 10$). Curve parameter Re/Re_{in} = ratio of axial mass flow to initial aixal mass flow, Ma_0 = centerline Mach number.

For external flows, on the other hand, the influence of mass extraction on $\partial w/\partial z$ in the free stream is negligibly small, so only g_r is affected. Mass extraction, therefore, leads always to fuller profiles.

4 Criterion for the Flattening of the Normalized Velocity Profile

A relation between $d(\bar{w}_0)/dz$ and the flow parameters can be derived by rewriting the momentum equation (1) for the centerline and at the wall. The z-derivatives of w in these two equations are substituted by

$$\left(\frac{\partial w}{\partial z}\right)_0 = \bar{w}\,\frac{\partial}{\partial z}\,\frac{w_0}{\bar{w}} - w_0\left(\frac{1}{\rho c^2}\,\frac{dP}{dz}+\frac{1}{A}\,\frac{dA}{dz}+\frac{S}{A\cos\epsilon}\,\frac{v}{\bar{w}}\right) \quad (12)$$

which follows from the mass conservation (2) and the equation of state (3), and by

$$\left(\frac{\partial w}{\partial z}\right)_1 = -\left(\frac{\partial w}{\partial r}\right)_1 \tan\epsilon \quad (13)$$

which is a consequence of the constancy of u_1 (4) and w_1 (5). Eliminating dP/dz from the two momentum equations and resolving for $d(w_o/\bar{w})/dz$ one obtains

$$\frac{w_0}{\bar{w}}\,\frac{d}{dz}\,\frac{w_0}{\bar{w}} = \frac{w_0^2}{\bar{w}^2}\,\frac{1}{A}\,\frac{dA}{dz} + \frac{1}{\cos\epsilon}\left[\left(1-\mathrm{Ma}_0^2\right)\left(\frac{\partial}{\partial r}\,\frac{w}{\bar{w}}\right)_1 + \frac{w_0^2}{\bar{w}^2}\,\frac{S}{A}\right]\frac{v}{\bar{w}} + \frac{\mu}{\rho\bar{w}^2}\left[\left(\frac{1}{r}\,\frac{\partial w}{\partial r}+\frac{\partial^2 w}{\partial r^2}\right)_0 - \left(1-\mathrm{Ma}_0^2\right)\left(\frac{1}{r}\,\frac{\partial w}{\partial r}+\frac{\partial^2 w}{\partial r^2}\right)_1\right] \quad (14)$$

Rewriting this equation in dimensionless form for an axially symmetric tubular flow, one finds from condition (9) the following criterion for profile flattening

$$\frac{d}{dz}\,\frac{w_o}{\bar{w}} = \frac{2}{R}\left\{\frac{w_o}{\bar{w}}\tan\epsilon - \frac{1}{\mathrm{Re}\;w_o/\bar{w}}\left[\left(1-\mathrm{Ma}_0^2\right)\frac{w_1'+w_1''}{\bar{w}} - 2\,\frac{w_0''}{\bar{w}}\right] - \frac{\mathrm{Re}_r}{\mathrm{Re}(\cos\epsilon)w_o/\bar{w}}\left[\left(1-\mathrm{Ma}_0^2\right)\frac{w_1'}{\bar{w}} + 2\left(\frac{w_o}{\bar{w}}\right)^2\right]\right\} < 0 \quad (15)$$

The primes mean partial differentiation with respect to r/R.

5 Discussion

5.1 Single Effects. Equation (15) shows that the profile flattening depends on Re, Re_r, Ma_0, ϵ and the local profile shape. The criterion is composed of three terms, which represent the action of channel shape, viscous force and mass injection/extraction, respectively. For each term in (15) to be negative (i.e., flattening) it follows that

channel shape

$$\epsilon < 0 \quad (16)$$

viscous force

$$F_\mu \equiv (1-\mathrm{Ma}_0^2)\,\frac{w_1'+w_1''}{\bar{w}} - 2\,\frac{w_0''}{\bar{w}} > 0 \quad (17)$$

mass injection / mass extraction

$$F_r \equiv (1-\mathrm{Ma}_0^2)\,\frac{w_1'}{\bar{w}} + 2\left(\frac{w_0}{\bar{w}}\right)^2 \begin{cases} >0 \\ <0 \end{cases} \quad (18)$$

Re and Re_r do not appear in these individual flattening criteria; they play the role of weight factors, which determine in (15) the relative importance of mass injection/extraction and variation of the cross-section with respect to the viscous effects.

Equation (16) shows that a channel convergence flattens the profile and a divergence has the opposite effect.

The influence of the viscous force and mass injection/extraction on the normalized profile depends on the profile shape and on the Mach number. Consider a profile variation $\delta(w_0/\bar{w}) > 0$. The numerical solutions of the flow equations (see Fig. 2) indicate that an extruding of the profile usually means the profile becomes more curved in the center and less curved and less steep at the wall, i.e.,

$$\delta\,\frac{w_0}{\bar{w}} > 0 \qquad \delta\,\frac{w_1'}{\bar{w}} > 0 \qquad \delta\,\frac{w_0''}{\bar{w}} < 0 \qquad \delta\,\frac{w_1''}{\bar{w}} > 0 \quad (19)$$

It follows from (17) and (18)

$$\delta F_\mu > 0 \qquad \delta F_r > 0 \quad (20)$$

So, in a first approximation, F_μ and F_r increase as the profile becomes extruded, and decrease as the profile is flattened. The criteria (17) and (18) then mean: if the normalized profile is sufficiently extruded, both the viscous force and injection produce flattening of the profile, whereas suction has an extruding effect. When going to sufficiently flat profiles, all actions reverse. The conclusion is that the viscous force and mass injection tend to establish an equilibrium profile, characterized by $F_\mu = 0$ or $F_r = 0$, respectively, while mass extraction is an inherently unstable process which promotes a run-away from the equilibrium condition $F_r = 0$. This explains the known phenomenon, shown also in Fig. 2, that mass extraction usually leads to much stronger profile variations than injection.

The equilibrium profiles are developed if the respective action is the only one present. So, the viscous equilibrium profile is developed in a flow with $\epsilon = 0$ and $\mathrm{Re}_r = 0$. For incompressible flow, $\mathrm{Ma}_0 \ll 1$, this is the Hagen-Poiseuille profile

$$\frac{w}{\bar{w}} = 2\left(1-\frac{r^2}{R^2}\right) \quad (21)$$

With (17) one verifies that it satisfies $F_\mu = 0$. Furthermore, with (18) it gives $F_r > 0$. This means that injection flattens the parabolic profile. This is confirmed by Fig. 2 and by the equilbrium profile for mass injection and incompressible flow (i.e., the profile developed for $\epsilon = 0$, $\mathrm{Re}_r \gg 1$ and $\mathrm{Ma}_0 \ll 1$) [10]

$$\frac{w}{\bar{w}} = \frac{\pi}{2}\cos\left(\frac{\pi r^2}{2R^2}\right) \quad (22)$$

which is flatter than the parabolic profile (21). As expected, the cosine profile satisfies the equilibrium condition $F_r = 0$.

At higher Ma_0 the equilibrium profiles become flatter [8]. This is indicated also by (17) and (18), which show that with rise of Ma_0 the equilibria $F_\mu = 0$ and $F_r = 0$ are shifted to larger w_0'', smaller w_1' and w_1'' and smaller $w_0/\bar{w}$, i.e., to flatter profiles.

5.2 Collective Effects. Both mass injection and viscous

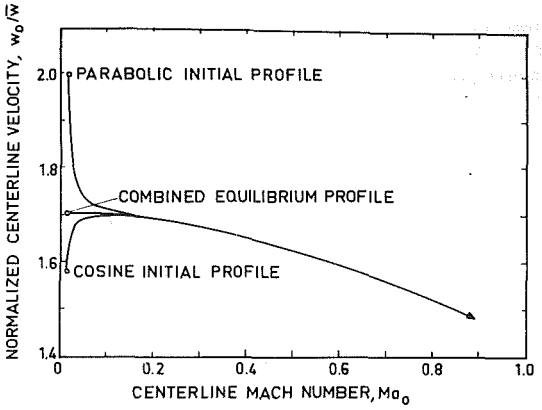

Fig. 3 Influence of mass injection with $Re_r = 10$ on the normalized center velocity of a laminar flow in a cylindrical tube, for different initial profiles (numerical results obtained with the method of [8, 9]).

effects tend to establish their respective equilibrium velocity profiles. When both actions are present, a profile somewhere between the two equilibrium profiles will be approached. The criterion (15), rewritten with the definitions of F_μ and F_r,

$$\frac{\mathrm{R\,Re}}{4}\frac{d}{dz}\left(\frac{w_0}{\bar{w}}\right)^2 = \mathrm{Re}(\tan\epsilon)\left(\frac{w_0}{\bar{w}}\right)^2 - F_\mu - \frac{\mathrm{Re}_r}{\cos\epsilon}F_r < 0 \tag{23}$$

shows that for $Re_r >> 1$ the combined equilibrium will lie close to $F_r = 0$, for $Re_r << 1$ close to $F_\mu = 0$. The addition of a channel convergence (divergence) shifts this equilibrium to flatter (less flat) profiles. Fig. 3 illustrates the development of the equilibrium profile for a flow in a cylindrical tube with mass injection (numerical solution of the flow equations (1)–(5) by the method described in [8, 9]). Three inlet profiles are presented: the parabolic profile (21), the combined equilibrium profile, and the cosine profile (22). The diagram shows the convergence of the profiles to the equilibrium profile, which varies little up to $Ma_0 = 0.2$ becomes flatter at high Mach numbers.

For the combination of mass extraction ($Re_r < 0$) and viscous force, the existence of an equilibrium profile is more problematic. If the profile is sufficiently extruded, both F_μ and F_r are positive. So the viscous term and the mass extraction term in (23) have opposite signs, but their absolute values increase both with further extrusion of the profile.

For weak mass extraction ($Re_r \gtrsim -2$), where the viscous action dominates, an equilibrium is reached, while for stronger mass extraction the extruding continues and the profile tends to diverge [4]. This is shown also by Fig. 2.

If the velocity profile is sufficiently flat, both F_μ and F_r are negative. Criterion (23) then predicts profile flattening provided that the mass extraction (i.e., $-\mathrm{Re}_r$) is sufficiently large. An interesting question is: if the initial profile satisfies these conditions, will the flattening of the profile persist in the downstream direction so that separation is avoided? Bankston et al. [5] came to the conclusion that this can be the case. However, the numerical results of van Ooijen et al. [7] in planar geometry show that mass extraction leads only initially to profile flattening and that further downstream separation profiles are developed. Computations in cylindrical geometry with the method described in [9] have given similar results. When a profile becomes flattened, the changes of the slope are concentrated in a region near the wall, which gets always narrower. Therefore, a certain variation of the slope w_1' will cause increasingly larger variations of the curvature w_1''. As F_μ contains w_1'', but F_r only w_1', the viscous term in (23) will finally grow faster and become comparable in magnitude with the mass extraction term. The result could be an asymptotic approach of a stable equilibrium profile or, as well, a reversal of the profile deformation with a run-away in the opposite direction. The problem is that, according to (15), the reversal depends critically on $w_1'' + (\mathrm{Re}_r + 1)w_1'$, which represents a difference between two large numbers. So, close to the reversal point, relatively small changes in w_1' and w_1'' become important. In numerical analysis this leads to the possibility that the deformation reversal or its nonappearance could be the result of slight errors in the calculation of curvature and slope of the velocity profile at the wall.

5.3 Symmetric Flow Between Flat Plates. The foregoing analysis can be extended to the case of a symmetric flow between flat plates, shown also in Fig. 1, which can be considered as an annular flow between two tubes of infinite radii. The criterion (14) is valid also for this case.

Using instead of r a coordinate h with the origin in the symmetry plane of the channel, the individual flattening criteria then are

channel variation

$$\epsilon < 0 \tag{24}$$

viscous force

$$F_\mu \equiv (1 - \mathrm{Ma}_0^2)\frac{w_1''}{\bar{w}} - \frac{w_0''}{\bar{w}} > 0 \tag{25}$$

mass injection / *mass extraction*

$$F_r(1 - \mathrm{Ma}_0^2)\frac{w_1'}{\bar{w}} + \left(\frac{w_0}{\bar{w}}\right)^2 \begin{cases} >0 \\ <0 \end{cases} \tag{26}$$

The index o refers now to the symmetry plane of the plates and the primes mean differentiation with respect to h/H. Equations (25) and (26) are slightly different from the corresponding equations (17) and (18) for the cylindrical case. The equilibrium profile for the viscous force ($F_\mu = 0$) at $Ma_o << 1$ is now given by the plane Poiseuille profile

$$\frac{w}{\bar{w}} = \frac{3}{2}\left(1 - \frac{h^2}{H^2}\right) \tag{27}$$

For this profile one finds from (26) $F_r < 0$, i.e., contrary to the cylindrical case, injection extrudes the parabolic profile. This is confirmed by the equilibrium profile for mass injection and extraction at $Ma_o << 1$ [11]

$$\frac{w}{\bar{w}} = \frac{\pi}{2}\cos\left(\frac{\pi}{2}\frac{h}{H}\right) \tag{28}$$

which is less flat than (27).

5.4 Profile Variation and Flow Stability. Can the general rules for the profile development be used to predict variations of the flow stability? Here again there is a considerable difference between internal and external flows.

For external flows, mass injection and extraction have a twofold action on the flow stability. As mentioned before, mass injection leads always towards separation profiles. These are characterized first, by a low profile stability, i.e., there is a decrease of the transition Reynolds number (formed with the thickness of the boundary layer), and second, by a larger thickness of the boundary layer, which means an increase of the Reynolds number of the flow. Both effects render the flow less stable [1].

For internal flows, there are two corresponding actions on the flow stability, but they may oppose each other. First, there is a change of the transition Reynolds number with the profile shape. Although the stability of internal flows is still less well understood than that of external flows, one may expect from the inflexion point criterion [1] that a transition to separation profiles is, in general, coupled with a decrease of the transition Reynolds number. Second, mass injection and extraction cause a change of the Reynolds number of the flow by the

variation of the mass flow. Therefore, a profile extrustion by mass extraction or a profile flattening by mass injection shift the transition Reynolds number and the flow Reynolds number in equal directions, so that without quantitative knowledge of the behavior of the transition Reynolds number, no theoretical conclusions on the flow stability can be drawn.

There are, however, some experimental data on the transition Reynolds number for these cases in axisymmetric cylindrical flows. For profile flattening by mass injection with $Re_r = 70$, the transition occurs at $Re = 10^4$, which is about four times higher than the transition Reynolds number without mass injection [12]. For profile extrusion by mass extraction, the transition to turbulence begins already at Reynolds numbers as low as a few hundred as soon as $Re_r \lesssim -6$ [5, 9]. These data show that the variation of the profile stability is large at high $|Re_r|$, so that it then may dominate the change of the flow stability.

6 Conclusions

Injection and extraction of mass can deform the normalized velocity profile of internal flow essentially in two ways. Either they flatten it, or they produce an opposite or extruding effect. This ambivalent behavior is in contrast to external flows. The reversal of the profile deformation depends on the profile shape and the Mach number. In general, if the profile is sufficiently extruded, both the viscous force and mass injection flatten the profile, whereas mass extraction has an extruding effect. Going to sufficiently flat profiles, all actions reverse. The viscous force and mass injection tend to establish an equilibrium profile while mass extraction is an inherently unstable process which promotes a run-away from the equilibrium condition. Viscous effects can slow down this run-away if the mass extraction is not too strong or if the profile is being flattened. It is uncertain whether in the latter case the viscous force can also induce a reversal of the profile deformation and a run-away in the opposite direction. An experimental investigation of the profile deformation by mass extraction with inlet profiles which are sufficiently flat to cause profile flattening would be desirable.

Acknowledgments

The author is indebted to Dr. F. Coyne Prenger and to Prof. Dr. Richard I. Loehrke for stimulating discussions.

References

1 Schlichting H., *Boundary-Layer Theory*, 7th ed., McGraw-Hill, 1979.

2 Weissberg, H. L., "Laminar Flow in the Entrance Region of a Porous Pipe," *Physics of Fluids*, Vol. 2, 1959, pp. 510–516.

3 Hornbeck R. W., "Laminar Entry Problem in Porous Tube," *Physics of Fluids*, Vol. 6, 1963, pp. 1649–1654.

4 Busse, C. A., "Pressure Drop in the Vapour Phase of Long Heat Pipes," 1967 IEEE Conf. Record of the Thermionic Conversion Specialist Conf., Palo Alto, 1967, pp. 391–398.

5 Quaile, J. P., and Levy, E. K., "Laminar Flow in a Porous Tube With Suction," ASME *Journal of Heat Transfer*, Vol. 97, 1975, pp. 66–71.

6 Bankston, C. A., and Smith H. J., "Vapor Flow in Cylindrical Heat Pipes," ASME *Journal of Heat Transfer*, Vol. 95, 1973, pp. 371–376.

7 van Ooijen, A., and Hoogendoorn, C. J., "Vapour Flow Calculations in a Flat-Plate Heat Pipe," *AIAA Journal*, Vol. 17, 1979, pp. 1251–1259.

8 Busse, C. A., and Prenger, F. C., "Numerical Analysis of the Vapour Flow in Cylindrical Heat Pipes," in: *Research and Development of Heat Pipe Technology*, K. Oshima et al., eds., Proc. 5th Int. Heat Pipe Conf., Part 1, JATEC, Tokyo, 1984, pp. 214–219.

9 Busse, C. A., and Loehrke, R. I., "Pressure Recovery in Cylindrical Condensers," in: *Heat Transfer 1986*, C. L. Tien et al., eds., Proc. of 8th Int. Heat Transfer Conf., Vol.. 4, Hemisphere, 1986, pp. 1701–1706.

10 Yan, S. W., "Further Investigation of Laminar Flow in Channels With Porous Walls," *J. Appl. Phys.*, Vol. 27, 1956, p. 267.

11 Yuan, S. W., and Finkelstein, A. B., "Laminar Pipe Flow With Injection and Suction Through a Porous Wall," *Trans. ASME*, Vol. 78, 1956, p. 719.

12 Huesmann, K., and Eckert, E. R. G., "Investigation of Laminar Flow and the Transition to Turbulence in Porous Tubes With Uniform Injection Through the Wall" (in German), Wärme- und Stoffübertragung, Vol. 1, 1968, pp. 2–9.

Journal of Fluids Engineering

Discussion

Velocity Fluctuations at the Walls of a Packed Bed of Spheres for Medium Re-Numbers[1]

W. E. Stewart.[2] The authors' new data on the distribution of axial exit velocity from a packed bed are interesting. Laser velocimetry is used in this study to measure angular averages of the velocity directly, in the manner proposed by Wang et al. (1978). The effects of inserted rods on the velocity profile are determined, and the fluctuations observed during the measurements are described. The traverses are done with an unusually fine mesh (1/47 of the tube radius), in a plane 4 mm above the mean height of the bed.

The quality of the data is impressive. However, the interpretation is difficult, because the outlet free space is a zone of rapid flow redistribution as shown by the measurements of Vortmeyer and Schuster (1983). Furthermore, the last layer of packing is likely to be atypical, with some particles protruding (as mentioned at the beginning of Section 3) and deflecting the flow from those locations. For both reasons, one expects systematic differences between the present velocity data and the averaged profiles inside the bed. In particular, spatial fluctuations of the interior flow distribution on a length scale of order d_p are likely to be masked by larger features in the redistributed downstream flow; thus the present data do not prove their absence.

The velocity peaks near the tube wall reported here are lower and broader than those observed by Price (1967) at the exits of beds of spheres, and by Stephenson and Stewart (1986) inside beds of cylinders. These differences, too, may be attributed plausibly to flow redistribution in the 4-mm space between the present authors' packed bed and the plane of their velocity measurements.

Additional References

Price, J., "The Distribution of Fluid Velocities for Randomly Packed Beds of Spheres," *Mech. Chem. Engng. Trans. Aust.*, MC4, 1968, pp. 7–14.

Stephenson, J. L., and Stewart, W. E., "Optical Measurements of Porosity and Fluid Motion in Packed Beds," *Chem. Engng. Sci.*, Vol. 41, 1986, pp. 2161–2170.

Vortmeyer, D., and Schuster, J., "Evaluation of Steady Flow Profiles in Rectangular and Circular Packed Beds by a Variational Method," *Chem. Eng. Sci.*, Vol. 38, 1983, pp. 1691–1699.

Wang, C. P., Bernard, J. M., and Lee, R. H., "Feasibility of Velocity Field Measurement in a Fluidized Bed with a Laser Anemometer," *Proc. of the Int. Workshop on Laser Velocimetry*, July 11–13, 1978, West Lafayette, Ind.

Hsueh-Chia Chang.[3] The authors indicate that the most surprising discovery of their detailed experimental investigation is that the interstitial velocity profile across the cross-section of a packed bed of spheres does not correlate well with the void fraction distribution at the Reynolds numbers they investigated. Intuitively, one would expect the velocity to be largest where the void fraction is largest. Instead, they find little fluctuation of the velocity profile and when it does fluctuate, it does so with characteristic period larger than the sphere diameter.

This phenomenon has actually been reported by Leron and Froment [1] as early as 1977. In fact, our previous modeling efforts on the radial dispersion of solutes, which require the detailed velocity profile, have taken care to avoid direct correlation between the two profiles [2].

The cause for this lack of correlation is not yet clear. The authors suggest that the unmeasured radial component of the velocity field somehow finishes the fluctuation. We suggest another possible cause. Both the velocity and void fraction distributions are spatially averaged quantities. It is true that the measurement volume for the authors Laser-Doppler apparatus is sufficiently small that it should be able to resolve the spheres. However, since the authors also azimuthally average their measurements by rotating the bed, this resolution would be smoothed out. This certainly is reflected in the conventional empirical correlation for the void fraction [3] which shows no or little fluctuation except for the slight increase near the bed wall. In this connection, it would be extremely interesting to delineate the azimuthal dependence of the velocity field at a given radius. We suspect that it probably will have a period of fluctuation close to the sphere diameter. The authors can easily extract this information from their present data by accounting for the rotational speed of the cylinder.

Additional References

1 Leron, J. J., and Froment, G. F., "Velocity, Temperature and Conversion Profiles in Fixed-Bed Catalytic Reactors," *Chem. Eng. Sci.*, Vol. 32, 1977, p. 853.

2 Chang, H.-C., "A Non-Fickian Model of Packed-Bed Reactors," *AIChE J.*, Vol. 28, 1982, pp. 208–214.

3 Kalthoff, O., and Vortmeyer, D., "Ignition/Extinction Phenomena in a Wall-Cooled Fixed-Bed Reactor," *Chem. Eng. Sci.*, Vol. 35, 1980, p. 1637.

Compressor Erosion and Performance Deterioration[1]

C. Balan.[2] Over the past years considerable effort has been expanded in both the development of erosion resistant materials as well as in improving the ability to compute the flow of particles through turbomachines. The overall objectives of the research is to reduce the problems related to ero-

[1]By R. H. Bahnen and C. G. Stojanoff, published in the September 1987 issue of the JOURNAL OF FLUIDS ENGINEERING, Vol. 109, p. 242.

[2]Department of Chemical Engineering, University of Wisconsin, Madison, Wis. 53706.

[3]Department of Chemical Engineering, University of Notre Dame, South Bend, Ind.

[1]By W. Tabakoff published in the September 1987 JOURNAL OF FLUIDS ENGINEERING, Vol. 109, p. 297.

[2]Cincinnati, Ohio 45215-6301.

Conference Report

Second International Conference on Laser Anemometry Advances and Applications Strathclyde, Scotland, 21–23 September 1987

By C. F. King[1]

Following their UK Symposium at the University of Durham in December, 1983 and a three day International Conference at the University of Manchester in December, 1985, this conference was organised by the LDA Users Group to follow the same successful format of having five internationally recognised invited lecturers, a wide range of refereed papers and a commercial exhibition of the latest instrument by all the leading manufacturers of laser equipment.

The invited lecturers each addressed a specific area of the LDA field. Bachalo's review of the evolution of particle size and velocity measurement technology and Boutier's of three dimensional laser velocimetry systems gave excellent overviews of two advancing fields while Wigley's lecture on laser anemometry techniques in internal combustion engines and that of Dybbs and Edwards on refractive index matching for difficult situations both gave detailed recommendations for the application for LDA techniques in very demanding situations.

It was observed at the first of this series of international conferences that there was a lack of feedback into the computational modelling of turbulent flows of data obtained using LDA. Here, two years later, Gosman presented an invited lecture on the application of LDA measurements to computational fluid dynamics. In his lecture he stressed the complementarity of LDA and computational fluid mechanics (CFM), LDA providing the boundary condition information and data for validation and development of computer models while CFM may be used to plan and guide LDA experiments, minimising data requirements and assisting in interpretation of results. He suggested that the full benefit of the interaction is best achieved in collaborative programmes using both LDA and CFM, with combustion and multiphase flow problems seen as the most demanding and fruitful areas for future collaborative research.

It is refreshing to observe that the field of laser anemometry is one where the applications drive the technical advances. The demand for techniques capable of making measurements in situations with very difficult access has given rise to index matching. Dybbs and Edwards have developed considerable expertise in this field which they have applied to flows in rod bundles, porous media and within the boundary layer roughness elements. In his presentation of the lecture Dybbs stressed the practicalities of the technique and the ability to obtain significant fluid dynamic information in these important flow fields which are unapproachable with other methods. The problems of making measurements in rod bundles and the results obtained using index matching were also demonstrated by the authors of contributed papers.

Wigley described the making of measurements in internal combustion engines as the application of a very powerful innovative technique in an essentially conservative industrial environment. He emphasised the need for a measurement technique capable of providing good quality data quickly and reliably to a conservative and cost conscious industry. The need for data from an otherwise hostile and non-invadable environment points to LDA as the correct tool but the genius of its application rests firmly on meticulous and painstaking attention to detail in the design and use of the system adopted. The internal combustion engine field is one which is being tackled by a number of research groups using LDA and contributed papers examined the variation of swirl velocity and of turbulence in the compression stroke as a function of crank angle and of induction throttling.

Three dimensional flow fields have posed challenges for experimentalists for many years and the development of LDA systems capable of making simultaneous measurements of all three components of velocity is a significant step forward. Boutier's review of the great variety of systems able to provide simultaneous measurement of the three components demonstrated the wide range of approaches taken, including three colour systems using three lasing lines of a single argon ion laser as the light source. He pointed out that although acquisition of vast quantities of high quality data is now possible, its presentation in a meaningful and readily grasped form is perhaps as much of a challenge as the development of the acquisition systems themselves.

The interaction of the laser system with the particles carried by a flow has given rise to a whole range of applications and advances. Particle sizing and the simultaneous measurement of velocity has been tackled by a wide range of techniques which Bachalo described as running the gamut from narrow-angle diffraction to wide-angle refractive measurements of light scatter. In his invited lecture he surveyed the techniques and presented sample results from the latest instrumentation. This is a field which is still rapidly advancing with more work needed in developing instrumentation that can perform reliably in very dense, high velocity and irregular-shaped particle environments. The uses to which such techniques are currently being put was also demonstrated by the contributed papers, including the sprays from pneumatic atomizers, pressure nozzles and nebulizers, while other authors described advances in technique, particularly the phase-doppler method. Wet steam droplets and bubbly flows have been investigated using LDA techniques and measurements in combustion and evaporating spray flows were also reported.

Fibre optics continued to be of interest both for miniaturisation and for improved access. Particle image velocimetry, an arriving art, has been applied to flow beneath waves while the flow fields investigated with established LDA techniques range from classical situations such as bluff bodies, cylinder wakes and sudden expansions to environmental flows, around buildings and over and around forest stands of coniferous trees.

The overall impression was of considerable progress in both techniques and fields of application, some exciting new developments in simultaneous particle sizing and velocity measurement with multiple point techniques such as PIV about to develop rapidly with the advent of cheap computing power.

The conference was sponsored by the University of Strathclyde and cosponsored by the royal Aeronautical Society and the Institution of Mechanical Engineers. The five invited lecturers and the forty three refereed papers are published in a conference volume available from BHRA, Publications Department, Cranfield, Bedford, UK. The LDA Users Group intend to hold a third international conference in 1989. A preliminary announcement and a call for papers will be issued in 1988.

[1]GEC Research Ltd., Engineering Research Centre, Whetstone, Leicester, UK.